UNIVERSITY OF DEBRECEN
Faculty of Engineering
Department of Mechanical Engineering

PROCEEDINGS OF THE INTERNATIONAL SCIENTIFIC CONFERENCE ON ADVANCES IN MECHANICAL ENGINEERING (ISCAME 2014)

09-10 October, 2014 Debrecen, Hungary

Edited by **Dr. Sándor Bodzás**
Dr. Tamás Mankovits

Kiadó: **University of Debrecen**
Faculty of Engineering
Department of Mechanical Engineering
4028 Debrecen, Ótemető str. 2-4.
Telefon: +36-52-415-155
Fax: +36-52-415-155 (77777)
Web page: www.eng.unideb.hu/gepesz

ISBN 978-963-473-751-3

PROCEEDINGS

OF THE

2nd INTERNATIONAL SCIENTIFIC CONFERENCE ON ADVANCES IN MECHANICAL ENGINEERING (ISCAME 2014)

09-10 October, 2014 Debrecen, Hungary

Organisational Chairman of the ISCAME 2014

MANKOVITS Tamás, Ph.D., University of Debrecen, HU

tamas.mankovits@eng.unideb.hu

Scientific Program Comittee

BUDAI István, Ph.D., University of Debrecen, HU

BODZÁS Sándor, Ph.D., University of Debrecen, HU

FAZEKAS Lajos, Ph.D., University of Debrecen, HU

KALMÁR Ferenc, Ph.D., University of Debrecen, HU

KULCSÁR Balázs, Ph.D., University of Debrecen, HU

RÁTHY Istvánné, Ph.D., University of Debrecen, HU

SZABÓ Tamás, Ph.D., University of Miskolc, HU

SZŰCS Edit, Ph.D., University of Debrecen, HU

TIBA Zsolt, Ph.D., University of Debrecen, HU

TÓTH János, Ph.D., University of Debrecen, HU

TÓTH László, D.Sc., University of Debrecen, HU

Technical Assistance

BAK Judit, University of Debrecen, HU

CONTENTS

TRENDS AND SOME ACTUAL MECHANICAL CHALLANGES IN LIFTING MACHINE'S DEVELOPMENT

[1]BOHÁCS Gábor, Dr., [2]ODONICS Boglárka, [3]GYIMESI András

[1]*Department of Materials Handling and Logistic Systems*
gabor.bohacs@logisztika.bme.hu

[2]*Budapest University of Technology and Economics*

Abstract
Lifting machines build one of the most important groups of industrial machinery. However these machines belong one of the oldest of mankind's history development at this area is far not yet over. New production philosophies and systems, ever increasing automation creates a continuous and solid background for this. The development's main areas include not only new machine structures, application of intelligent sensors and informatics but new structural materials and drive units as well. Mechanical issues cannot be neglected regarding these machines either. Important questions from mechanical issues have significant role regarding realization of the machines. These can be vibrational and deformation issues, control of various mechanisms. Our special interest focuses now on the contact of driven and towed wheels as this question is essential during the fine positioning of forklift type materials handling machines in automatic operational mode. The paper gives a short overview on the applicable mechanical models as well.

Keywords: *Lifting machines, towed wheels, forklifts, cranes.*

1. INTRODUCTION

Complex industrial machinery can fail even upon small technical details, which we suppose that is already well known. This must be however avoided during an early phase of the development. In the framework of a research project focusing on the improvement of constructional logistics processes (KTIA- AIK-12-1-2013-0009) funded by the National Development Agency a demonstrational construction system is also to be realized. In the current state of the research a demonstrational system is to be realized, where the transport vehicle is substituted by an automatic guided vehicle [1]. This vehicle should operate in confined spaces, which raise extra requirements on the kinematics. Besides this actual application the examined situation arise in other application fields as well. The next section presents such a possible application.

2. TRENDS IN LIFTING MACHINES' DEVELOPMENT

There are some general trends, such as application of new materials, system integration, and increasing suitability to various production philosophies such as Lean. New constructions are typical as well, In this area cost effectiveness is one of the main issues. Main points of the developments is however automation, increasing intelligence and decentralised control. These principles have effect of the machines' construction as well. Most frequently used machines in production facilities are the automated guided vehicles. These may have diverse

constructions, some examples are presented in Figure 1.

AGVs' most frequent application field in manufacturing plants is transportation. These are frequently organized in routes which result in the so-called Milkrun systems (Figure 2. [2]). These are essential components of the implementation of Forklift-Free Factories. This one is an important concept in intralogistics: it aims that the materials supplied to the assembly lines must be in an appropriate form for further handling without additional materials handling devices. This means usage of small storage containers, which can be lifted by human workers and roller carriages.

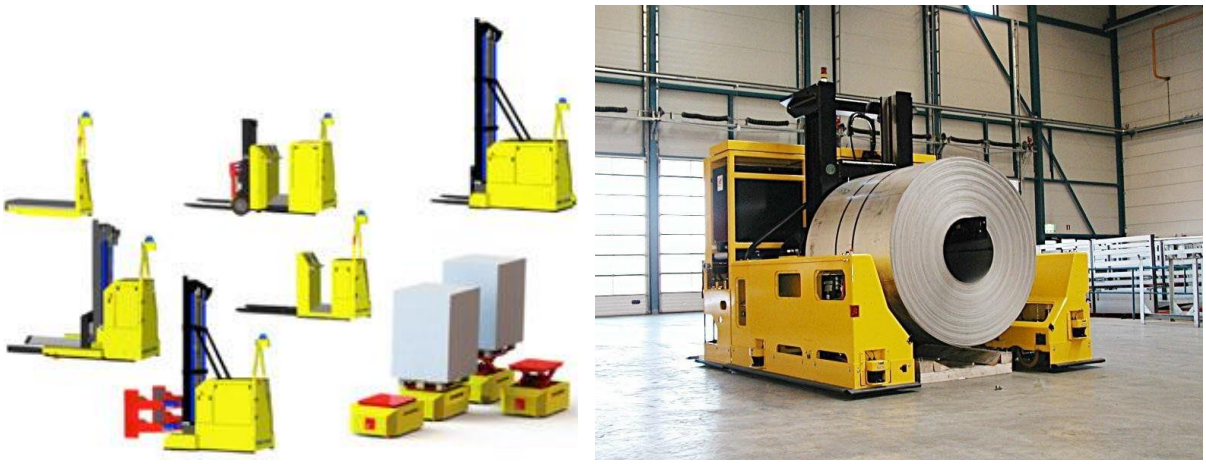

Figure 1. AGV types

This concept has only one significant disadvantage. The Milkrun trains have limited freedom of movement, therefore, these can only pass by the assembly lines, cannot go deeper. However it would be preferable, because the materials are required at different locations.

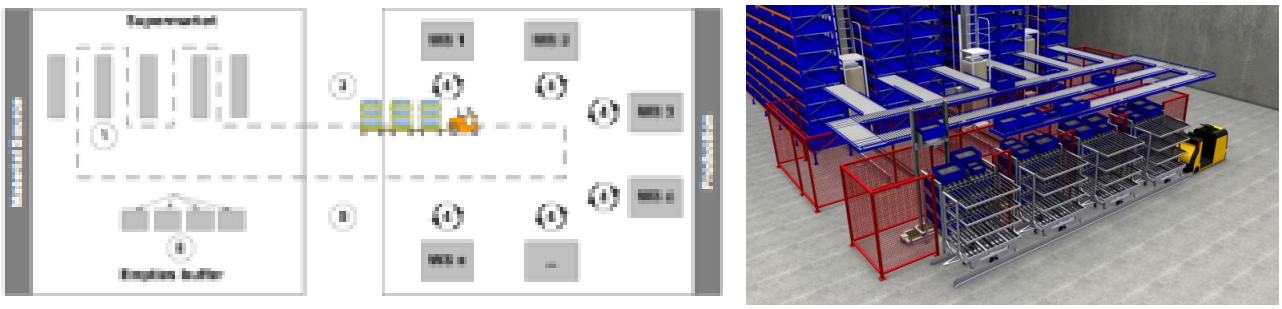

Figure 2. Milkrun principle

From the above problem comes the idea of a smaller scale AGV, which is able to operate deeper in the assembly and manufacturing zones. This machine would require as free kinematics as possible. Because of economic issues in our concept we decided for the differential drive. Figure 3. shows the proposed vehicle's top view. It has two driven and one castor (towed) wheel in the middle.

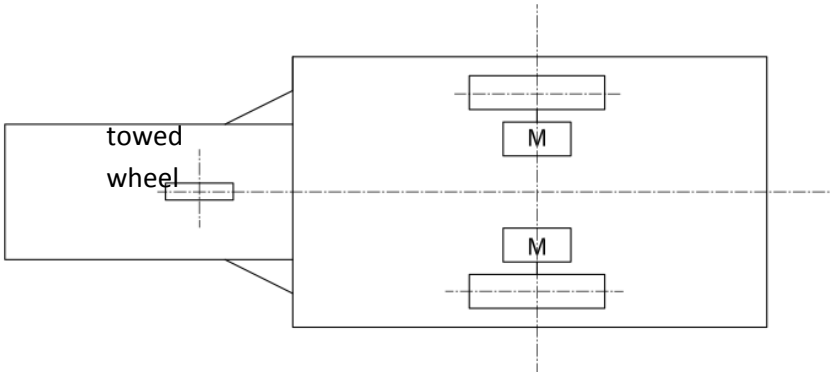

Figure 3. Concepted AGV

Motion control of this vehicle is expected to be difficult. It should be considered that such a system has several complex subsystems. First of all, navigational information comes from complex sensors. The AGV will move upon this information using conventional electric DC drives. The final motion path is however influenced by the mechanical problems as well. One of the top issue is the connection between the flooring and the wheel.

Dynamic models are principally used for the vehicles control, like the one shown in Figure 3. In this model the castor wheels role is simplified. However unregular motion of this wheel has significant effect.

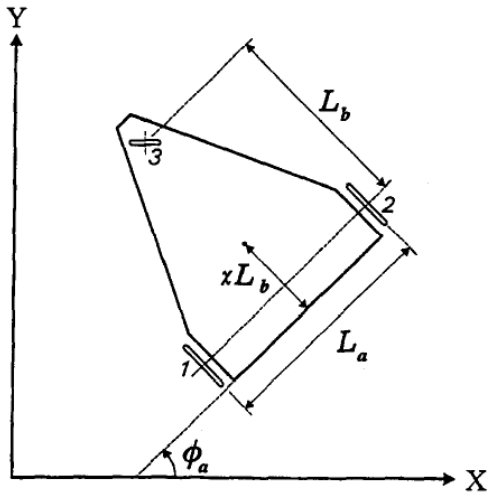

Figure 4. Simple mechanical model of trolley without shimmy [3]

In the “Dynamics of towed wheels” dissertation Dénes Takács and Gábor Stépán dr. [4] analyse the effect of the lateral vibration of towed wheel. Using two different small degree of freedom mechanical model, they show that what kind of effects the lateral vibration have for the linear stability of the rigid wheel and a flexible wheel model [Figure 4].

The flexibility of the towed wheel suspension and the FTS structure, and also the flexibility of the towed wheel material cause this lateral vibration, the shimmy. For this reason, the system will be unstable. In general the system has many vibration spectrum and the wheel-surface connection can not be well determined. Therefore simulate the effect of the shimmy is inexact/incorrect.

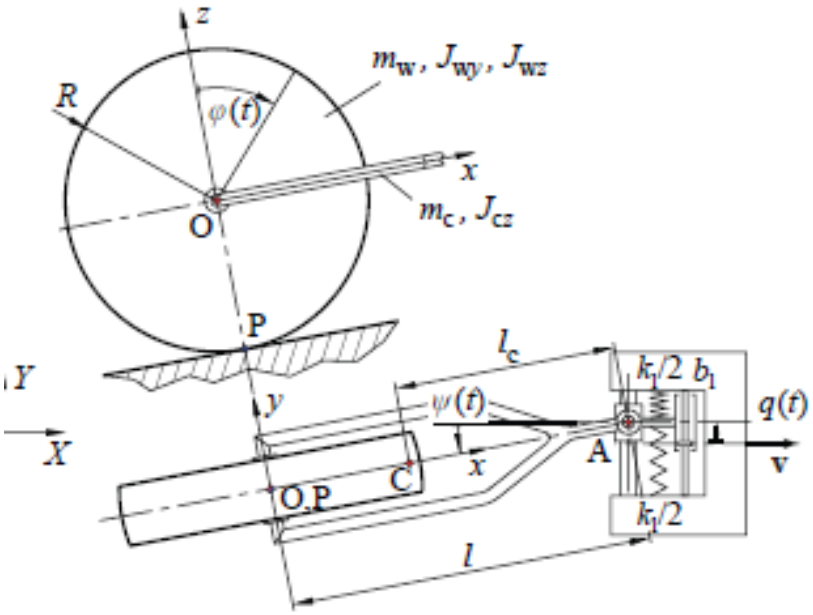

Figure 5. Mechanical model of towed rigid wheel [2]

In our case we analyse the effect of the towed wheel instability during the turning. At the start of the turning, the shimmy may cause divergence from the trajectory. Therefore, by different trajectories the divergence can be reduced.

3. SUMMARY

This paper addresses a specific problem of a special AGV machine. The research is at the modelling phase now, but we expect that model analysis will lead to useful experiences before implementation of the machine itself.

4. REFERENCES

[1] **SCHULZE, L., BEHLING S., BUHRS S.:** *Automated Guided Vehicle Systems: a Driver for Increased Business Performance,* Proc. of the Int. MultiConference of Engineers and Computer Scientists 2009 March 19-21 Hong Kong.

[2] **DEWITZ, M., GALKA, S., GÜNTHNER W.A., S.:** *Drive-Thru Loading Concept for In–Plant Milk Runs*, Proceedings of the XX International Conference MHCL'12, 2012.

[3] **YAVIN Y.:** *Modelling and Control of the Motion of a Trolley: Effect of Motor Dynamics on the Dynamical Model,* Mathematical and Computer Modelling 30, 1999, pp. 141 - 146

[4] **DÉNES TAKÁCS, GÁBOR STÉPÁN DR.:** *Dynamics of towed wheels – Nonlinear Theory and Experiments*, PhD Dissertation, 2010

DETERMINATION OF CONTACT CURVES OF A NEW TYPE CONICAL GEAR DRIVE

[1]BODZÁS Sándor, Dr., [2]DUDÁS Illés, Prof. Dr.

[1]Ph.D., assistant professor
Department of Mechanical Engineering, University of Debrecen,
Debrecen, Ótemető str. 2-4., H-4028
bodzassandor@eng.unideb.hu

[2]D.Sc. professor, professor emeritus
Institute of Production Science, University of Miskolc, Miskolc, Egyetemváros, H-3515
illes.dudas@uni-miskolc.hu

Abstract
With the knowledge of the advantageous characteristics of the cylindrical worm gear drives having arched profile in axial section and the conical worm gear drives with linear profile in axial section, a new geometric type conical worm gear drive has been designed, that is the conical worm gear drive having arched profile in axial section [2]. The objective of the publication is determination of the contact curves between the gear pair elements (conical worm and face gear).

Keywords: *arched profile, contact curve, worm, face gear*

1. INTRODUCTION

The advantages of the conical worm having arched profile in axial section is the concave – convex tooth connection because of which the contact stress between the teeth is lower that is why it could be achieve higher performance than the gear drives having linear profile [1, 3]. Thanks to the arched profile, the load-carrying oil film can be formed more easily between the teeth [3, 5].

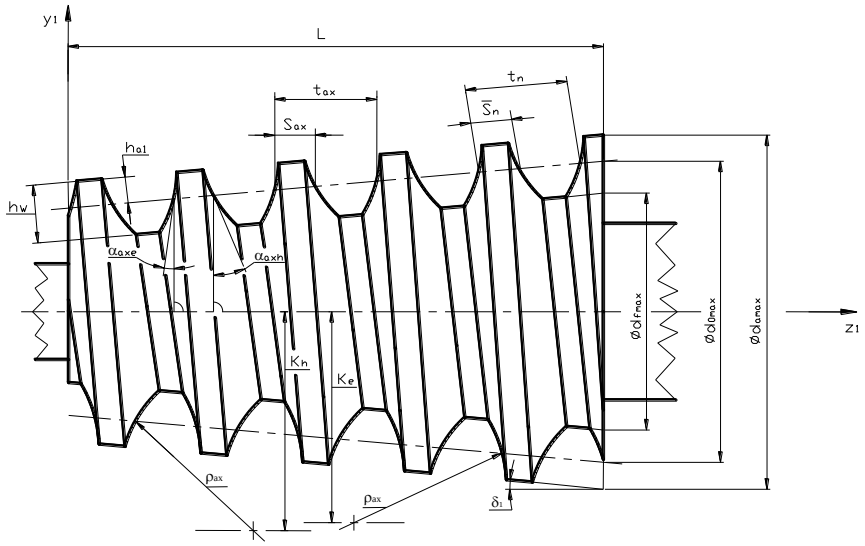

Figure 1. The geometric establishment of conical worm having arched profile [1]

With advisable choice of the centre of the arch radius high dedendum of tooth thickness that is why high tooth strength could be achieved than using linear profile (Figure 1) [1, 3].

The other advantages of the gear drive we can get jointless drives by simply shifting (setting) the worm into an axial direction.

Determination of the contact curves between the conical worm and the face gear is important for the objective of the defining of the geometric establishment and the capacity of the drive pair, the appropriate contact area, etc.

2. DETERMINATION OF THE CONTACT CURVES

In order to draw the spatial coordinates which describes the tooth surfaces at least 4 coordinate systems should be used: for the first member K_{1F} (x_{1F}, y_{1F}, z_{1F}) and for member two K_{2F} (x_{2F}, y_{2F}, z_{2F}) fixed rotational coordinate system, and for member one K_1 (x_1, y_1, z_1) and for the second member K_2 (x_2, y_2, z_2) fixed stationary coordinate systems. Relatively to these coordinate systems, the location of the rotational coordinate system can be drawn [3, 4, 5, 6].

For the determination of the contact curves we could utilize that the two tooth surface wrap each other so the contact points between the surfaces are the points of the both tooth surface.

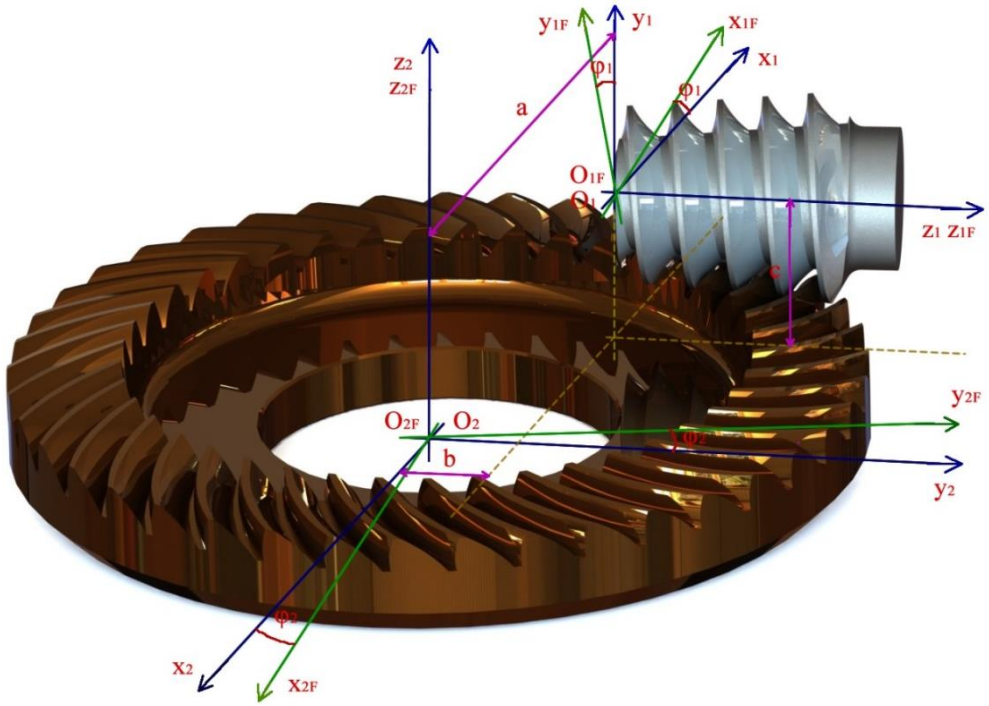

Figure 2. Coordinate systems with bypass axis of rotation in order to draw the tooth surfaces

Given the two parametric vector – scalar function of the conical worm having arched profile [1]:

$$\left.\begin{aligned} x_{1F} &= -\eta \cdot \sin\vartheta \\ y_{1F} &= \eta \cdot \cos\vartheta + p_r \cdot \vartheta \\ z_{1F} &= p_a \cdot \vartheta + \sqrt{\rho_{ax}^2 - (K_e - \eta)^2} \end{aligned}\right\} . \qquad (1)$$

We are looking for the surface fixed to K_{2F} connected to $\vec{r}_{1F} = \vec{r}_{1F}(\eta, \vartheta)$ surface, we can use the fact that during the movement of these two surfaces they wrap each other and taking into consideration that

$$\varphi_2 = i_{21} \cdot \varphi_1 \tag{2}$$

we can state that this wrapping can be described by one motion parameter (φ_1) [5, 6].

On the tooth surfaces of the mashing elements, as a contact line between the wrapping surfaces, can be defined by solving the contact equation which expresses the I. Law of connection

$$\vec{n}_{1F} \cdot \vec{v}_{1F}^{(12)} = \vec{n}_{2F} \cdot \vec{v}_{2F}^{(12)} = \vec{n} \cdot \vec{v}^{(12)} = 0 \tag{3}$$

and vector-scalar function describing the tooth surface (1), at the same time [3, 4, 5], where the matrix of the kinematic motion mapping is:

$$P_1 = \begin{bmatrix} 0 & -1 & -i_{21} \cdot \cos\varphi_1 & -b \cdot i_{21} \cdot \cos\varphi_1 \\ 1 & 0 & i_{21} \cdot \sin\varphi_1 & b \cdot i_{21} \cdot \sin\varphi_1 \\ i_{21} \cdot \cos\varphi_1 & -i_{21} \cdot \sin\varphi_1 & 0 & a \cdot i_{21} \\ 0 & 0 & 0 & 0 \end{bmatrix}. \tag{4}$$

Using the received equations and knowing of the geometric parameters of the worm (Figure 1) we have carried out a computer program for determination of the contact curves (Figure 3, Figure 4).

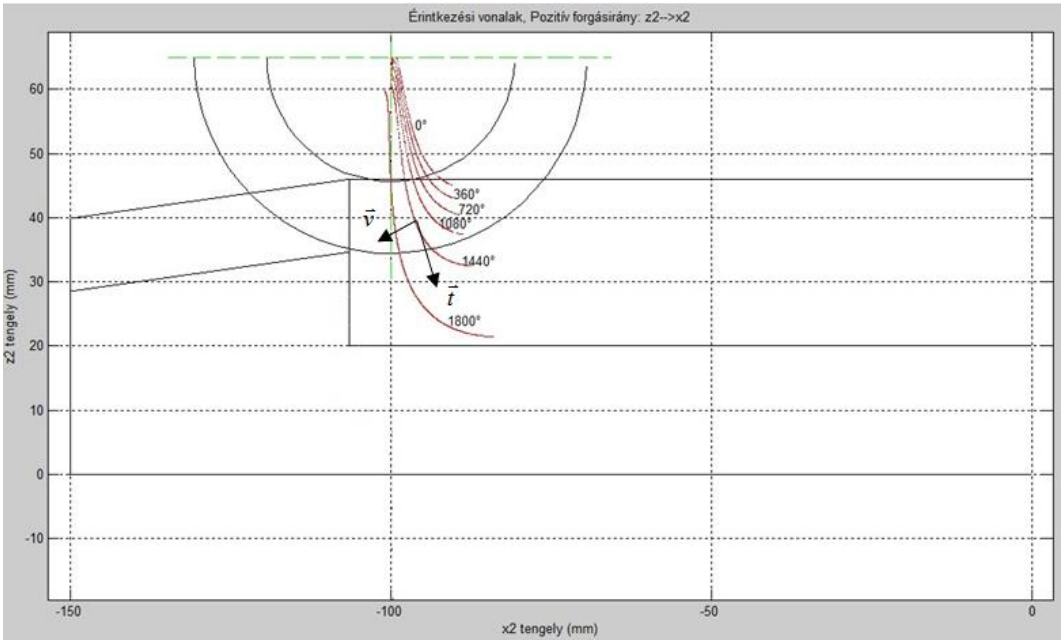

Figure 3. Calculated contact curves on discreet angular displacement (φ_1) values (d_{0k}= 57,522 mm, z_1= 1, m_{ax}= 5 mm, ρ_{ax}= 32 mm, K_e= 37,615 mm, K_h= 45,305 mm, α_{axe}= 11°, α_{axh}= 36°)

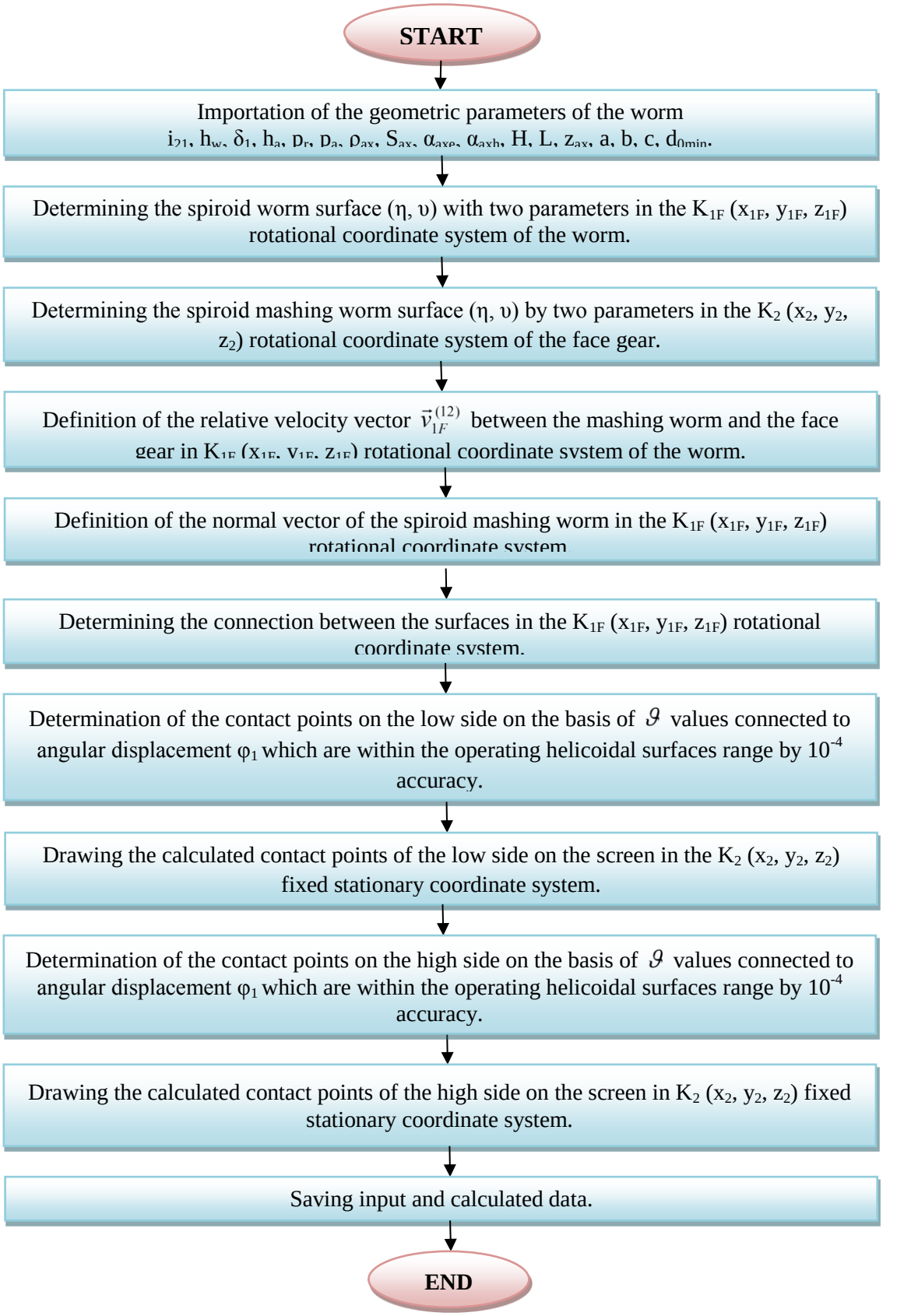

Figure 4. Flowchart of determination of the contact curves

Changing of the worm arc radius (ρ_{ax}) and the axial profile angle (α_{ax}) values we have examined the position of the contact curves.

We have received the optimum position based on adjustment of Figure 3 because in this case the contact curves expands to high surface. The relative velocity vector is nearly perpendicular to the tangent line of the contact curves that is why this gear drive is favourable in terms of assurance of lubrication conditions.

3. CONCLUSIONS

We have carried out a new geometric conical worm gear drive that is the conical worm gear drive having arched profile in axial section [2].

Based on the double wrapping method we have determined the common points of the tooth surfaces of conical worm and face gear that is the contact points in operating helicoidal surfaces range. During wrapping the numbers of the contact points gives the contact curves.

Changing of the geometric parameters of the worm (ρ_{ax} and α_{ax}) we have defined the optimum tooth establishment position in terms of strength and the formation of the appropriate load-carrying oil film.

4. ACKNOWLEDGEMENT

This research was supported by the **European Union** and the **State of Hungary, co-financed by the European Social Fund** in the framework of **TÁMOP 4.2.4. A/2-11-1-2012-0001 'National Excellence Program'**.

5. REFERENCES

[1] **BODZÁS, S.:** *Kúpos csiga-, tányérkerék- és szerszám felületek kapcsolódásának elemzése,* Ph.D. értekezés, Miskolci Egyetem, 2014., p. 154., Doktori témavezető: Prof. Dr. Dudás Illés, DOI 10.14750/ME.2014.006

[2] **DUDÁS, I., BODZÁS, S., DUDÁS, I. SZ., MÁNDY, Z.:** *Konkáv menetprofilú spiroid csigahajtópár és eljárás annak köszörüléssel történő előállítására*, Szabadalmi bejelentés napja: 2012.07.04., Szabadalmi lajstromszám: 229 818

[3] **DUDÁS, I.:** *Csigahajtások elmélete és gyártása,* Műszaki Kiadó, Budapest, 2007. ISBN 978-963-16-6047-0

[4] **HEGYHÁTI, J.:** *Untersuchugen zur Anwendung von Spiroidgetrieben*. Diss. A. TU. Desden, 1988.

[5] **LITVIN, F. L.:** *A fogaskerékkapcsolódás elmélete*. Műszaki Könyvkiadó, Budapest, 1972.

[6] **LITVIN, F. L., FUENTES, A.:** *Gear Geometry and Applied Theory*, Cambridge University Press, 2004., ISBN 978 0 521 81517 8

TOOL CONDITION MONITORING USING MACHINE LEARNING

[1]DEÁK Krisztián, [2]KOCSIS Imre, Dr., [3]VÁMOSI Attila, [4]KEVICZKI Zoltán

[1] *Faculty of Engineering, University of Debrecen*
deak.krisztian@eng.unideb.hu

[2] *Faculty of Engineering, University of Debrecen*
kocsisi@eng.unideb.hu

[3] *Faculty of Engineering, University of Debrecen*
vamosi.attila@eng.unideb.hu

[4] *FAG Magyarország Kft.*
zoltan.keviczki@schaeffler.com

Abstract
On the other hand the late exchange of cutting tool also increases the cost of production because getting parts out of the preset tolerances may require rework for its use, when it does not cause bigger problems such as breaking of cutting tools or the loss of the part. When the flank wear is the limiting tool life, the time predetermination that a cutting tool must be used for the machining occurs within the limits of tolerance can be done without difficulty. Extended Taylor equation predict the time when a certain VB flank value of the tool edge occurs. Sound and vibration measurement in both time and frequency domains along with signal processing techniques have been applied. Intelligent machine learning methods are used to make state decision easier. Some methods are presented for diagnosis and prognosis, artificial neural network (ANN) is created to evaluate the remaining useful life (RUL) of the tool.

Keywords: *machine, tool, wear, diagnosis, machine learning*

1. INTRODUCTION

Millions of products are manufactured daily by a variety of processes. A basic method to form bulk metal into a desired final shape is through the process of metal cutting, also referred to as machining. Metal cutting is essentially the removal of excess material from a workpiece by moving a working tool over the surface of the workpiece at a certain depth, speed, and feed rate. Conventional machining operations are turning, milling, and drilling. Tool wear is the loss of material on the edge of the cutting tool. Although tool wear can be minimized, it cannot be eliminated. Unfortunately, excessive or even a small quantity of tool wear may cause a defect in a machined component. For this reason, many approaches to tool condition monitoring (TCM) have been proposed through the years. Sensor based TCM, and specifically those methods that are based on vibration related properties such as force, acceleration, and acoustic emission (AE). These sensor types are known to be most effective for TCM. Excellent overviews of sensor assisted TCM, published by Dan and Mathew [9], Byrne et al. [7], Scheffer and Heyns [28, 29].

2. TOOL WEAR

2.1. Tool wear modes

Tool wear is caused by mechanical loads, thermal loads, chemical reactions, and abrasive loads. The load conditions are in turn influenced by the cutting conditions and materials. The different loads can cause certain wear mechanisms that may occur in combination [8].

- Abrasive wear resulting from hard particles cutting action
- Adhesive wear associated with shear plane deformation
- Diffusion wear occurring at high temperatures
- Fracture wear due to fatigue

Other wear mechanisms are plastic deformation and oxidation, which are not very common in industry. It is estimated that 50% of all tool wear is caused by abrasion, 20% by adhesion, 10% by chemical reactions and the remaining 20% by the other mechanisms [14]. Abrasion is basically the grinding of the cutting tool material. The volume of abrasive wear increases linearly with the cutting forces. Higher hardness of the tool material can reduce the amount of abrasive wear. During adhesion, the high pressures and temperatures on the roughness peaks on the tool and the workpiece cause welding. These welding points are broken many times every second due to the workpiece movement and as a result cause removal of the tool material [14]. Diffusion wear occurs at even higher cutting speeds, where very high temperatures are present (especially when using hard metal tools). There are some wear types: nose wear, flank wear, crater wear, notch wear, chipping, cracking, breakage, plastic deformation. (Figure 1.) [8].

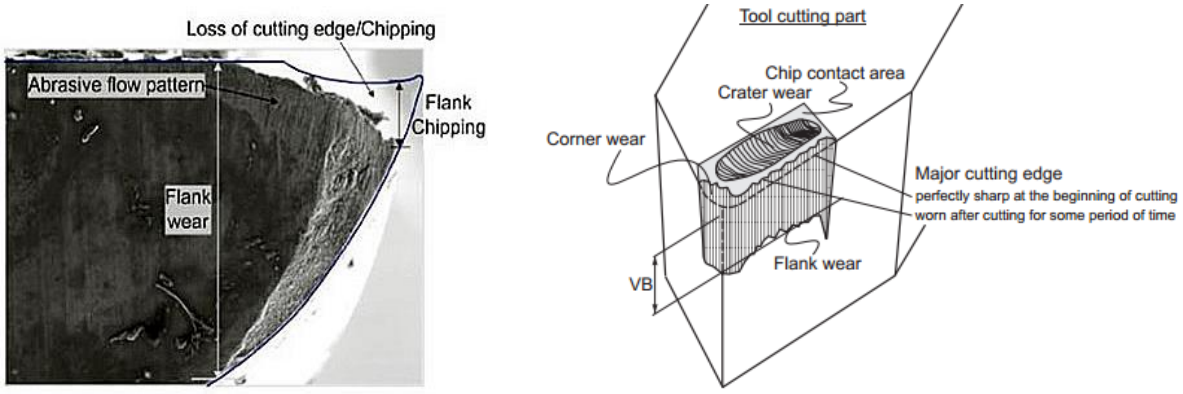

Figure 1. Cutting tool wear modes [38, 39]

The most widely researched tool failure modes for turning with single point tools are flank wear, breakage (fracture), and crater wear. Flank and crater wear are accepted as normal tool failure modes, because the other failure modes can be avoided by selecting the proper machining parameters. The growth of flank and crater wear is directly related to the total cutting time, unlike some of the other failure modes.

Estimation of tool wear during CNC milling using neural network-based sensor fusion was implemented by Ghosh et.al [22]. On-line metal cutting tool condition monitoring using multi-layer perceptron neural networks was studied by Lister and Dimla [10]. Tool condition monitoring using artificial intelligence methods has been carried out by Balazinski et.a l [18].

Cho and Ko estimated tool wear length in finish milling using a fuzzy inference algorithm [33]. Intelligent process supervision for predicting tool wear in machining processes was done Alique by and Haber [26]. Prediction of flank wear by using back propagation neural network modeling when cutting hardened H-13 steel with chamfered and honed CBN tools is used by Ozel and Nadgir [34] Also tool cutting force modeling in ball-end milling using multilevel perceptron was implemented by Zuperl and Cus [35]. Rivero et.al [3] worked on tool wear detection in dry high-speed milling based upon the analysis of machine internal signals and Orhan et.al [27] evaluated tool wear by vibration analysis during end milling of AISI D3 cold work tool steel with 35 HRC hardness. Furthermore tool wear perdition from acoustic emission and surface characteristic via an artificial neural network has been carried out by Wilkinson and Reuben [8, 25].

2.2. Taylor equation for prediction the tool life

The simple Taylor equation for tool life estimation is:

$$V_C * T^n = C \tag{1}$$

where C: tool life [min], V_c: cutting speed [m/min], T: cutting time [min]
The extended Taylor equation is more complex:

$$T=C * V^A * f^B * ap^D * VB^E \tag{2}$$

where C: tool life [min], Vc: cutting speed [m/min], T: cutting time [min], ap: depth of cut [mm], VB flank wear [mm], f: feed [mm/rev], A,B,C,D,E: algebraic structure parameteres of Taylor equation.

The most important wear type from the process point of view is the flank wear, therefore the parameter which has to be controlled is the width of flank wear land, VB. This parameter must not exceed an initially set safe limit, which is about 0.4-0.6 mm for carbide cutting tools. VB is influenced by the cutting parameters and the stage of wear of the tool (Figure 2.).

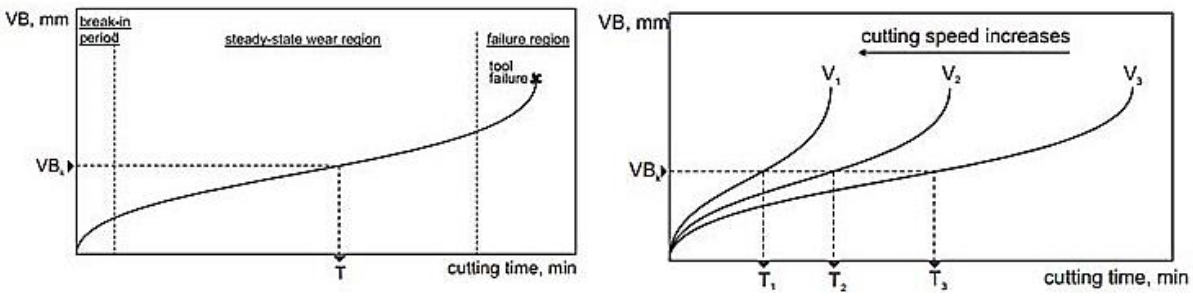

Figure 2. Taylor curves for tool life expectancy [38, 39]

3. TOOL WEAR MEASUREMENT

Tool Wear Measurement Wear measurements of tool inserts are done through the implementation of an appropriate international standard, ISO 3685. Flank wear is quantified in terms of VB, which is the mean of the wear height on the tool flank. The length of flank wear is also measured in terms of b. (Figure 3.)

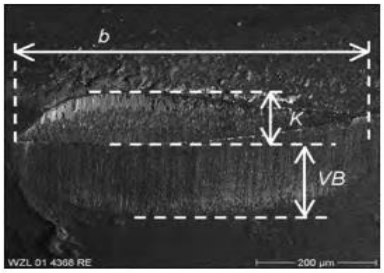

Figure 3. Tool wear measurement method [8]

Tool wear stages: it is assumed by most authors that tool wear consists of an initial, a regular, and a fast wear stage [37].

4. TOOL CONDITION MONITORING (TCM)

Direct and indirect systems: TCMSs can be divided in two categories, namely, direct and indirect. Direct methods are concerned with a measurement of volumetric loss at the tool tip, while indirect methods use a pattern in sensor data to detect a failure mode [7]. Direct methods do not utilize vibration and will not be discussed here. In general, direct methods are sensitive to dirt and cutting chips, and consequently they are not commonly accepted in industry. Indirect methods have found more acceptance in industry due to the fact that most indirect methods are easily interpreted, cost effective, and often more reliable than direct methods.

4.1. Vibration measurement

Acceleration measurement uses piezoelectric accelerometers can measure the machine vibration caused by oscillations of cutting forces. It is well known that high frequency vibrations (higher than 1 kHz) yield large acceleration levels, giving accelerometers an advantage over force based monitoring. Vibration measurement is a very good tol for analyzing bearings, gearboxes and rotary machines and it is sufficient way to obtain information about tool wear as well. Wei et al. used vibration analysis based on EMD for wind turbine gearbox pitting fault detection [17]. Various authors have shown that acceleration levels change with tool wear. Scheffer et al. [28, 30] reported on the use of an accelerometer for wear monitoring during hard turning. It was found that certain frequencies show repeatable amplitude increase with increasing tool wear. These frequencies corresponded to the tool holder natural frequencies. Some authors, for example, Bonifacio and Diniz [5], also found that a wear sensitive frequency will increase with increasing tool wear and then suddenly decrease near the end of tool life. This can be attributed to an increased damping effect due to plastic deformation and microbreakage of the cutting edge [8].

One of the main difficulties of monitoring tool wear with vibration is to identify the frequency range that is influenced by tool wear, since machining processes entail various mechanisms that produce vibrations that are not related to tool wear. The frequency range of vibrations produced during ordinary machining operations usually falls between 0 and 10 kHz. From the literature, it can be concluded that the frequency range sensitive to tool wear depends entirely on the type of machining operation, and must be determined experimentally for each individual case.

Table 1 Typical tool wear vibration frequencies

Authors	Wear frequency [Hz]
Jiang and Xu [36]	0-117, 520
Rao [6]	1850, 3200, 4800
Akihito and Fujita [21]	500-800
Pandit and Kashou [19]	4300-4700
Weller et al. [12]	0-4000
Martin et al. [24]	2000-2500
Fag et al. [11]	0-150, 2000-2500

According to Jiang and Xu [36] the tool wear process can be divided into five stages: initial stage of wear, regular stage of wear, micro-breakage stage, fast wear stage and tool breakage. Rao [6] indicated the 1850, 3200, 4800 Hz frequencies for TCM. Further researches [21, 19, 12, 24, 11] revealed other frequencies when tool vibration could be detected. (Table 1.)

It was found that the total amount of vibration energy in the frequency range of 4-8 kHz increased as the length of the cutting edge wear-land increased.

There are two important vibration frequencies present during cutting, the natural frequencies of the tool holder and its components, and the frequency of chip formation.

The chip formation frequency can be calculated with simple equations that take the machining conditions into account. The tool holder natural frequencies and chip formation frequency are independent. Generally, tool wear has a larger effect on the vibration amplitudes at the tool holder natural frequencies but can influence chip formation frequencies as well.

Another phenomenon important to machining operations is tool chatter vibrations. These are self excited vibrations resulting from the generation of different chip thicknesses during machining. Initially, cutting forces excite a structural mode of the machine workpiece system. This leaves a wavy surface finish on the workpiece.

Vibration monitoring is wide spread method because of its simplicity and cost-effectiveness. Both velocity and acceleration sensors are attached on the machine/ bearing house to obtain signals. It is important to fix the sensors properly either with glue or magnet or screw with regards to the frequency limit requirements. For data acquisition, DAQ units are used, sometimes compact units like National Instrument CompactRio (Figure 4.) is propagated with Labview software application where virtual instruments (VIs) could be built. CompactRio has an own computer, FPGA unit, Ethernet connection up to 8 slots for DAQs creating a versatile, flexible measurement.

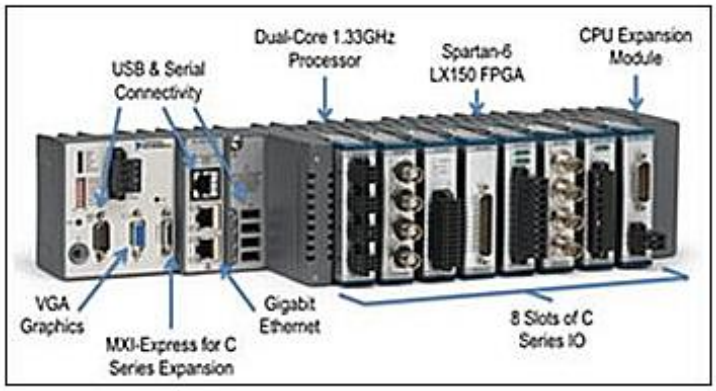

Figure 4. NI CompactRio measurement device [20]

4.2. Sound measurement

Sound from a machining operation measured, for example, near the cutting zone on a lathe contains a variety of cutting information. Some components of this sound have been used to monitor conditions of the cutting edge.

Low frequency noise spectra resulting from the rubbing action of the tool and workpiece were used to monitor tool flank wear [1]. A significant increase of the noise level in the frequency range 2.75-3.50 kHz occurred, ranging from 9 to 24 dB [8].

Machine noise exhibited a characteristic frequency at around 4-6 kHz for a large variety of workpiece-material combinations and operating conditions. The sound pressure level (SPL) at the characteristic frequency showed good correlation with tool wear. The SPL dropped off before the rapid increase in the maximum flank wear VBmax which showed the reaching of the tertiary wear zone. [8, 15].

5. SIGNAL PROCESSING TECHNIQUES

Signal Processing for Sensor-Based Tool Condition Monitoring is basically feature extraction step that is probably the most important step, because here the sensor signals must be condensed and reduced to only a few appropriate wear sensitive values.

Time domain analysis extracts features from the time domain are usually fundamental values such as the signal mean or RMS. Other techniques include the shape of enveloping signals, threshold crossings, ratio between time domain signals, peak values, and polynomial approximations of time domain signals. Time domain analysis is widely used monitoring method. Mostly Root Mean Square (RMS), Kurtosis, skewness, peak value, Crest Factor are calculated.

Frequency domain is the power or energy of certain frequency bands in the fast Fourier transform (FFT) is often suggested as a feature for TCM. It is very challenging to identify spectral bands that are sensitive to tool wear. It is even more difficult to determine exactly why these frequencies are influenced by tool wear. Power in certain bands will often increase due to higher excitation forces because of the increase in friction when the tool starts to wear.

Sometimes a peak in the FFT will also shift due to changing process dynamics as a result of tool wear. Some authors suggest that two frequency ranges be identified from the original signal by Bonifacio and Diniz [5]. The one range must be sensitive to tool wear, the other

must be insensitive. For instance, if the measurement was made from 0 to 8 kHz, it must be split (using appropriate filters) into a 0 to 4 kHz signal and a 4 to 8 kHz signal.

Statistical processing: In the case of statistical features, signals are assumed to have a probabilistic distribution, and consequently, useful information can be extracted from the statistics of the distribution. The main features are those that describe the probability distribution of a random process (variance, standard deviation, skewness, kurtosis, etc.) and coefficients of time series models. There are also miscellaneous other statistical features, such as cross correlations, the coherence function, and the harmonic mean. The use of statistical process control (SPC) methods is also reported by some authors.

Trending, RUL estimation: A very simple decision making technique is to trend features and to establish threshold values. When a certain feature or set of features crosses a threshold value, an estimation of the tool condition can be made.

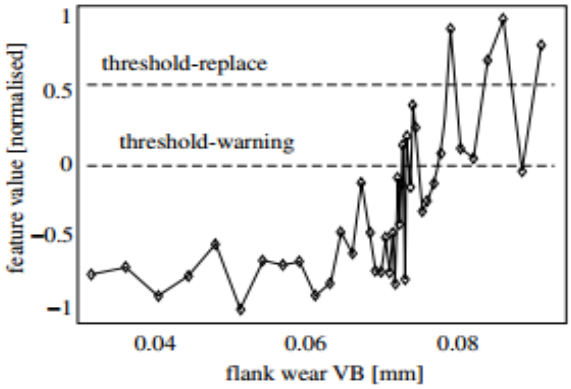

Figure 5. Remaining useful life (RUL) estimation and thresolding

Time–Frequency domain: the most common time frequency domain processing method in TCM applications is STFT and wavelet analysis. It is often stated that wavelets are used because they provide information about the localization of an event in the time as well as in the frequency domain. Lee and Tarng [16] use the discrete wavelet transform for cutter breakage detection in milling and find that the technique is reliable even under changing machining conditions. Wavelet is used as a filter to enhance wear sensitive features in the signals. However, the results are not compared with conventional digital filtering. A comparative study between wavelets and digital filtering for tool wear monitoring was carried out by Scheffer [28]. It was found that, although the wavelet packets act as automated filters, a very similar (if not better) result could be achieved with appropriate digital filtering. Wavelet transform is a versatile, effective method for processing of noisy signals. Wavelets have been established as more effective tools in machine fault diagnosis. Wavelet transforms have advantages over traditional Fourier transforms for representing functions that have discontinuities and sharp peaks, and for accurately deconstructing and reconstructing finite, non-periodic and/or non-stationary signals. Both discrete wavelet transform (DWT) and continuous wavelet transform (CWT) are continuous-time transforms.

$$STFT\,\{f(w,t)\} = \int_{-\infty}^{+\infty} f(t) * g(t-u) * e^{-\mathrm{j}wt}\,dt \tag{3}$$

$$CWT\ (a,b) = \frac{1}{\sqrt{a}} \int_R^R \gamma\ (\frac{t-b}{a})f(t)dt \tag{4}$$

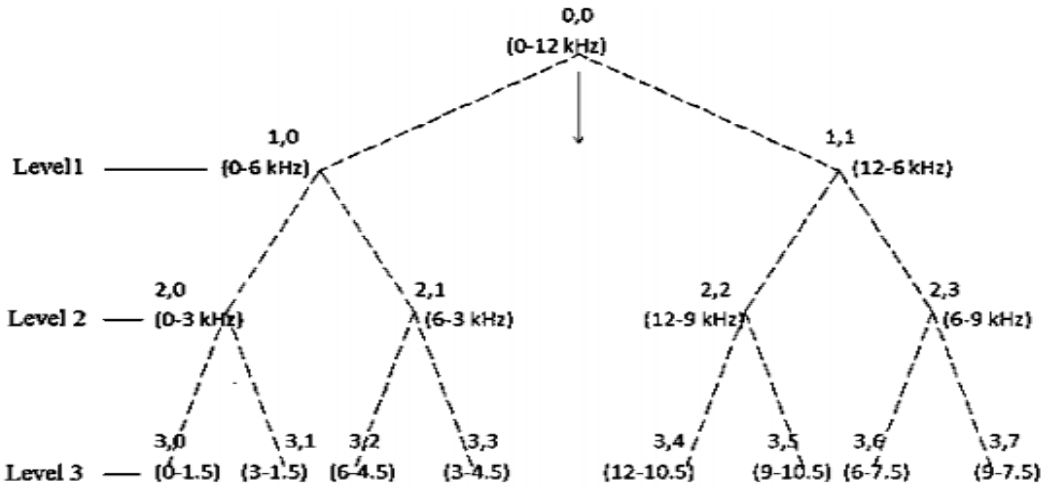

Figure 6. Wavelet decomposition tree based on frequency division

6. MACHINE LEARNING METHODS FOR TCM

The use of Neural Networks (ANNs) as a secondary, more sophisticated signal processing and decision making technique is often found in TCM applications. The simultaneous utilization of many features and the robustness towards distorted sensor signals are two of the most attractive properties of ANNs. Neural networks also assist in the fusion of sensor information for TCM. In other words, combining features from acceleration, AE, and force signals in a ANN can result in a method that can predict the tool condition with increased accuracy, researched by Silva et al. [31]. The successful implementation of ANNs is dependent on the proper selection of the network structure, as well as the use of the correct training and testing methods. It is important to make a distinction between supervised and unsupervised ANN paradigms. Unsupervised ANNs are trained with input data only, and are usually used for discrete classification of different stages of tool wear. Supervised ANNs are trained with input and output data, and these are used for continuous estimations of tool wear
Artificial Neural Networks (ANNs) make the inspection and diagnosis of the system easier and faster. Human inspection does not give precise, accurate information about the machine condition especially in subtle and sensitive operation conditions. ANNs have their own learning capacity so they are good tools for analyzing even complicated machines and devices. Therefore, using ANNs in condition monitoring are getting wide spread besides other intelligent machine learning methods, like Fuzzy methods, Support Vector Machines (SVM). The multi-layer feed-forward , radial basis function , wavelet neural networks, Adaptive Neuro-Fuzzy Inference System (ANFIS), Multi Layer Perceptron (MLP), and Self Organizing Map (SOM) are among the most referenced networks both in rotary machine and tool condition monitoring.

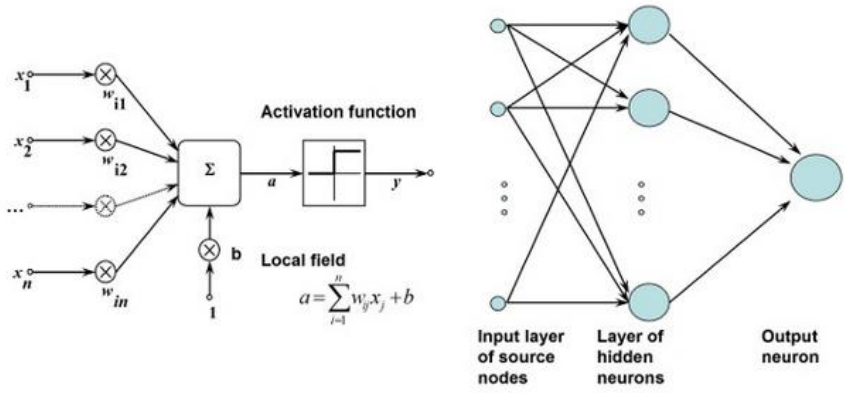

Figure 7. ANN structure and topology

7. EXPERIMENT

7.1. Cutting machine, tool, material and parameters

Cutting lathe used in the experiment is showed in Figure 8. Cutting tool is covered by wear resistant coat to withstand the harsh condition during cutting. TiC, TiN, CrN, Al2O3, CBN, PCBN coats can increase wear resistance significantly.

Figure 8. Turning machine and tool in experiment

Machine: Optimum D 280 x 700 G lathe
Tool: CNGA120408S01030A, ISO, CB7015, Chamfer: 0.25 mm × 25◦Cutting-edge radius: 0.01 mm
Tool holder: DCLNR 2525M 12-2
Workpiece: ABNT 1038 (AISI 1038), Composition: C 0.93% – 1.05%, Si 0.15 – 0.35%, Mn 0.25 – 0.45%, Cr 1.35 – 1.60% Hardness: HRC62
Diameter: 50 mm, length of cut: 100 mm / Cutting speed: 150, 170, 200, 300 m/min / Feed speed: 0.1, 0.2, 0.3, 0.4 mm/rev / Depth of cut: 1, 2, 3, 4 mm
Coolant condition: dry

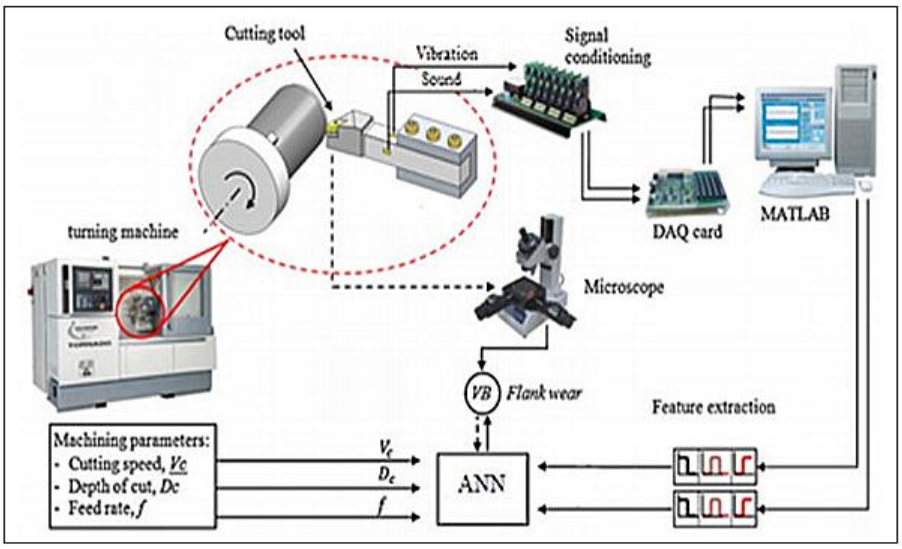

Figure 9. System of the experiment

Microscope for VB measurement: Olympus PX61
Vibration sensor: PCB 603 C01 and Soundbook 3D axis vibration sensor, microphone: electric
DAQ sound and vibration kit and data processing software : NI 9234 DAQ, Labview 2013
Optional sound and vibration control system: Soundbook professional measurement tool with its SINUS Samurai software (Figure 10.)
Sound processing software: Audacity
Neural Toolbox for ANN topology construction
PC for data analysis: Acer Aspire 5542G

Nowadays, the machining of the hardened steels is spreading in the practice more and more. The hard turning can be a good alternative solution to the grinding machining in several cases. The turning operation produces chips, being totally recyclable and re-usable, while grinding operations generate not recyclable slurry, containing the material pieces of the grinding grits and metal particles as well.

7.2 Vibration measurement for TCM

The NI 9234 is a 4-channel C Series dynamic signal acquisition module for making high-accuracy audio frequency measurements from integrated electronic piezoelectric (IEPE) and non-IEPE sensors with NI CompactDAQ or CompactRIO systems. The NI 9234 delivers 102 dB of dynamic range and incorporates software-selectable AC/DC coupling and IEPE signal conditioning for accelerometers and microphones. The four input channels simultaneously digitize signals at rates up to 51.2 kHz per channel with built-in anti-aliasing filters that automatically adjust to your sampling rate.

Figure 10. NI 9234 DAQ sound and vibration modul with PCB603 sensor (left) and Labview program (middle), Soundbook for vibration measurement for TCM

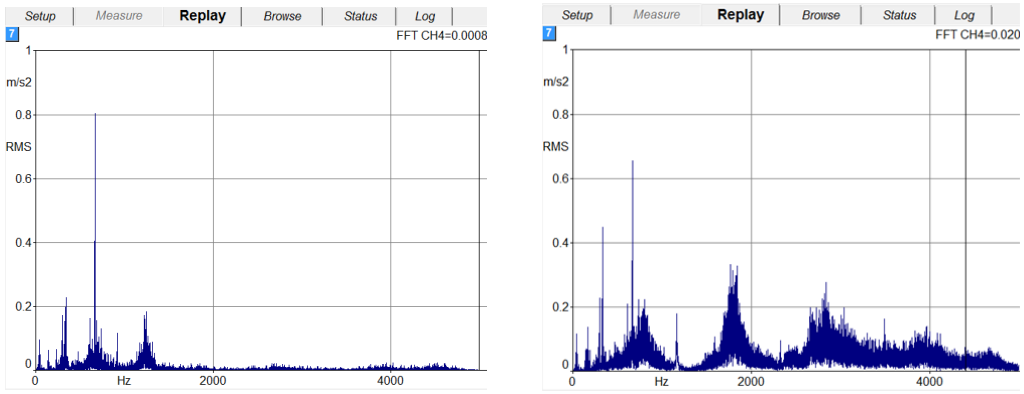

Figure 11. Frequency of an excellent tool edge /VB=0,05 mm/ (left) and frequency of a worn tool edge /VB=0,4 mm/

Figure 11 on the left shows the specrum of an intact tool. Most energy of the spectrum falls between 0-1000 Hz. If it is compared to the right hand image certain frequencies are increased in the weared tool spectrum. Peaks emerge 1800 Hz and around 2500..3000 Hz.

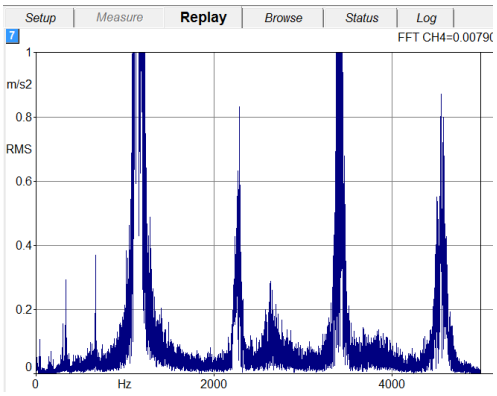

Figure 12. Frequency spectrum of chatter phenomena, /VB= 0,4 mm/

Figure 12 shows a very good example for the machine chatter phenomena. Self-excited vibration causes extreme peaks in the spectrum. During machining typical harsh sound can be detected that ruin the surface topology of the workpiece therefore it should be avoided.

7.3. Sound measurement for TCM

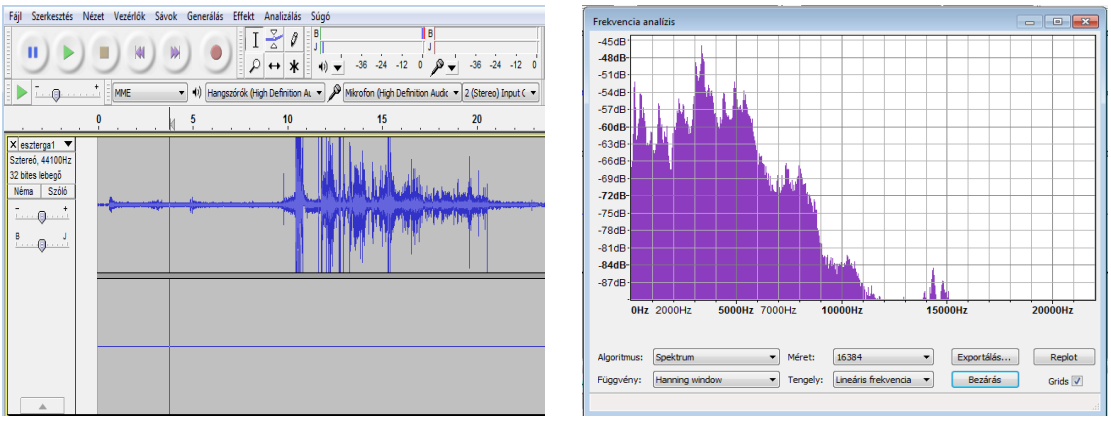

Figure 13. Sound pressure level values (left) and sound spectrum of a normal tool with intact edge /VB=0,05 mm/ cutting after FFT by Audacity software (right)

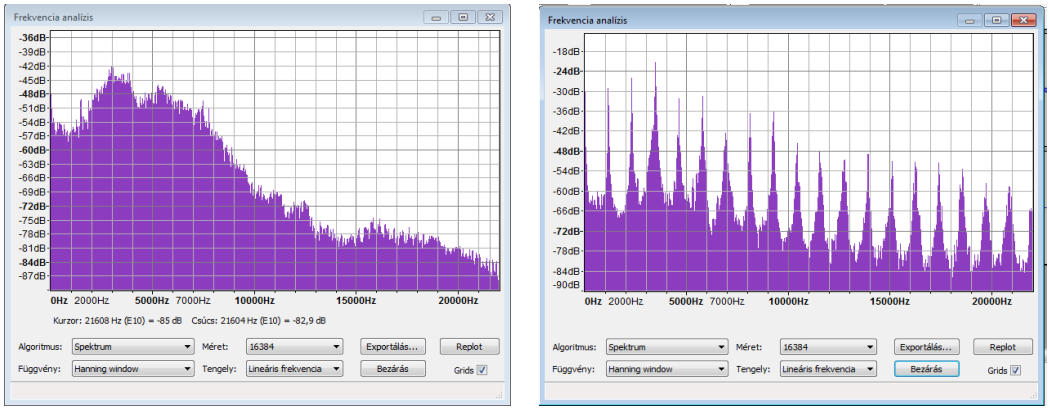

Figure 14. Sound spectrum of a normal tool cutting with worn edge /VB=0,4 mm/ after FFT by Audacity software (left) and the sound spectrum of chatter phenomena after FFT by Audacity software

Figure 13 describes the noise amplitude and the sound spectrum of the cutting process after Fourier transform. All figures are made in Audacity software. Between 10…11 s chatter occurred in the experiment as Figure 14 shows. Typical repeated peaks emerge in the spectrum which perfectly describes this damaging technological phenomena. After 11 s normal cutting process was recorded, then its FFT spectrun was created as Figure 13 presents it on the right side. In the Figure 14. on the left side the spectrum of the worn tool is presented. To compare to the spectrum of the new tool edge spectrum higher SPL values were measured in high frequencies above 10 KHz which might be a precursor of the tool edge wear on the basis of these experiments.

7.4. Taylor equation and flank wear calculation for RUL

Tool wear describes the gradual failure of cutting tools due to regular operation. VB flank wear describe the tool wear rate with good efficiency, coefficients were determined as see below.

$$T=1.86 * 10^{6} * V^{-1.92} * f^{-0.78} * ap^{-0.20} * VB^{2.22} \quad (5)$$

$$VB=1.90 * 10^{-3} * V^{0.84} * f^{0.31} * ap^{0.06} * T^{0.40} \quad (6)$$

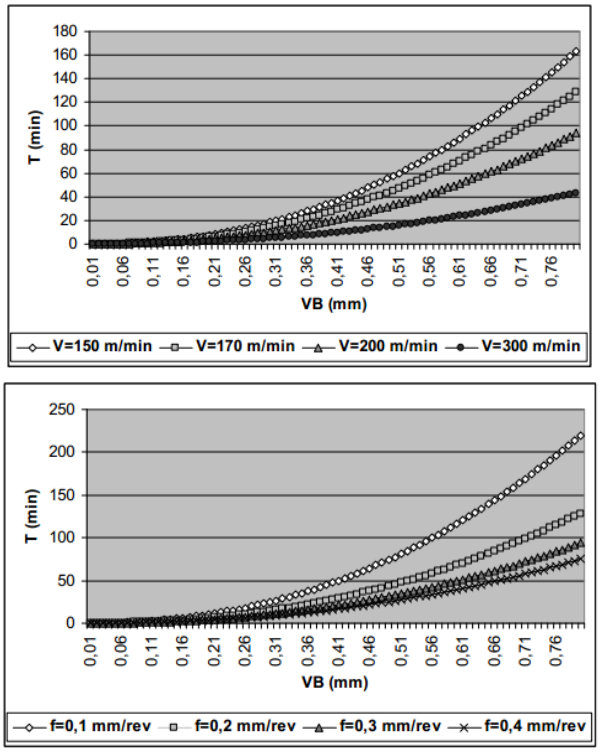

Figure 15. Influence of cutting speed (left) and feed (right) on tool life for different flank wear [23]

To determine the parameters of the algebraic structure Taylor the following cutting conditions were used: cutting speed = 100, 140, 180 and 220 [m/min], feed = 0.2,

0.3, 0.4, 0.5 and 0.6 [mm/rev] and depth of cut of 1.5; 3.0 and 5.0 [mm] for ABNT 1038 (AISI 1038), and these parameters cutting were combined in different ways. The 227 values of flank wear (VB) were measured at eight different cutting conditions [23]. The cutting tool was cemented carbide, P20 type, insert square, with rake angle γ = -6°, clearance angle α= 6° and cutting edge angle χ= 75°. Figure 15, 16 show the change of VB values because of the cuttting parameters on the basis of the previous measurements [23]. Figure 17. represents the accelaration values in the cutting time that shows exponential growth on the basis of the measurements.

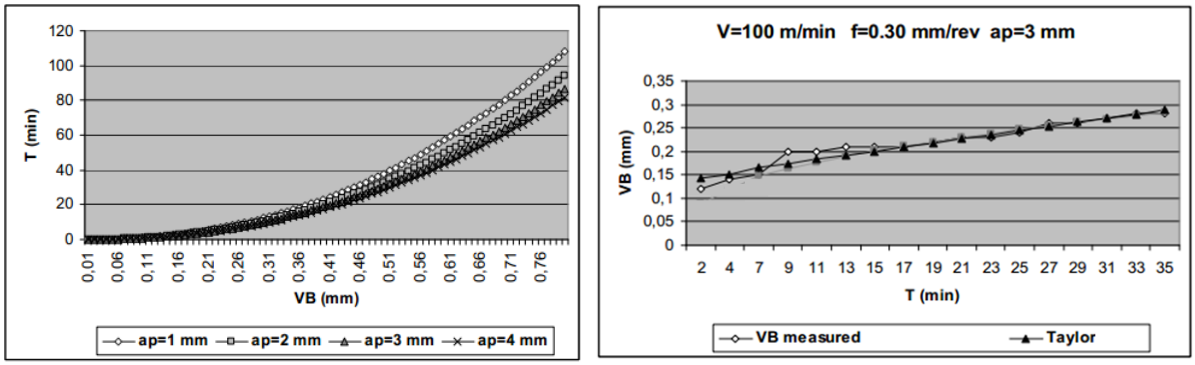

Figure 16. Influence of depth of cut (left) on tool life for different flank wear [23] and VB measured –VB calculated curve (right)

Table 2. Results of the measurement: Influence of cutting speed on tool life for different flank wear, f = 0.3 [mm / rev], ap = 2 [mm]

v [m/min]	150	170	200	300	VB[mm]
T [min]	52,51	41,27	30,19	13,81	0,3
T [min]	57,52	45,22	33,09	15,12	0,5
T [min]	163,42	128,25	93,82	43,01	0,8

Table 3. Measured and calculated flank wear (VB) values, vibration levels, speed V=100 [m/min], feed f=0.30 [mm], ap=3 [mm]

T [min]	VB measured [mm]	VB calculated [mm]	Vibration level [m/s^2]
2	0,12	0,1432	5,42
4	0,14	0,152	5,94
7	0,15	0,1652	6,12
9	0,2	0,174	6,68
11	0,2	0,1828	6,71
13	0,21	0,1916	6,95
15	0,21	0,2004	7,48

17	0,21	0,2092	7,39
19	0,22	0,218	8,11
21	0,23	0,2268	9,46
23	0,23	0,2356	10,89
25	0,24	0,244	12,51
27	0,26	0,2532	14,58
29	0,26	0,262	16,87
31	0,27	0,2708	19,12
33	0,28	0,2796	21,2
35	0,28	0,2284	24,6

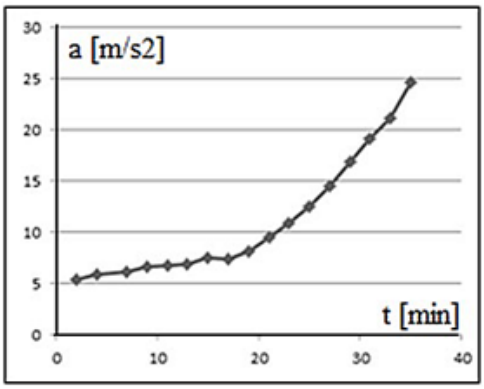

Figure 17. Tool vibration average measured values during the cutting process

7.5 Optical measurement of VB flank wear and digital image processing

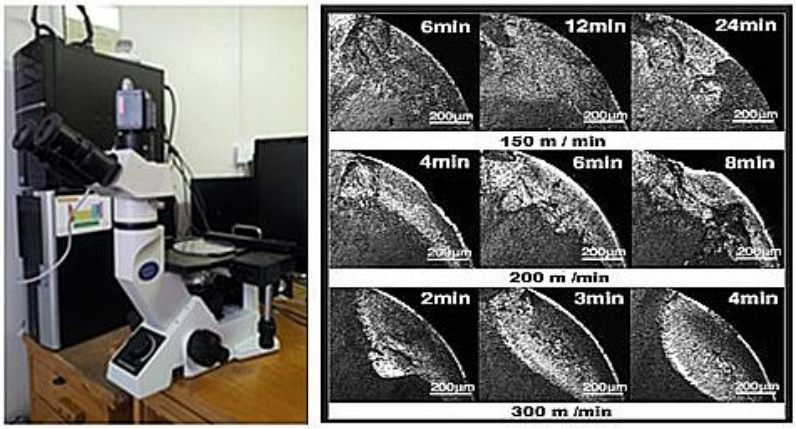

Figure 18. Olympos BX61 optical microscope with analytic software (left) and tool edge wear at different cutting speeds in time (right)

Here, in this article and experiments LOM and SEM miscoscopes were used to the 2D image acquisition. Then, it was necessary to remove background noise by filtering in order to

assure that sensor noise does not introduce false information. Images were pre-processed to extract some specific piece of information. Contrast enhancement was applied to assure that relevant information can be detected. Feature extraction is the extraction of image features at various levels of complexity. Edge detection was used to detect edges of the wear regions. Prewitt edge detector was used and compared to Sobel detector that produced higher efficiency. Thresholding was applied to set and determine the gray value percentage of the LOM and SEM images. Segmentation helped to divide the digital image into multiple segments to simplify and/or change the representation of an image into something that is more meaningful and easier to analyze. Figure 18. presents the wear of the tool edge in defferent times from 2…24 minutes.

8. ARTIFICIAL NEURAL NETWORK (ANN) FOR TOOL CONDITION DIAGNOSIS AND RUL ESTIMATION

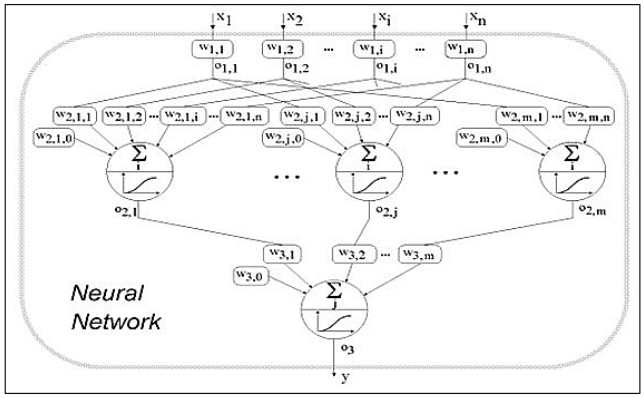

Figure 19 ANN structure for TCM applied in the experiment

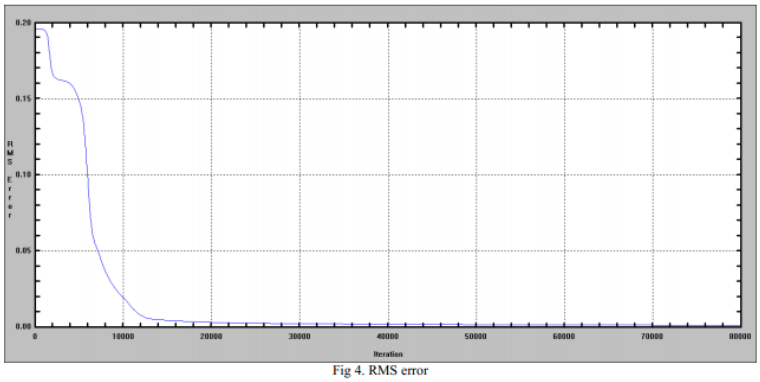

*Figure 20. Root Mean Squared (*RMS) error in the number of iterations of the ANN

In this section, based on the experimental data, the tool life modeling and prediction is carried out by using multi layer perceptron (MLP) neural networks. MLP neural network is one of the most popular supervised (ANN) which has the ability to solve nonlinear problems. A four-layer (MLP) is used, including 5 inputs (cutting speed, feed rate, depth of cut, average vibration acceleration, average SPL level), 2 hidden layers containing 5 neurons, and an output layer with a single neuron (VB flank wear). (Figure 19.)

Hidden layers must have equitable covering rate on learning data therefore, the best architecture and parameters of the (MLP) model are chosen through several tests which are not presented in this paper. Sigmoid, Gaussian and Hyperbolic Scant transfer functions have been applied for neurons of hidden and output layers, respectively. The obtained Root Mean Squared (RMS) error and correlation between the estimated and experimental data is presented in Figure 20.

9. CONCLUSION

Tool condition monitoring (TCM) is very important in all technological process. With TCM tool breakdowns can be reduced, tool ware is estimated and the remaining useful life (RUL) of the tool as well. Tool life is desribed by Taylor equation influenced by cutting parameters. Tool wear modes was descibed in this article, flank wear (VB) had a good correlation with the tool condition. VB was measured by directly and indirectly. Vibration and sound level measurement were applied in the research, then spectrum by Fourier transform was created. Direct VB measurement under optical microscope was used to compare indirect and direct values. Hard turning in dry condition was used due to its enviromental friendly behaviour and precision. Vibration and sound values increased significiantly in certain frequency ranges as VB flank wear became larger. Five input parameters (depth of cut, speed, feed rate, vibration acceleration, sound pressure values) and one output parameter (VB flank wear) descibed the multi layer perceptron (MLP) neural network that was created. As the number of iteration increased the error value decreased, minimal error was detected in the research. Later, ANFIS, SVM machine learning methods will be applied to compare the efficiency of different systems. More parameters will be used (cutting force, temperature, surface roughness) to create a hybrid expert measurement.

10. REFERENCES

[1] **A. B. SADAT, S. RAMAN:** *Detection of tool flank wear using acoustic signature analysis*, Wear 115, 1987., pp. 265-272.

[2] **AMIR MAHYAR KHORASANI, MOHAMMAD REZA SOLEYMANI YAZDI ,MIR SAEED SAFIZADEH:** *Tool Life Prediction in Face Milling Machiningof 7075 Al by Using Artificial Neural Network(ANN) and Taguchi Design of Experiment (DOE)*, IACSIT International Journal of Engineering and Technology, Vol.3, No.1, 2011, ISSN: 1793-8236

[3] **A. RIVERO, L.N. LÓPEZ DE LACALLE, M. L. PENALV:** *Tool wear detection in dry high-speed milling based upon the analysis of machine internal signals*, Mechatronics, Vol 18, 2008., pp. 627–633.

[4] **A. SOKOLOWSKI, J. KOSMOI:** *Utilization of vibration measurements of machine tool elements in the monitoring of the cutting tool condition*, Proc. 4th World Meeting On Acoustic Emission and 1st Znt. Conf on Acousfic Erntksion in Manufacturing, 1991, pp. 327-333.

[5] **BONIFACIO, M.E.R. AND DINIZ, A.E.:** *Correlating tool wear, tool life, surface roughness and tool vibration in finish turning with coated carbide tools*, Wear, 173, 1994, pp. 137 144.

[6] **B.S. RAO:** *Tool wear monitoring through the dynamics of stable turning*, Trans. ASME, J. Eng. Zndust., 1986, pp. 108.

[7] **BYRNE, G., DORNFELD, D., INASAKI, I., KETTELER, G., KONIG, W., AND TETI, R.:** *Tool Condition Monitoring (TCM) The status of research and industrial application*, Ann. CIRP, 44, 1995, pp. 541-567.
[8] **CLARENCE W. DE SILVA:** *Vibration and shock handbook*, 2005, ISBN 0-8493-1580-8
[9] **DAN, L. AND MATHEW, J.:** *Tool wear and failure monitoring techniques for turning a review*, Int. J. Machine Tools Manuf., 1990, 30, pp. 579-598.
[10] **D.E. DIMLA SR. A, P.M. LISTER:** *On-line metal cutting tool condition monitoring.II: tool-state classification using multi-layer perceptron neural networks*, International Journal of Machine Tools & Manufacture, Vol 40, 2000, pp 769–781.
[11] **D.X. FANG, Y. YAO and G. AMDT:** *Monitoring groove wear development in cutting tools via stochastic modelling of three dimensional vibration*, Wear, 151, 1991, pp. 143-156.
[12] **J.E. WELLER, M.H. SCHRIER and B. WEICHBRODT:** *What sound can be expected from a worn tool?*, Trans. ASME, J. Eng. Indust., 13, 1969, pp. 525-534.
[13] **J.M. GRUESO, F.A. ROJAS:** *Dimensional Analysis Helps Assess Cost-Performance Tools for Turning*, Machines and Metals Magazine, Brazil, 2009
[14] **KOPAC, J.:** *Influence of cutting material and coating on tool quality and tool life* J. Mater. Process. Technol., 78, 1998, pp. 95-103
[15] **L. C. LEE:** *A study of noise emission for tool failure prediction*, Int. Mach. Tool Des. Res. 26, 1986, pp. 205-215.
[16] **LEE, B.Y. AND TARNG, Y.S.:** *Milling cutter breakage detection by the discrete wavelet transform*, Mechatronics, 9, 1999, pp. 225-234.
[17] **WEI TENG, FENG WANG, KAILI ZHANG, YIBING LIU, XIAN DING**: *Pitting fault detection of a wind turbine gearbox using empirical mode decomposition*, Strojniski vestnik – Journal of Mechanical Engineering 60, 1, 2014, pp. 12-20.
[18] **M. BALAZINSKI, E. CZOGALA, K. JEMIELNIAK, J. LESKI:** *Tool condition monitoring using artificial intelligence methods*, Engineering Applications of Artificial Intelligence, Vol 15 , 2002, pp. 73–80.
[19] **M.S. PANDIT and S. KASHOU:** *A data dependent system strategy of on-line tool wear sensing*, Trans. ASME, J. Eng. Indust., 104, 1982, pp. 217-223.
[20] National Instrument Kft.: http://www.ni.com/compactrio/
[21] **N. AKIHIKO and S. FUJITA:** *Development of a cutting tool failure detec*tor, BUZZ. Jpn. Sot. Prec. Eng., 23., 1989, pp. 134-139.
[22] **N. GHOSH, Y.B. RAVI, A. PATRA, S. MUKHOPADHYAY, S. PAUL, A.R. MOHANTY, A.B. CHATTOPADHYA**: *Estimation of tool wear during CNC milling using neural network-based sensor fusion*, Mechanical Systems and Signal Processing, Vol 21, 2007, pp. 466–479.
[23] **NOEMIA GOMES, JOSÉ EDUARDO, ARIMATEA QUARESMA FERRAZ:** *Life Prediction of Cutting Tool by the Workpiece Cutting Condition Advanced Materials Research*, Vol. 223., 2011, pp. 554 - 563© Trans Tech Publications, Switzerlanddoi:10.4028/www.scientific.net/AMR.223.554
[24] **P. MARTIN, B. MUTE1 AND J.D. DRAPIER**: *Influence of lathe tool wear on the vibration sustained in cutting*, Proc. 15th int. Machine Tool Design and Research Conf., 1974., pp. 251-274.
[25] **P. WILKINSON, R. L. REUBEN**:*Tool wear perdition from acoustic emission and surface characteristic vi a an artificial neural network*, Mechanical Systems and Signal Processing, 13(6), 1999, pp. 955-966.

[26] **R. E. HABER, A. ALIQUE**: *Intelligent process supervision for predicting tool wear in machining processes*, Mechatronics, Vol 13, 2003, pp. 825–849.
[27] **S. ORHAN, A. OSMAN ER, N. CAMUS-CU, E. ASLAN**: *Tool wear evaluation by vibration analysis dur ing end milling of AISI D3 cold work tool steel with 35 HRC hardness*, NDT&E International, Vol 40, 2007, pp. 121–126.
[28] **SCHEFFER, C.:** *Development of a tool wear monitoring system for turning using artificial intelligence*, Ph.D. thesis, 2002, Department of Mechanical and Aeronautical Engineering, University of Pretoria, South Africa.
[29] **SCHEFFER, C. and HEYNS, P.S.:** *Tool condition monitoring systems an overview*, pp. 316 323.International Conference on Competitive Manufacturing (COMA '01), Stellenbosch, South Africa,31 January 2 February, 2001.
[30] **SCHEFFER, C. and HEYNS, P.S.,:** *Wear monitoring in turning operations using vibration and strain measurements*, Mech. Syst. Signal Process., 15, 2001, pp. 1185-1202.
[31] **SILVA, R.J., RUEBEN, R.L., BAKER, K.J., and WILCOX, S.J.**: *Tool wear monitoring of turning operations byneural network and expert system classification of a feature set generated form multiple sensors*, Mech. Syst. Signal Process., 12, 1998, pp. 319-332.
[32] **SILVA, R.J., BAKER, K.J., WILCOX, S.J., AND REUBEN, R.L.**: *The adaptability of a tool wear monitoring systemunder changing cutting conditions*, Mech. Syst. Signal Process., 14, 2000, pp. 287-298.
[33] **T. J. KO, D. W. CHO:** *Estimation of tool wear length in finish milling using a fuzzy inference algorithm*, Wear, Vol 169, 1993, pp. 97-106.
[34] **T. OZEL, A. NADGIR:** *Prediction of flank wear by using back propagation neural network modeling when cutting hardened H-13 steel with chamfered and honed CBN tools*, International Journal of Machine Tools & Manufacture, Vol 42, 2002, pp. 287–297.
[35] **U. ZUPERL, F. CUS**: *Tool cutting force modeling in ball-end milling using multilevel perceptron*, Journal of Materials Processing Technology, Vol 153–154, 2004, pp. 268–275.
[36] **Y.C. JIANG and J.H. XU**: *In-process monitoring of tool wear stage by the frequency band energy method*, Ann. CIRP, 36, 1987, pp. 45-48.
[37] **ZHOU, Q., HONG, G.S., and RAHMAN, M.**: *A new tool life criterion for tool condition monitoring using a neural network*, Eng. Appl. Artif. Intell., 8, 1995, pp. 579-588.
[38] http://www.microsystems.uk.com/english/success_factors_micro-milling_hardened_steels.html
[39] http://me.emu.edu.tr/me364/ME364_cutting_wear.pdf

EVALUTION OF BULLET RESISTANCE OF DIFFERENT STEEL ALLOYS IN ARMY APPLICATION

[1]GÁVAY György, [2]GYARMATI József, [3]SZAKÁL Zoltán, [4]KALÁCSKA Gábor

[1]National University of Public Service, Faculty of Military Sciences and Officer Training, Department of Maintenance, Hungary, Budapest

[2]National University of Public Service, Faculty of Military Sciences and Officer Training, Department of Maintenance, Hungary, Budapest

[3]Szent Istvan University, Faculty of Mechanical Engineering, Institute for Mechanical Engineering Technology, Hungary, Gödöllő

[4]Szent Istvan University, Faculty of Mechanical Engineering, Institute for Mechanical Engineering Technology, Hungary, Gödöllő

Abstract

This paper shows metallographic tests of various plates which were hit by bullets. The aim of our research was to define how the crystal structure of the different kinds of armors changes during the penetration of the bullets. We examined three kinds of plates using different types of bullets. The plates that have been shoot had different hardness and the bullets had various speed. Specimens were made from the proper segments of the damaged armor plates. The examinations of metallographic specimens help us to define the changes of the crystals, especially the cracks as well as the size of the effect zone.

***Keywords**: defense capabilities, armor, material testing*

1. INTRODUCTION

Research and development of armors becomes a very important area for the military and the civil security users nowadays. There is a significant need for good quality armor that has a low weight and great protection again up to date bullets explosives and IED (Improvised Explosive Device). Users of the armors are not only the army but also the police and civil security organizations.

One of the aims of the military industrial developments is enhancing the protective abilities of body armors, but the outcome is used by the police and the security also. The aim of the Research and Development of body armor is to extend the protection against the up to date special bullet that has a great hardness and muzzle velocity. These armors made from metallic and non metallic material also.

Another important application area of the armors is the civilian and the military armor protected vehicles. Using the new demands that based on the experiments of the last decades

new class of armor protected vehicles was developed. These are the MRAP (Mine-Resistant Ambush Protected) that has a great protection again the bullets, mines and IED and it has special quality and shape armor.

Base on the above mentioned and well known area the National University of Public Service, Faculty of Military Sciences and Officer Training, Department of Maintenance in Budapest and the Szent István University, Faculty of Mechanical Engineering, Institute for Mechanical Engineering Technology in Gödöllő launched a joint research. The aim of the research was to describe the material structure changes during the shutting, therefore an experimental test was carried out. The standards about the ballistic resistance of armors don't define the damage of metallic structure [1] [2].

During the test three different kinds of plates was shouted using three different kinds of bullets. In this experiment, 150 shot has been fired. Grindings were made from the proper segment of the bullet hit armor, and examining of these the changes of the crystals was defined especially the cracks.

During the examination of the grindings the next topics was examined:

- the crystal structure of steels;
- the changes of the rolling grain;
- the formation of cracks;
- the size of damaged zone of the plate;
- the fragment formation from the plates;
- the bullet deformation.

2. RESEARCH OBJECTIVES

The original objective of the research was to document the process of bullet penetration through the metallic material.

Plates cut from three steel types with different quality have been used for the examination:

- a hot rolled steel plate with 8 mm thickness;
- 8 mm armour plate of a Russian made armoured vehicle;
- 6.5 mm armour plate that is used for the civil security service vehicles manufactured nowadays.

The aim of the examinations of the hot rolled steel plate was the comparison with the armour plates, so it was used as a reference plate.

The plates were shot with bullets having different material and speed. The speed of the bullet was set with the alteration of the gunpowder charge weight. The following principles have been taken into consideration when planning the impact speed:

- there has to be penetration and dent;
- the damaged plates have to comparable, so the different plates have to be shot with bullets having the same type and speed.

In the interest of credibility all shots having the same parameters were executed three times (with the same cartridge and gunpowder charge, as well as plates having the same material). Based on this the detailed research objectives were the following:

- documentation of the changes happening in the metallic crystal structures of the different steel types;
- identification of the damage zone;
- identification of the defence capability reduction based on the deformation and structural change in case of dent;
- influence of the mechanical properties of steel on penetration;
- influence of the bullet's rigidity on penetration.

3. THE PROCESS OF MEASUREMENT

3.1. Test shooting

An authorized / certified test shooting range was rented for the execution of the test shooting. The shooting range provided us the cartridge for the shooting with the correct gunpowder charge. The shooting was executed with a ballistic test barrel[1]. The main elements of the laboratory are shown by graph 1.

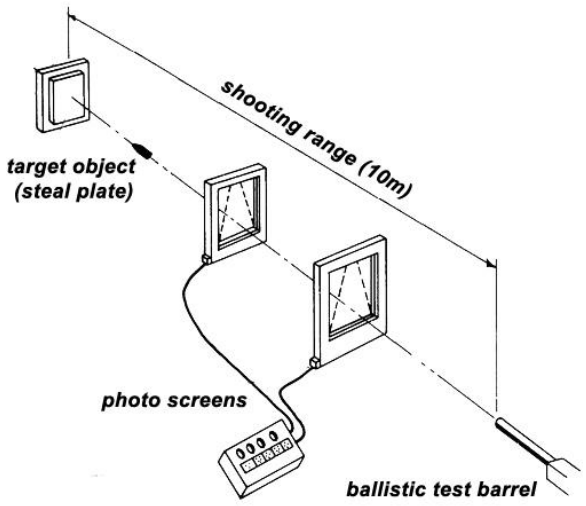

Figure 1. The main elements of the laboratory

3.2. Mechanical researches

The supplier provided a self-certification for the reference plate and 6.5 mm armour plate, mechanical examinations have been carried out on the bullets used for the research and on the 8 mm plate.

The measured and available data of the plates:

- armour plate with 8 mm thickness, the tensile strength (R_m) is 1400 N/mm^2, hardness is 288 HV 30;
- armour plate with 6.5 mm thickness, the tensile strength (R_m) is 1700 N/mm^2;

- tensile strength of the reference plate (R_m) is 400 N/mm^2.

The 8 mm plate contained 1.26% manganese, while the 6.5 mm plate contained 1.18% and the reference plate contained 0.6%. Two different bullets were used for the examination, one with soft steel core and 166 HV30 hardness, the other with carbid core and 905 HV30 hardness.

3.3. Preparation of plates for specimen production

The cutting specimen is shown by graph 2. The cutting took place along the “a”, “d” and “b” edge of graph 2, to make the configuration of the specimens shown on the right side of graph 2 possible. The examination could be carried out in the direction of the strands in the rolled plate (along the “c” edge) and sheer as well (parallel surface with the “a” edge).

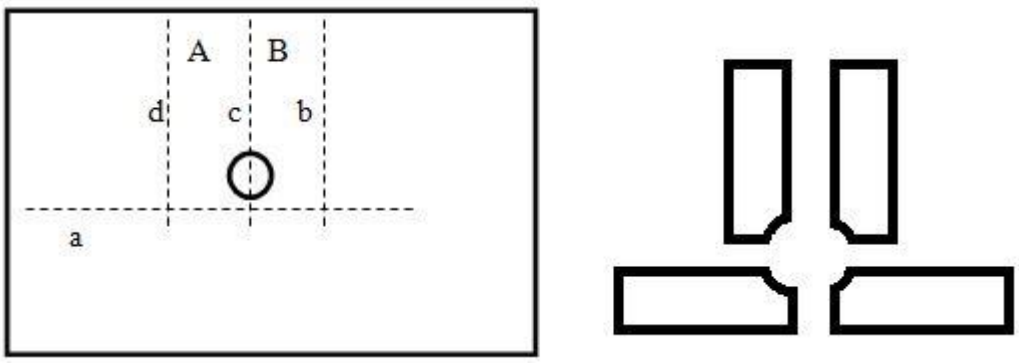

Figure 2. Precut of the plates

3.4. Production of specimens

Figure 3. Specimen

100 ecimens were created during the research. Figure 3 shows a specimen.

3.5. Analysis of specimens

The specimens were analysed on the faculty of Mechanical Engineering of SZIE. The prepared specimens were examined with a microscope. Figure 4 a and 4b show the damaged surfaces of the examined materials.

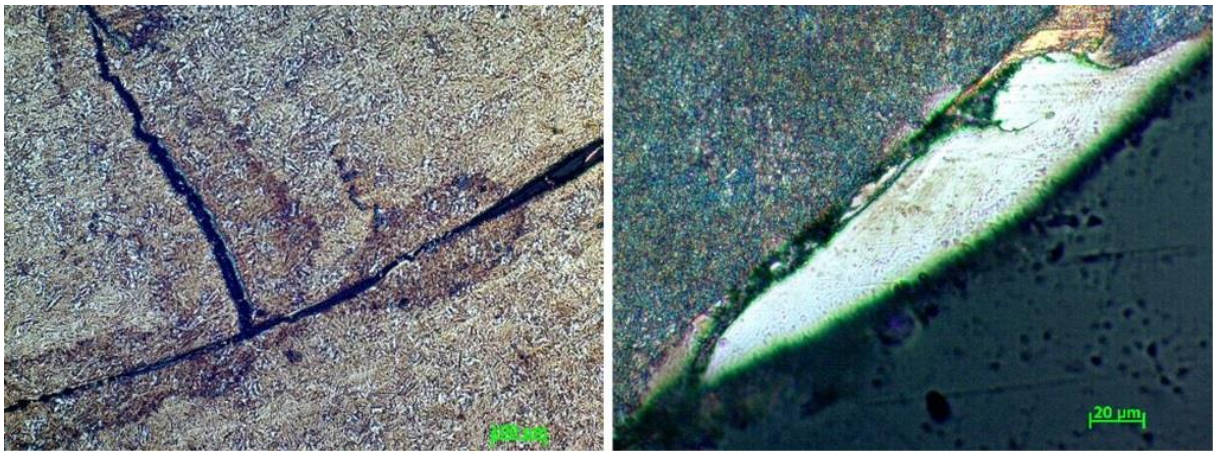

a) b)

Figure 4. Pictures of the examination
a -cracks in the direction of the strands in the rolled plate and sheer as well, b – foreign material on he damaged surface

4. THE RESULTS OF THE EXAMINATION

During the analysis of the specimens the damaged materials could be sorted into 3 groups based on the deformations:

- in the first case the material behaved rigid under the examination circumstances, penetration of the bullet took place;
- in the second case the material behaved tough under the examination circumstances, penetration of the bullet took place;
- in the third case there was no bullet penetration, only dent.

Figure 5 demonstrates the rigid behaviour of the material. When the bullet entered the material, it pushed the material in front of itself, in which the increased tension tore the backside, while no permanent deformation happened.

Figure 6 demonstrated the tough behaviour of the material. In the moment of bullet impact the encounter of the plate and the cartridge caused a crater-like folding, after which the bullet pushed the material in front of itself during the impact and a tension greater than the material's yield point evolved because of the increased loading. During penetration the bullet did not push out a significant amount of material, but it was distorted into its environment.

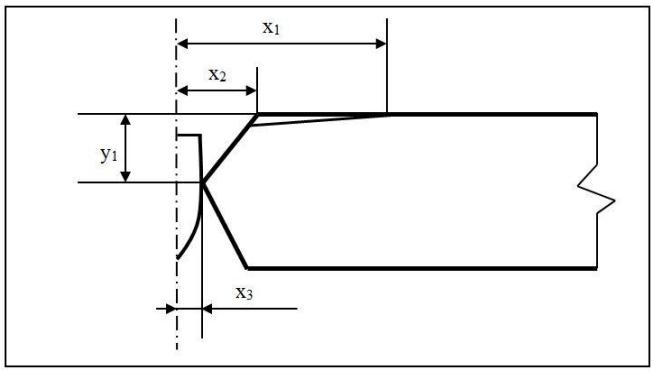

Figure 5. The rigid behaviour of the material

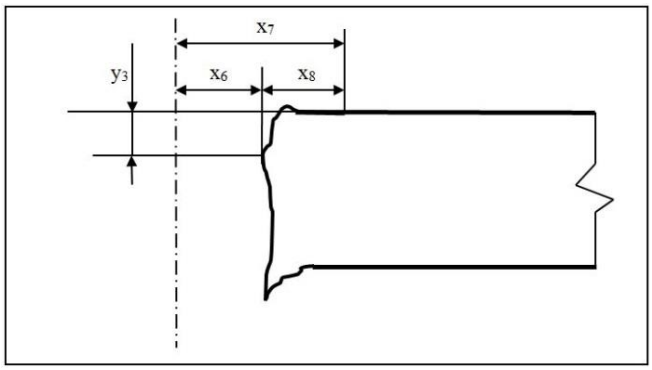

Figure 6. The tough behaviour of the material

Figure 7 demonstrates when no penetration happened, the bullet only bruised the surface. The material compacted in the impact zone (x_5).

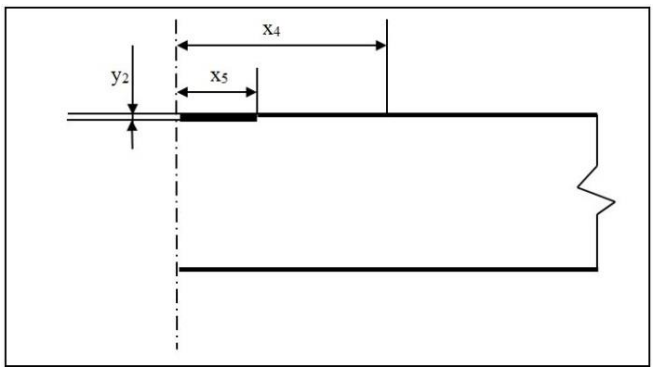

Figure 7. No penetration happened

The damages that belong to the groups where penetration happened were different, but it could be stated, that the border of the material structure changes deformation zone was never more than 2 mm measured from the edge of the damage. It was 5 mm if measured from the centre of the hard metal / carbid bullet core (centre of the hit). The quality of the damages was

different based on the ranges, used bullets and the quality of the targets. When the same bullets and target, but another range were used, the difference in the amount of material structure changes could be observed. Based on the examination of the specimens it could be stated that the penetration of the reference material did not cause any cracks in the material's deformation zone area. In these cases none or only a minor fragmentation effect could be expected. The deformation speed caused by the impact of the bullet did not exceed the material's typical amount in any of the penetration phases, so no brittle fracture occurred.

In cases of penetration the examined armour suffered permanent structure changes, in which cases the bullet entering the inside of the material deformed the strands in the rolled plate. The core of the carbide bullet did not deform, the tips of the collected bullets remained uninjured. The local tension peak evolving at the bullet's tip caused cracks in one part of the material. The core of the bullet expanded the cracks and so moved forward while ripping out the material in front of it and as a result fragmentation effect was caused. The strands in the rolled plate leaned near the ripped part of the material. The tightest part of the hole that evolved after the penetration – which is approximately the same size as the core of the bullet – can be found in the middle of the material thickness, and this hole broadens in the shape of a cone towards the other side. Friction evolved between the touching materials during the penetration of the bullet. The tensile stress caused by the friction tore down the rear part of the bullet, which still broke through the plate.

In case of bullet penetration the environment of the hole that evolved in the 8 mm material was smooth, cracks parallel with the hole could only be observed in some cases.

With the same calculated shooting range and bullet type the 6.5 mm armour material was damaged in a similar way. In these cases the evolved cracks were parallel with the strands in the rolled plate that formed during the manufacturing of the raw material. With the increase of the energy of the impact, new cracks causing material tear formed sheer to the previous ones. This was presumably caused by the fact that the friction formed during the penetration of the bullet core was bigger than in case of the 8 mm plate.

The rigidity and so the compressing force developing the friction was bigger in case of the 6.5 mm plate. According to the experiments the 6.5 mm armour material provides the same penetration protection as the 8 mm plate, although it has a smaller material thickness. At the same time a larger fragmentation effect evolved due to the separation of the layers of the rolled plate in case of bullet penetration.

The soft core bullet only broke through the reference material during the tests. At the time of the penetration the bullet core as well as the target object suffered permanent shape changes. The deformation of the core was significant, the size of the mushroom-like shape was two times the original diameter of the bullet.

The microscopic metal examination proved that no cracks evolved in the deformation zone of the reference material in case of shots resulting in penetration.

The soft steel core only bruised the 8 mm material, but there was no bullet penetration. The material deformed close to the fractured surface, in maximum 1 mm distance. The depth of the dent and the height of the convex surface that formed on the rear side of the plate is different in case of the various shots. Even in case of the smallest, 10 m shooting range

neither reached 0.1 mm. No major changes in the material structure happened apart from the compressed layer. The strands in the rolled plate became disfigured in the deformation zone, but the material structure remained undamaged beyond the zone.

Figure 8. The mushroom-like shape of the bullet

In case of the 6.5 mm armour plate the same impact energy didn't just cause deformation near the surface. The whole structure of the material expanded like a "rubber band". The impact left a visible mark at the rear side of the plate. No cracks appeared in either cases and there was neither material tear nor fragmentation effect.

The 10 m range shot and mild steel core bullet caused cracks leading towards the centre of the material at the border of the buckle zone on the 6.5 mm material.

5. CONCLUSION

A penetration examination method that uses standards, but is more detailed has been developed during the research. This method can be further improved in the direction of the simulation examination of target material's fragmentation effect and structural deformation.
Further research areas can be the following:

- supplying of data for the computer simulation in case of different range shots;
- examination of the consequences of works that are needed when configuring the ballistic protective components and cause changes in the material structure in case of different range shots;
- examination of the fragmentation effect in case of different range shots;
- examination of the penetrating bullet's orbit, movement, energy, killing and injuring effect depending on the shot range, bullet type and target material;
- examination of the armour's protection capability;
- deformation caused by the bullet having decreasing speed because of the increasing shot range.

6. REFERENCES

[1] *MSZ K Standard 1114-1* (1999) Body armours. Bulletproof vests
[2] *NIJ Standard 0101.06* (2008) Ballistic Resistance of Body Armor
[3] **GYARMATI J., KALÁCSKA G., SZAKÁL Z., GÁVAY GY., SEBŐK I.:** *Lövedék páncéllemezen történő áthaladás metallográfiai vizsgálata*, Hadmérnök, IX. évfolyam 3. szám 2014. pp: 91-104. ISSN 1788-1919
[4] **SEBŐK, I., GÁVAY, G.:** *Destructive testing of metallic and non-metallic material,* Mechanical Engineering letters: R and D: Research and development, 2013, pp. 28-33.

GRADED OPEN-CELL ALUMINIUM ALLOY FOAMS OBTAINED BY A SINTERING AND DISSOLUTION PROCESS

[1]GHERASIM Gabriel, [2]ŞUTA Silvia, [3]THALMAIER Gyorgy
[4]SECHEL Niculina, [5]VIDA – SIMITI Ioan

[1,2]Ph.D. student, [3]assistant, [4]lecturer, [5]professor

[1,2,3,4,5]Technical University of Cluj-Napoca,
103-105 Muncii Ave., 400641 Cluj-Napoca, Romania

[1]gabi_g65@yahoo.com
[2]sutasilvia@yahoo.com
[3]gyorgy.thalmaier@sim.utcluj.ro
[4]niculina.sechel@stm.utcluj.ro
[5]Vida.Simiti@stm.utcluj.ro

Abstract

Multilayered open cell metallic foams were obtained by the dissolution and sintering process starting from 5754 aluminum alloy powder and using NaCl as the pore precursors. The average particle size of the aluminum alloy was about 1500 microns and polyhedral shaped. The NaCl powder used, also polyhedral shaped, was divided in three particle size ranges (125-250 μm, 315-400 μm and 500-630 μm). Each size range of NaCl powder with the appropriate quantity of aluminum alloy powder was homogenized, and then layers of these mixtures were poured into the mold and cold pressed at different pressures (450, 550 and 650 MPa).

The green compacts were sintered in a vacuum furnace (10^{-5} torr) at 570 ° C, for 180 minutes. Elimination of the pores precursors of the sintered samples was done in flowing hot water (70˚C) for 24 hours. Samples in which NaCl was removed were dried and the mass loss was calculated, also their relative density and porosity. Compression tests were done on the obtained metal foams in order to evaluate their compression strength and energy absorbing capacity.

Keywords: *Aluminum foam, Powder metallurgy, Sintering and dissolution process*

1. INTRODUCTION

Metal foams are class of materials which has specific physical and mechanical properties[1, 2] [1, 2]. The unique properties of metallic foams make them desirable for a wide variety of applications, including filters, thermal barriers or as a core material for structural sandwich panels. Aluminum foams also have the potential for use in energy absorption [1-3].

There is a relatively high diversity of methods of making foams, classified according to several criteria but the most used classification by the aggregation state of the starting metal: liquid, solid and vapor state [2].

Microcellular metals are now commercially available; as a result these are nowadays an area of intense research in both academia and industry [4].

A method of producing metal foam is through the sintering and dissolution process by mixing the space holder and metal powders, pressing the mixture, sintering the green compact followed by dissolution of the space holder. The advantage of this method is the possibility to control the porosity, the pores size and shape depending on the amount, shape and size of the used space holder. The space holders used are mainly salt [5-8], carbamide [9], sugar [10] which are eliminated by dissolution, before or after sintering.

In order to customize the mechanical properties of the metallic foams obtained mainly by powder metallurgy multi-layer metal foams have been developed having a pore size or density gradient, controlled by the amount and size of the space holder used, or a density gradient obtained by varying the amount of space holder. Metal foam with pore size gradient has a higher densification stress, higher deformation ability and better energy absorption efficiency than foams with a density gradient [11].

2. EXPERIMENTAL METHOD

Multilayered open cell metallic foams were obtained by the dissolution and sintering process starting from 5754 aluminum alloy powder and using NaCl as the pore precursors. The average particle size of the aluminum alloy was less 1500 microns and polyhedral shaped obtained by mechanical disintegration of the master alloy. The NaCl powder used was also polyhedral shaped, Three particle size ranges (125-250 μm, 315-400 μm and 500-630 μm) were used during this research. The space holder particles were dried in an oven at 120 °C for two hours. Each size range was mixed with the appropriate quantity of aluminum alloy powder (space holder / Al-alloy powder used was 60 /40 % wt.) and homogenized. Layers of these mixtures were poured into a hardened tool steel mold and cold pressed at different pressures (450, 550 and 650 MPa).

The green compacts were sintered in a vacuum furnace (10^{-5} torr) at 570 °C, for 180 minutes. Elimination of the pore precursors from the sintered samples was done in flowing hot water (70˚C) for 24 hours.

Samples in which NaCl was removed were dried and the mass loss, their relative density and porosity was calculated. Compression tests were done on the obtained metal foams in order to evaluate their compression strength and energy absorbing capacity according to the ISO 13314 prescriptions.

The microstructure of the as obtained samples was analyzed by scanning electron microscopy on Jeol-JSM 5600 LV microscope.

The deformation behavior of our samples was evaluated by compression test. These tests were done on samples having using a ZWIK/ROELL Z005 universal testing machine, with a crosshead velocity of 0.5 mm/min.

3. RESULT AND DISCUSSION

The compaction pressures influences the connections of the powder particles as well as the fragmentation of the space holder particles. Increasing the pressure results in an increase of the contact surface between the particles and a partial destruction of the surface oxide layer from the particles surface, this has a positive influence on the sintering process. A compaction pressure over certain values leads to a fragmentation of the space holder particles, and in the reduction of the metal foams pore size. Pressing at significantly higher pressure often causes cracking of the samples. Low compaction pressures will reduce the final mechanical properties by reducing the contact area of the samples and the width of the sintering necks too

[5].

Layers of the mixtures were poured into the mold and cold pressed at different pressures (450, 550 and 650 MPa), these values ensure a good stability of the green compacts and the space holder removal during the dissolution step.

The sintering temperature was chosen at 570 °C. This temperature is approximately 95% of the melting temperature of the Al alloy (T_m = 600 °C). Getting close to the melting temperature of the alloy facilitates the mass phenomena between particles during the sintering process.

Since the sintering was done in vacuum, some liquid phase is formed which also facilitated the growth of the sintering necks. Without a careful control of the sintering regime the molten alloy would ooze out from the samples and this can lead to a non-homogeneous structure and distribution of the pores in the metal foam. A slight increase of the sintering temperatures above 580 °C is enough to partial melt the Al powder ant tho accumulate the melt at the base of the sintered samples *(Figure 1).*

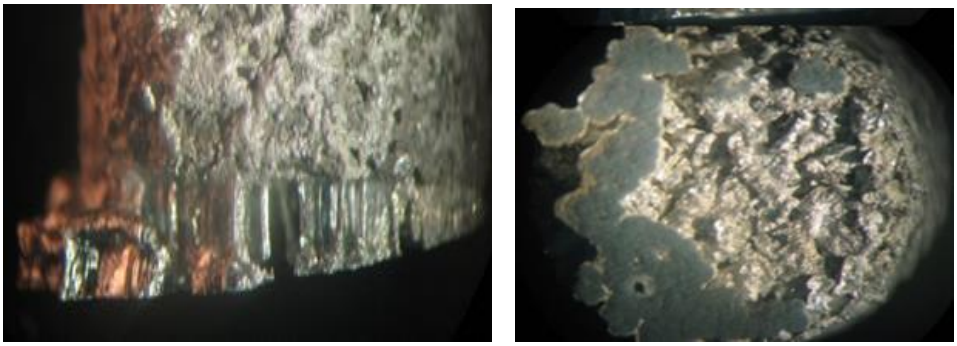

Figure 1. Melted alloy in the incorrectly sintered samples

The sintering time needed for obtaining a good degree sintering was 180 minutes. The sintering time is relatively large due the particles dimensions. As known from the sintering theories the time needed for reaching the same degree of sintering differs greatly when the particles size differs [12]. In most cases, NaCl could not be completely dissolved from the samples. A larger amount of residual NaCl was observed in metallic foams which have been compacted at high pressures.

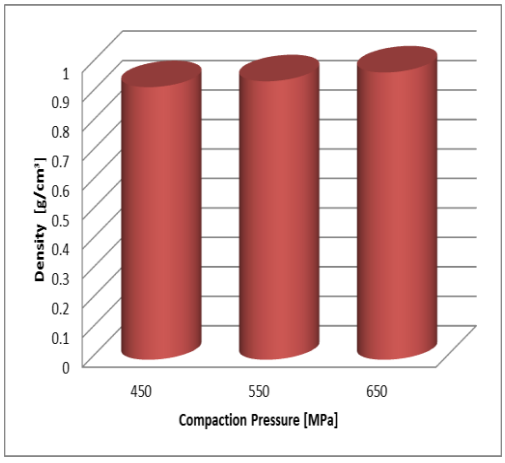

Figure 2a. Density metal foams depending on the compaction pressure

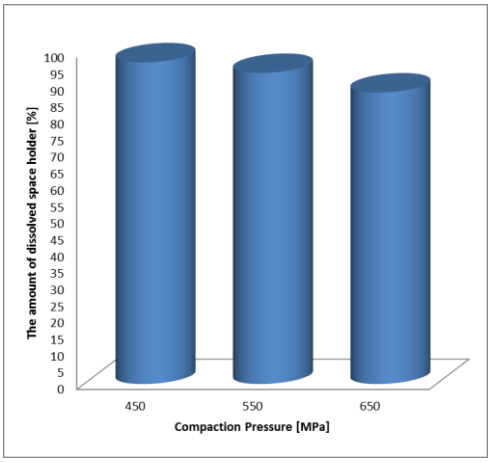

Figure 2b. The percentage of the space holder dissolved

The high-pressure compacting, and small particle size of the pore precursor) does not facilitate its dissolution from the sintered samples. In some cases, at the compaction pressure of 650 MPa the residual NaCl percentage can reach up to 12%.In addition the residual NaCl increases the relative density of the foams and have a negative influence on it's corrosion resistance.

The obtained multilayer metal foams are stacks overlapping layers of different pore size (figure 3) but having similar densities.

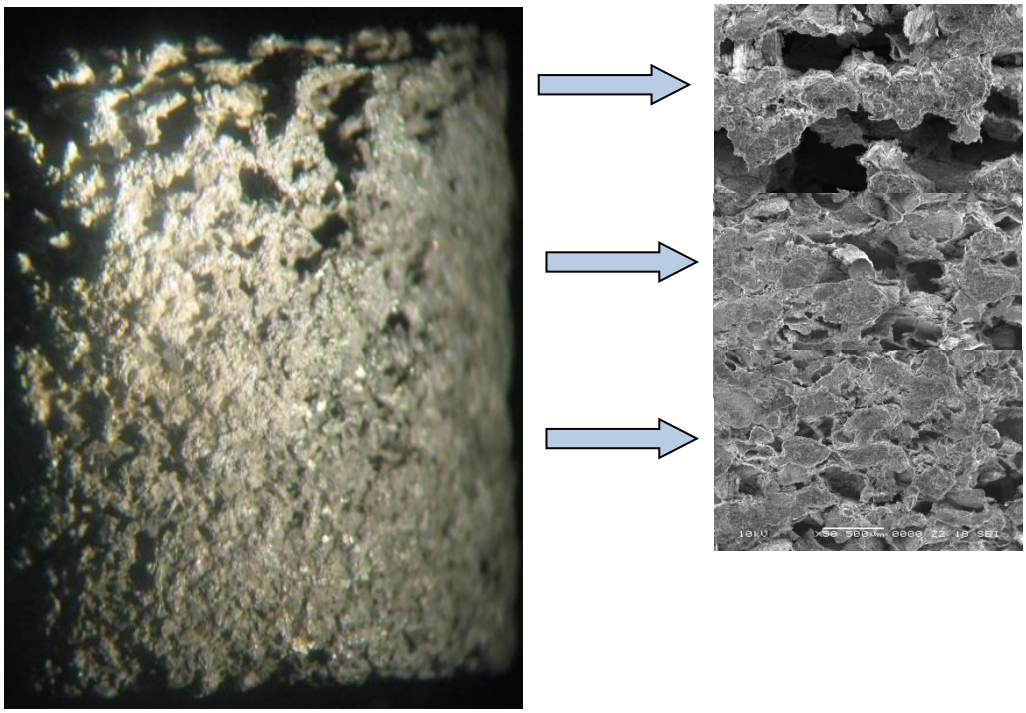

Figure 3. Images of the surface of the gradual foams

Observing the SEM images in *Figure 3* it can be seen that the metal foam structure is relatively uniform and can be considered a negative replica of the skeleton consists of NaCl particles. It is also possible to identify the pore size gradient. Certain defects were identified compared to the ideal structure because the powder particles during compaction and may be re-arranged or two or more precursor particles unite and after dissolution a large pore was generated. In *Figure 4* the stress-strain graphs of cell size-graded metal foams obtained at different compaction pressures. As can be seen from Figure 4 graphs do not show the classical compressive strain curve of metal foams, which has three distinct zones.

Table 1. Results of compressive properties for cell size graded aluminum foams

Compacting pressure [MPa]	Relative density [%]	Plateau stress [MPa]	Absorbed energy [MJ/m^3]	Energy absorption efficiency [%]
450	0.348	4.17	78.46	37
550	0.355	10.62	268.94	58
650	0.367	11.7	246,2	51

According to the classification behavior of metallic foams compressive made by R. Florek et al. in [13], our cell size-graded metal foams are ductile materials without a clear plateau stress.

Table 1 summarizes the results obtained during our quasi static compression tests. One can observe that having similar densities there is a significant increase of the plateau stress and an even bigger increase in the absorbed energy due to the stronger sintering necks. An increase in the energy absorption efficiency is also observed.

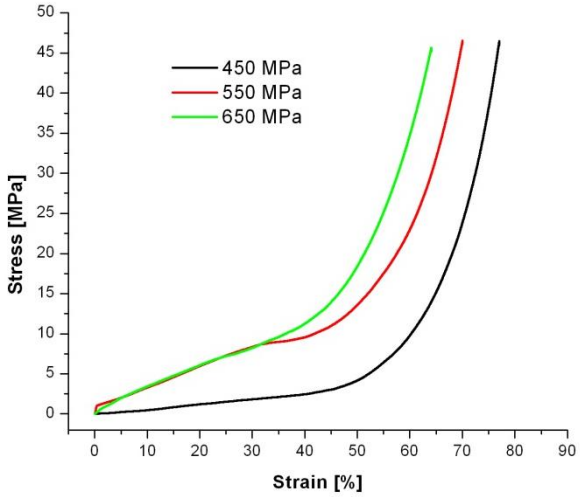

Figure 4. Typical compressive stress-strain diagrams' for the three type of samples

4. CONCLUSIONS

By SDP process we obtained cell size graded metal foam starting from Al 5754 alloy powder and NaCl as space holder particles.

We demonstrated that optimal compacting pressure lays around 550 MPa, higher pressure causes disintegration of the space holder particles and an increase of the number of the entrapped NaCl particles. Lower compacting pressures don't assure large enough contact surfaces between the aluminum particles.

Sintering in vacuum at temperatures close to the melting point of the alloy reduce the sintering time but also increase the possibility of droplet formation by the partial melting of the alloy.

Our cell size-graded metallic foams are ductile but during the compression tests present no clear compression plateau similar to other authors' findings. However the sample pressed at 550MPa presents a plateau at higher strains (30-40%). Before that the behavior is linear. These samples present high densification strain and good energy absorption capability and efficiency.

5. ACKNOWLEDGEMENTS

This work was partially supported by the strategic grant POSDRU/159/1.5/S/137070 (2014) of the Ministry of National Education, Romania, co-financed by the European Social Fund – Investing in People, within the Sectoral Operational Programme Human Resources Development 2007 – 2013

6. REFERENCES

[1] **M.F. ASHBY, A.G. EVANS, N.A. FLECK, L.J. GIBSON, J.W. HUTCHINSON AND H.N.G. WADLEY**: *Metal Foams,* 2000, A Design Guide, Boston: Butterworth-Heinemann

[2] **J. BANHART:** *Manufacture, characterization and application of cellular metals and metallic foams,* Progress in Material Science, 46, 2001, pp. 559-632

[3] **J. T. BEALS, M. S. THOMPSON:** *Density gradient effects on aluminium foam compression behaviour*, Journal of Materials Science, vol. 32, 1997, pp. 3595-3600.

[4] http://dx.doi.org/10.1016/B978-0-444-53770-6.00024-1

[5] **Y. ZHAO, F.HAN, T. FUNG:** *Optimisation of compaction and liquid-state sintering in sintering and dissolution process for manufacturing Al foams*, Materials Science and Engineering, A364, 2004, pp. 117–125

[6] **S. OZAN, S. BILHAN:** *Effect of fabrication parameters on the pore concentration of the aluminum metal foam, manufactured by powder metallurgy process,* Int. J. Adv. Manuf. Technol., vol. 39, 2004, pp. 257-260

[7] **Z. HUSSAIN, N.S.A. SUFFIN:** *Microstructure and Mechanical Behaviour of Aluminium Foam Produced by Sintering Dissolution Process Using NaCl Space Holder*, J. Eng. Sci., vol. 7, 2011, pp. 37-49

[8] **R. SURACE, L.A.C. DE FILIPPIS, A.D. LUDOVICO, G. BOGHETICH**: *Influence of processing parameters on aluminium foam produced by space holder technique*, Materials and Design vol. 30, 2009, pp. 1878–1885

[9] **B. JIANG, N.Q. ZHAO, C.S. SHI, X.W. DU, J.J LI, H.C. MAN**: *A novel method for making open cell aluminum foams by powder sintering process*, Mater. Lett., vol. 59, 2005, pp. 3333-3336

[10] **N. MICHAILIDIS, F. STERGIOUDI:** *Establishment of process parameters for producing Al - foam by dissolution and powder sintering method*, Mater. Design, vol. 32, 2011, pp. 1559-1564

[11] **A. HASSANI, A. HABIBOLAHZADEH, H. BAFTI:** *Production of graded aluminum foams via powder space holder technique*, Materials and Design, 2012, vol. 40, pp. 510-515

[12] **I. VIDA, SIMITI, N. JUMATE, GY. THALMAIER, N. SECHEL, V. MOLDOVAN**: *Study of gradual porous metallic membranes obtained by powder sedimentation,* J. Porous Mat., Vol. 19, No 1, 2012, pp. 21-27

[13] **R. FLOREK, F. SIMANČÍK, M. NOSKO, J. HARNÚŠKOVÁ**: *Compression test evaluation method for aluminium foam parts of different alloys and densities*, Powder Metallurgy Progress, Vol.10, No 4, 2012, pp. 207-212.

CAN BUS SYSTEM DEVELOPMENTS OF VEHICLES

KERTÉSZ József, B.Sc.

University of Debrecen, Faculty of Engineering,
4028 Debrecen, Ótemető Street 2-4
kertesz_jozsef@eng.unideb.hu

Abstract
CAB bus (for Controller Area Network) is a vehicle bus standard, which is designed to allow microcontrollers and devices to communicate with each other. This communicate network may be expanded by more CAN devices. In this paper I demonstrate development possibilities of CAN by a system diagnostic. The measurement was implemented with PSA MUX system supported by Brassai Sámuel Grammar School and Technical School in Debrecen.

Keywords: *CAN devices, diagnostic, pedal position*

1. INTRODUCTION

A modern car has many ECU (Electronic Control Unit) communicating in real time with each other on CAN bus network. According to the PSA-MUX measurement, the communication network capacity usually are not utilized, it means that more CAN devices could be applied. Furthermore in spite of the structure and operation of the system, it is relatively simple, the troubleshooting and system diagnostic is often difficult for the most well equipped service facility as well. The investigated PAS MUX system is introduced in the next figure.

Figure 1. PSA MUX system

2. INVESTIGATION OF MULTIPLEX NETWORK

2.1. Resistance measurement

The measurement was started with checking the device in terms of injury-free state. The parallel CAN_H and CAN_L cables are connected to a common resistance hence the injury-free state can be analyzed by a simple resistance measure. This method is introduced in the next figure. Between the H and L cable the resultant of the parallel resistances can be measured. The resultant resistance is 61.3 Ohm, it means that the applied resistance is a 120 Ohm element.

Figure 2. Resistance measurement

2.2. Visualization and detecting of CAN message

An additional measurement and CAN message visualization was implemented by PicoScope 4223, which is a CAN special oscilloscope. Before starting the investigation, I have to setup the necessary software on a computer. The next picture shows the assembled system (see Fig. 3).

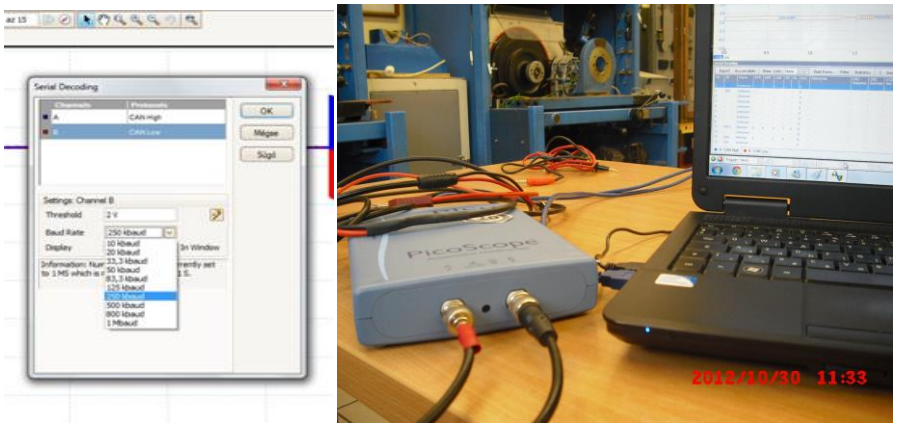

Figure 3. PicoScope 4223

After connecting the PSA MUX- PicoScope-PC, I performed the basic setups on the software, for example the speed of each channel, and the visualization of CAN_H and CAN_L.

At first, I investigated the reliability of CAN network on PSA MUX by fault generation. The Interface consists of many integrated potentiometers to modify and simulate different extreme operation parameter. After measuring the idle power, and full load, I simulated a cable-breaking on the CAN_H and CAN_L part by the software, in order to test and detect the operation of network. I recorded the original and the defective signals in a particular measure range to compare them to each other easier. Firstly, I break the L cable of ECU (Engine Control Unit) CAN network.

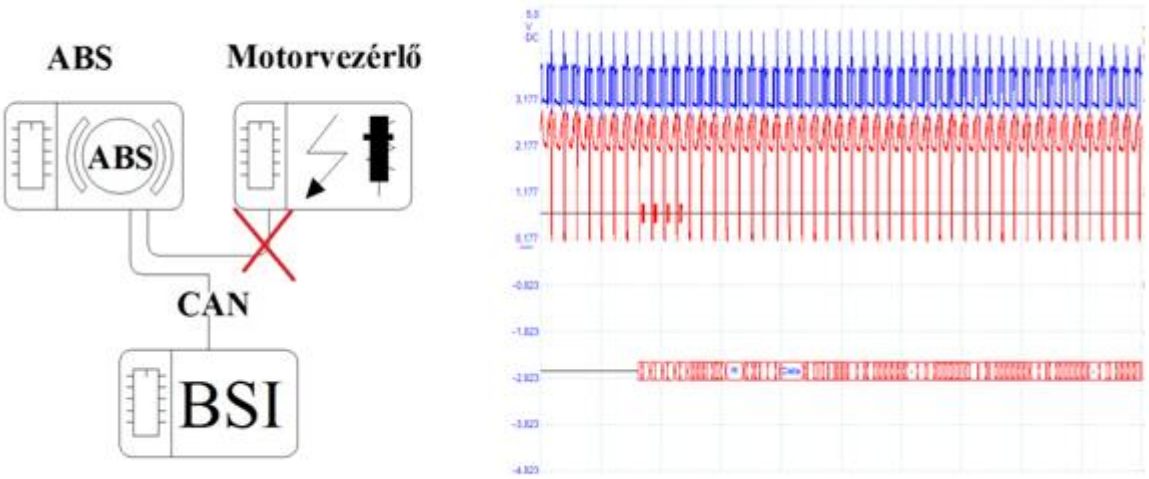

Figure 4. ECU L cable-breaking

As the displayed figure shows, the signals have become totally incomprehensible; however the central display informs the drivers with a “stop” subtitle about the failure. The performance of the ICE (internal combustion engine) was not reduced, in spite of cable-braking. Nevertheless there is a possibility to have the both cable-breaking on CAN_H and CAN_L. In this case the ECU cannot communicate with the other control unit, so presumably the vehicle cannot operate either. Due to the both cable-breaking there were no detectable signals on the software, but the car was not stopped. The ECU operated the engine with reduced power and performance, to provide safe stop for the driver.

In the next step, I tried to simulate special situations, to convince about load ability of CAN network. The communication speed of the tested PSA MUX C5 system is 256 kbit/s which is a relative low performance. Most of modern car’s bus networks are 1Mbit/s at least.

I created an spacial case, in which the temperature of engine is 120 °C, and I simulated an emergency breaking from 150 km/h to stop. In this case many sensors and actuators have to operate and communicate with each other on CAN in the same time. Due to many signals the load of network is increasing, and this state can be detected. (See Fig. 5.)

Naturally the generated fails are recorded on the car error memory, which can be deleted by an appropriate devices and software. I connected the Bosch FSA 740 diagnostic device to the PSA MUX car, to delete and identify the failures from the car memory, since in actual situation we have to find and repair the cable-braking. However the CAN system does not

give information about the type of failure. The memory contains “CAN problems” messages, but the trigger of the mistake is not known and described, which enhances the failure repair.

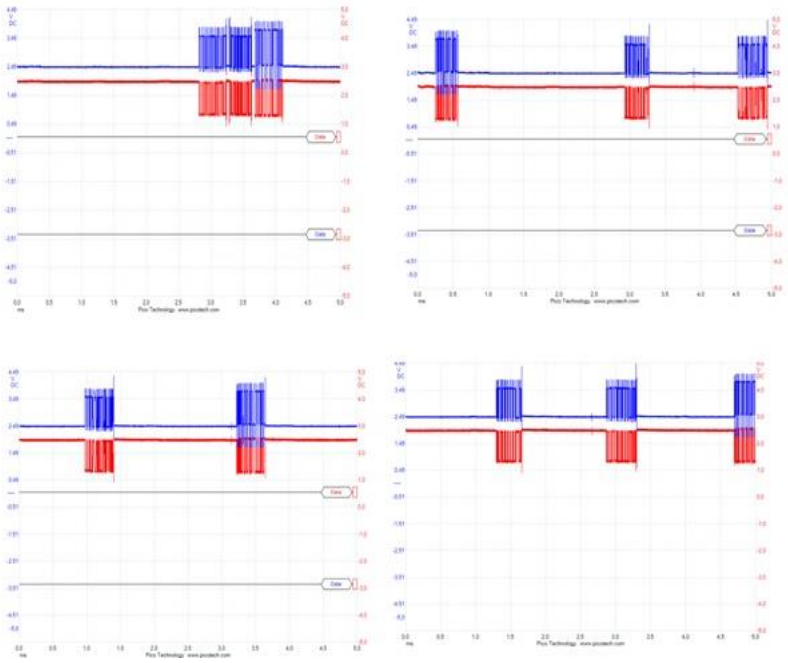

Figure 5. Signals about special situation

3. RESULTS

The results of measure demonstrate, which CAN communication capability is not utilized. So there is possibility to supplement the system with more CAN devices. Furthermore it will be necessary to develop the onboard-diagnostic system of the communication network to facilitate the failure detecting.

4. CONCLUSION

Most of car sensors provide analogue signals transmitted to the central ECU, where an integrated CAN-Controller creates suitable CAN messages. This process can be seen in the next figure.

Since, the capacity of the network are not utilized, we can expand it with more devices and nodes. In the original construction the electric signals of sensors have to go through more levels and cable-networks, so that the ECU can process this information. Because of the non-direct connect the information can become incorrect, and amend the content of message. The communication time can be reduced with direct connected CAN sensors. However, only sensors should be transformed whose signals are processed by more control units (CU) and actuators, e.g. gas-pedal position sensor. We have to integrate a Controller - Transceiver unit to the sensor, which convert the analogue position signal to digital CAN signal, therefore it can be connected directly to the CAN network. Because of the directly method, the actuators and CU can use immediately the information. This construction can be seen in the next figure.

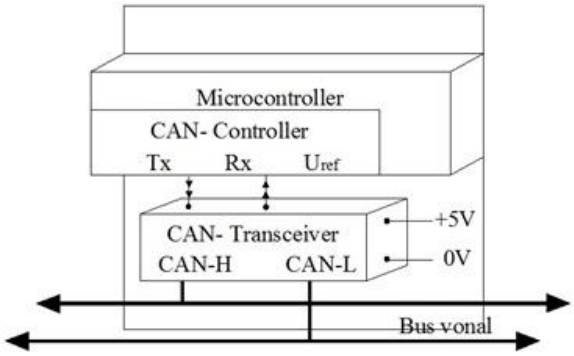

Figure 6. CAN topology

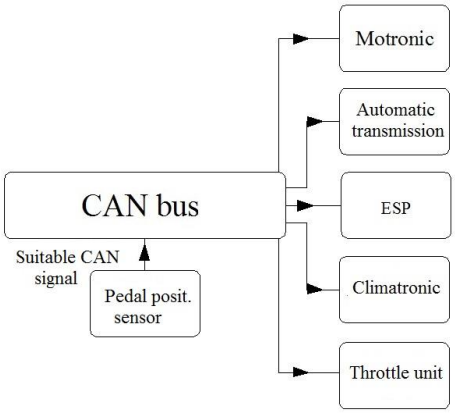

Figure 7. New position sensor construction

The diagnostic problem can be solved with a split network, which contains more numbered control resistance. These resistance should be connected on-board diagnostic system to help find easily the possible cable-breaking point. Since, the most of CAN failure is a mechanical problem e.g. cable-breaking, contact problems can be found easily if we create more small electric circuits (see Fig. 8).

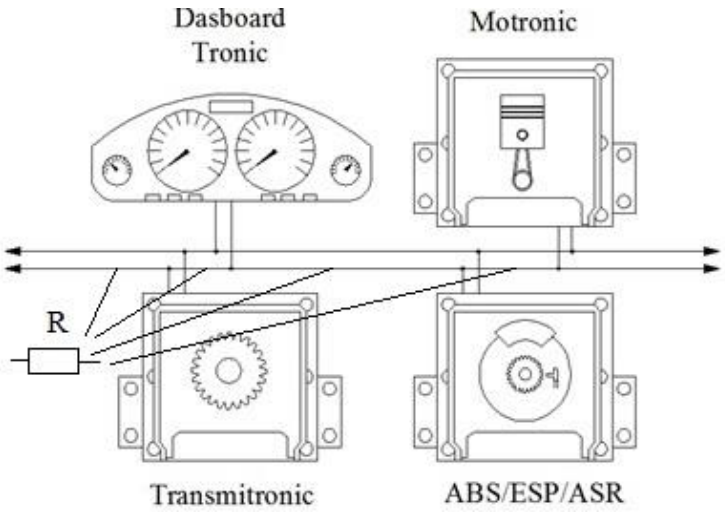

Figure 8. Application of control resistance

5. REFERENCES

[1] **CSÚRI GY.:** *„Intelligens, decentralizált adatkommunikációs rendszer alkalmazása gépjárművekben. A CAN rendszer kialakításának előzményei, felépítése, működése, gyakorlati megvalósítása, valamint várható fejlődési irányai*" (Tanulmány) Győr, 2001

[2] **LENTE CS.:** *„Gépjárművek elektronikája és diagnosztikája I."* Debreceni Egyetem Műszaki Kar Gépészmérnöki Tanszék, Debrecen, 2012

[3] **CSÚRI GY.:** *„Controller Area Network (CAN) 2. rész"* AUTÓSZAKI, 1998

[4] BOSCH , „Benzinmotorok irányító rendszerei- Motronic- rendszerek"

[5] **KERTÉSZ J.:** *„Gépjárművek multiplex hálózatának diagnosztikai vizsgálata"* Debreceni Egyetem Műszaki Kar Gépészmérnöki Tanszék, Debrecen, 2012

[6] **WOLFHARD L.:** *„ CAN System Engineering"* Springer London, 2013

[7] **CHIN L., CHUNG H., KUN-CHUN C.,PING J. MUH S.:** „ *EMI Prevention of CAN-Bus-Based Communication in Battery Management Systems*", International Journal of Engineering & Computer Science IJECS-IJENS Vol: 13 No:05, 10/2013

[8] **FENG KONG ; HENTS TECHNOL. INC, JIANGSU ; LIYAN ZHANG ; JIE ZENG ; YUHUA ZHANG:** *„Automatic Measurement and Control System for Vehicle ECU Based on CAN Bus"* Automation and Logistics, 2007 IEEE International Conference on, 2007

MACHINE CONDITION MONITORING IN BEARING MANUFACTURE USING VIBRATION ANALYSIS AND INTELLIGENT APPROACHES

[1]KEVICZKI Zoltán, [2]DEÁK Krisztián, [3]KOCSIS Imre

[1]FAG Magyarország Ipari Kft, Industrial Engineering
zoltan.keviczki@schaeffler.com

[2]Univerity of Debrecen, Faculty of Engineering
deak.krisztian@eng.unideb.hu

[3]Univerity of Debrecen, Faculty of Engineering
kocsisi@eng.unideb.hu

Abstract
Rolling bearings are one of the most important parts of the rotary machines. The most breakdowns derive from bearings defects. That is why so important to use a sort of condition monitoring techniques of the bearings. Several bearing diagnosis methods are widely used in industrial life. Most crucial techniques apply vibration measurement in both time and frequency domain. The widely used DSP (Digital Signal Processing) techniques are presented in this paper FFT (Fast Fourier Transform) DFT (Direct Fourier Transform); Wavelet transform. Machine learning methods such as ANN (Artificial Neural Network); ANFIS (Adaptive Neuro-Fuzzy Interference System) and SVM (Support Vector Machine) are overviewed which are widely applied in bearing condition monitoring and for RUL (Remaining Useful Life) estimation of bearings. FIS (FAG Industrial Service) expert system is presented as an efficient tool for bearing diagnosis.

Keywords: bearing, condition monitoring, diagnosis, neural network, machine learning.

1. INTRODUCTION

Bearing, especially roller bearings are applied in every domestic and industrial applications. They are crucial part of machines and responsible for the most breakdowns. Condition monitoring helps to keep clear to unexpected failures and able to act before the problems happen. For reducing machinery downtime and maintenance time supervision is necessary before breakdown. By continuous condition monitoring, the behaviours of the bearings can be monitored in industrial and laboratory conditions.

Elastic deformation of the bearings under load transmission called Hertz – elastic deformation [1] [9]. The theory means: under load, due to an elastic deformation, the line or point contact becomes elliptic in shape. Elastic deformation has two parts in case of bearings:

1. Shape deformation in connection point of outer ring and rolling element
2. Shape deformation in connection point of inner ring and rolling element.

The connection between rolling element and loading can be described with the next functions:

$$Q = K_n \times \delta^n \quad (1)$$

where:

- Q: rolling elements weight
- K_n: constant, take notice of relationship, between rolling element and raceway
- δ: connection elastic deformation
- n: index, which depend on connections relation
  - point connection: n = 3/2
  - line connection: n = 10/9

Beyond a certain time of running surface fatigue appears inside the material. In the beginning fatigues cracks are small then become larger resulting the breakdowns of the bearings.

2. RUL AND LIFE TIME ESTIMATION OF ROLLER BEARINGS

Health of the bearings can be determined Remaining Useful Life (RUL) [2][4] a process which is based on two approaches. First is a diagnostic second is the prognostic method. Diagnostics methods determine the defects of the bearings and the prognostics methods transform these defects which provided by sensors. RUL calculations are useful in maintenance, which is the key in prognostic module. Prognostic process has two phases learning and an exploitation phases. RUL distribution can be used in condition monitoring which signs the defects and triggers the maintenance action [3]. For bearing diagnosis and RUL estimation ANN (Artificial Neural Network) and SVM (Support Vector Machines) as machine learning methods are widely used and several experiments details it. [23, 24] Rotary machines are diagnosed by vibration analysis in lot of researches, signal model-based fault detection and diagnosis for induction motors using features of vibration signal in two-dimension domain was introduced. [25]

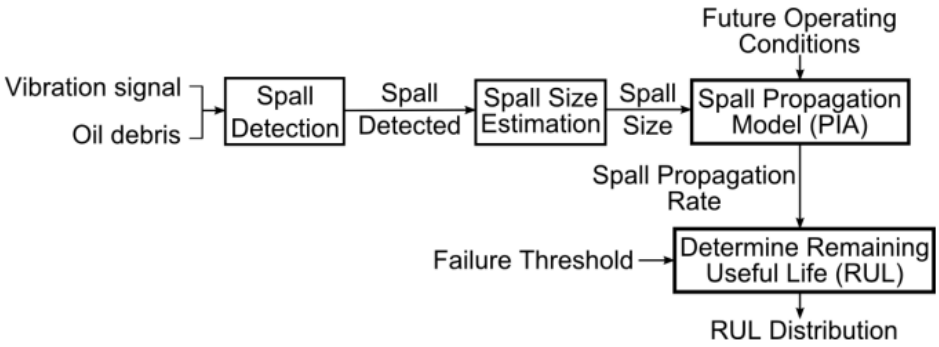

Figure 1. RUL method

Bearing life - expectancy depends on many factors. Bearings of the same life time has to be use variable, because the rate of the deviation to high, and have to define a typical value from frequency distributions of the bearings lives.

Survive probability of bearings (S) [27, 28, 29]: it represents, how many bearings are able to reach and survive their life between in same conditions.

Probability of defects (F) [27, 28, 29]: it defines the number of the bearings, which break down in certain time.

The next relationship can be use between two probabilities:

$$F = 1 - S \tag{2}$$

Figure 2 shows fatigue life distribution function of bearings. These were measured under the same loads and the types and features of geometry were same.

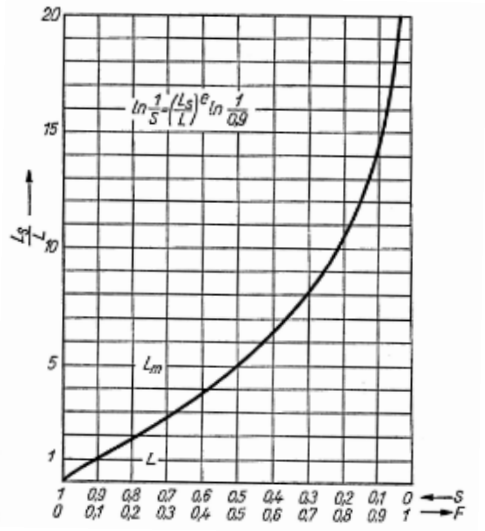

Figure 2. Rolling bearings life functions

Where:

- L_S/L = ratio between L_S and L,
- S and F = probability of breakdown.

The distribution curve shows 100 bearings were diagnosed. The numbers of the bearings, which reach and survive the limit can be seen in the figure 2.

Due to the high distribution bearing manufactures define one or two typical point on the curve, which belong to lifetime and loading capacity values are determined.

Useful lives, which are signed in the diagram are the followings:

- L: the fatigue life, which 90% of the bearings are able to reach or survive. The C dynamic loading capacity refers to 90% survives probability and each bearing catalogues include it.
- The C dynamic loading capacity gives, the number of the bearings which are designed by the dynamic loading capacity and reach and survive 90% of the calculated life but other 10% does not even though the correct assembly and running because they break down.
- L_m: median life, 50% of the bearings survive.

By means of Weibull distribution is able to give the connection between the rolling bearings fatigue life and survive probability [27, 28, 29].

$$\ln\frac{1}{S} = \left(\frac{L_S}{L}\right)^e \ln\frac{1}{0,9} \tag{3}$$

Where: L_s and S probability of survival, L life, which belongs to 90% probability of life, and *e* is the Weibull – variance coefficient.

The variance value is the following:

- Ball bearings: *e* = 10/9,
- Rolling bearings: *e* = 9/8.

Bearings should be planed to life expectancy. Between the L the nominal life of bearings, C the dynamics loading capacity of bearings and P the equivalent load of bearings, following equation is:

$$L = \left(\frac{C}{P}\right)^{p} \tag{4}$$

Where: a p life index, value of p:

- ball-bearings: p = 3,
- Rolling bearings p = 10/3.

Result of the equation L is in one million turns.
Bearing, which works in stationary speed of revolution, the life-span usually is given in hour:

$$L_h = \frac{10^6 L}{3600n};\ [h] \tag{5}$$

Where: n, speed on revolution [1/sec]

In case of some bearings, which are use in for example in railway applications, life give in one million kilometres.

$$L_{Gm} = \frac{\pi D L}{1000};\ [Gm] \tag{6}$$

Where: D is the diameter of the wheel in meter.

Rolling bearing has loading capacity value which is found in bearing catalogues.
Relationships of the loading capacity can be found in the following table (Table 1) [27, 28, 29]:

dg = Diameter of the rolling element [mm]; α = contact angle of the bearing; Z = number of the rolling elements in one line; i = number of the rolling element lines, leff = effective length of the roller.
Bearing defects have two main groups:

1) Primer defects:
    a) Wear
    b) Impact marks
    c) Smearing
    d) Surface defects
    e) Corrosion
    f) Electric faults

2) Secunder defects:
   a) Spalls
   b) Cracks

Table 1 Dynamic loading capacity

Bearings type			Dynamic loading capacity
Radial ball bearings	$d_g \leq 25{,}4\ mm$		$C = f_c(i\cos\alpha)^{0,7} Z^{2/3} d_g^{1,8}$
	$d_g > 25{,}4\ mm$		$C = 3{,}647 f_c(i\cos\alpha)^{0,7} Z^{2/3} d_g^{1,4}$
Radial roller bearings			$C = f_c\left(il_{eff}\cos\alpha\right)^{7/9} Z^{3/4} d_g^{29/27}$
Axial ball bearings	$d_g \leq 25{,}4\ mm$	$\alpha \neq 90°$	$C_a = f_c(\cos\alpha)^{0,7}\tan\alpha\, Z^{2/3} d_g^{1,8}$
		$\alpha = 90°$	$C_a = f_c Z^{2/3} d_g^{1,8}$
	$d_g > 25{,}4\ mm$	$\alpha \neq 90°$	$C_a = 3{,}647 f_c(\cos\alpha)^{0,7}\tan\alpha\, Z^{2/3} d_g^{1,4}$
		$\alpha = 90°$	$C_a = 3{,}647 f_c Z^{2/3} d_g^{1,4}$
Axial roller bearings		$\alpha \neq 90°$	$C_a = f_c\left(l_{eff}\cos\alpha\right)^{7/9}\tan\alpha\, Z^{3/4} d_g^{29/27}$
		$\alpha = 90°$	$C_a = f_c l_{eff}^{7/9} Z^{3/4} d_g^{29/27}$

3. DIGITAL SIGNAL PROCESSING TECHNIQUES IN BEARING DIAGNOSIS

All rotating parts of the machine generate alternate forces which cause vibration. Vibrations cause mechanical signal and the transducer transfers it to electrical signal.

Data acquisition (DAQ) process converts analog signal to digital that is called A/D conversion.

According to Nyquist–Shannon sampling theorem signal can be exactly reconstructed from its samples if the sampling frequency is twice higher than the highest frequency of the measured signal, and it requires an infinite number of samples.

There are three main domains: time domain, frequency domain, time – frequency domain.

3.1. Time domain method

In industrial life widely used condition monitoring method is the time domain analysis. In low frequency range are several techniques able to use which smaller then 5kHz. The most known techniques is the RMS (Root Mean Square) [5, 10, 14], but on the other hands Kurtosis [7,8] was found more useful than RMS and Crest Factor (CF) [6]. Skewness and peak value are applied in same frequency range then the other two (RMS and CF).

Crest Factor is able to describe small size defects because it is equal to ratio of the peak acceleration to the RMS value.

Figure 7-10 show how to calculate the statistical parameters.

$$Skewness = \frac{n}{(n-1)(n-2)}\sum\left(\frac{x_i - \bar{x}}{s}\right)^3 \quad (7)$$

$$Kurtosis = \left\{\frac{n(n+1)}{(n-1)(n-2)(n-3)}\sum\left(\frac{x_i-\bar{x}}{s}\right)^4\right\} - \frac{3(n-1)^2}{(n-2)(n-3)} \quad (8)$$

$$Impulse\ Factor = \frac{peak}{\frac{1}{N}\sum_{i=1}^{N}|x(i)|} \quad (9)$$

$$Shape\ Factor = \frac{RMS}{\frac{1}{N}\sum_{i=1}^{N}|x(i)|} \quad (10)$$

3.2. Frequency domain method

These methods use functions which transform time spectrum into frequency spectrum. Fourier transform (FT) [9] is a practical way to calculation of a discrete set of complex amplitudes by using Fourier series coefficients. Coefficients show the frequency spectrum of the original time-domain signal.

$$\hat{f}(\xi) = \int_{-\infty}^{\infty} f(x)e^{-2\pi i x\xi}dx \quad (11)$$

Discrete Fourier transform calculate whit data sequences which are discretised of N values. The sequence of N complex numbers x0, x1, ... , xN-1 is transformed into an N-periodic sequence of complex numbers.

However the better solution for analysis of vibration records is the fast Fourier transformation (FFT). FFT [9, 10, 14] input signals contain structural frequency components. The most important difference between FFT and DFT is the velocity of the calculation.
The FFT is defined by the formula:

$$X_k \overset{\text{def}}{=} \sum_{n=0}^{N-1} x_n \cdot e^{-i2\pi kn/N}, k \in Z \quad (12)$$

The DFT is defined by the formula:

$$X_k \overset{\text{def}}{=} \sum_{n=0}^{N-1} x_n \cdot e^{-i2\pi kn/N}, k \in Z \quad (13)$$

Convolution is a mathematical operation on two functions. The result of the operation is a new function, which looks like as a modified version of one of the original functions.

Convolution is defined as the integral of the product of the two functions after one is reversed and shifted.

$$(f * g)(t) \overset{\text{def}}{=} \int_{-\infty}^{\infty} f(r)g(t-r)dr = \int_{-\infty}^{\infty} f(t-r)g(r)dr \quad (14)$$

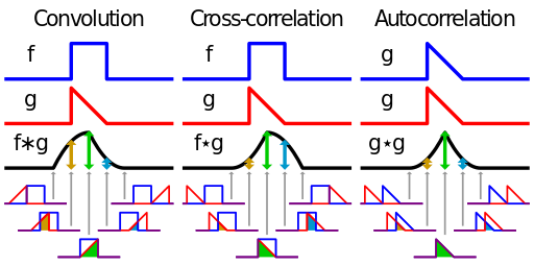

Figure 3. Result of the DFT

For complex-valued functions f, g defined as a discrete convolution of f and g:

$$(f * g)[n] \stackrel{\text{def}}{=} \sum_{m=-\infty}^{\infty} f[m]g[n-m] = \sum_{m=-\infty}^{\infty} f[n-mg[m] \tag{15}$$

To recognise bearing defects before break downs a sort kind of diagnostic methods has to be used in the maintenance process. Diagnostic systems are constantly developing, so bearing diagnostics become easier.

a) Frequency of Outer Ring: defect is on the raceway of the outer ring [12].

$$BPFO = \frac{1}{120}\frac{zi_4}{k_2}(n_2 - n_4)(1-\gamma);\ [Hz] \tag{16}$$

Where:

z = number of the rolling elements
k_2 = the greatest common divisor of i4 and z
n_2 = rotational speed of Inner Ring
n_4 = rotational speed of Outer Ring
i_4 = number of the defects on Outer Ring raceway
γ = mean diameter; def.: $\gamma = \frac{r_3}{r_k}\cos\alpha$, where r3 radius of the rolling elements, r_k mean cage radius and α contact angle

b) Frequency of Inner Ring: defect is on the raceway of the inner ring [12].

$$BPFI = \frac{1}{120}\frac{zi_2}{k_1}(n_4 - n_2)(1+\gamma);\ [Hz] \tag{17}$$

Where:

i_2 = number of the defects on Inner Ring raceway,
k_1 = the greatest common divisor of z and i_2.

c) Frequency of rolling elements: defect is on the surfaces of the rolling elements [12].

$$BSF = \frac{v}{120}\frac{d_k}{3}(n_4 - n_2)(1-\gamma^2);\ [Hz] \tag{18}$$

Where:

v = number of the defects (v ϵN)
d_k = mean diameter of the cage.

d) Frequency of Cage: derive from cage defects [12].

$$FTF = \frac{1}{120}[n_2(1-\gamma) + n_4(1+\gamma)]; [Hz] \tag{19}$$

e) Spin frequency: derive from rolling elements breakdowns [12].

$$BSF = \frac{1}{120}(n_4 - n_2)(1-\gamma^2)\sin\alpha\,; [Hz] \tag{20}$$

These frequencies can be defined from easier formulas, because sometimes the necessary data don't known. With 20% accuracy bearing faults can be calculated with formulas as see below:

- Frequency of Outer Ring: $BPFO = 0{,}4zf_h; [Hz]$
- Frequency of Inner Ring: $BPFI = 0{,}6zf_h; [Hz]$
- Frequency of Rolling elements: $BSF = 0{,}23zf_h; [Hz]$
- Frequency of Cage $FTF = 0{,}4f_h; [Hz]$

Sometimes inner ring and cage frequencies present together with sidebands of rev and cage frequency in case radial loading bearings.

Beyond these frequencies, bearings have own frequencies between 2 – 60 kHz. On the other hand, bearings have another frequency which refers to the contamination of lubricant.

3.3. Time – frequency domain method

In digital signal processing the wavelet transform is the most useful method. Wavelet transform is usually compared to Fourier transform [18, 19, 21].

STFT [12] it is very simple to use in the continuous –time case. In this case, the function is multiplied with a window function. The window function is nonzero, only a short period of time.

$$STFT\{x(t)\}(r,\omega) \equiv X(r,\omega) = \int_{-\infty}^{\infty} x(t)\omega(t-r)e^{-j\omega t}dt \tag{21}$$

On the other hand, when the time is discrete, the function is:

$$STFT\{x(n)\}(m,\omega) \equiv X(m,\omega) = \int_{-\infty}^{\infty} x[n]\omega(n-m)e^{-j\omega n} \tag{22}$$

Because the data to be transformed could be broken up into frames.

Wavelet transform is useful for diagnosing non-stationary processes. It is widely applied both in bearing condition monitoring and tool wear monitoring. [26] Moreover, wavelet method has other advantages. In bearing fault diagnostic discrete wavelet transform (DWT) [11, 15] is better than the continuous wavelet transform (CWT) [11, 15]. Both of them are continuous – time (analog) transforms.

CWT used in time – frequency analysis. This method enables to separate the signal in time and frequency domain.
CWT function defined as:

$$\psi(t) = 2sinc(2t) - sinc(t) = \frac{\sin(2\pi t) - \sin(\pi t)}{\pi t} \tag{23}$$

The DWT is based on sub band coding and the discrete form of the CWT.
DWT function is:

$$\psi_{m,n}(t) = a^{-\frac{m}{2}}\psi(a^{-m}t - nb) \tag{24}$$

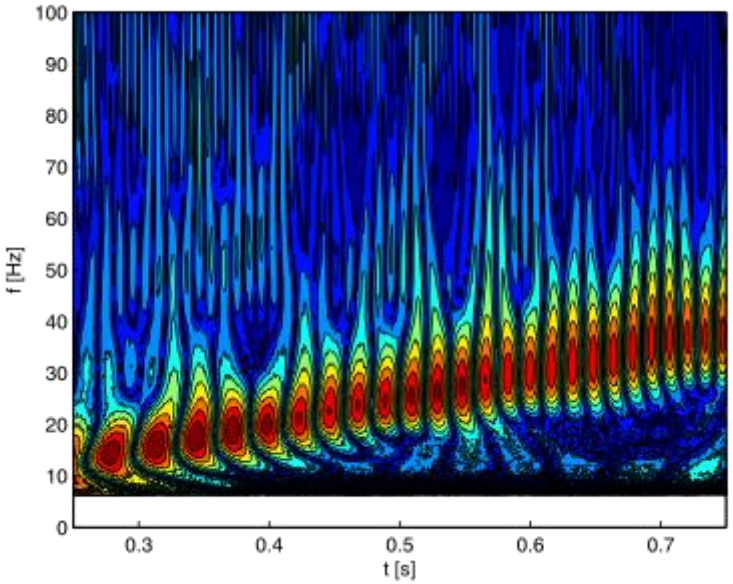

Figure 4. Wavelet technique: defect detection

3.4. Expert systems in bearing condition monitoring

Nowadays, vibration diagnosis is the most applied techniques for identifying machine damage at an early time. Rolling bearings defects can be detected accurately. The FAG Industrial Services (F'IS) can be applied in wide range ranging from simple vibration monitors to complex monitoring systems. The Fag vibration measuring device helps to detect the damage of the rotating components in early time. We can reduce the machines unplanned downtimes and the maintenance costs.

In this study, the FAG Detector III is presented. The detector can be use for detect the source of problem by analysing time signals and spectra, optional two plane balancing and phase reading. This measuring instruments are able to do rout causes analysis. It means that correct imbalances, show amplitude phase relations and we can recognize the machine

resonance areas right on location. The trend line helps to plan the maintenance, increase the level of machine availability.

Figure 5 FIS; FAG Detector

It can measure the velocity and acceleration of the vibration signal according to ISO10816.

Table 1 Properties of the FAG detector

Characteristic value	Measurement range	Frequency range
Vibration velocity	0 – 5,52 [m/s]	10Hz – 1kHz
Acceleration	0 – 37 [g]	2 – 20 kHz
Measurement point temperature	-20 ^{0}C – 550 ^{0}C	-
Rotation speed	120 – 10000 [1/min]	-

FIS system has a data collector for up to 1600 measurement points and storage capacity of up to 300 time signals. Acceleration transducers have magnetic base to attach them to the bearing houses.

Entry data analysis makes the decision simplier and faster that is a great advantage of using FI'S.

4. MACHINE LEARNING METHODS IN BEARING FAULT DIAGNOSIS

4.1. ANN neural network

Artificial Neural Networks [14, 20] systems based on many non –linear computational elements. These elements are usually works in parallel and computations levels are high. ANN has an adaptive nature and they can use learning methods. Neural networks able to learn the characteristics of the input signals because they can adapt to changes.

Artificial Neural Networks contains weights, which are has strength connections between two layers elements.

Artificial Neural Network has three main domains. The interconnection pattern between the different layers of neurons, learning process for updating the weights of the interconnections and activation function that converts a neuron's weighted input to its output activation.

Weight sum can be calculated with the following formula:

$$f(x) = K(\sum_i w_i g_i(x)) \tag{25}$$

where:

K = predefined function,

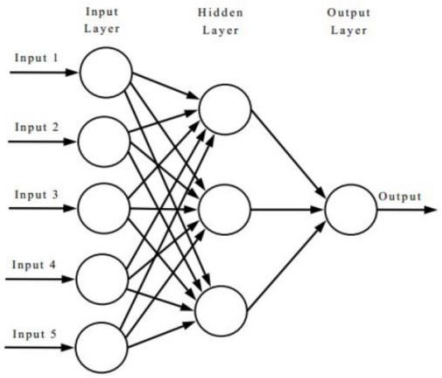

Figure 6 Artificial Neural Network

4.2. Fuzzy systems

Fuzzy logic uses membership functions Fuzzy logic systems [7, 16, 22] seems closer to the way our brains work. We aggregate data and form a number of partial truths which we aggregate further into higher truths which in turn, when certain thresholds are exceeded, cause certain further results such as motor reaction. A similar kind of process is used in artificial computer neural network and expert systems. ANFIS is a hybrid system which merges the ANN algorithms with fuzzy theory.

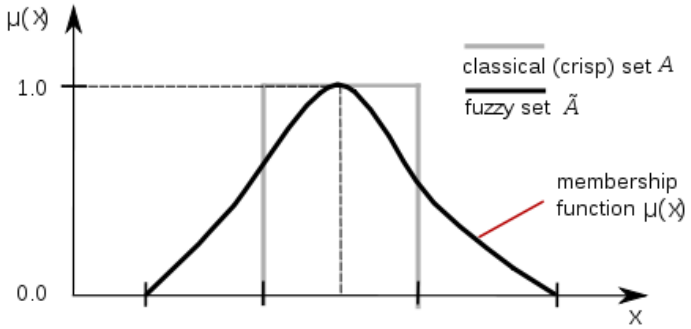

Figure 7 Membership functions of a fuzzy set

4.3. SVM

SVM methods are used for analyze data, pattern recognition, classification, regression analysis. Support Vector Machine (SVM) [13, 17, 20] method can be interpreted as a transformation to put the lower dimensional data to a higher dimension space. Support vector machine constructs a hyperplane or set of hyperplanes in a high or infinite-dimensional space, which can be used for classification, regression. The hyperplanes in the higher dimensional space are defined as the set of points whose dot product with a vector in that space is constant.

SVM gets non separable patterns to separated patterns the existing failure or incipient failure is getting more identifiable because failure diagnostics is in the higher dimensional space.
Two hyperplanes should be choosen if the training data are linearly separable in a way that they separate the data and there are no points between them, and then try to maximize their distance this is called "the margin". These hyperplanes can be described as follows:

$$w \cdot x - b = 1 \tag{26}$$

and

$$w \cdot x - b = -1 \tag{27}$$

Distance of the two hyperplanes are $\frac{2}{\|w\|}$, so we want to minimize ||w||. To prevent data points from falling into the margin, we add the following constraint: for each i either

$$w \cdot x_i - b \geq 1, \qquad for\ x_i \tag{28}$$

of the first class, or

$$w \cdot x_i - b \leq -1, \qquad for\ x_i \tag{29}$$

of the second.
Taking the equation:

$$y_i(w \cdot x_i - b) \geq 1, for\ all\ 1 \leq i \leq n \tag{30}$$

We can put this together to get the optimization problem:

Minimize (in w, b)

$$\|w\| \tag{31}$$

subject to (for any i = 1, …, n))

$$y_i(w \cdot x_i - b) \geq 1 \tag{32}$$

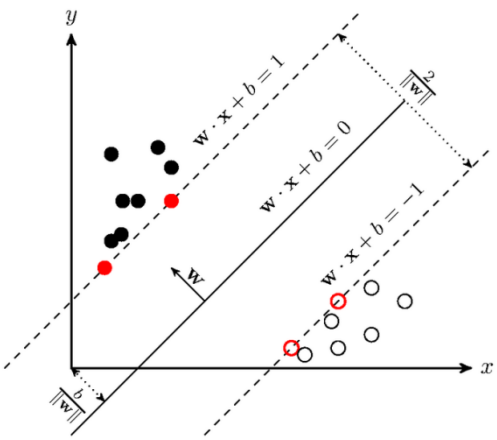

Figure 8. SVM functions

4.4.Adaptive neuro Fuzzy inference systems (ANFIS)

Condition of the ball bearings mostly use a kind of time domain methods and wavelet transforms. ANN (Artificial Neural Network) [20] and ANFIS (Adaptive Neuro Fuzzy Interference Systems). are widely used. ANFIS systems are able to recognize the localization of the bearing defects able to recognize.
Adaptive Neuro Fuzzy Interference Systems has two main rule:

1. If X = A1 and Y = B1, then T1 = p1X + q1Y + r1
2. If X = A2 and Y = B2, then T2 = p2X + q2Y + r2

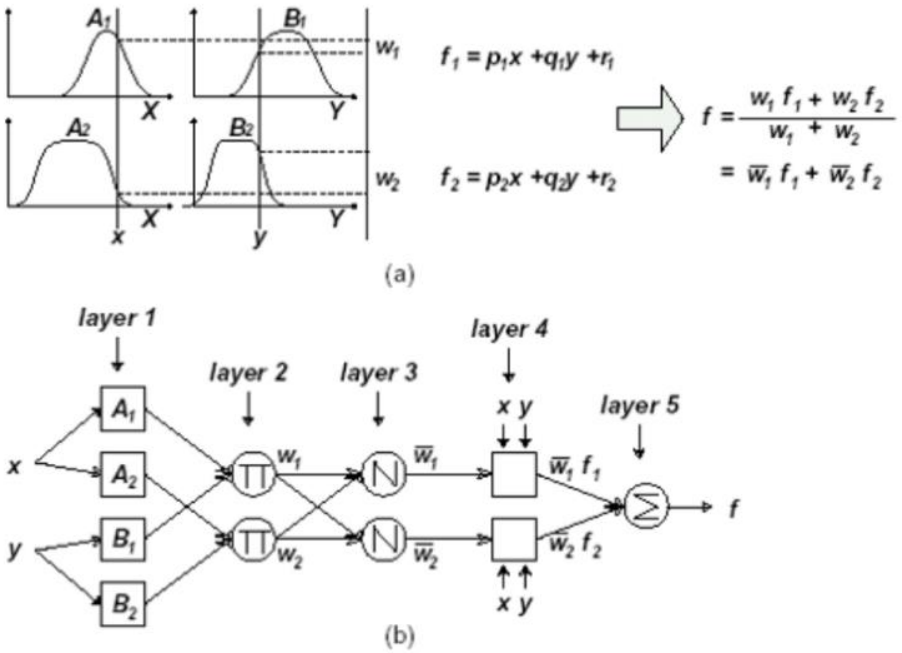

Figure 9. ANFIS functions and method

5. CONCLUSIONS

Vibration monitoring is the most important tool of the maintenance system in industrial life. To the defect of the bearings in early time is necessary part of condition monitoring. Several diagnostics systems use a sort of Time domain methods Root Mean Square (RMS), Kurtosis, Skewness, Crest Factor (CF). Others use frequency domain methods; Fourier Transform (FT), Fast Fourier Transform (FFT), Discrete Fourier Transform (DFT) and finally some use Time –frequency domain STFT (Sort Time Fourier Transform), Discrete Wavelet Transform (DWT), Continuous Wavelet Transform (CWT).

Other kind of expert systems are in machine condition monitoring. F'IS system can be used in wide range. Using this system the maintenance time can be reduced and machine reliability as well.

Further experiments aim at researching bearings in test-rig and real applications as a part of a common research between FAG Hungary Ltd. and University of Debrecen, Faculty of Engineering.

6. REFERENCES

[1] **AVRAHAM, H.:** *Bearing Design in Machinery – Engineering Tribology and Lubrication,* Marcel Dekker Inc, New York, 2003, pp. 323-329.
[2] **XIAO-SHENG SI, WENBIN WANG, CHANG-HUA HU, DONG-HUA ZHOU:** *Remaining useful life estimation – A Review on the statictical data driven approaches,* Europen Journal of Operational Research, 2010
[3] **MEDJAHER, K., TOBON-MEJIA, D. A., ZERHOUNI, N.:** *Remaining useful life estimation of ctritical components whit application to bearings,* IEEE Transactions on Reliability, 2012, pp. 292-302
[4] **EDWIN SUTRISNO, HYUNSEOK, ARVIND SAI SARATHI VASAN, MICHAEL PECHT**: *Estimation of Remaining Useful Life of Ball Bearings using Data Driven Methodologies,* Center of Advanced Life Cycle Engineering, 2012, (CALCE)
[5] **TANDON, N. :** *Acomparison of some vibration parameters for the condition monitoring of rolling elements bearings,* Measurement, v12, 1994, pp. 385-289.
[6] **MCFADDEN P. D, TOOZHY M. M.:** *Application of synchronous averaging to vibration monitoring of rolling elements bearings,* Mechanical Systems andSignal Processing, v 14, n5, 2000, pp. 891-906
[7] **VILLIAMS T., RIBADENEIRA X., BLILINGTON S., KURFESS T.:** *Rolling element bearing diagnostics in run-to-failure lifetime testing,* Mechanical Systems and Signal Processing v 15, n 5, 2003, pp. 979-993.
[8] **LIU B., LING S. F., GRIBONVAL R.**: *Bearing failure detection using matching pursuit,* NDT&E International, v 35, 2002, pp. 255-262.
[9] **VAFAEI, S., RAHNEJAT, H., AINI, R.:** *Vibration monitoring of high speed spindles using spectral analysis techniques,* Internation Journal of Machine Tools & Manufacture 42, 2002, pp. 1123-1234.
[10] **TANDOM, N., CHOUDHURY, A.:** *A review of vibration and acoustic measurement methods for the detection of defects in rolling element bearings,* ITMME Centre, Indian Institute of technology, 1999, pp. 469-480.
[11] **RAJESH KUMAR, MANPREET SINGH**: *Outer race defect width measurement in taper roller bearing using discrete wavelet transform of vibration signal,* Measurement, 46, 2013, pp. 537-545
[12] **LIU, W. Y., HAN J. G., JIANG J. L.:** *A novel ball bearing fault diagnosis approaches based on term window method,* Measurement, 46, 2013, pp. 4032-4037.
[13] **DIEGO FERNÁNDEZ-FRANCOS, DAVID MARTÍNEZ-REGO, OSCAR FONTENLA-ROMERO, AMPARO ALONSO-BETANZOS**: *Automatic bearing fault diagnosis based on one-class v-SVM,* Computers & Industrial Engineering, 64, 2012, pp. 357-365
[14] **JAE-SEOB KWAK, MAN-KYUNG HA**: *Neural network approach for diagnosis of grinding operation by ecoustic emission and power signals,* Journal of Materials Processing Technology, 147, 2004, pp. 65-71.
[15] **KUN FENG, ZHINONG JIANGM WEI HE, QIANG QIN**: *Rolling element bearing fault detection based on optimal antisymmetric real Laplace wavelet* Measurement 44, 2011, pp. 1582-1591
[16] **SAMANTA B., AL-BALUSHI K.R., AL-ARAIMI S.A.:** *Bearing fault detection using artificial neural networks and genetic algorithm,* EURASIP, Applied Signap Processing, 2004, pp. 366-377.
[17] **YANG J., ZHANG Y., ZHU Y.**: *Intelligent fault diagnosis of rolling element bearing*

based on SMVs and fractal dimension, Mechanical Systems and Signal Processing, v21, n5, 2007, pp. 2012-2024.

[18] **LI C.J., MA J.**: *Wavelet decomposition of vibrations for detection of bearing-localized defects*, NDT&E International, v 30, 1997, pp. 143-149.

[19] **NIKOLAU N. G., ANTONIADIS I. A.:** *Rolling element bearing fault diagnosis using wavelet packets*, NDT&E International, v 35, 2002, pp. 197-205

[20] **SAMANTA B., AL-BALUSHI K.R., AL-ARAIMI S.A.**: *Artificial neural network and support vector machines whit genetic algorithm for bearing fault detection*, Engineering Applications of artificial Intelligence, v 16, 2003, pp. 657-665.

[21] **RUBIN R., MEGHETTI U.**: *Application of the envelope and wavelet transform analyses for the diagnosis of incipient faults in ball bearings*, Mechanical Systems and Signal Processing, v 15, n 2, 2001, pp. 287-302.

[22] **LIT T. I., SINGONAHALLI J. H., IYER N. R.**: *Detection of Roller bearing defects using expert system and fuzzy logic*, Mechanical Systems and Signal Processing, v 10, n 5, 1996, pp. 595-614.

[23] **DEÁK, K., KOCSIS, I.:** *Machine fault diagnosis, prognosis and condition monitoring based on machine learning*, Annual Session of Scientific Papers, IMT Oradea, 2014

[24] **DEÁK, K., KOCSIS I., VÁMOS, A.:** *Application of machine vision in manufacturing of bearings using ANN and SVM*, ICAI: International Conference on Applied Informatics, 2014.

[25] **VAN TUAN DO, UI-PIL CHONG.**: *Signal Model-Based Fault Detection and Diagnosis for Induction Motors Using Features of Vibration Signal in Two-Dimension Domain*, Strojniški vestnik – Journal of Mechanical Engineering, 57, 2011, pp. 655-666.

[26] **NING FANG, P SRINIVASA PAI, NATHAN EDWARDS**: *Tool-Edge Wear and Wavelet Packet Transform Analysis in High-Speed Machining of Inconel 718*, Strojniški vestnik – Journal of Mechanical Engineering, 58, 2012, pp. 191-202.

[27] **KOZMA M., MOLNÁR L., RADICS I., TÓTH L., VALASEK I., VÁMOS E., ZALAI A.**: *Tribológiai kézikönyv,* Műszaki könyvkiadó, 1983

[28] **VALASEK, I., TÖRÖS, M.:** *Tribológia,* Képzőművészeti kiadó, 2007

[29] **VÁMOS, E.:** *Tribológiai kézikönyv,* Műszaki könyvkiadó, 1983

STRUCTURAL MODELLING OF CLOSED-CELL METAL FOAMS

[1]MANKOVITS Tamás, Dr., [2]BUDAI István, Dr., [3]BALOGH Gábor, [4]GÁBORA András, [5]KOZMA István, [6]VARGA Tamás Antal, [7]MANÓ Sándor, [8]KOCSIS Imre, Dr., [9]TÓTH László, Dr.

[1]Department of Mechanical Engineering, University of Debrecen, Debrecen, Hungary
tamas.mankovits@eng.unideb.hu

[2]Department of Engineering Management and Enterprise, University of Debrecen, Debrecen, Hungary
budai.istvan@eng.unideb.hu

[3]Department of Mechanical Engineering, University of Debrecen, Debrecen, Hungary
balogh.gabor@eng.unideb.hu

[4]Department of Mechanical Engineering, University of Debrecen, Debrecen, Hungary
andrasgabora@eng.unideb.hu

[5]Department of Material Sciences and Technology, Széchenyi István University, Győr, Hungary
kozma@sze.hu

[6]Department of Mechanical Engineering, University of Debrecen, Debrecen, Hungary
tomivarga27@gmail.com

[7]Orthopedic Clinic, University of Debrecen, Debrecen, Hungary
manos@med.unideb.hu

[8]Department of Basic Technical Studies, University of Debrecen, Debrecen, Hungary
kocsisi@eng.unideb.hu

[9]Department of Mechanical Engineering, University of Debrecen, Debrecen, Hungary
Laszlo.toth@bayzoltan.hu

Abstract
The finite element simulation of metal foams is a demanding engineering task. Furthermore, metal foams due to their complex geometry are also difficult to be modelled by 3D CAD software. The extremely complex geometry of the metal foam is often modelled by idealized models. In this paper the stronger-cruciform weaker hemisphere model is used. The cell wall sizes and the cell sizes of the metal foams were determined by microscopic measurements which were used to build up the 3D CAD model.

Keywords: *metal foams, 3D model, cruciform, cell size.*

1. INTRODUCTION

As functional light weight materials, closed-cell metal foams are widely used in vehicle industry, military industry and also in medical applications. Its high stiffness to weight ratio, good acoustic insulation and excellent energy absorption capability make them ideal materials for a variety of further applications. In the past few years, several researchers focused on the finite element modeling of metal foams with more or less success, but it is still one of the greatest challenges. Instead of modeling the complex internal structure directly, idealized structural approaches (unit cell, statistical models, etc.) are often used where the cells are represented by miscellaneous two- or three dimensional models according to the structure behavior [1-5]. 3d model created by the help of X-ray tomography (beam model, voxel and tetrahedral element methods) [6,7] is another possibility. The aim of this research is the preparation for the finite element simulation of the metal foam under compression using 3d CAD model. A microscopic analysis of the metal foam is investigated to determine the average cell size for obtaining the required size of the specimens according to the ISO 13314 [8].

2. METAL FOAM SPECIMENS

The experiments were performed with closed-cell aluminum foam (Metal Matrix Compsite Duralcan F3S.20S). According to the ISO 13314 standard all spatial dimensions of the specimen have to be at least 10 times the average cell size. The measured average cell size is 1.33 *mm*, so according to the ISO standard the chosen size of the specimen is 14.5 *mm* × 14.5 *mm* × 14.5 *mm*.

The specimen cut is carried out by a STRUERS Labotom-15. 16 pieces of test specimen are manufactured, see in *Figure 1*.

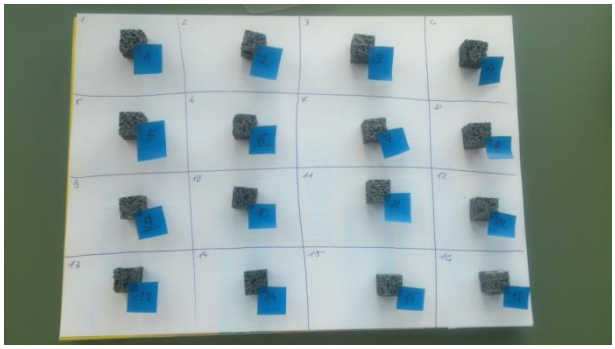

Figure 1. Test specimens

3. CAD MODELLING OF METAL FOAMS USING IDEALIZED MODELS

Great efforts have been made in representing closed-cell metal foams. As a result, a number of idealized models have been developed and summarized in [2], see in *Table 1*.

The metal foams were investigated of which idealized model can be used for modelling. Finally the stronger-cruciform-weaker-hemisphere model was chosen which is very similar to the weaker cruciform-stronger-hemisphere model and the cruciform-hemisphere model. In *Figure 2.*, the schematic diagram of the chosen model is illustrated, where t_1 is the wall thickness of the hemispherical sections, while t_2 is the wall thickness of the cruciform.

Table 1 Idealized models

Gibson-Ashby's Skeleton Cubic Cell Model [9]	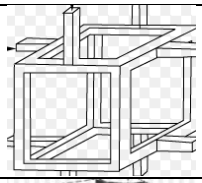
Simone-Gibson's Tetrakaidecahedral Model [10]	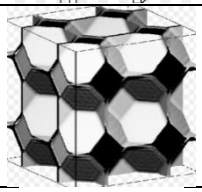
Santosa and Weitzbiski's Truncated Model [2,11]	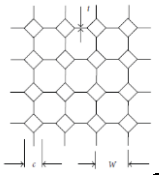
Meguid's Cruciform-hemisphere Model [2,12]	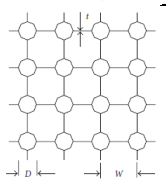
Weaker cruciform-stronger-hemisphere Model [2]	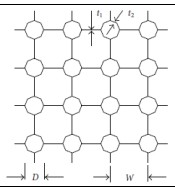

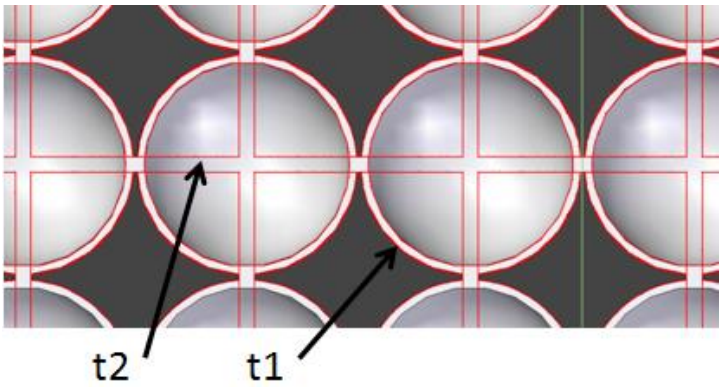

Figure 2. Schematic diagram of the model

The 3D model of the metal foam specimen is built in Solid Edge software, see in *Figure 3*. It is indispensable to compare the mass and the volume ratio of the specimen and the CAD model at different t_2/t_1 ratio which showed quite a good agreement, see in *Table 2*. The average volume ratio determined by the weight measurement was 85,78%.

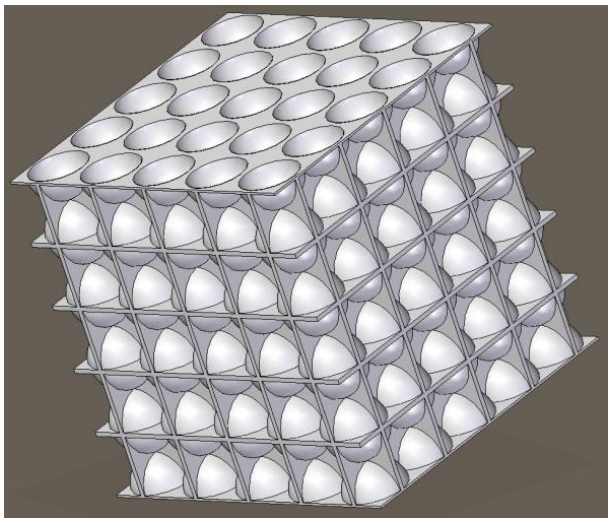

Figure 3. 3D model of the metal foam

Table 2. The volume ratio at different t_2/t_1 ratio

t_2/t_1	Volume [mm^3]	Volume ratio [%]
1	448,32	85,29
2	373,68	87,75
4	336,48	88,96
6	324,072	89,37
8	317.744	89,57
12	311.68	89,78

4. CONCLUSIONS

The case when $t_1/t_2=1$ gave the best agreement to the weight measurement. For later investigations and finite element simulation the case when the wall thickness of the hemisphere sections and the cruciform are equal will be applied.

5. ACKNOWLEDGEMENT

This research was supported by the Europian Union and the State of Hungary, co-financed by the European Social Fund in the framework of TÁMOP 4.2.4.A/2-11-1-2012-0001 'National Excellence Program'.

6. REFERENCES

[1] **HODGE, A.M., DUNAND, D.C.:** *Measurement and Modeling of Creep on Open-cell NiAl Foams*, Metallurgical and Materials Transactions A, 34(10), 2003, pp. 2353-2363.

[2] **HASAN, A.:** *An Improved Model for FE Modeling and Simulation of Closed Cell Al-Alloy Foams,* Advances in Materials Science and Engineering, Article ID 567390, 2010, 12 pages, doi:10.1155/2010/567390

[3] **KOU, D.P., LI, J.R., YU, J.L., CHENG, H.F.:** *Mechanical Behavior of Open-cell Metallic Foams with Dual-size Cellular Structure*, Scripta Materialia, 59(5), 2008, pp. 483-486.

[4] **FILICE, L., GAGLIARDI, F., UMBRELLO, D.:** *Simulation of Aluminium Foam Behavior in Compression Tests*, The Arabian Journal for Science and Engineering, 34(1), 2009, pp. 129-137.

[5] **MIEDZINSKA, D., NIEZGODA, T.:** *Initial Results of the Finite Element Analyses of the Closed Cell Aluminium Foam Microstructure under the Blast Load*, CMM-2011 Computer Methods in Mechanics, 9-12 May, 2011, Warsaw, Poland.

[6] **ADZIMAN, M.F., DESPHANDE, S., OMIYA, M., INOUE, H., KISHIMOTO, K.:** *Compressive Deformation in Aluminium Foam Investigated Using a 2D Object Oriented Finite Element Modeling Approach*, Key Engineering Materials, 2007, pp. 353-358, 651-654.

[7] **JIROUSEK, O., DOKTOR, T., KYTYR, D., ZLÁMAI, P., FÍLA, T., KOUDELKA, P., JANDEJSEK, I., VAVRIK, D.:** *X-ray and Finite Element Analysis of Deformation Response of Closed-cell Metal Foam Subjected to Compressive Loading* Journal of Instrumentation, 8 C02012, 2013, doi:10.1088/1748-0221/8/02/C02012

[8] ISO 13314:2011 *Mechanical Testing of Metals – Ductility Testing – Compression test for Porous and Cellular Metals*.

[9] **GIBSON, L.J., ASHBY, M.F.:** *Cellular Solids*, Cambridge University Press, Cambridge, UK, 1997, 2nd edition.

[10] **SIMONE, A.E., GIBSON, L.J.:** *Aluminum foams produced by liquid-state processes*, Acta Materialia, 46(9), 1998, pp. 3109-3123.

[11] **SANTOSA, S., WIERZBICKI, T.:** *On the Modeling of Crush Behavior of a Closed-cell Aluminum Foam Structure*, Journal of the Mechanics and Physics of Solids, 46(4), 1998, pp. 645-669.

[12] **MEGUID, S.A., CHEON, S.S., EL-ABBASI, N.:** *FE Modelling of Deformation Localization in Metallic Foams*, Finite Elements in Analysis and Design, 38(7), 2002, pp. 631-643.

EXPERIMENTAL INVESTIGATION OF SELF-LUBRICATING SLIDING BEARINGS

[1]MARINKOVIĆ Aleksandar, [2]STANKOVIĆ Miloš, [3]MILOVIĆ Ljubica, [4]LAZOVIĆ Tatjana, [5]MARKOVIĆ Svetislav

[1]Associate Professor
[1]University of Belgrade, Faculty of Mechanical Engineering
amarinkovic@mas.bg.ac.rs

[2]Research Associate
[2]University of Belgrade, Inovation Center Faculty of Mechanical Engineering
mstankovic@mas.bg.ac.rs

[3]Associate Professor
[3]University of Belgrade, Faculty of Technology and Metallurgy
acibulj@tmf.bg.ac.rs

[5]Lecturer
[5]Technical College Čačak
svetislav.markovic@vstss.com

Abstract
Self-lubricating sliding bearings are widely used in numerous industrial applications, primary regarding their specific lubrication mechanism. This lubrication mechanism is a main advantage compared with classical sliding bearings, where their production is not so complicate and makes lower price. This kind of bearing could be simple to assembly and in operating produce less noise and vibrations. According to their material and type of operating, self-lubricating sliding bearings could operate with oil (grease) in its own material structure or even without any amount of lubricant. Besides numerical analysis and calculations, at Faculty of Mechanical Engineering, University of Belgrade numerous experimental investigations of those bearings have been conducted, regarding own laboratory with test rig. This paper presents only selected results of those experiments, where portable DAQ acquisition with LabVIEW software tool was applied.

Keywords: *Self-lubricating sliding bearings. Experiments, friction coefficient, data acquisition*

1. INTRODUCTION

Self-lubricating sliding bearings are common in use nowadays, which means they are been applied in most of machines we need for use in our everyday work and live. We can easy understand this fact if we know several advantages this sort of bearing compared with classical sliding and rolling bearings. Generally, their production is pretty simple, which makes the price lower, for simple mounting they could be made in segments, and in operating they produce less noise and vibrations. Regarding the fact that they do not need any additional lubrication during the opearting, those bearings are very practical for maintenance and they

have long operating life, which are probably most important reasons for their universal use. There are two different sorts of self-lubricating sliding bearings:

- Sliding bearings that work without using any amount of oil or grease. These bearings are made of special plastics, graphite or some ceramics materials.
- Sliding bearings that contain lubricant, either in special storage or in their own material structure. The example and best known in this group are porous metal bearings made by sintering process and they are the product of powder metallurgy [1] (Cheng, 1986).

Mechanism of self-lubrication in porous metal bearings makes lubrication process better, but coefficient of friction still takes values in wide interval. That can be understand if we know that in bearing life it works in regimes from boundary to hydrodynamics lubrication. Lubrication quality and kind of regime are been defined due to all parameters which have impact to friction. Besides working regime parameters, bearing temperature, quality and quantity of oil supply, a significant impact has doubtless a coefficient of friction value that used to be measure due to experimental investigations. Those investigations are been conducted on special test rigs and equipment in aim to simulate real working conditions subjected to explore main parameters trend such are among others, temperature and coefficient of friction values during the sliding bearing exploitation.

2. TEST RIGS AND DAQ EQUIPMENT

Experimental investigations of self-lubricating sliding bearings are carrying out in Laboratory of Machine Design Department on Mechanical Engineering Faculty, University of Belgrade. The Department has a long tradition in investigations of bearing, where realization of those experiments is been done using two different test rigs during last several decades. The first version of test rig USL 1 (*Figure 1*), has been designed, manufactured and installed 1988. by Prof. Janković, since than started experiments of self lubricated sliding bearings [2]. Numerous tests and investigations of porous metal bearings are conducted in the Laboratory, among them significant are "*pv*" bearing curve determination, such as dependence of temperature and coefficient of friction during the exploitation of those bearings. Some results of theoretical analysis and experiments done on this test rig were published, among them could be mentioned [3].

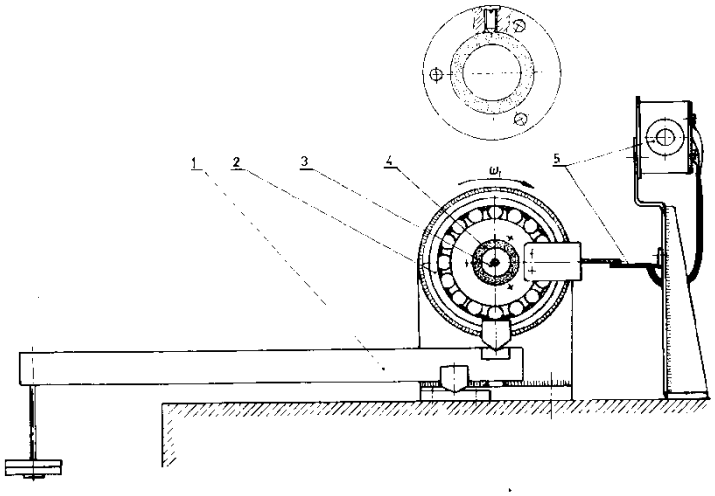

Figure 1. Concept for testing self-lubricating sliding bearings

New testing machine, based on same concept, but improved, under the name USL 5-30 is been designed in cooperation with bearings factory "Sinter" from Užice, Serbia, started at the end of last Century (*Figure 2*). Compared with old test rig, testing with new one could have more various, means wider range of bearing diameter and more precise control of rotational velocity. Experiments on new one system USL 5-30 are more efficient, much easier to realise and give results that better fit to real operating conditions. Using this test rig system for experiments it is possible to apply portable NI DAQ system [4]. Main reason for DAQ applying in this measurement is need of continually following two channels for friction torque by DNS and bearing temperature simultaneously. Even not necessary to have high sample rate for this kind of experiments, advantages of getting results and its disposal for further analyses is evident (*Figure 3*).

Figure 2. New test machine for experimental investigations

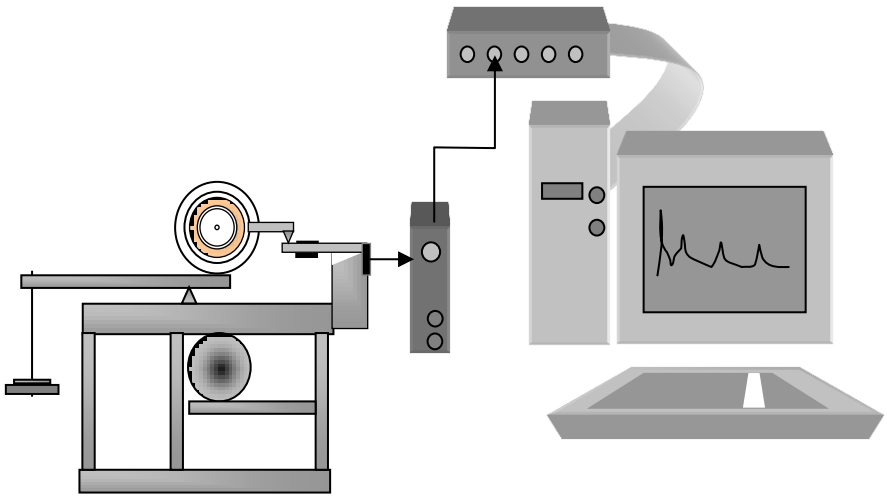

Figure 3. Elements of DAQ equipment

3. EXPERIMENTS PROCEDURE AND SAMPLES

Procedure for experimental investigations of sliding bearings used to be grouped into three parts, depending on the properties or the purpose of the research:

- Experimental study of mechanical and tribological characteristics of bearing materials,
- Investigation of oil or grease behavior for the bearing lubrication improvement and
- Experimental study of sliding bearing working performances.

Before one can access the experimental research it is necessary to make the program and the research methodology which must be in accordance with technical and other capabilities that are available. When it comes to self-lubricating bearings in general, one can organize several phases of which been constitute their experimental research:

- Preparation of the samples, the detailed control, laboratory analysis and measurement;
- Warm up (running in) of bearing samples before the official test;
- Execution of the planned experiments and
- Collection, processing and analysis of results obtained by experiments.

Here are presented just a part of experimental investigations attended to study sliding bearing working performances [5]. Samples for testing have dimensions Φ20 / Φ30 × 20mm, as a common dimension for some household and agriculture machines purpose. A small bearing peaces of cylindrical shape were cut into sections aimed to analyze their inner surface before and after the experiments in working conditions (*Figure 4*).

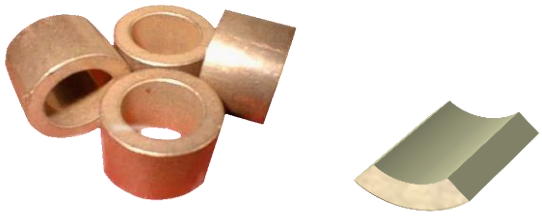

Figure 4. Porous bearing samples with segment for surface analysis

Bearings were selected from two kinds of materials: sintered bronze (CuSn10) and same material with addition of 1% of C (graphite) with corresponding physical characteristics (*Table 1*). Before testing realization, complete physical and metallographic analysis and samples selection has been conducted.

Table 1 Bearing material characteristics

Material		CuSn10	CuSn10 + 1%C
density,	g/cm^3	6,4 … 6,5	6,54 … 6,58
open porosity,	%	22,45 … 23,17	18,3 … 19,3
radial fracture force,	N	3500 … 3600	1750 … 1900
hardness,	HB	33,26 … 36,24	33 … 36

Before testing of temperature and coefficient of friction trends, all selected bearings were worked out a couple of hours, just to be prepared aim to simulate real exploitation conditions. Measuring of operating temperature and coefficient of friction rates for running bearings were been worked out. The dependence of those parameters in time has been done under boundary conditions of “pv” characteristics: radial load of F = 170 N and rotation speed n = 4780 rpm.

Experiments are been conducted under the common external environmental conditions, temperature about 20 ± 3^0C and the air humidity range (40…70)%.

4. RESULTS AND COMMENTS

This investigations shows that both temperature and coefficient of friction values of porous metal bearing become constant after (30...50) minutes and it's dependence from time can be best polynomial approximate. It used to be said that those results represent only a single regime of investigation (*Figure 5*), where similar tests are performed for other characteristic working regimes. Presented results are in correlation with some theoretical and previous experimental investigations, those are showing that self-lubricating bearings are become to be stable with friction coefficient and temperature and it could gives us a conclusion about necessary testing time aimed to simulate real working conditions.

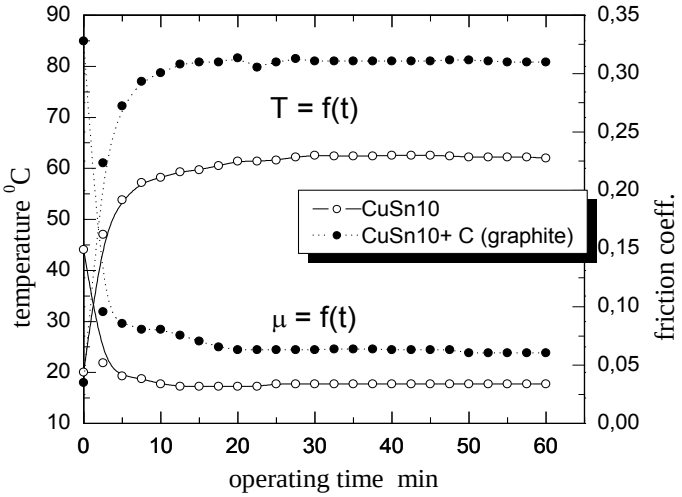

Figure 5. Trend of bearing temperature and coefficient of friction due to a working time

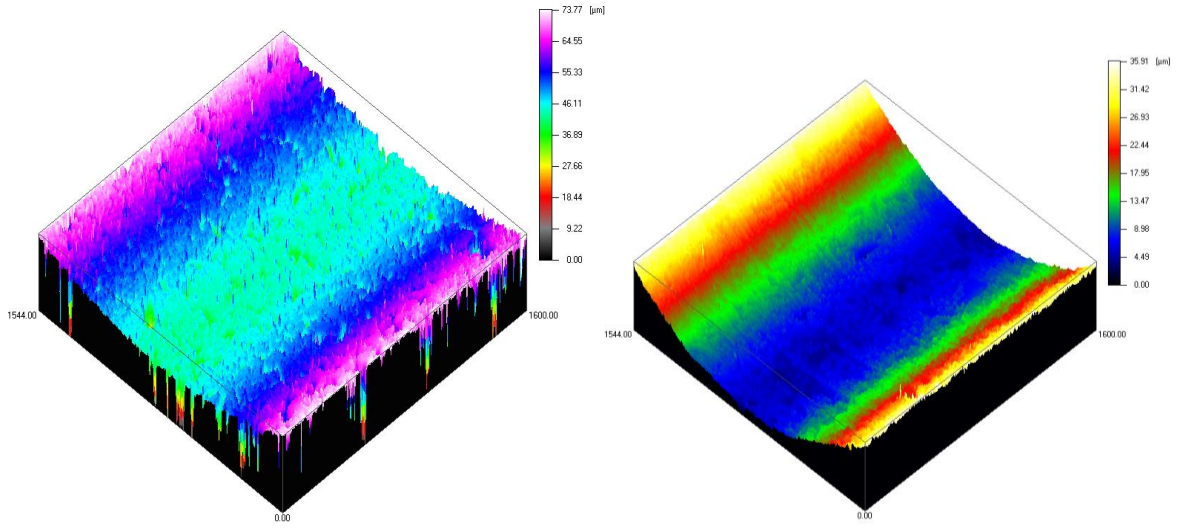

Figure 6. Bearing surface segment (before and after experiments)

Bearing surface and profile analysis, before and after experiments were also been made and this measurement has been conducted on testing center "Nanofocus AG" in AC2T, Center for Competence in Tribology W. Neustadt, Austria. It is very interesting and easy to observe differences of those surfaces (*Figure 6*). It is easy to observ that pores on the surface were almost closed after some period of work due to a wear process and contact in shaft bearing interface, that obviously dominant occurs in starting period of bearing exploitation.

After this short results overview, here used to be said that testing of second group of self-lubricating bearings those are working without any lubricant are in starting phase, because of significant expansion of polymer materials last years. By eliminating lubrication from machinery, equipment manufacturers can minimize the costs and risks associated with maintenance for the end user. Because of lubrication problem and costs, which are dominant during the working life, a possible solution is to apply dry running plastic sliding bearing. Plastic bearings are produced on polymer basis which is optimized with fibre reinforcement and solid lubricants. They are an ideal solution for machinery that requires clean and oil-free operation [6]. Plastic bearings are doing well in dirty environments since there is no oil to attract dust and dirt. Some composites with polymer thin surface could be also very interesting material for further investigations this kind of bearings [7].

5. CONCLUSIONS

Numerous experimental investigations were been focused on "pv" characteristics determination, temperature and friction quality trends in operating. Experiments presented here, made on porous metal bearings show that temperature and coefficient of friction values become constant about hour of work under the corresponding load. Those relations can be best approximate by polynomial (*Figure 5*), for most of typical regimes in bearing exploitation.

According to presented results, one could conclude that C (graphite) content in sintered bronze has respectable influence on friction, wear and temperature rates regarding its solid lubricant performances. Appropriate value of the graphite content must be determined for any particular case taking in account not only the tribological properties. The mechanical properties of the obtained sintered material used also to be considered, since the higher content of graphite (more than 1-3% or higher) tends to decrease them and make them not useful for the bearing purpose.

Bearing-shaft interface should also take into account consider porous surface character as an important parameter for its behaviour. Numerous channels in material structure started from open pores on the surface and going into the bearing volume, some of them almost 0,1mm deep from the surface (*Figure 6*). But after several hours in exploitation, size beds became quite smooth, that could be observed on the surface. One can see there are no more deep pores, just a bearing surface with roughness less than 10μm, which means that pores in interface are been closed for further exploitation process.

The results shown in this paper are only a couple among lot of them made during a long period in the Laboratory of Machine Design Department. New acquisition system with some new composite and polymer materials, we are currently dealing with, allow further experimental investigations in this field on Mechanical Engineering Faculty University of Belgrade.

6. REFERENCES

[1] **CHENG J.A., LAWLEY A., SMITH W.E., ROBERTSON J.M.:** *Structure property and performance relations in selflubricating bronze bearings: commercial premixes*, The International Journal of Powder Metallurgy, vol.22, 1986, No.3.

[2] **JANKOVIĆ M.:** *Project of Bearing test rig USL1*, Mechanical Engineering Faculty University of Belgrade, 1988.

[3] **JANKOVIĆ M., MARINKOVIĆ A.:** *Experimental determination Dependence of Temperature and Coefficient of friction in time for Porous Metal Bearings*, International Paper Tribology in Industry, Vol.18, Kragujevac, 1996, pp.61-64.

[4] **MARINKOVIĆ A., VENCL A., WALLACE P.:** *Portable DAQ equipment with LabVIEW as a tool for tribology experiments and condition monitoring*, Proceedings of 10th International Conference on Tribology Serbiatrib '07, Kragujevac, 2007, pp. 105-108.

[5] **MARINKOVIC A., LAZOVIC T., STANKOVIC M.:** *Experimental Investigation of Porous Metal Bearings*, Proceedings of the 15th International Conference on Experimental Mechanics – ICEM15, pp.2718/1-2718/6, Porto, 2012, Portugal.

[6] **MARINKOVIĆ A. STANKOVIĆ M.:** *Advantages and Applications of Self-Lubricating Plastic Bearings*, Proceedings of International Conference in Tribology, Serbiatrib 2013, pp. 135–140.

[7] **STANKOVIĆ M., VENCL A., MARINKOVIĆ A.:** *A Review of the Tribological Properties of PTFE Composites Filled with Glass, Graphite, Carbon or Bronze Reinforcement*, Proceedings of International Conference in Tribology, Serbiatrib 2013, pp. 135–140.

THEORETICAL INVESTIGATION OF PRESSURE-CHARACTERISTIC IN CASE OF GAS EXPLOSION

[1]MIKÁCZÓ Viktória, [2]SZEPESI Gábor

[1]Ph.D. student
[1]Institute of Energy Engineering and Chemical Machinery Department of Chemical Machinery
mikaczo.viktoria@uni-miskolc.hu

[2]associate professor
[2]Institute of Energy Engineering and Chemical Machinery Department of Chemical Machinery
szepesi@uni-miskolc.hu

Abstract
In case of gas explosion close the ignition point the flame front builds up, rising and moving forward with burning velocity. This velocity calculated with equations which can be find in several relevant literature. This paper shows a method to calculate a pressure-time function in case of gas explosion based on the burning velocity in spherical vessels.

Keywords: *gas explosion, propane, burning velocity, pressure curve*

1. INTRODUCTION

In case of gas explosion the flame front builds up nearby the ignition source. This flame front expands and moving forward with a defined velocity depends on time. Flame speed can be calculated by several equations published in many relevant references.

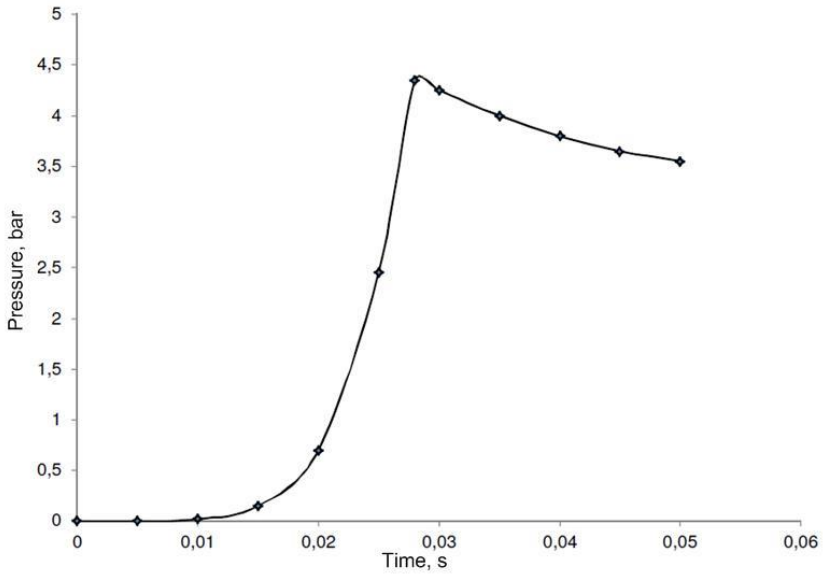

Figure 1. Pressure rise characteristic

In enclosures where the explosion occurs, flame front builds up, and typical pressure profile develops like *Figure 1* shows. This pressure profile depends on gas concentration, laminar burning velocity which specified by burning gas, and the geometry of the vessel.

2. MECHANISM OF GAS EXPLOSION

When explosion occurs in a closed volume, a boundary layer separates burnt and unburnt sides of material. (*Figure 2*)

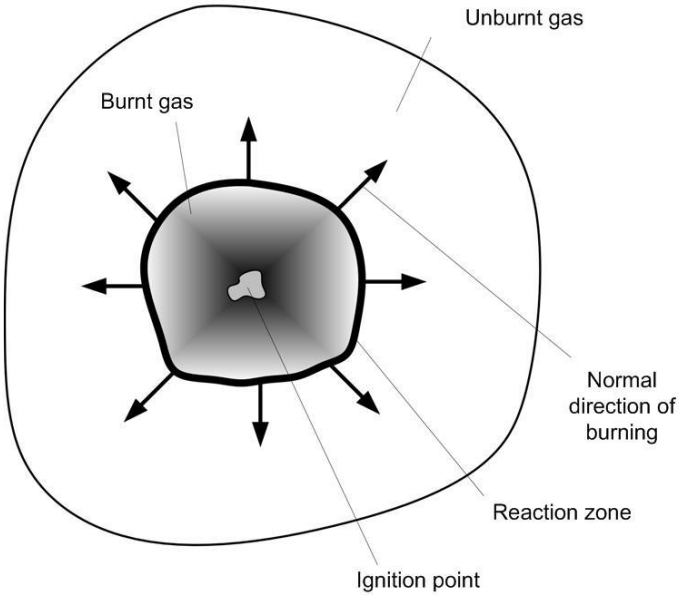

Figure 2. Scheme of gas explosion

According to some assumption, velocity of flame front is not comparable with sound speed [1], so the pressure will be constant in the vessel. If the gas phase (including burnt and unburnt gas) behaves an ideal gas, the following equation can be written:

$$P \cdot V_u = \frac{m_u \cdot R_0 \cdot T_u}{M_u} \tag{1}$$

and

$$P \cdot V_b = \frac{m_b \cdot R_0 \cdot T_b}{M_b} \tag{2}$$

The pressure is constant in this system, $P = P_b = P_u$. Changes of amount of material during explosion in closed volume:

$$\frac{dm_b}{dt} = A_f \cdot \rho_u \cdot S_0 \tag{3}$$

Left side of the equation separable into two parts, which refer to flame speed and burning velocity:

$$\rho_b \frac{dV_b}{dt} + V_b \frac{d\rho_b}{dt} = A_f \cdot \rho_u \cdot S_0 \tag{4}$$

r is the distance between the falme front and the centre of ignition. The area of the flame can be calculate with: $\frac{dV_b}{dr} = A_f$. A_n is flame speed normal to spread direction of the flame. When explosion takes place in tube, A_n area equals with cross-section of flow ($\pi \cdot d^2/4$). Flame speed according to its definition is $\frac{dr}{dt} = S_f$. Using equation (4):

$$S_f = \left(\frac{\rho_u}{\rho_b}\right) \cdot S_0 - \left(\frac{V_b}{\rho_b \cdot A_f}\right)\left(\frac{d\rho_b}{dt}\right) \tag{5}$$

If flame front is complex, $A_f \neq A_n$ the eq. 5 must be modify. If change of density is very small, the second part of the right side in equation (5) can be neglected. Then flame speed is:

$$S_f = \left(\frac{\rho_u}{\rho_b}\right) \cdot S_0 \tag{6}$$

In equation (6) $\frac{\rho_u}{\rho_b}$ called expansion factor, which is defined by the following equation:

$$E = \frac{T_b M_u}{T_u M_b} = \frac{T_b N_b}{T_u N_u} \tag{7}$$

where

$$N_u = \frac{m_u}{M_u},\ N_u = \frac{m_u}{M_u} \tag{8}$$

In the beginning of explosion process, T_u and T_b might to handle as constants. Differenced equation (1) by time:

$$V_t \cdot \frac{dP}{dt} = \frac{dm_b}{dt}\left[\frac{R_0 \cdot T_b}{M_b} - \frac{R_0 \cdot T_u}{M_u}\right] \tag{9}$$

where $V_t = V_u + V_b$ in case of explosion in closed volume, and $dm_u/dt = -dm_b/dt$. Taking into consideration equation (1) and (3), and $\rho_u = m_u/V_u$, equation (9) develops the following form:

$$V_t \cdot \frac{dP}{dt} = A_f \cdot S_0 \cdot P \frac{M_u}{R_0 \cdot T_u}\left[\frac{R_0 \cdot T_b}{M_b} - \frac{R_0 \cdot T_u}{M_u}\right] \tag{10}$$

Applying equation (7), equation (10) in simplified form:

$$V_t \cdot \frac{dP}{dt} = A_f \cdot S_0 \cdot P(E-1)\ . \tag{11}$$

In the initial period of explosion the flame expands to r_b radius, so flame area is:

$$A_f = 4 \cdot \pi \cdot r_b^2 \tag{12}$$

With the help of burning velocity the flame radius:

$$r_b = S_f \cdot t = E \cdot S_0 \cdot t \tag{13}$$

Expansion factor will be constant, according to some thesis. Then, apply equation (11), (12) and (13):

$$V_t \cdot \frac{dP}{dt} = P \cdot E^2(E-1) \cdot S_0^2 \cdot 4 \cdot \pi \cdot t^2 \tag{14}$$

and

$$\frac{1}{P}\frac{dP}{dt} = \frac{4 \cdot \pi \cdot E^2(E-1) \cdot S_0^3 \cdot t^2}{V_t} \tag{15}$$

After integrate the equation:

$$\ln P = \frac{4 \cdot \pi \cdot E^2 \cdot (E-1)}{3 \cdot V_t} \cdot S_0^3 t^3 + Const \tag{16}$$

and integrate between P_0 and P:

$$P = P_0 \cdot e^{\frac{E^2 \cdot (E-1)(S_0 \cdot t)^3 \cdot 4 \cdot \pi}{V_t}} \tag{17}$$

When radius is equal with R in case of spherical vessel, equation (17) can be simplified by the following:

$$P = P_0 \cdot e^{E^2 \cdot (E-1)\left(\frac{S_0 \cdot t}{R}\right)^3}. \tag{18}$$

3. SPECIFICATION OF PRESSURE CHARACTERISTIC IN CASE OF GAS EXPLOSION

With equation (18) can define pressure rise in vessels in case of explosion. Examinations are in 20 l spherical explosion chamber, with stoichiometric propane-air mixture (4,08 V/V % mixture, so $\Phi = 1$). [2] Measurements are in atmospheric pressure and room temperature.
In equation (18) the E expansion factor from reference [3], where $E = 7{,}97$. Results of

equation (18) are significantly influenced by laminar burning velocity, which can estimate by many equations from some references [4]. One of them published by Dahoe [6]:

$$S_L = \frac{r}{3}\left(\frac{P_i}{P}\right)^{\frac{1}{\gamma_u}} \frac{1}{P_e - P_i} \cdot \left[1 - \left(\frac{P_i}{P}\right)^{\frac{1}{\gamma_u}} \left(\frac{P_e - P}{P_e - P_i}\right)\right]^{-2/3} \frac{dP}{dt} \tag{19}$$

Radius of flame front can determine by the following equation:

$$r_b = r\left(1 - \frac{P_i \cdot T_u \cdot P_e - P}{P \cdot T_i \cdot P_e - P_i}\right)^{1/3} \tag{20}$$

Manton solved equation (19) in reference [7]. With this equation, many gas-air mixtures were investigated and explosion pressures estimated. The same measurement can be found in reference [7] which measured in this paper. Results shows in *Table 1*.

Based on measurements of reference [7], given initial section of pressure rise function. This is not the whole curve, because of decreasing tendencies of pressure after reaching maximal overpressure. With spread of flame front the amount of unburnt materials are decreasing and it slows down explosion process. (*Figure 1*) According to theory of Dahoe, laminar burning velocity was 0,407 m/s in case of 4,08 V/V % propane-air mixture. (*Table 1*) To specify ordinary flame speed of this mixture used method of least squares.

Table 1 Results of the measurement for propane-air mixture

Time, [ms]	**Pressure increase, [cmHg]**	**Flame velocity, [cm/s]**	**Radius of flame front, [cm]**
11.07	0.52	40.3	2.751
12.16	0.727	40.5	3.074
13.86	1.151	40.6	3.579
14.79	1.447	40.9	3.857
15.35	1.634	40.6	4.016
16.67	2.174	41.3	4.408

Table 2 shows several flame speeds according to relevant references.

Table 2 Flame speed by references

Model	**Flame speed, [m/s]**
Manton [7]	0.407
Dahoe [4]	0.414
Metghalchi [5]	0.382
Rallis [5]	0.369
Babkin [4]	0.349
This paper	*0.3635*

As *Figure 3* shows, measurements in initial gas explosion are in a good correlation with theoretical equation (18). (Least squares of differences are $4 \cdot 10^{-6}$)

4. CONCLUSION

This paper gives a method to estimate initial section of pressure-time function in case of gas explosion. Investigation and estimation of the whole explosion process can be a further project. In the future should test effects of safety systems against explosions and vent ducts [8] [9], and their effects to pressure-time characteristics in case of dust-air and gas-air mixtures. The further project will be to prepare numerical simulations for whole explosion process, and compare the results with experimental data.

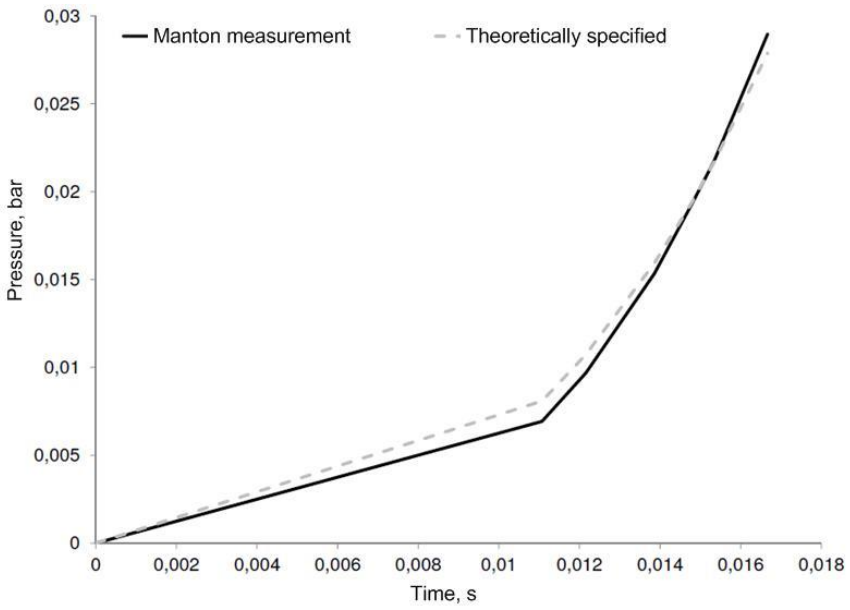

Figure 3 Functions of pressure rise

5. ACKNOWLEDGEMENT

This research was carried out as part of the TAMOP-4.2.1.B-10/2/KONV-2010-0001 project with support by the European Union, co-financed by the European Social Fund.

6. REFERENCES

[1] **R. J. HARRIS:** *Gas Explosions in Buildings and Heating Plant*, 1989, ISBN 0 419 13220 1

[2] **DOMNINA RAZUSA, VENERA BRINZEAA, MARIA MITUA, DIMITRU OANCEAB:** *Temperature and pressure influence on explosion pressures of closed vessel propane-air deflagrations*, Journal of Hazardous Materials, 174, 2010, pp. 548-555

[3] **L.-K. TSENF, M. A. ISMAIL, G. M. FAETH:** *Laminar Burning Velocities and Markstein Numbers of Hydrocarbon/Air Flames*, 1993, Combustion and Flame 95:410-426

[4] **S. HUZAYYIN, H. A. MONIEB, M. S. SHEHATTA, A. M. A. ATTIA:** *Laminar Burning Velocity and Explosion Index of LPG-air and Propane-Air Mixtures*, Fuel 87,

2008, pp. 39-57
[5] **LAMES K. CECK:** *Burning Velocities of Mixtures of Air with Methanol, Isooctane, and Indolene at High Pressure and Temperature*, 1982, Combustion and Flame 48:191-210
[6] **E. DAHOE, J. F. ZEVENSBERGEN, S. M. LEMKOWITZ, B. SCARLETT:** *Dust Explosions in Spherical Vessels: The Role of Flame Thickness in the Validity of the 'Tube Root Law'*, J. Loss Prev. Process Ind. Vol. 9. No. I., 1996, pp. 33-44
[7] **JOHN MANTON, GUENTHER VON ELBE, BERNARD LEWIS:** *Burning-Velocity Measurements in a Spherical Vessel With Central Ignition*, PII: S0082-0784 (53) 80048-2, pp. 358-363
[8] **XINGQING YAN, JIANLIANG YU, WEI GAO:** *Duct-venting of Dust Explosions in a 20 l Sphere at Elevated Static Activation Pressures*, Journal os Loss Prevention in the Process Industries, DOI: 10.1016/j.jlp.2014.07.016
[9] **XINGQING YAN, JIANLIANG YU:** *Dust Explosion Venting of Small Vessels at the Elevated Static Activation Overpressure*, Powder Technology, Volume 261, July 2014, pp 250-256, DOI: 10.1016/j.powtec.2014.04.043

List of Symbols

Symbol	Name	Unit
P	Pressure	bar
V_u	Volume of unburnt gas	m^3
m_u	Mass of unburnt gas	kg
R_0	Universal gas constant	J/molK
T_u	Temperature of unburnt gas	K
M_u	Molar mass of unburnt gas	kg/kmol
V_b	Volume of burnt gas	m^3
m_b	Mass of burnt gas	kg
T_b	Temperature of burnt gas	K
M_b	Molar mass of burnt gas	kg/kmol
A_f	Area of flame	m^2
ρ_u	Density of unburnt gas	kg/m^3
S_0	Laminar burning velocity	m/s
A_n	Area of flame normal to spread direction	m^2
S_f	Burning velocity	m/s

ρ_b	Density of burnt gas	kg/m^3
N_u	Amount of unburnt gas	mol
N_b	Amount of burnt gas	mol
E	Expansion factor	-
P_i	Initial pressure	bar
Φ	Equivalence ratio	-
γ_u	Rate of specific heats	-
T_i	Initial gas temperature	K
α, r	Radius of explosion chamber	m
r_b	Radius of flame front	m

EXPERIMENTAL *J*-INTEGRAL DETERMINATION OF DIFFERENT WELDMENTS REGION AT LOW TEMPERATURE

[1]MILOVIĆ Ljubica, [2]ALEKSIĆ Vujadin, [3]MARINKOVIĆ Aleksandar, [4]LAZOVIĆ Tatjana, [5]STANKOVIĆ Miloš

[1]Associate professor
[1]University of Belgrade, Faculty of Technology and Metallurgy
acibulj@tmf.bg.ac.rs

[2]Researcher
[2]Institute for testing of materials-IMS Institute
vujadin.aleksic@institutims.rs

[3,4]Associate professor
[3,4]University of Belgrade, Faculty of Mechanical Engineering
[3]amarinkovic@mas.bg.ac.rs, [4]tlazovic@mas.bg.ac.rs

[5]Researcher
[5]University of Belgrade, Faculty of Mechanical Engineering, Innovation Center
shomyguca@yahoo.com

Abstract
Behavior of welded joint regions (parent material, weld metal and heat-affected zone) in the presence of crack is presented. Specimens were made of high-strength low-alloy steel and were tested at -40°C. Diagrams load versus crack opening displacement, resistance curves and J versus crack extension are analyzed.

Keywords: *fracture mechanics, crack, high-strength low-alloy steel, J integral.*

1. INTRODUCTION

Classical approach to metallic welded structures calculation based on the assumption that the material is homogeneous and isotropic is represented by allowable stress design and safety factor. Such design approach turned out to be not sufficiently reliable because structure failures during their exploitations may occur under stresses that are less than allowable ones. Main reason for that are material defects existing in real structures. Cracks are the most dangerous among those defects.

The majority of metallic structures are manufactured by welding. No matter how good a welded joint is carried out, it represents a defect of material because it disrupts its homogeneity. That is why a welded joint is potential location where cracks can initiate and represents stress concentrators.

In order to have a complete metallic structure characterization, it is necessary to understand material behaviour in the presence of cracks, i.e. the estimation of material resistance to crack initiation and propagation. As the result of such approach we get structures of lower mass with significantly reduced fracture risk.

Elastic-plastic fracture mechanics study crack growth after material yield stress is exceeded and is applied to materials that exhibit time-independent, nonlinear behaviour (i.e., plastic deformation) [1]. Energy parameter assessing material resistance to crack propagation in elastic-plastic region is defined by *J* contour integral which describes crack-tip singularity. A critical value of *J* is a size-independent measure of fracture toughness. Its critical value for Mode I fracture, J_{IC}, represents elastic-plastic fracture mechanics parameter [2].

Dependence of *J* integral versus crack extension is called *J-R* or *R* resistance curve and it represents fracture mechanics parameter which defines material resistance to crack development [3].

In this paper *J* integral is experimentally determined on specimens taken from butt welded plates made of high strength low alloyed steel (HSLA) for shipbuilding and pressure vessels manufacturing.

2. MATERIAL AND METHODS

The manufacturing of welded structures using HSLA steels is recommended because structural mass is reduced due to high strength, saving the material and energy.
HSLA steel NIONIKRAL 70 (NN70) used in this experimental investigation was produced in electro furnace, casted in ingots and rolled into slabs and finally rolled in plates 16 mm thick [4]. Its chemical composition is given in Table 1, while its mechanical properties are given in Table 2.

Table 1 Chemical composition of NN70 (weight %)

C	Si	Mn	P	S	Cr	Ni	Mo	V	Al
0.106	0.209	0.220	0.005	0.0172	1.2575	2.361	0.305	0.052	0.007

Table 2 Mechanical properties of NN70

Specimen orientation	Yield stress $R_{p0,2}$, [MPa]	Tensile strength R_m, [MPa]	Total impact energy tested at -40°C E_{tot}, [J]
PM, parallel to rolling direction	780	820	107
WM	718	791	28
HAZ	750	800	57

For fracture mechanics testing, standard SE(N)B specimen was used, Figure 1. Specimen dimensions were B=12 mm, W=16 mm, $2s$= 64 mm, a_0/W=0.5, where s is half distance between support rollers.

Specimens were tested using partial unloading testing technique on universal testing machine INSTRON 8803 of 500 kN capacity at temperature of -40°C.

Fatigue cracks were positioned in parent material (PM), weld metal (WM) and heat-affected zone (HAZ). Current crack length and *J*-integral values were calculated using standard testing procedure according to ASTM E 1820-08 [5]. During testing, the temperature was kept at -40°C ±1°C using liquid nitrogen. *CMOD* values were measured using standard INSTRON clip gage. Load was recorded graphically and digitally. Commercial software was used for data acquisitioning.

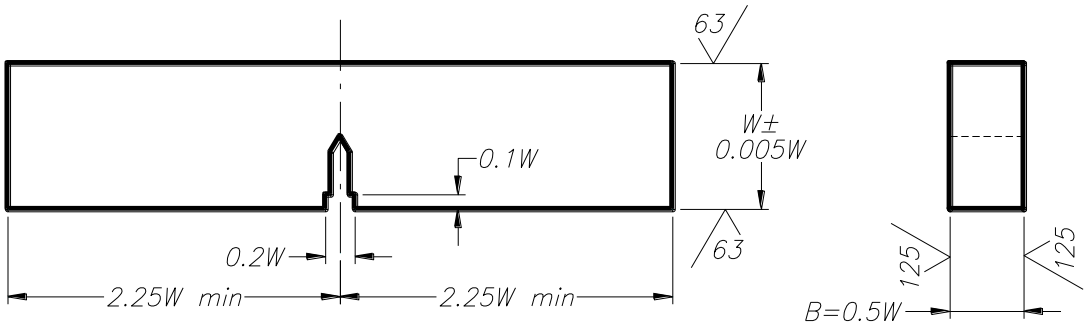

Figure 1. SE(N)B specimen made of NN 70

3. RESULTS AND DISCUSSION

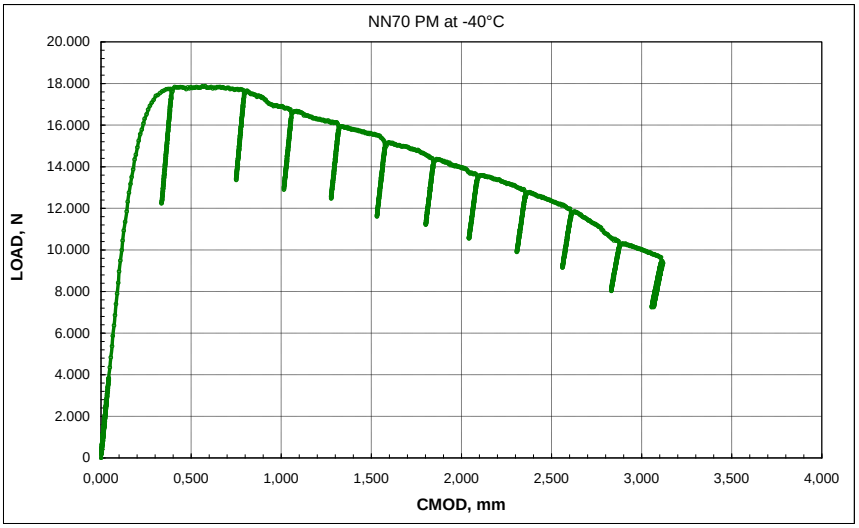

Figure 2. Load-CMOD curves for PM obtained at test temperature of -40°C

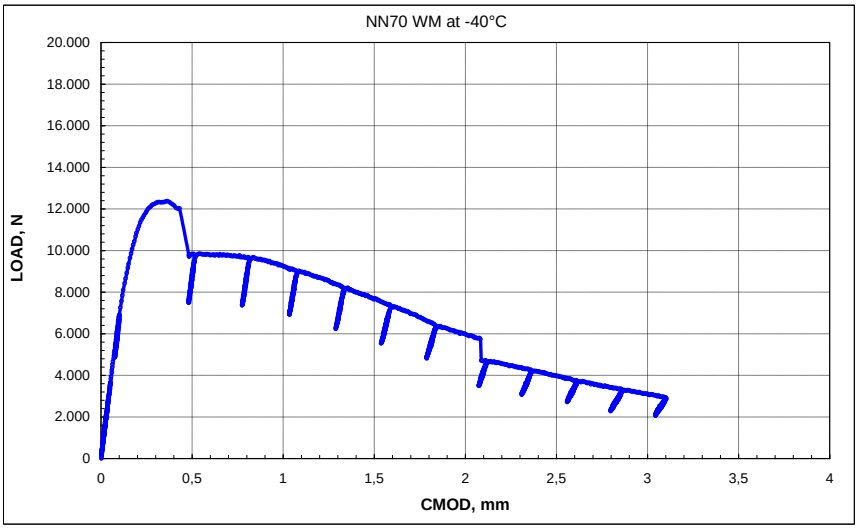

Figure 3 Load-CMOD curves for WM obtained at test temperature of -40°C

Obtained curves load versus *CMOD*, for different welded joint constituents are shown in Figures 2, 3 and 4.

Characteristic resistance curves for different welded joint constituents are shown in Figure 5.

J_{IC} was calculated according to standard ASTM E 1820-08 and obtained curves are presented in Figures 6, 7 and 8.

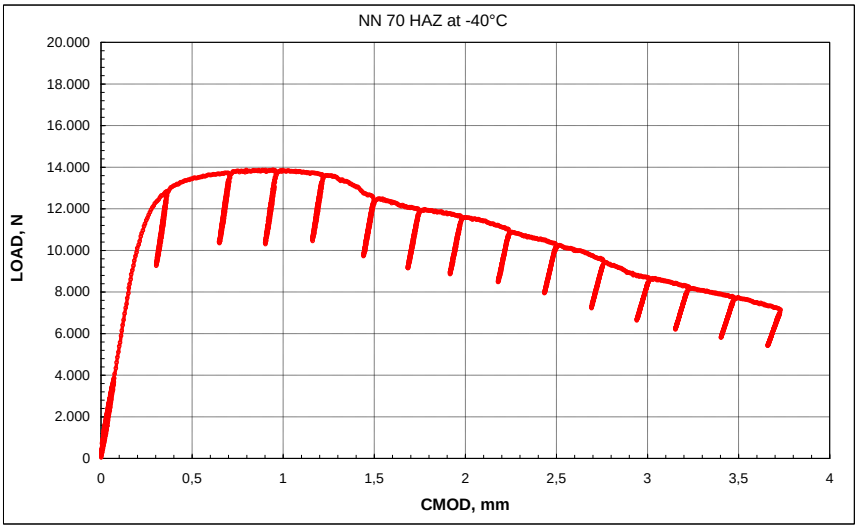

Figure 4. Load-CMOD curves for HAZ obtained at test temperature of -40°C

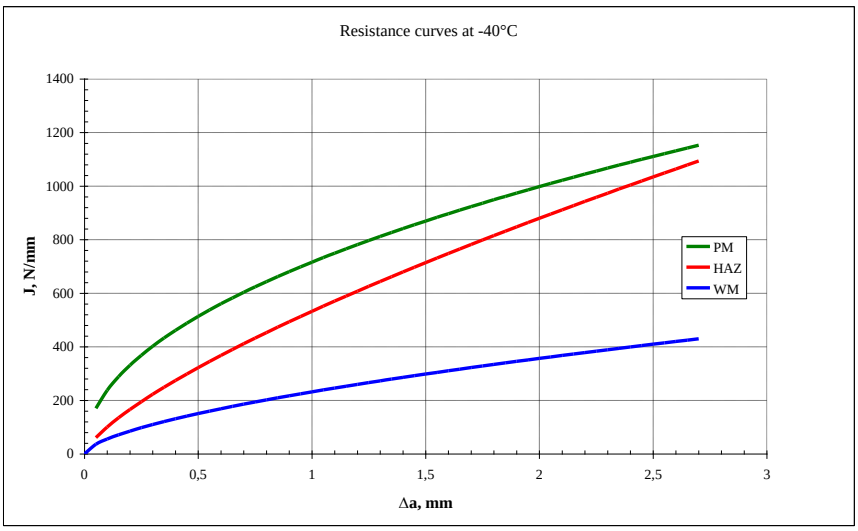

Figure 5. J-R curves for PM, WM and HAZ obtained at test temperature of -40°C

It can be seen from given mechanical properties in Table 2, that PM has a satisfactory toughness whereas WM is boundary acceptable according to code of practice for pressure vessels design. HAZ toughness is greater than those of WM which may be explained by notch position; the notch was most probably positioned in local softened HAZ with higher impact toughness than in WM but lower comparing to PM.

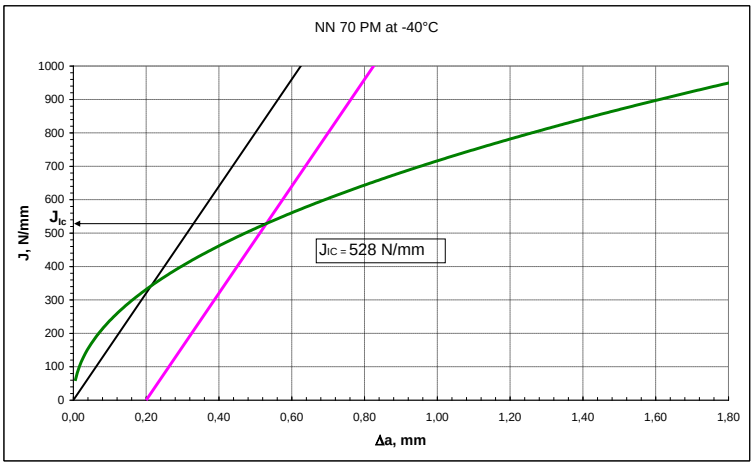

Figure 6. Plot J versus Δa for PM obtained at test temperature of -40°C

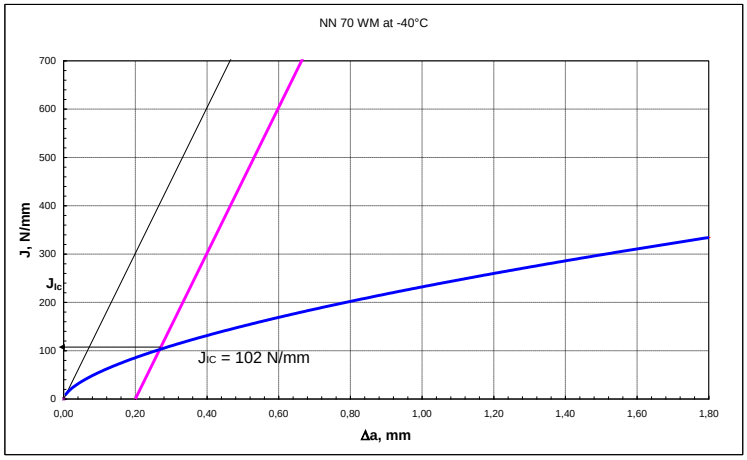

Figure 7. Plot J versus Δa for WM obtained at test temperature of -40°C

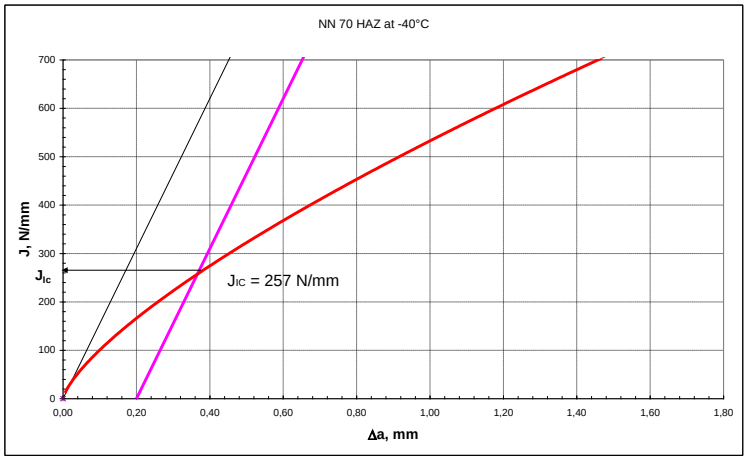

Figure 8. Plot J versus Δa for HAZ obtained at test temperature of -40°C

Load versus *CMOD* curves shown in Figures 2, 3 and 4 describes the behaviour of notched specimen exposed to load. PM curve, Figure 2, shows stable crack growth during complete experiment. Maximal load of 17.867 N was reached at *CMOD* = 0.579 mm. PM exhibits good behaviour under load at temperature of -40°C, curve is continual, no pop-in, which may indicate that NN 70 is suitable for producing of pressure vessels for low temperature

operating conditions. In WM, Figure 3, pop-in can be seen meaning that, when crack entered in local brittle zone, it propagated fast, after that crack entered in zone of higher toughness where had continued to grow stably. Crack propagated until the end of experiment when clip-gage linear capacity was exhausted, at *CMOD* value of 3.103 mm. In Figure 4 it can be observed that fatigue crack was positioned in locally softened zone of HAZ with higher toughness, so the growth of crack was stable. HAZ behaviour is similar to PM only that maximal load in HAZ (13.872 kN) was reached at lower load values than in PM but also at higher *CMOD* values (0.944 mm) than in PM, indicating good toughness in HAZ.

Resistance curves given in Figure 5 show the energy amount needed for crack propagation. Relatively high values are needed for crack propagation in PM, for 1 mm of propagation *J* was approximately 720 N/mm. *J* value in WM were drastically lower comparing to PM (for crack propagation of 1 mm *J* was approximately 235 N/mm). *J* value in HAZ are lower than for appropriate ones for PM but much higher than for WM (for crack propagation of 1 mm *J* was almost 520 N/mm) which can be explained by the fact that crack was positioned in local softened zone with surprisingly high toughness. After stable crack growth through HAZ, crack reached PM where continued to grow stably.

Values of J_{IC} parameter are used for characterization of material resistance to crack growth. Experimentally obtained values for J_{IC} at -40°C of PM show relatively high value of 528 N/mm, Figure 6, and J_{IC} value for WM was 102 N/mm showing that, in pressure vessels, the weakest part will be WM, Figure 7. High J_{IC} value in HAZ of 257 N/mm, Figure 8, confirms the suitability of investigated welded material for pressure vessel fabrication.

4. CONCLUSION

Impact testing ant fracture mechanics testing show that NIONIKRAL 70 steel is suitable for manufacturing of pressure vessels for applications up to -40°C.

5. ACKNOWLEDGEMENTS

Authors acknowledge the financial support of the Serbian Ministry of Science, project TR 35011. The authors are thankful to Peter Rozsahegyi, Bay-Logi Institute for Logistics and Production Systems, Miskolc, Hungary, for valuable help in experiments. The authors also express their appreciation to Professor Blagoj Petrovski from the University of Belgrade, for invaluable help and suggestions in writing this paper.

6. REFERENCES

[1] **ANDERSON, T. L.:** *Fracture mechanics*, Taylor &Francis, USA, 2005, 636 p.
[2] **RICE, J. R.:** *A Path Independent Integral And Approximate Analysis Of Strain Concentration By Notches And Cracks*, Journal of Applied Mechanics, 1968, 35: pp. 379-386.
[3] **SEDMAK, S., PETROVSKI, B., SEDMAK, A.:** *The Resistance to Crack Growth of Different Regions of Weldments in a Real Structure*. International Journal of Pressure Vessels & Piping, 1992, 52: pp. 313-335.
[4] **MILOVIĆ, LJ., VUHERER, T., ZRILIĆ, M., MOMČILOVIĆ, D., JAKOVIĆ, D.:** *Structural Integrity Assessment Of Welded Pressure Vessel Produced Of HSLA Steel*, Journal of Iron and Steel Research International, 2011, 18(1-2): pp. 888-892.
[5] *ASTM International E 1820* (2008) *Standard test method for measurement of fracture toughness*, 48 p.

HVOF SPRAYED COATINGS REMELTING WITH LASER BEAM

[1]MOLNAR András EWE, [2]BUZA Gábor Dr., [3]BALOGH András Dr.,
[4]FAZEKAS Lajos Dr.

[1]*University of Miskolc*
a.molnar2007@gmail.com

[2]*BAY-ATI Institute for Materials Science and Technology*
buza@bzaka.hu

[3]*University of Miskolc*
balogh.andras@uni-miskolc.hu

[4]*University of Debrecen*
fazekas@eng.unideb.hu

Abstract
In this study, NiCrBSi powders were sprayed using a high velocity oxygen fuel technique on C 45 steel substrate. The deposited coatings are compared in terms of their chemical composition and microstructure. The structure and morphologies of Ni-based coatings were investigated by X-ray diffraction (XRD), scanning electron microscopy (SEM) and energy dispersive spectrometer (EDS.) Microstructures of the coatings have been revealed to the presence of a large amount of dispersed Ni and Cr carbide and borides in the Ni matrix. Microhardness of the coatings is found to in the range of 550–830 Hv, which is higher than the substrate material.

Keywords: *Thermal spray process, laser beam, remelting*

1. INTRODUCTION

High Velocity Oxy-Fuel Thermal Spraying

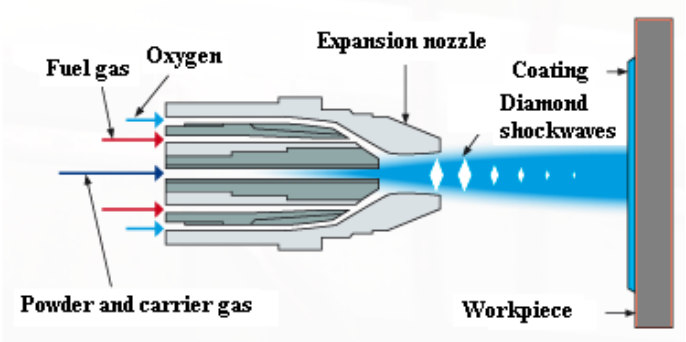

Figure 1. Schematic diagram of the HVOF process

This type of spraying differs from conventional flame spraying in that the combustion process is internal, and the gas pressure is much higher than that used in the atmospheric

burning flame spraying processes. In this process the combustion fuel gas (hydrogen, propane, or propylene) and oxygen are fed to the spray gun together with the spray material.

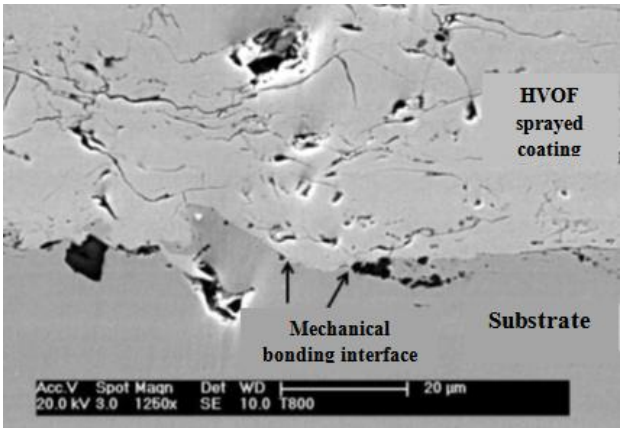

Figure 2. Cross-section of T800 HVOF coating on stainless steel substrate [2]

Splat formation and structure of HVOF coating

The splat is the base building block of the structure in HVOF coating. These splats are formed when a stream of molten and semi molten particles impacts on the substrate (Figure 2). The molten droplets are in general spherical in shape before impacting on the substrate surface, followed by flattening, rapid solidification and cooling processes [1]. Then continuous impacting of particles will increase the thickness of the coating. The produced microstructure of this thermal spray is a
complex mixture of lamellas (*Figure 3*).

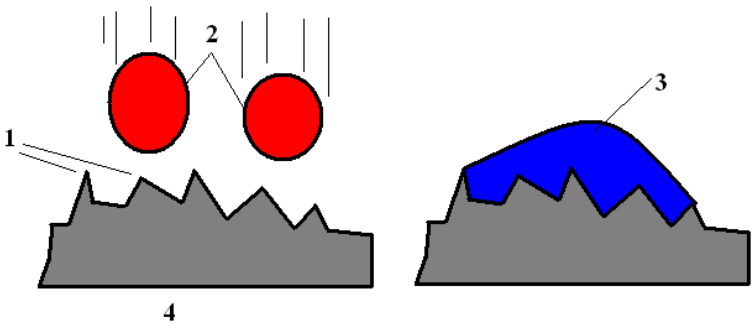

Figure 3. Schematic diagram of adhesion of a particle to a substrate asperity. (1) asperities, (2) particle in flight, (3) particle mechanically locked to the substrate, (4) substrate [1].

Microstructure of HVOF-Sprayed coatings

The HVOF coating generally consists of lamellar splats (droplets of semi-molten or molten powders), unmelted particles, voids and oxidised particles (Figure 4). The typically HVOF coating also contains certain defects, such as oxide inclusions in metallic coatings, which are usually seen as dark phase areas in the coating cross section. As a result of the low temperature, only mechanical bonding is produced between the coating and the substrate.

Also, HVOF coatings may contain unmelted particles and pores, which produce an inhomogeneous structure.

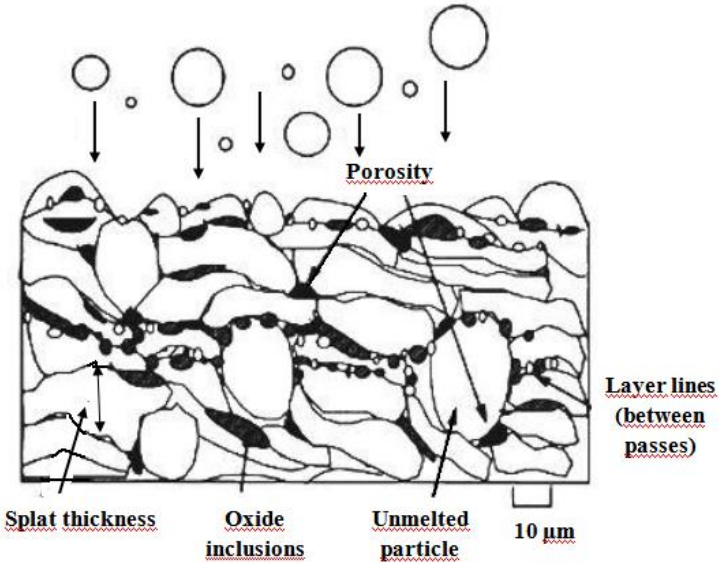

Figure 4. Thermal spray coating microstructure showing common features [3]

A typical cross section of HVOF sprayed coating is shown in figure 5. The powder will fully melt or partially melt due to flame temperature which varies from 2500 °C to 3200 °C depending on the fuel, fuel/oxygen ratio and gas pressure. Use of the HVOF process has been growing rapidly specially for materials which are sensitive to phase transformations due to oxidation, decarburisation, or evaporation, because this process has relatively low flame temperatures and low exposure time in the flame. The high kinetic energy and low thermal energy will result in better adhesive bonding and high density coating with relatively low residual thermal stress which results in coating thicknesses between 100 □m and 300 □m [2].

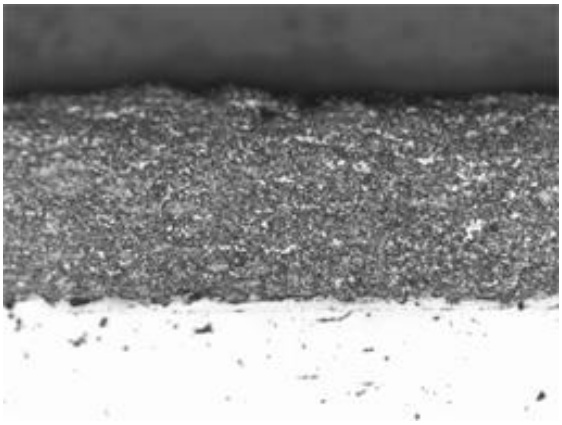

Figure 5. HVOF sprayed, tungsten carbide. HVOF on steel substrate [3]

In recent years, there has been a significant growth in the use of this technique to spray cermets, metallics and ceramics. HVOF coatings have recently gained more popularity and are now extensively studied for protection against corrosion and wear [3, 4 - 7]. Furthermore, HVOF technology has found many applications such as automotive, aircraft, oil and other

industries, the goal of this technique in all applications is to increase the lifetime of the surfaces as compared with uncoated substrate surfaces [8 - 11].

2. METHODS AND EXPERIMENTAL PROCEDURE

Figure 6 shows an experimental procedure of the two step process: coating deposition using a flame spraying torch and coating remelting with laser. The two influencing parameters of substrate surface preparation, that is, surface preparation with grit blasting and preheating of the substrate for the reduction of temperature stresses, were used. The spray process parameters chosen were the distance of the torch nozzle from the substrate surface and the mixture ratio of acetylene and oxygen. Specimens were tested for microstructure and chemical analysis.

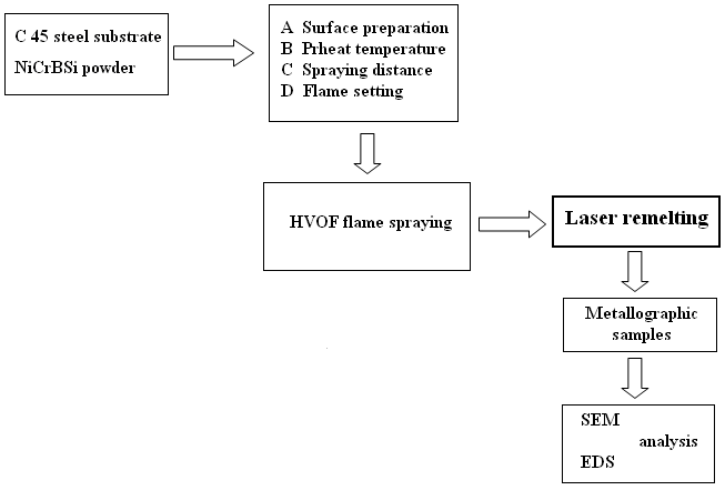

Figure 6. Work procedure plan

The application of a laser can improve the properties of thermally sprayed coatings. Improvements recently studied concern biomedical coatings, thermal barrier coatings, wear resistant composite coatings, corrosion resistant alloys, and wear resistant coatings engraved with a laser (anilox rolls). Most of the laser treatments correspond to the process of cladding, and only a few papers concern alloying or hard phase dispersion.

2.1. The flame-spray process

The surface of the bars were prepared by grit blasting using angular Al_2O_3 1% grit with nominal grain size of 0.5 mm before applying the flame-spray depositing process in order to eliminate grease and oxide, and to improve the adherence between the coating and the substrate (Figure 7).

The flame-spray process was completed with a TOPGUN UTP gun at a pressure of 2.5 bar for the oxygen gas and of 1 bar for the acetylene. Feedstock consumption was 9.0 kg/h and the optimal spraying distance was 150 mm (*Table 1*).

Table 1 Flame spray parameters for the NiCrBSi powders

Acetylene flow rate l/min	Oxyigen flow rate [l/min]	Feedstock carrier gas (air) flow rate [l/min]	Spray distance [mm]	Spray velocity [m/s]	Scanning step [mm]
6	16	35	180	150	5

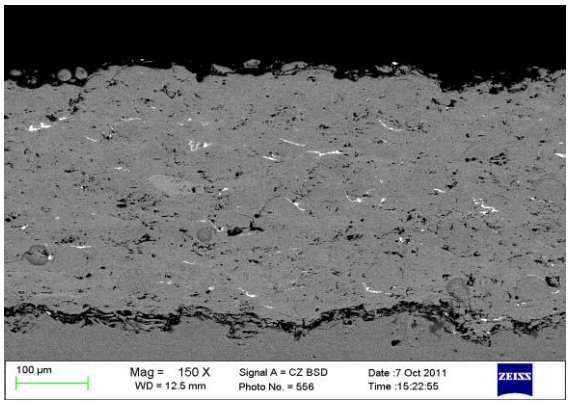

Figure 7. Cross-section of NiCrBSi HVOF coating on steel substrate (N=150X)

Table 2 CO_2 laser operating parameters

Frequency (f) [Hz]	Pulse duration (t_p) [µs]	Scanning speed [mms^{-1}]	Defocusing (z) [mm]	Spot diameter (d) [mm]
1500	20	2	+100	3

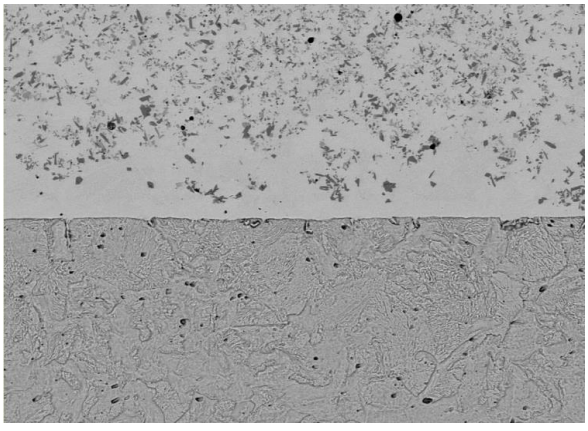

Figure 8. Microtructure of a HVOF flame sprayed NiCrBSi coating fused by laser (N=50X).

After spraying, the flame-spray coatings were laser remelted. Incomplete melting along the full thickness of the coating means a lack of metallurgical bonding between substrate and coating, and is a frequent outcome of the process. An alternative technique used for post-treatment coating consists of using a laser beam to melt the flame-sprayed layer (*Figure 8*). The BAYATI TRUMPF TLC 105 5 KW CO_2 laser equipment with a nominal power of 1900

W was used to this end in our testing and A Kugler LK- 190 laser focusing head at a focal distance of 125 mm was used for thermal treatment. Equipment optics was protected by a 2 bar pressure cross current of air (*Table 2*).

2.2. SEM - EDS analysis

Composition profiles of NiCrBSi 2760, UB5 + laser melted samples carried out by EDS on the cross section. The EDS analysis of FS-sprayed and in situ remelted samples shows a similar evolution of the chemical composition (Figure 9). (These profiles were not recorded on the complete thickness of the samples, as the chemical composition was uniform across the whole thickness of the coatings). The EDS analysis reveals also a high Cr content of the layer, probably due to the formation of Cr carbides and borides during the melting (*Figure 9*).

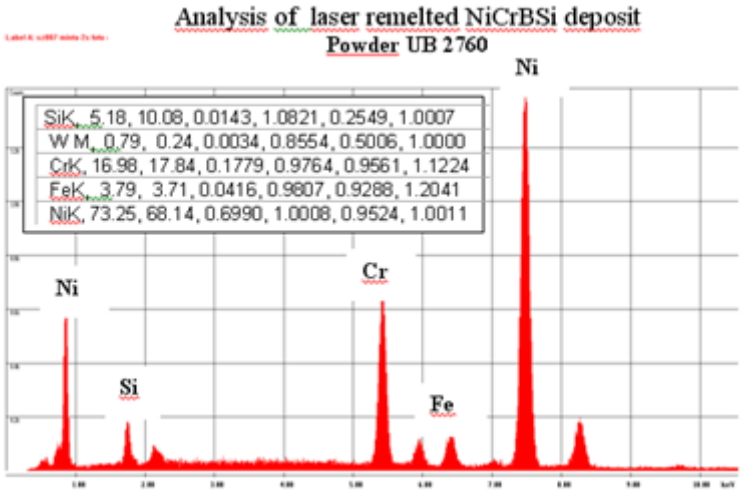

Figure 9. Details of the substrate coating interfaces: FS + laser remelted

3. CONCLUSIONS

In this work, three different thermal sprayed NiCrBSi coatings have been compared: UB5 – 2760 HVOF flame sprayed with a subsequent fusion treatment of laser (FS + laser). Their micro hardness and microstructure, properties were studied.

- *Microstructure*: all coatings show a similar microstructure composed mainly of a Ni solid solution matrix with dendritic structure and common phases precipitated on it with different distribution, size. Laser remelted coatings show a uniform distribution of small and rounded precipitates, which results in a harder material. Precipitates presented in FS + laser are similar in size but they are not homogeneously distributed. Finally the FS + laser coatings exhibit the biggest precipitates which are additionally characterized by a needle shape.
- Results show that in situ laser remelting induces the growth of a dendritic microstructure that strongly decreases the HVOF FS-sprayed coating porosity.
- The in situ process allows the construction of denser coatings than FS with finer structures, without cracks and porosity. The coating is metallurgically bonded to the substrate, which probably will increase the adhesion.

7. REFERENCES

[1] **T. GÓMEZ-DEL RÍO, M.A. GARRIDO, J.E. FERNÁNDEZ, M. CADENAS, J. RODRÍGUEZ:** *Influence of the deposition techniques on the mechanical properties and microstructure of NiCrBSi coatings,* Journal of Materials Processing Technology, Volume 204, Issues 1–3, 11 August 2008, pp. 304-312

[2] **CORDIA, M., DELOGU, P., NENCI, F.,:** *Microstructural aspects of wear-resistant stellite and colmonoy coatings by laser processing.* Wear 119 (2), 1987, pp. 137–152.

[3] **LI, Q., ZHANG, D., LEI, T., CHEN, C., CHEN, W.:** *Comparison of laser-clad and furnace-melted Ni-based alloy microstructures.* Surf. Coat. Technol. 137, 2001, 122–135.

[4] **KIM, H.J., HWANG, S.Y., LEE, C.H., JUVANON, P.:** *Assessment of wear performance of flame sprayed and fused Ni-based coatings*. Surf. Coat. Technol. 172, 2003, pp. 262–269.

[5] **MING, Q., LIM, L.C., CHEN, Z.D.:** *Laser cladding of nickel-based hardfacing alloys.* Surf. Coat. Technol. 106, 1998, pp. 174–182.

[6] **MIGUEL, J.M., GUILEMANY, J.M., VIZCAINO, S.:** *Tribological study of NiCrBSi coating obtained by different processes.* Tribol. Int. 36, 2003, pp. 181–187.

[7] **XIN, H., HU, C., BAKER, T.N.:** *Microstructural assessment of laser nitrided Ti–6Al–4V alloy.* J. Mater. Sci. 35 (13), 2000, pp. 3373–3382.

[8] **MOLIAN, P.A., RAJASEKBARA, H.S.:** *Laser melt injection of BN powders on tool steels.* Part I. Microhardness and structure. Wear 114 (1), 1987, pp. 19–27.

[9] **ATAMERT, S., BHADESHIA, H.:** *Comparison of microstructures and abrasive wear properties of stellite hardfacing alloys deposited by arc welding and laser cladding.* Metall. Trans. A 20, 1989, 1037.

[10] **MONSON, P., STEEN, W.M.:** *Comparison of laser hardfacing with conventional processes.* Surf. Eng. 6 (3), 1990, pp. 185–193.

[11] **OBERLANDER, B.C., LUGSCHEIDER, E.:** *Comparison of properties of coatings produced by laser cladding and conventional methods.* Mater. Sci. Technol. 8, 1992, pp. 657–665.

THERMAL SPRAYED NICRBSI COATINGS MODIFICATION WITH DIFFERENT METHODS

[1]MOLNÁR András EWE, [2]FAZEKAS Lajos, Dr. , [3]RÁTHY Istvánné, Dr.
[4]BALOGH András, Dr.

[1]*University of Miskolc*
a.molnar2007@gmail.com

[2]*University of Debrecen*
fazekas@eng.unideb.hu

[3]*University of Debrecen*
rathyne@eng.unideb.hu

[4]*University of Miskolc*
balogh.andras@uni-miskolc.hu

Abstract
Thermal spray processes, especially high velocity oxygen fuel (HVOF), are widely used coating techniques in many gas, oil industrial applications and to protect automobil worm parts materials from various degradation processes such as wear, erosion, high temperature and corrosive atmosphere. In addition, inhomogeneous structures of the HVOF coatings limit their effectiveness to be used as physical barriers to inhibit corrosive species from getting into contact with the substrate to be protected. As a result, improvement against corrosion by such coatings is limited in most cases. In order to further improve the corrosion resistance of the coating properties, laser surface modification could be considered as a potential technique to eliminate or reduce the defects of the coatings. Laser surface modification via re-melting, offers many advantages including precisely controlled treatment dimensions, particularly in depth, and minimum heat-affected zones, resulting in no thermal effects on substrate materials.

Keywords: *HVOF, NiCrBSi-based coating, laser remelting*

1. INTRODUCTION

Ni-based coatings are used in applications where corrosion and wear resistance at moderate and elevated temperatures are required [1 - 5] NiCrBSi alloy is one of the alloys with betterperformances [6 - 7]. The addition of Si and B increase the self-fluxing capabilities of the Ni alloy, improving its ability to produce coatings by melting process. B addition reduces the melting point due to the presence of a eutectic phase at 3.6% wt. The broad solidification interval of the Ni alloys with high-boron content makes easier to get coatings by thermal spray process.

After the spraying process, the coating was melted at 1025 °C by either using a flame or a laser. The melting process by flame consists of applying an oxyacetylene flame on the coating until the melting temperature is reached. It is a manual process, and then the final quality of the coatings

depends on the ability and experience of the operator. The melting process by laser consists of applying a CO^2 laser working with 1900 W of power on the coating.

The quality of the coatings manufactured by thermal deposition techniques depends on several parameters such as the sprayed particle size, the deposition temperature, the combustion gases, the feed speed, the angle and rate of deposition (continuous or intermittent), the spray distance, the temperature of the substrate, the pressure applied during the process and, of course, the deposition technique. All these parameters should be carefully selected in order to obtain the best properties for each application.

Among the techniques employed to melt and spray material, flame spray and plasma spray processes are widely used. The coatings produced by flame spray are characterized by a high porosity and a poor adhesion to substrate. For that reason, this technique is commonly combined with a subsequent melting process. Laser cladding is a spray technique usually employed to produce coatings for valuable components and products. It is characterized by producing coatings with a very low porosity and, consequently, better wear and corrosion resistance are expected [8 - 11].

1. 1. Laser beam interaction with materials

When a laser beam is incident on the surface of material, such as a metal (Opaque material), some of the energy is absorbed into the near-surface regions, and some reflected. In these materials, Absorptivity depends on the material, laser wavelength, temperature of material, and surface roughness [10]. The portion of the incident optical energy that is absorbed is of interest in material processing.

1. 2. Laser surface treatment

Lasers have been used in numerous applications, such as communication, medical and material processing. Laser surface treatment is used to change the surface microstructures to enhance locally some specific properties of the surface such as hardness, wear and corrosion resistance. This process includes surface heating, alloying and cladding. *Figure 1* is schematic showing a simple classification of laser surface treatment. *Figure 1* show the different techniques of laser surface treatment.

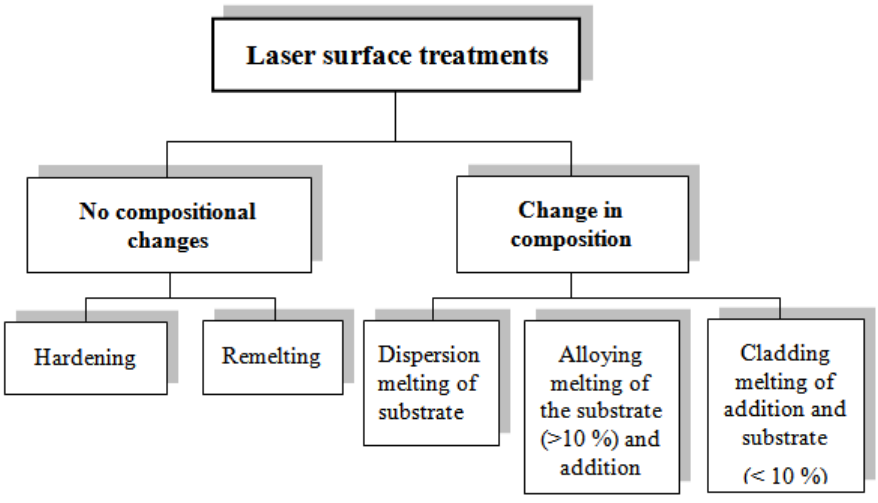

Figure 1 Laser surface processing [11]

The absorbed optical energy (photons) is immediately transformed to cause vibrational motion of electrons in the affected zone by the excitation of electrons from their equilibrium states to some excited states. These vibrations are transmitted into the structure of the material within an extremely short period of time. The optical energy is converted to heat, which gradually transfers to adjacent atoms. The temperature will increase as more photons are absorbed. Moreover, the temperature will rise rapidly, and the near-surface region undergoes extreme heating and cooling rates (10^3-10^{10} K/s), very high thermal gradient (10^6-10^8 K/m) and a rapid solidification velocity (1-30 m/s) [12]. The flow of heat in the material can be described by conventional heat equation.

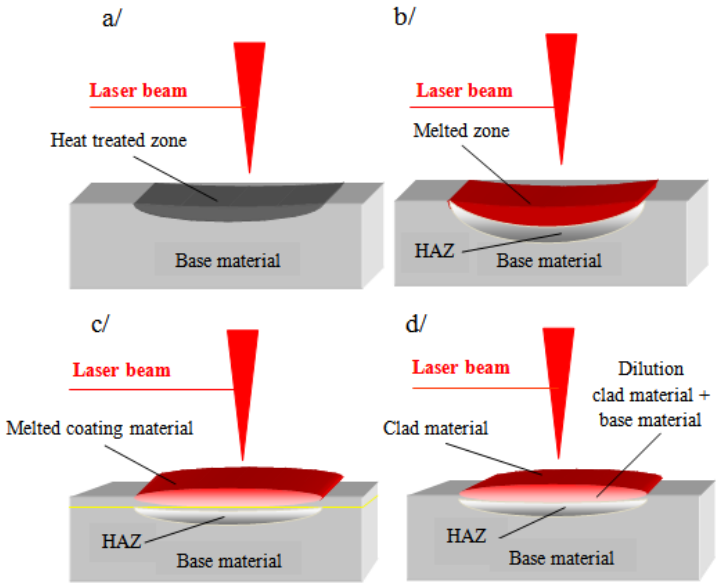

Figure 2. Laser surface treatment techniques; (a) laser transformation hardening, (b) laser surface melting, (c) laser alloying, (d) laser cladding

Laser transformation hardening

When the laser beam heats the surface of material, the surface may be hardened by a solid state transformation mechanism (Figure 2 a/). Following heating, the laser energy is reduced or switched off or the beam moved off to another area, and the cold bulkmaterial then quenches the heated surface; this will cause extremely rapid cooling.

Laser surface alloying

Laser surface alloying is variation on the surface melting process by adding another material into the melt pool. This process produces a surface layer which is different from the substrate (*Figure 2 b/*). The potential of surface alloying to reduce consumption of expensive alloying elements is both strategically and commercially significant. The process of laser surface alloying (LSA) is similar to the surface melting with the laser; however, to modify the surface chemical composition, a desired alloying element should be added to the melt pool. The technique has become more and more popular, since there are several different ways of introducing the alloying element into the thin surface layer melted by the laser beam [12-14].

Laser surface melting

In this type of processing, the laser beam is used to melt a small region of the substrate surface. This processing does not change chemical compositions within the melted layer, but changes its microstructure, in terms of a refined and possibly metastable microstructure in small localised areas of base material (Figure 2 c/). The features of this process are: flexibility resulting from possibilities of computerisation (software control) of the process and automation, and it has small thermal penetration and therefore minimum distortion. By this procedure fine homogeneous structure can be obtained due to rapid cooling rates, where the unaffected substrate acts as a heat sink. When the beam traverses past, the solidification process starts from the solid/melt interface towards the surface.

Laser cladding

This method involves melting and adding another material as in the alloying process. However, dilution in this process is kept to minimum. This technique creates metallurgical bonding of the clad layer with the substrate to improve the surface properties of a material which will be subjected to corrosion, erosion or wear (Figure 2 d/).

2. THE EXPERIMENTAL PROCEDURE

A NiCrBSi UTP UB - 2760 alloy with an average grain size of 125 μm and a melting point of 976 -1063 ˚C was used as the coating material. The surface state before the flame spray process was typical for machining, with a rust- and impurity-free average surface roughness *R*a = 1.1 μm. The chemical composition of all the used materials is described in *Table 1-2*.

2.1 Feedstock materials

Table 1. Chemical composition and hardness of substrate steel

Grade of steel	Composition , [wt. %]			Hardness [HV 1]	
	C	Mn	Si	Normalized	Hardened
C 45*	0,45	0,60	0,30	200 - 235	480 - 515

*Wn. 1.1191 DIN Ck 45

Table 2. Chemical composition and particle size of used self-fluxing NiCrBSi spray powders

Trade mark	Composition, [wt %]						Particle size [μm]	Hardness of coating [HRC]	Melting range [C^o]
	Ni	Cr	Si	B	C	Fe			
UB5-2760*	Balance	15,0	4,4	3,2	0,75	3,5	-125 - +45	60	964 - 1063

One NiCrBSi super-alloy powder was used as coating material. The powder was composed of spherical particles with an average size of 66 μm. The substrate material was Ck 45 steel in the form of bar, with a L = 300 mm and diameter of 50 mm in *Table 1*.

NiCrBSi powders from Böhler – UTP referenced as grade UB 5-2760, was chosen as feedstock material. The composition of the sprayed powders is listed in *Table 2*.

2. 2. The flame-spray process

The surface of the bars were prepared by corundum blasting using angular Al_2O_3 1% particle with nominal grain size of 0.5 mm before applying the flame-spray depositing process in order to eliminate grease and oxide contamination, and to improve the adherence between the coating and the substrate.

Table 3 Flame spray parameters for the NiCrBSi powders

Thermal spray process	Acetylene flow rate [l/min]	Propane flow rate [l/min]	Oxygen flow rate [l/min]	Powder carrier gas (air) flow rate [l/min]	Spray distance [mm]	Spray velocity [m/s]	Scanning step [mm]
HVOF	-	62	240	15	180	450	6

The flame-spray process was completed with a UNY-SPRAY-JET UTP and a UTP TOP GUN AIR HVOF guns at a pressure of 2.5 bar for the oxygen gas and of 1 bar for the acetylene (Table 3). Powder consumption was 9.0 kg/h and the optimal spraying distance was 150-180 mm.

2.3. The laser remelting process

After spraying, the flame-spray coatings were laser remelted. Incomplete melting along the full thickness of the coating means a lack of metallurgical bonding between substrate and coating, and is a frequent outcome of the process. An alternative technique used for post-treatment coating consists of using a laser beam to melt the flame-sprayed layer; in our experiment we used the two-stage method. The BAYATI 5 kW CO_2 laser equipment with a nominal power of 1900 W was used to this end in our testing and a Kugler LK - 190 laser focusing head at a focal distance of 125 mm was applied for thermal treatment. Equipment optics was protected by a 2 bar pressure cross current of air.

The laser equipment was used in continuous mode with argon as protective gas. The different process parameters and their influence on the layers obtained were studied under the above conditions. The most satisfactory results were achieved with the following parameters: power density on the surface of the piece of 38 W/mm^2, beam scanning speed of 150 mm/min and a laser beam diameter of 3 mm. In addition, in order to reduce cracking risk, the test specimens were preheated in a furnace and their cooling rate after the laser treatment was slowed by placing them in perlite.

Table 3. CO^2 laser operating parameters

Frequency (f) [Hz]	Pulse duration(t_p) [μs]	Scanning speed [mm/s]	Defocusing (z) [mm]	Spot diameter (d) [mm]
1500	20	2	+ 100	3

3. MICROSTRUCTURE AND LAYER HARDNESS

Scanning electron microscope techniques with energy dispersive spectroscopy ZEISS EVO MA 10 instrument (SEM–EDS) were used to metallographic investigation and analyse the coatings microstructures and micrhardness (*Figure 6 – 9*). Specimens for micro-structural analysis were firstly ground and polished to a mirror finish and then etched with solution of $1HCl:10HNO_3:10H_2O$. Figure 6 and 7 shows the structure obtained after laser remelting. It can be clearly seen that the matrix phase is a solid solution of Ni with some Cr and Fe providing a dendrite structure; there is an interdendrite lamellar eutectic phase made up mainly of Ni and small amounts of Si.

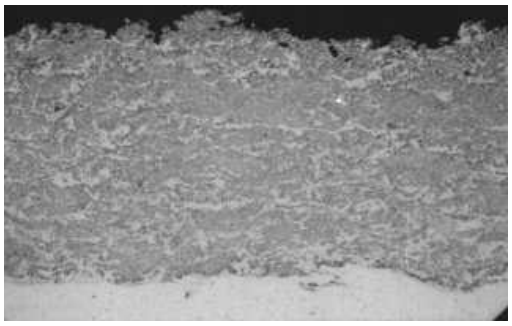

Figure 6. HVOF thermal sprayed layer (N = 150)

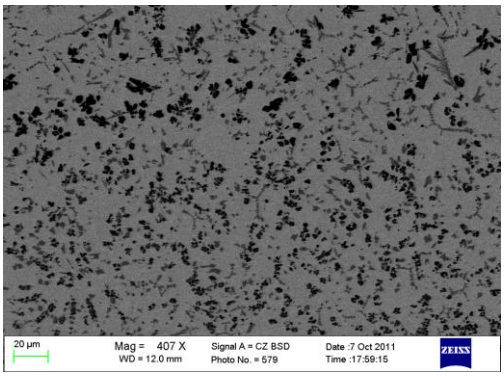

Figure 7. Micro-structure of a HVOF flame sprayed NiCrBSi coating fused by laser (M=407x).

Micro-hardness tests were carried out according to the ASTM E-384 standard with Mitutoyo MVK-H1 micro-hardness tester.

The surface is dotted with very hard precipitates, mainly of Cr (approximately 80 % by mass). This confirms the tendency of these alloys to form carbides and borides, thus supporting the results for similar alloys obtained by other researchers, who have identified these precipitates as chromium carbides and borides (mainly Cr_7C_3 and CrB) in a Ni solid solution with a dendrites morphology.

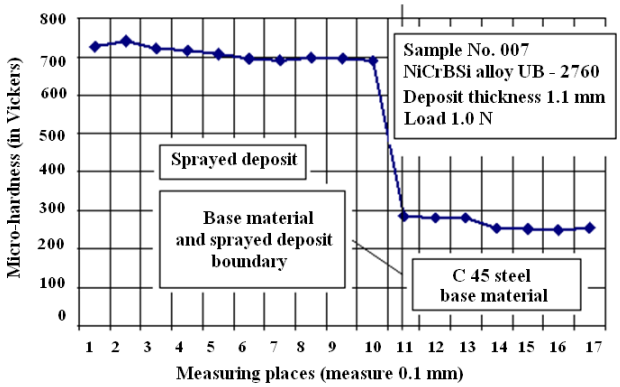

Figure 8. Micro-hardness testing results of the UB5-2760 NiCrBSi coatings as a function of the distance from the surface.

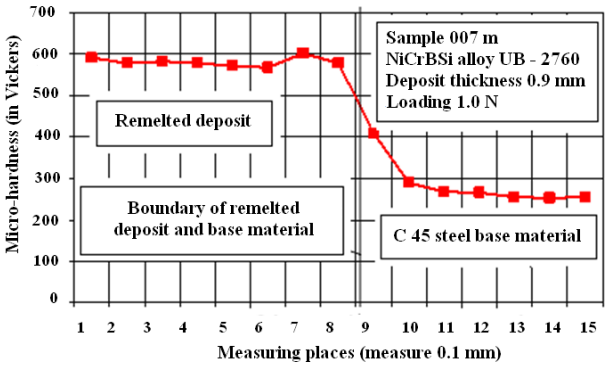

Figure 9. Micro-hardness testing results of the UB5-2760 NiCrBSi laser remelted coatings as a function of the distance from the surface.

4. CONCLUSIONS

In this work, thermal sprayed NiCrBSi coatings have been tested: UB5 – 2760 HVOF flame sprayed with a subsequent remelting treatment of laser (HVOF FS + laser). Their micro-hardness and microstructure, properties were studied.

- *Micro-hardness* was determined by depth sensing indentation. A fine uniform distribution of equated precipitates increase the hardness, as it can be observed in laser remelted coatings. The non-homogeneous distribution of precipitates decreases the hardness values in FS + laser coatings.
- All coatings show a similar microstructure composed mainly of a Ni solid solution matrix with dendrites structure and common phases precipitated on it with different distribution and size. Laser remelted coatings show a uniform distribution of small and rounded precipitates, which results in a harder material.
- Results show that in situ laser remelting induces the growth of a dendrite microstructure that strongly decreases the HVOF FS-sprayed coating porosity.

5. REFERENCES

[1] **MOHSEN MOHAMED:** *Rakhes Laser Surface Modification of HVOF Coatings for Improvement of Corrosion and Wear Performance.* Ph. D thesis 2013. University of Manchester

[2] **DAVIS, J.R.:** *Handbook of thermal spray technology.* 2004: ASM International.

[3] **TURUNEN, E.:** *Diagnostic tools for HVOF process optimization*, Materials Science and Engineering 2005, University of Technology: Helsinki. p. 144.

[4] **MAGNANI, M.:** *Influence of HVOF parameters on the corrosion and wear resistance of WC-Co coatings sprayed on AA7050 T7.* Surface and Coatings Technology, 2008. 202(19): pp. 4746-4757.

[5] **SUUTALA, J., J. TUOMINEN, and P. VUORISTO:** *Laser-assisted spraying and laser treatment of thermally sprayed coatings.* Surface & Coatings Technology, 2006: pp. 1981-1987.

[6] **GUILEMANY, J.M., S. DOSTA, AND J.R. MIGUEL:** *The enhancement of the properties of WC-Co HVOF coatings through the use of nanostructured and microstructured feedstock powders.* Surface and Coatings Technology, 2006. 201(3-4): pp. 1180-1190.
[7] **ASL, S.:** *Effect of heat treatment on wear behavior of HVOF thermally sprayed WC-Co coatings*. Wear, 2006: pp. 1203-1208.
[8] **ASL, S.K.:** *Study of phase transformations in heat treatment of HVOF thermally sprayed WC-17Co coating*, 2008. pp. 161-166.
[9] **GERARD, B.:** *Application of thermal spraying in the automobile industry.* Surface & Coatings Technology, 2006: pp. 2028-2031.
[10] **KOUTSKY, J.:** *High velocity oxy-fuel spraying.* Journal of Materials Processing Technology, 2004. 157-158(SPEC. ISS.): p. 557-560.
[11] **STEEN, W.:** *Laser Material Processing*. Third ed. 2003, London: Springer.
[12] **J. KUSINSKI, S. KAC, A. KOPA, A. RADZISEWSKA, M. ROZMUS-GÓRNIKOWSKA, B. MAJOR, L. MAJOR MARCZAK AND A. LISECKI:** *Laser modification of the materials surface layer* – a review paper Bulletin of Polish Academy Sciences Technical Sciences, Vol. 60, No. 4, 2012
[13] **DUTTA MAJUMDAR, J. AND I. MANNA:** *Laser processing of materials.* Sadhana Academy Proceedings in Engineering Sciences, 2003. 28(3-4): p. 495-562.
[14] **ION, J.C.:** *Laser Processing of Engineering Materials.* First ed. 2005, Oxford, UK: Elsevier Butterworth-Heinemann

ENERGY CONSUMPTION OF TOMATO DRYING

[1]ÖRVÖS Mária, Dr., [2]SCHNEIDER Gyula, [3]VÁRKONYI Zsombor

[1]*University of Technology and Economics,*
orvos@vegyelgep.bme.hu

[2] *University of Technology and Economics,*
gyuszi.schneider@gmail.com

[3] *University of Technology and Economics,*
zsombor.varkonyi@gmail.com

Abstract
Tomato is perishable in fresh form, therefore a conserving procedure is required, like convectional drying. To preserve nutrition values and lessen the energy demand it is essential to set the proper process parameters. We constructed equipment to examine the properties and energy consumption of halved tomatoes during convectional drying. An optimal model was chosen to describe the moisture ratio temporal change. We established a mathematical model to calculate the momentary energy consumption as well as the specific energy need for the total process.

Keywords: *tomato, convective drying, energy consumption*

1. INTRODUCTION

Tomato is grown all over the world and consumed in several forms due to its unique taste and positive effects on the human body [1]. This vegetable is perishable in fresh form, therefore a conserving procedure is required to equalise the market supply [2]. Such a procedure can be natural - by sun radiation -, or artificial - by convection, radiation or microwaves. Convectional drying is one of the most common drying methods and used in several sizes, and forms for different materials [3]. The advantage of artificial drying is that the process time can be decreased significantly, and can be used on industrial scales, and independent from climatic conditions [4]. To preserve the nutrition values and to lessen the high energy demand of drying it is essential to know the energy demand and to set the proper process parameters.

2. METHODS

The drying gas temperature should be less than 70°C to retain the colour, shape, rehydration and other properties of the dried product. Above 70°C the degradation of lycopene is more rapid [5], while for ascorbic acid this limit is 60°C [6].

The moisture content of the dried material is usually specified relative to dry material $X\ \left[\frac{kg\ water}{kg\ dry\ material}\right]$ or to total mass $x\ \left[\frac{kg\ water}{kg\ dry\ material+kg\ water}\right]$. The average initial moisture content of tomato is 95% relative to wet material [3], which is typically decreased to 10% after the drying process [4].

The mass change of tomatoes during drying can be expressed with the ratio of actual and initial moisture content relative to dry material, using the following equation:

$$\mathrm{MR} = \frac{\mathrm{X_i} - \mathrm{X_e}}{\mathrm{X_0} - \mathrm{X_e}} \tag{1}$$

Where X_e is the equilibrium moisture content, X_0 is the initial, while X_i is the actual. In our case neglecting X_e does not cause significant error, because it is substantially less than the others [3].

Several models can be applied to fit a curve to the measured data for tomato drying. One, fitting our results with the smallest possible error was established by Handerson-Pabis, which is given as:

$$\mathrm{MR} = \mathrm{a} \cdot \mathrm{e}^{-\mathrm{b} \cdot \mathrm{t}} \tag{2}$$

Where *a* and *b* are parameters dependent from the drying air temperature and velocity. The proper fit of the model was verified by many measurements [8]. The calculated constants and the chosen curve can be seen in *Figure 2*.

Using the interpretation of moisture content together with Eq. (1) and (2) the mass of tomato in function of time can be written as:

$$m(t) = m_{dry\ material} \cdot X_0 \cdot \mathrm{a} \cdot \mathrm{e}^{-\mathrm{b} \cdot \mathrm{t}} + m_{dry\ material} \tag{3}$$

The temporal mass variation is given as the derivative with respect to time:

$$\frac{d\,m(t)}{dt} = -b \cdot m_{dry\ material} \cdot X_0 \cdot \mathrm{a} \cdot \mathrm{e}^{-\mathrm{b} \cdot \mathrm{t}} \tag{4}$$

A theoretical heat wattage need can be interpreted as the moisture reduction per unit time multiplied by the latent heat of evaporation ($\mathrm{r_p}$).

$$P_1(t) = -\frac{d\,m(t)}{dt} \cdot r_p \tag{5}$$

The average heat power calculated for *n* measurement points by the process time equals the average theoretical heat consumption.

$$E_1 = \bar{P_1} \cdot t_{final} = t_{final} \cdot \frac{1}{n} \sum_{i=1}^{n} \left(\frac{dm}{dt}\right)_i r_p = \frac{t_{final} \cdot r_p}{n} \cdot \sum_{i=1}^{n} \left(\frac{dm}{dt}\right)_i \tag{6}$$

For convectional drying the factual energy need (E_2) can be obtained from the wattage according to the change in drying air condition.

$$\mathrm{E_2} = P_2(t) \cdot\ t = A \cdot v_G \cdot \rho_G \cdot c_G \cdot \left(T_{G,in} - T_{G,out}\right) \cdot t \tag{7}$$

where $A\ [m^2]$ is the cross section area of the drying chamber, $v_G\ \left[\frac{m}{s}\right]$ is the velocity, $\rho_G\ \left[\frac{kg}{m^3}\right]$ the density, $c_G\ \left[\frac{kJ}{kg\ K}\right]$ the specific heat capacity, $T_{G,in}$, $T_{G,out}\ [°C]$ inlet and outlet temperature of drying air, while $t\ [s]$ is the total time of procedure.

E_2 is always higher than E_1, considering that the diffusion resistance and the heat demand of warming were not taken into consideration at the calculation of E_1. The connection between the two values can be given with a correlation factor:

$$E_1 \cdot C = E_2 \tag{8}$$

The heat power also can be calculated with the heat transfer coefficient, transfer area and temperature difference between the drying air and the tomato surface.

$$P_3 = \alpha \cdot A_{tomato} \cdot (T_G - T_{tomato}) \tag{9}$$

The heat transfer coefficient for tomato is not constant during the drying process. Initially simultaneous heat- and mass transfer (α_0) is present, while at the end of the drying practically just convective heat transfer (α_C) occurs. In case of total convective heat transmission the α_C can be estimated with modelling it as connected flat sheet and hemisphere [9].

The heat transfer coefficient with simultaneous heat- and mass transfer, typical at the beginning, can be calculated from the maximum of P_2 value defined in Eq. (7) along with Eq. (9).

$$\alpha_0 = \frac{P_{2,max}}{A_{tomato} \cdot (\bar{T}_G - \bar{T}_{tomato})} \tag{10}$$

Knowing the initial and final heat transfer coefficient, as well the drying time to reach 1% moisture content ($t_{1\%}$), the momentary value is given, according to Eq. (11) [8].

$$\alpha(t) = \frac{A \cdot \ln(t_{1\%}) - B}{\sqrt{t_{1\%}}} \tag{11}$$

Specific energy consumption e $[J/kg]$, which is the quotient of the total energy need E $[J]$ and the initial mass m_0 $[kg]$, is a common characteristic to describe the energy demand of the drying method [7].

$$\mathrm{e} = \frac{\mathrm{E}}{\mathrm{m_0}} \tag{12}$$

3. EXPERIMENTAL MEASUREMENTS

We constructed experimental equipment in order to measure the energy need of convectional drying. A schematic view of this laboratory sized convectional dryer is shown in *Fig. 1*.

During the measurement halved tomatoes were dried from an initial m_0 weight without any pre-treatment, with constant $\dot{m}_{air}$ air mass flow and $\bar{T}_G$ average air temperature. The total mass of the tomatoes - measured by a digital scale - was collected with computer with *15 min* sampling time, while the temperature and humidity of inlet and outlet air from an air condition transmitter was collected with *1 min.*

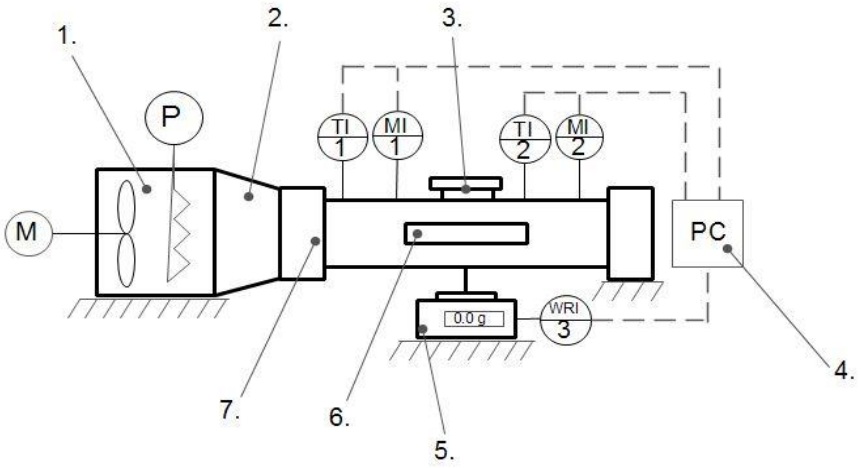

Figure 1 Convectional dryer
1. wire heated fan, 2. confusor, 3. feed slot, 4. data logger computer
8. digital scales, 6. eyehole, 7. drying chamber

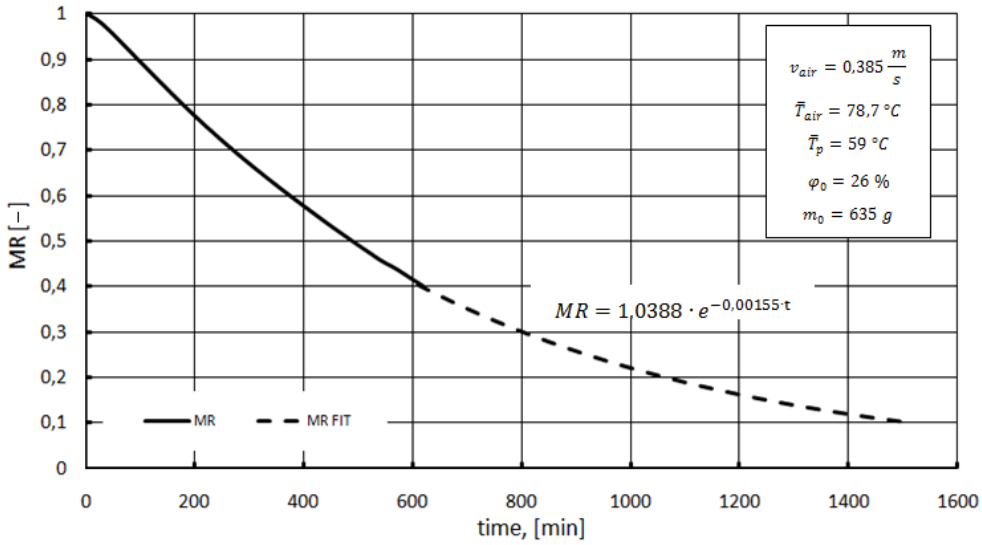

Figure 2 Moisture ratio of tomato vs. drying time for convective drying

4. RESULTS

Figure 3 shows the moisture ratio in function drying time for experiments conducted with different drying air velocities. During the measurements the parameters of drying process were approximately identical with the values written on *Fig. 2*.

The wattage requirement of drying $P_2(t)$ can be calculated according to Eq. (7). The determined values can be seen in *Fig. 5*. The values of $P_{2measured}(t)$ curve were corrected with the heat loss, occurring during the measurement. The time which is required to dry the product from the initial 95% moisture content to the final 10% can be obtained from Eq. (2), thus finally the energy need can be calculated as well.

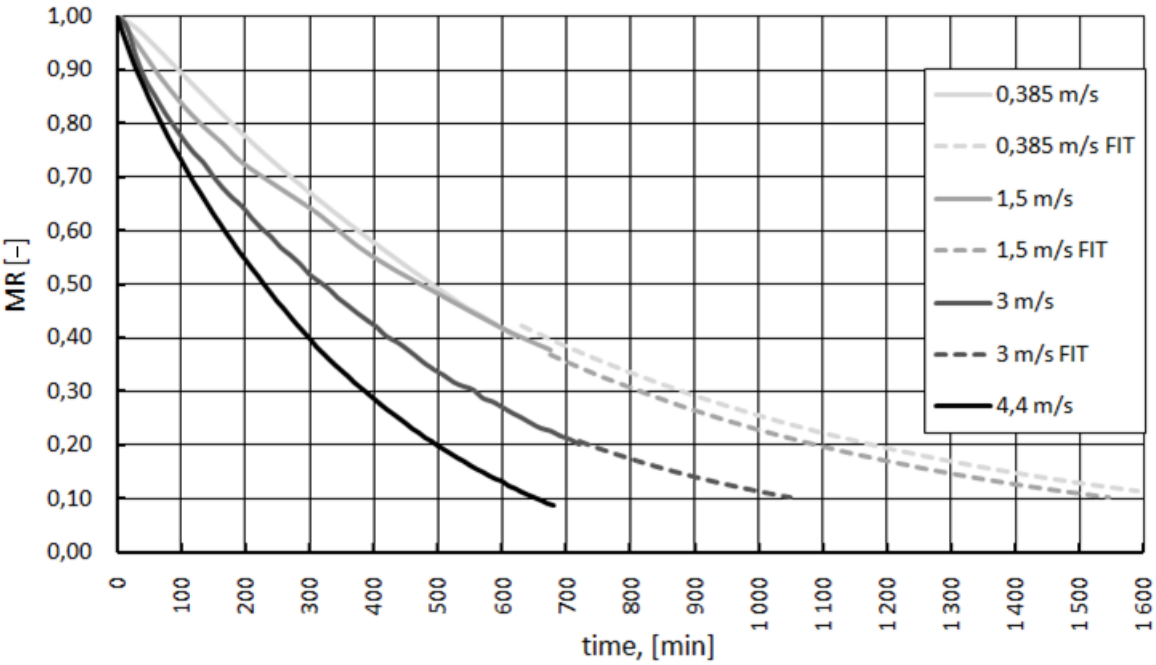

Figure 3. Variation of measured and calculated moisture ratio at constant air velocities

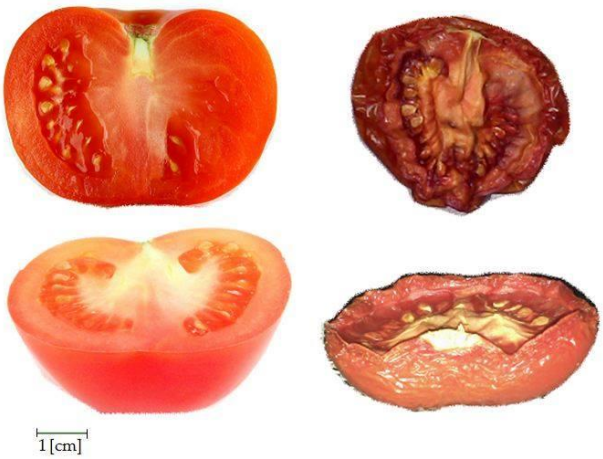

Figure 4. Fresh and dried halved tomato

Figure 4 shows the shape and color of the tomato at the beginning and end of the drying process.

Eq. (2) was used to calculate drying time to reach 1% moisture content ($t_{1\%}$). With $t_{1\%}$, α_C and α_0 a curve was fitted with MATLAB to determine the A and B parameters in Eq. (11). The calculated heat transfer coefficient also can be seen in *Fig. 5*.

To specify the relation between the *C* correlation factor and air speed as well temperature for Eq. (8) would require further measurements and more detailed mathematical model in the future [8]. In the present paper we used it as a constant value to determine the specific energy demand.

For our laboratory and pilot measurements the results are 13,827 MJ/kg; 12,77 MJ/kg; 12,62 MJ/kg; 12,54 MJ/kg specific energy need beside 0,385 m/s; 1,5 m/s; 3 m/s; és 4,4 m/s air velocities.

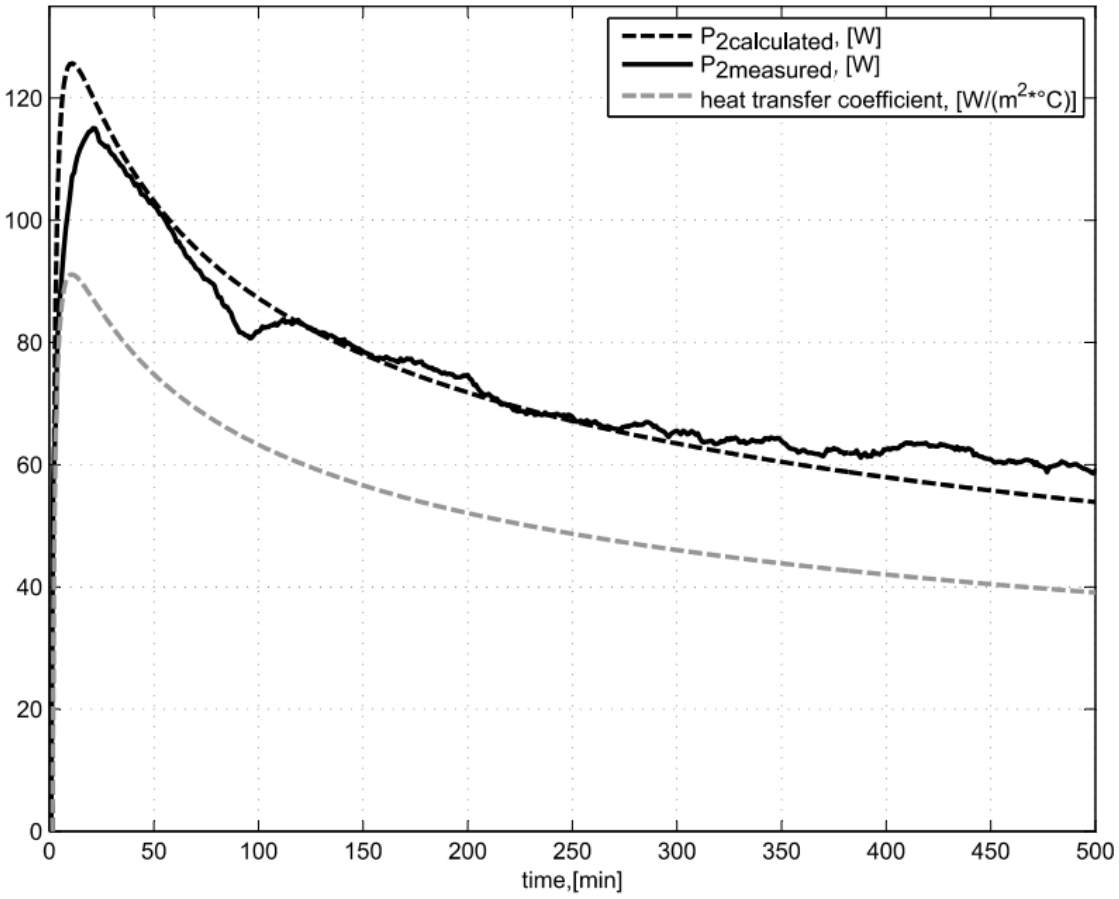

Figure 5. Thermal power demand and heat transfer coefficient vs. drying time for convectional drying of halved tomatoes

5. CONCLUSIONS

The constructed experimental equipment is suitable to measure the drying process of different shrinking agricultural materials with high initial moisture content. We found that the Handerson-Pabis model is appropriate to describe the moisture reduction of halved tomato drying. The described mathematical model can be used to calculate the temporal variation of heat transfer coefficient and wattage demand as well the specific energy consumption for the total process.

6. REFERENCES

[1] **FRANCESCHI S. ET AL.:** *Tomatoes and risk of digestive tract cancers.* International Journal of Cancer, no. 59, 181–184 (1994).

[2] **CHARLES TAIWO AKANBI ET AL.:** *Drying characteristics and sorption isotherm of tomato slices.* Journal of Food Engineering, vol. 73, 2006, pp. 157-1263

[3] **IBRAHIM DOYMAZ:** *Air-drying characteristics of tomatoes.* Journal of Food Engineering, no. 78, 1291-1297 (2007)

[4] **BLAKE RINGEISEN, DIANE M. B., PIETER S.:** *Concentrated solar drying of tomatoes.* Energy for Sustainable Development, 2014

[5] **HABIB KOCABIYIK ET AL.:** *The effects of middle infrared radiation intensity in the qualiy of dried tomato products.* International Journal of Food Science & Technology, no. 49, 2014, pp. 703-710
[6] **ENGIN DEMIRAY ET AL.:** *Degradation kinetics of lycopene, β-carotene and ascorbic acid in tomatoes during hot air drying*. LWT – Food Science and Technology, no. 50, 2013, pp. 172-176
[7] **ALI MOTEVALI ET AL.:** *Evaluation of energy consumption in different drying methods.* Energy Convesion and Management, no. 52, 2011, pp. 1192-1199
[8] **SCHNEIDER GY., VÁRKONYI ZS.:** *Szárítás időbeli lefutásának analitikus modellezésea szárítási paraméterek függvényében.* BUTE Stundent Reseach Work, 2014
[9] **BIHARI P. ET AL.:** *Gyakorlati feladatok gyűjteménye és sedéglet.* BUTE Department of Energy Engineering, 2011, pp. 75-76

FINITE ELEMENT MODELLING OF COLD ROLLING PROCESS

[1]PÁLINKÁS Sándor, [2]KRÁLLICS György, Dr., [3]BÉZI Zoltán

[1]University of Debrecen, Faculty Engineering, Department of Mechanical Engineering; 4028 Debrecen, Ótemető u. 2-4., Hungary
palinkassandor@eng.unideb.hu

[2]University of Miskolc, Faculty of Materials Science and Engineering, Institute of Physical Metallurgy, Metalforming and Nanotechnology; 3515 Miskolc-Egyetemváros, Hungary;
krallics@eik.bme.hu

[3]Bay Zoltán Nonprofit Ltd. for Applied Research, Institute for Logistics and Production Engineering (Bay-Logi); 3519 Miskolc, Iglói út 2., Hungary;
zoltan.bezi@bayzoltan.hu

Abstract
A lot of problems arise even recently concerning the control of flatness and profile of rolled strip in industrial circumstances. In the course of planning of the cold-rolling technology of geometrically true strip that is exempt of internal deformation stresses - i.e. flatness strip - it is necessary to take into consideration the elastic and thermal deformation of working rolls, the basic sheet-metal forming of rolls, the existing crown of basic material as well as the wearing of the rolls. Quality demands for the shape characteristics of strips have been increased recently by the modern industrial branches. The final shape of the sheet is influenced by the construction and stiffness of the mill stand and the shaping parameters through the deformation patterns of roll gap. The purpose of our research was the modelling of shape defects (crown) developing during cold rolling in order to identify parameters that can improve the technological precision of production of sheets.

Keywords: *3D finite element method, Cold rolling, Detection of waviness, Elasticity of mill stand, Flatness defects.*

1. INTRODUCTION

It is necessary to know the exact shape of a rolled strip both during hot and cold rolling. There is a close relationship between the flatness of a strip made during cold rolling and the profile of a strip made during hot rolling. In addition to decrease the costs of energy and of tools, it is necessary to meet the quality demands in the course of the optimization of rolling technology of cold rolled strips. As far as the quality is concerned, it is very important to roll a strip where the extent of deformation is always identical along its width. As a consequence, the condition of flatness is that the deformation is identical along the width of strip:

$$\frac{\partial \lambda(x)}{\partial x} = 0 \qquad (1)$$

where:
λ – lengthening coefficient,
x – running coordinate along the width of strip.

The following phenomena can be observed on the outgoing strip in case if this condition is not met:

- Owing to the different values of lengthening coefficients, the length of strip fibres with elementary width are different along the width; this causes residual internal stress in the case of thick strips and waviness in the case of thin strips.
- During rolling, the distribution of tensile stress along the strip width is non-uniform on the delivery side and on the rolling-up side, which in extreme cases can even cause rupture of the strip.
- After splitting the strip into bands, the individual bands will become curved ("sword-like") [1].

As a consequence of the high values of external tensile stress applied during cold rolling, the strip can have apparent flatness during deformation in spite of the fact that the above condition relating to the roll gap is not met. However, the waves appear (Figure 1.) or can appear (depending on the thickness of strip) or cut strip bands can become "sword-like" after the significantly high external tensile strength disappears.

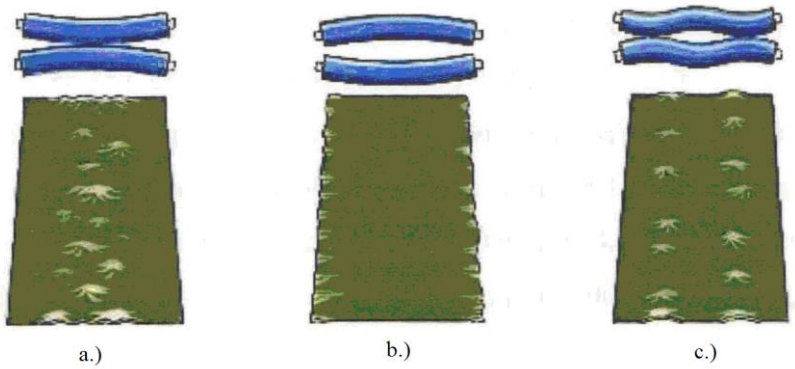

Figure 1. Typical shape defects during cold rolling [2]
(a) – middle waviness, (b) – edge waviness, (c) – local waviness

2. COMPLEX FINITE ELEMENT MODEL

A number of different theoretical models have been developed for the mechanical analysis of deformation processes of rolling [3-4]; these theoretical models can be applied for determining the pressure of rolling, output and moment as well as for following the deformation of tool elements of elastic deformation. As recently the capacity of computers has continuously been growing, papers dealing with the complex modelling of rolling process have been published [5-7]. The elastic system developed by the rolls and mill stand interacts directly with the elastic-plastic sheet material and as a result of this interaction, a rolled product is made whose local geometry can be followed in this process of finite element model as well. From the point of view of making high quality sheet products, it is very important to produce sheets without waviness and to determine the conditions of developing the instability. The main purpose of our research work was the exact mapping of roll gap developing during cold rolling; the aim of our research work was the production of a geometrically exact

product. In order to promote our main purpose, our further aim was to compare the results obtained during the calculations by means of the finite element model with the real results obtained during the experiments. In order to realize this aim, it was necessary to perform a lot of rolling experiments by using the VON ROLL experimental mill stand (Figure 2.) located at the Department of Physical Metallurgy and Metalforming of Institute of Physical Metallurgy, Metalforming and Nanotechnology of University of Miskolc.

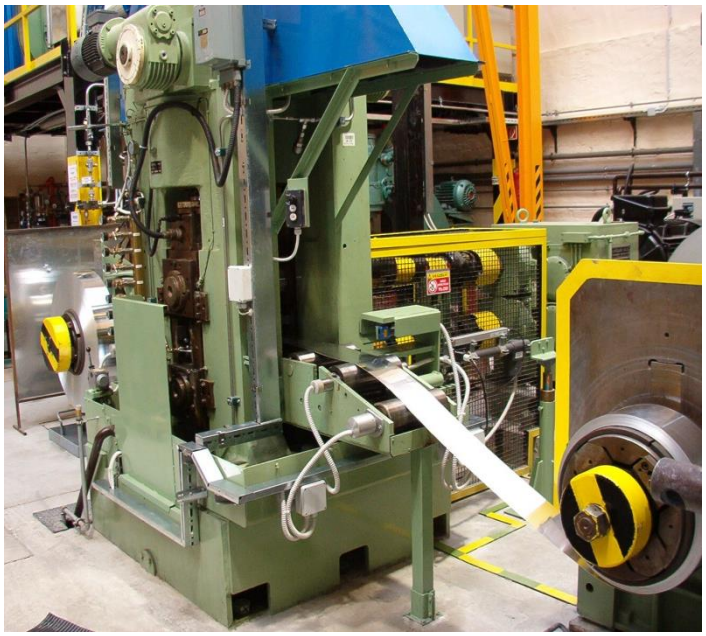

Figure 2. The VON ROLL experimental mill stand

The modelling was performed in 3D by using the 2010.1 version of MSC.Marc non-linear finite element software. The finite element method can effectively be used for describing the non-linear processes. The correction of exactness of solution is much more difficult during the non-linear analysis than during the linear analysis. The consistency of continuum-mechanical equations is necessary for the exact finite element discretization moreover it is very important that the applied material-model can match exactly to the physical process to be modelled.

The complex model developed by us [8] consists of joining three simulation steps (Figure 3.); the first model serves for determining the elasticity of experimental roll mill stand, the second model demonstrates the model of whole roll-system which contains the finite element analysis of the real cold rolling process. Here the shape of roll gap developing during cold rolling is determined. The third model deals with the detection of waviness. A simplification was made in order to realize it because the time necessary for detection of the waviness would have been so long in the second model which couldn't be able to treat by means of the available computer capacities.

The first model was necessary for determining the elasticity of roll mill stand as in order to model the rolling process exactly, it is necessary to follow the resultant elasticity of experimental roll mill stand which involves the elasticity of roll mill stand (consisting of the elasticity of mill stand frame and of the machine-parts being in the line of action of pressure of rolling) in addition it contains the elasticity of rolls (flattening, the elastic deflection of centre-line of rolls) as well. Then the determined elastic constant was involved in the second model which serves for determining the shape of roll gap developing during rolling.

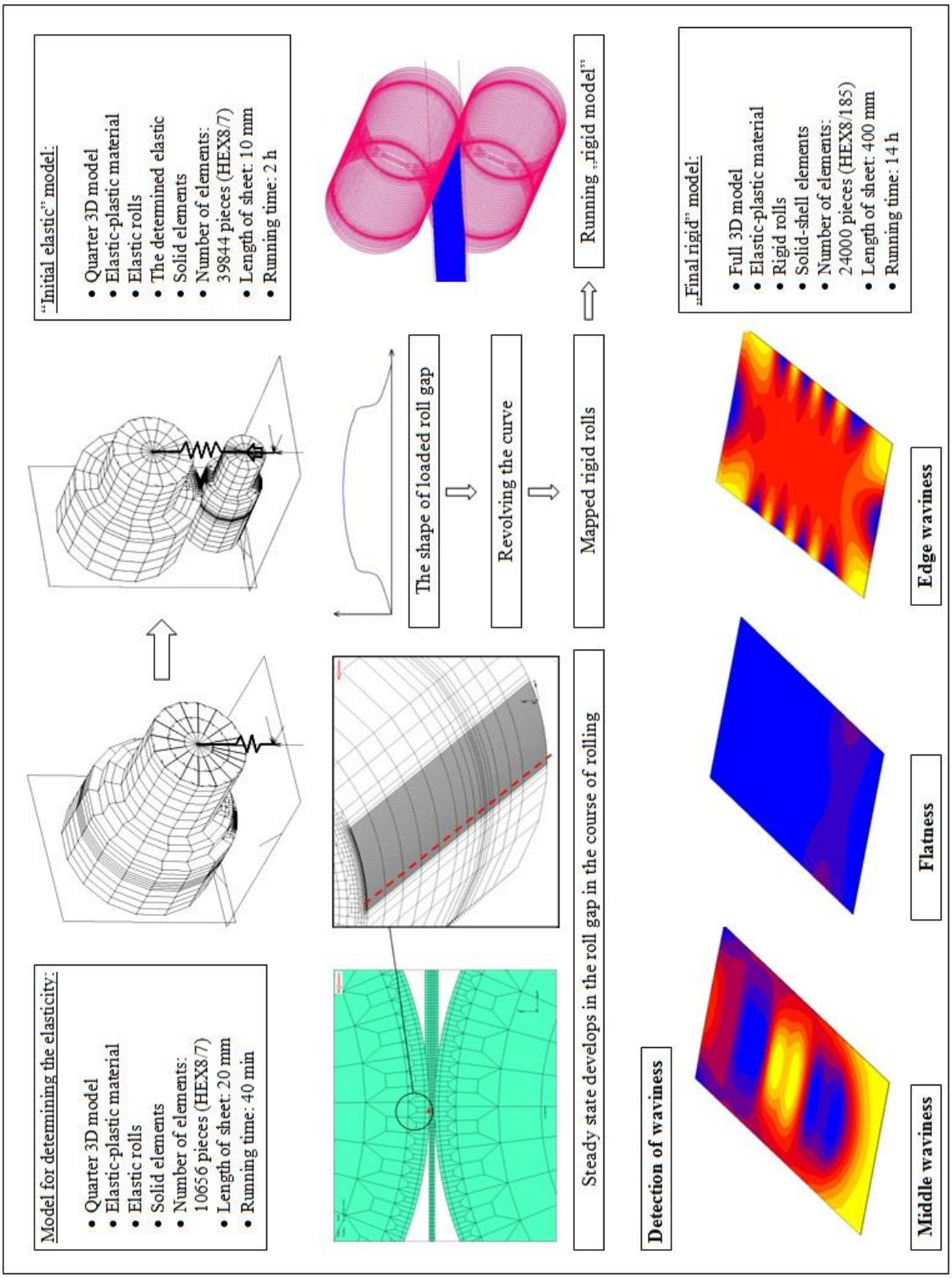

Figure 3. Demonstrating of complex 3D modelling of cold rolling process [8]

In the course of making the model for demonstrating the waviness, our main aim was to develop a method by which the process of forming of a sheet long enough for demonstrating the waviness can be simulated. A steady state develops in the roll gap in the course of rolling and by utilizing it, the „final rigid" model serving for demonstrating the waviness was developed. In the course of developing the model, the generating line of roll (Figure 4.) exposed to the highest torsion of loaded roll gap developing along the width of work roll in the „initial elastic model" was mapped then rigid rolls were developed by revolving them according to the loaded shape of roll-gap. So, after performing the further steps of simulation, it became possible to detect the medium-wave, edge-wave- and wave-free states developing during rolling.

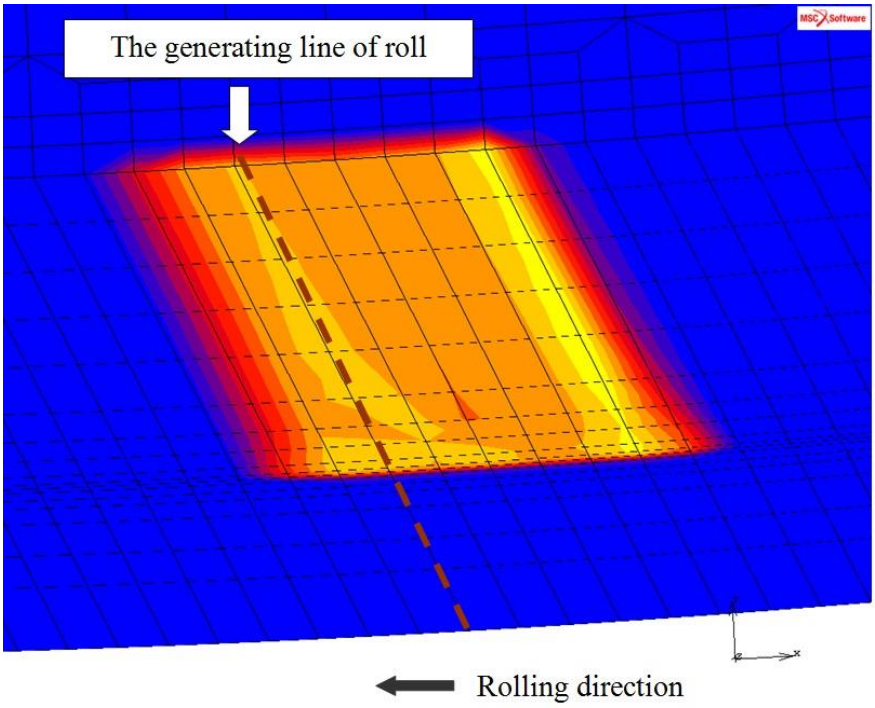

Figure 4. Selection of the generating line of roll

In the course of developing the „final rigid" model, rigid rolls were used identical with the roll-geometry developing during rolling of rolls consisting of solid elements in the „initial elastic" model (Figure 5.); this geometry contains the total elastic effect of roll mill stand. Altogether 24000 pieces of solid-shell (HEX8/185) type elements were used for meshing the elastic-plastic basic material. By this method, the quantity of calculations necessary for the simulation process could significantly be decreased. 2 hours was necessary for rolling a sheet with a length of 10 mm in the „initial elastic" model, while the simulation time of rolling a sheet with a length of 400 mm is 14 hours by using the new method. This length was enough for detection the waviness developing in the sheet.

3. CONCLUSIONS

As a result of our research work, a complex finite element model was developed for the comprehensive description of cold rolling process. In the course of developing the finite element model, the formed material was supposed a linearly elastic isotropic hardening

material while the rolls making the forming were supposed linearly elastic rolls during the different rolling steps. The complex model includes the deflection of the rolls and the different rolling parameters, the flattening of rolls moreover the model calculates by taking into consideration the elastic deformation of roll mill stand in addition it is suitable for detecting the waviness by means of the steady state developing during rolling.

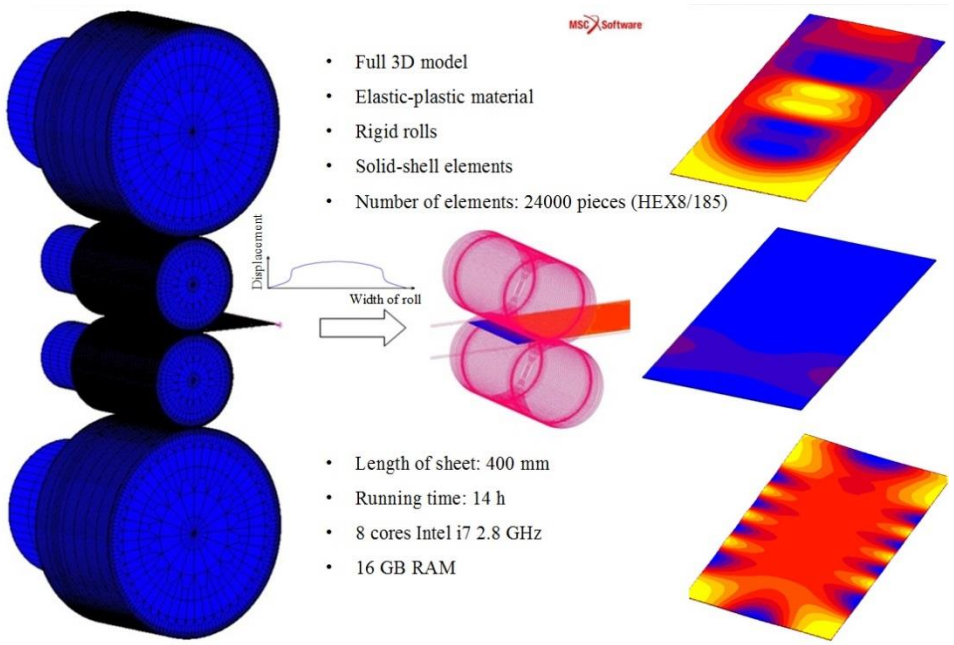

Figure 5. The simplification of simulation of rolling process

4. REFERENCES

[1] **PÁLINKÁS, S., KRÁLLICS, GY., BÉZI, Z.:** *Modelling of Crown on Cold Rolled Aluminium Sheet*, Materials Science Forum 752., 2013, pp. 115-124.
[2] **ROBERTSON, L.:** *VIDIPLAN – Automatic shape control for rolling mills*, 1981
[3] **JOHN G. LENARD**: *Metal Forming Science and Practice*, Elsevier Science Ltd., 2002
[4] **SOMERS, R.R., ET AL.**: *Verification and Applications of a Model for Predicting Hot Strip Profile, Crown and Flatness*, AISE Year Book, 1984, pp. 441-450.
[5] **ABDELKHALEK, S., MONTMITONNET, P., POTIER-FERRY, M., ZAHROUNI, H., LEGRAN, N., BUESSLER, P.:** *Strip flatness modelling including buckling phenomena during thin strip cold rolling*, Ironmaking and Steelmaking, Vol. 37. No. 4., 2010, pp. 290-297.
[6] **XIAODONG WANGA, QUAN YANG, ANRUI HE**: *Calculation of thermal stress affecting strip flatness change during run-out table cooling in hot steel strip rolling*, Journal of materials processing technology 207., 2008, pp. 130-146
[7] **DEREK E. SLAUGHTER:** *Strip Crown Prediction, Developing a Refined Dynamic Roll-Stack Model for the Hot Rolling Process*, Faculty of the Virginia Polytechnic Institute and State University, 2009, PhD thesis
[8] **PÁLINKÁS, S., KRÁLLICS, GY., BÉZI Z.:** *Modelling of waviness on cold rolled aluminium sheet*, International Scientific Conference on Advances in Mechanical Engineering (ISCAME) Debrecen, 2013, pp. 143-152.

EXAMINATION OF EVAPORATION RATE FROM FREE WATER SURFACE FROM LITERATURE SOURCES

[1]POÓS Tibor, Dr., [2]SZABÓ Viktor

[1]Budapest University of Technology and Economics, Faculty of Mechanical Engineering
poos@vegyelgep.bme.hu

[2]Budapest University of Technology and Economics, Faculty of Mechanical Engineering
szabo1viktor1@gmail.com

Abstract
There are many industrial facilities with free surface water reservoir for different technological purposes. On the free surface heat transfer and diffusion occurs, whereby the vapor diffuses into the ambient air, therefore the water loss should be replaced. There are many empirical correlations to calculate the quantity of the evaporated water. These methods largely differ from each other. We compared several equations to analyze the evaporation rate from free surface.

Keywords: *Heat- and mass transfer, Evaporation, Evaporation rate*

1. INTRODUCTION

Evaporation from free liquid surface occurs commonly in everyday-life and industrial processes e.g. open-air reservoirs, pools and swimming-pools, as well as at the fluid-filled storage pools of fuel assemblies in nuclear power plants. Evaporation from free surfaces can be realized by natural or forced convection. Evaporation intensity can differ in case of still or rippling surfaces. A number of publications discuss the measurement of surface evaporation; their results are based on experiments. The conditions of these experiments considerably differ from each other depending on the climatic conditions of measurements and whether evaporation was tested on free surfaces or capillary substances. Based on the experiments, correlations to best describe the phenomenon were identified by regression analysis; in general, they can be applied only in limited conditions.

2. METHODS

According to special sources, Dalton was the first author in 1802 [1] to discuss the issue and to describe the problem of evaporation. He concluded that the intensity of evaporation is proportionate to the partial pressure difference of the liquid surface and the main mass of air and the speed of air flow. The correlation proposed by Carrier [2] is mostly applied for specifying water surface evaporation:

$$N_{H2O}^{Carrier} = \frac{(C_1 + C_2 v_G)(p_{sat,f} - \varphi p_{sat,G})}{r_F}, \quad (1)$$

where C_1 and C_2 are constant, v_G is the velocity of gas, $p_{sat,f}$ is the saturation pressure of water

surface, $p_{sat,G}$ is the saturation pressure of humid gas, φ is the relative humidity, r_F is the latent heat of vaporization. Equation (1) was determined by Carrier for the case of air flowing above a water surface. According to Tang et al. [3], the correlation published by Carrier results in differences in case of pools whose water surface is still, with no rippling, as confirmed by several authors [2-10]. Investigations by Tang et al. [3] concluded that such difference is caused by the fact that the relation between experiments conducted in different climatic conditions [11] and between evaporation rate and partial pressure difference is not linear. By studying this assumption, the authors [3-10] have come to the conclusion that free water surface evaporation can be defined by the following correlation:

$$N_{H2O}^{Tang} = \frac{(C_1 + C_2 v_G)(p_{sat,f} - \varphi p_{sat,G})^n}{r_F}, \quad (2)$$

where n is a constant. Tests were performed on free water surfaces of *1.16x1.16 m* size, and surfaces covered by a moistened material, subject to forced air speed of *0.1-1.7 m/s*. Results were processed in the form of similar equations by sources [2], and [4-10]. A summary of the constants in the correlations proposed by the authors is included in Table 1.

Table 1 Constants proposed by authors [2-10]

Ref.	Year	C_1	C_2	n	Experimental conditions
[2]	1918	0.0887	0.0782	1	no data
[4]	1924	0.1538	0.069	1	no data
[5]	1931	0.0838	0.0508	1	in wind tunnel and in outdoors placed containers
[6]	1936	0.109	0.0859	1	in lakes and containers
[7]	1942	0.07549	0.0339	1	in containers
[10]	1966	0.0369	0.0266	1	no data
[10]	1966	0	0.0372	1	no data
[9]	1971	0.036	0.025	1	no data
[8]	1993	0.06741	0.0515	1	on indoor and outdoor unoccupied swimming pools
[3]	2004	0.2253	0.2464	0.82	evaporation from free surface
[3]	2004	0.7581	0.4257	0.7	evaporation of a wet tissue's surface

Sartori performed further tests; in his publication [12] he examined free water surface evaporation in case of forced convection, where he also discussed literature on free water surface evaporation. According to Sartori, the evaporation rate is influenced by the driving force of temperature as well, on the basis of which he made a distinction between three cases ($T_f > T_G$; $T_{G,dp} < T_f < T_G$; $T_f < T_{G,dp}$). Sartori concluded that the evaporation rate is also influenced by the length of liquid surface in the direction of convection in addition to the relative humidity and temperature of the ambient air and the temperature of the main mass of water. Sartori concluded that the evaporation rate is also influenced by the length of liquid surface in the direction of convection in addition to the relative humidity and temperature of the ambient air and the temperature of the main mass of water. The correlation proposed by Sartori [12] is:

$$N_{H2O}^{Sartori} = (0.00562 {v_G}^{0.8} L^{-0.2} - 0.01529 L^{-1})(\rho_{v,f} - \varphi \rho_{v,G}), \quad (3)$$

where L represents the characteristic length, $\rho_{v,f}$ and $\rho_{v,G}$ are the saturated densities evaluated at the water surface temperature and ambient air temperature. During the measurements the temperature of free water surface ranging from *10÷40 °C* and greater *5 °C* in relation to each ambient air temperature, wind velocity of *3 m/s*, relative humidity of *45 %* or *100 %* for each air temperature, *10÷100 m* characteristic length. In their publication [13], Bower and Saylor examined water evaporation caused by free convection, in the course of which they described the phenomenon by dimensionless numbers *Sh-Ra*. In the course of the experiments conducted, the temperature of the water surface was not constant during evaporation. The equation proposed by Bower and Saylor:

$$Sh = 0.23Sc^{1/3}Ra^{0.321}, \tag{4}$$

where *Ra* represents the Rayleigh-number. The range of Rayleigh-number: $9.6 \cdot 10^5 < Ra < 5.7 \cdot 10^8$, the water temperature was approximately *43 °C*, characteristic length between *152÷609 mm*. From the equation (4) the evaporation rate can be evaluated by using constants of publication [13]:

$$N_{H2O}^{Bower} = \frac{D\left(\rho_{v,f} - \varphi\rho_{v,G}\right)}{L} 0.23 \cdot 0.6^{1/3} \left(\frac{g\left(\rho_f - \rho_G\right)L^3}{\frac{\left(\rho_f - \rho_G\right)}{2} va} \right)^{0.321}, \tag{5}$$

where D is the diffusion coefficient for water vapor in air, g is the gravitational acceleration, ρ_f and ρ_G are the air/vapor mixture densities at the water surface and ambient, v kinematic viscosity, a is the thermal diffusivity.
In case of swimming-pools, it is particularly important to specify water replacement. Several authors [3], [8] have discussed the subject, making a distinction between cases of still, undisturbed liquid surface and disturbed, rippling liquid surface. Based on the correlation applied most frequently [14]:

$$N_{H2O}^{[14]} = (25 + 19v_G)\left(Y_f - Y_G\right) \tag{6}$$

where A_f is the surface of heat and mass transfer, Y_f represents the absolute humidity of gas on dry basis of water surface, Y_G represents the absolute humidity of gas on dry basis of gas. Equation (5) has no special conditions, only that this is used to calculate to evaporation rate of swimming pools. In his publication, Shah [15] proposed the correlation below to determine the quantity of water evaporated in case of an undisturbed water surface:

$$N_{H2O}^{Shah} = 35\rho_f\left(\rho_G - \rho_f\right)^{1/3}\left(Y_f - Y_G\right), \tag{7}$$

where ρ_f is the density of air near the water surface. Shah verified equation (6) for cases of *0.073÷425 m^2* surface, *7÷94 °C* water temperature, *6÷35 °C* air temperature, *28÷98%* relative

humidity and *210÷80156 Pa* pressure difference between the water surface and the air.

Volodin et al. [16] and Pecherkin et al. [17] studied heat transfer during evaporation of Freon mixtures in the film flow over smooth and structured surfaces. Zhukov and Pavlenko [18] reported results obtained in studying heat transfer and development of critical phenomena in thin layers of oil during evaporation.

The connection between heat transfer and mass transfer has been analyzed by a number of authors [19-21], applying various methods for description. In case of a plane liquid surface, shape resistance is negligible compared to friction resistance, therefore the analogy of heat, mass and impulse transfer can be applied for determining the evaporating water quantity. Based on similarities of temperature, concentration, and speed profiles, Treybal [19] has developed the analogy of heat and mass transfer, whereby the following can be stated for heat transfer and mass transfer factors: $J_H = J_M$.

Based on the interpretation of the heat and mass transfer factors:

$$J_H = \frac{Nu}{RePr} Pr^z = \frac{Sh}{ReSc} Sc^z = J_M, \tag{8}$$

where *Nu* is the Nusselt-number, *Re* is the Reynolds-number, *Pr* is the Prandtl-number, *Sh* is the Sherwood-number, *Sc* is the Schmidt-number, and *z* is a constant. It can be deduced:

$$\frac{\alpha}{k_c \rho c} = \left(\frac{Sc}{Pr}\right)^z = Le^z, \tag{9}$$

where α represents the heat transfer coefficient, k_c is the mass transfer coefficient, c is the specific heat of air. As in case of an air-water system $Le^z \cong 1$, the following correlation between the heat transfer and the mass transfer coefficients can be stated:

$$\frac{\alpha}{k_c \rho} = \frac{\alpha}{\sigma} = c_G \tag{10}$$

Based on equation (9) the evaporation rate:

$$N_{H2O}^{Treybal} = \frac{\alpha}{c_G}\left(Y_f - Y_G\right), \tag{11}$$

where the heat transfer coefficient "α" can be evaluated from the appropriate *Nu=f(Re)* equation.

Evaporation to the gas flowing above the surface of liquids can also be calculated on the basis of the theory of unimolecular diffusion, requiring the mass transfer coefficient (k_G) to be determined [1].

Correlation (7) in case of *Z=2/3*:

$$J_M = \frac{k_C \rho_G}{v_G \rho_{v,f}} Sc^{2/3} \tag{12}$$

Using correlations $k_c = k_G RT$ and $\rho_{v,f} = \frac{m_v}{V} = \frac{p_v M_{H2O}}{RT}$ the mass transfer coefficient can be stated:

$$J_M = \frac{k_G RT \frac{PM}{RT}}{v_G \rho_{v,f}} Sc^{2/3} \tag{13}$$

From this, the evaporation coefficient specified by the diffusion theory is:

$$\sigma_{dif} = \frac{J_M v_G \rho_f}{PMSc^{2/3}} RT \tag{14}$$

And the evaporation rate is:

$$N_{H2O}^{dif} = \frac{J_M v_G \rho_f}{PMSc^{2/3}} RT(Y_f - Y_G) \tag{15}$$

There are other useful studies to understand the nature of evaporation [22] and to compare the results by various author in this speciality [23].

3. RESULTS

In the comparison of various literature data, the correlations recommended by references were calculated by taking the values represented in Table 2.

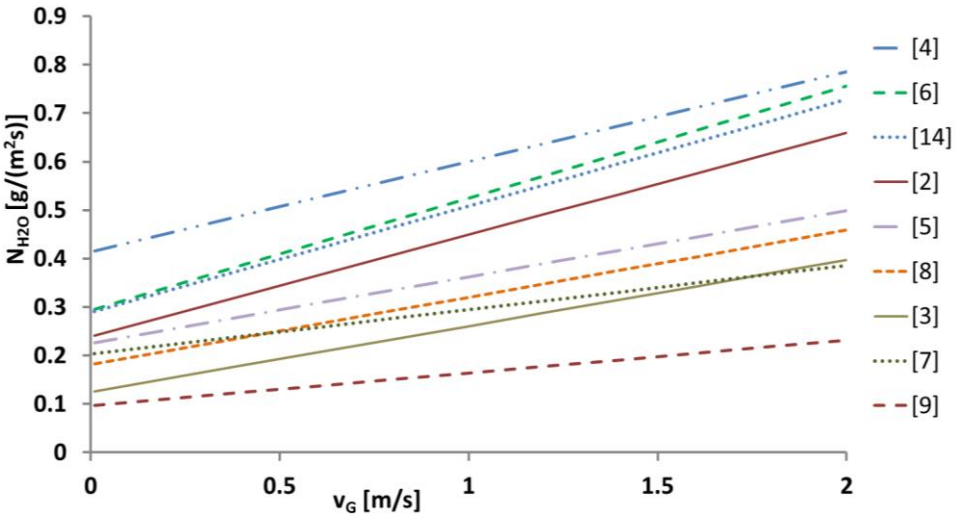

Figure 1 Comparison of evaporation rate figures taken from the literature

Equation (2) was performed on the basis of Table 1 by using the constants recommended by various authors. Figure 1 shows a comparison of the results of evaporation rate, by changing the velocity of gas as parameter in range *0÷2 m/s*.

Figure 1 shows the results of the evaporation rate from the literature. Differences in the steepness of fictive curves fitted on the points from the straight lines taken from the literature can be justified by the fact that equations in the literature apply to cases without heat sources, with evaporation from pools left alone. The difference between the values of the two extreme

curve [4] and [9] is approximately fourfold. Further researches are needed to make the evaporation rate more exact within a given range of measurement conditions.

Table 2 Values used for presentation

v_G	$p_{sat,f}$	φ	$p_{sat,G}$	r_f	Y_f	Y_G
m/s	Pa	%	Pa	kJ/kg	g_{H2O}/kg_{dG}	g_{H2O}/kg_{dG}
0÷2	7352.5	26.5	2855.4	2450	49.33	7.71

4. CONCLUSIONS

The goal of our work, evaporation from a liquid surface was examined on the basis of several literature results. Figure of the evaporation rate were specified on using literature sources, which largely differs from each other. In the cases examined, evaporation was not only consequent upon environmental impacts, but it was also assisted by the heat source of the liquid. This case has been discussed deficiently by literature on the description and calculation of evaporation. We recommend further examinations to create *Nu-Re* correlations of the analogy between heat and mass transfer. For this examination we will construct a suitable experimental apparatus.

5. ACKNOWLEDGEMENT

Special thanks for “Richter Gedeon Talentum Foundation (H-1103 Budapest, Gyömrői str. 19-21, Hungary)” for financial supporting this research.

6. REFERENCES

[1] **TREYBAL R. E.:** *Mass-transfer operations*, 3rd edition, McGraw-Hill Company, New York, USA, 1981.
[2] **SZENTGYÖRGYI S., MOLNÁR K., PARTI M.:** *Transzportfolyamatok (Transport processes)*, Tankönyvkiadó, Budapest, Hungary, 1986.
[3] **ÖRVÖS M.:** *Diffúziós eljárások és berendezések (Diffusion processes and equipments*), 1st edition, Budapest, Hungary, 2006.
[4] **LARBI S.:** *Heat and Mass Transfer with Interaction Effects Analysis Between an External Flow and a Capillary Porous Body*, International Review of Mechanical Engineering, 2008, 2(5): pp. 797-802.
[5] **HSIAO K.:** *Heat and Mass Mixed Convection for Viscoelastic Fluid Past a Stretching Sheet with Ohmic Dissipation through a Porous Space*, International Review of Mechanical Engineering, 2009, 3(1): pp. 22-28.
[6] **MERKLEIN M., WIELAND M., STOEHR T., LECHLER J., GRUENER M.:** *Analytic Methods for the Calculation of the Heat Transfer Coefficient*, International Review of Mechanical Engineering, 2010, 4(2): pp. 208-215.
[7] **VOLODIN O. A., PAVLENKO A. N., PECHERKIN N. I.:** *Heat transfer and wave characteristics of a binary Freon film flowing over a three-dimensional texture surface*, High temperature, 2013, 51(6): pp. 785-794.
[8] **PECHERKIN N. I., PAVLENKO A. N., VOLODIN O. A.**: *Heat transfer at evaporation of falling films of Freon mixture on the smooth and structured surfaces*, Thermophysics and Aeromechanics, 2011, 18(4): pp. 579-589.

[9] **ZHUKOV V. I., PAVLENKO A. N.**: *Critical Phenomena at Evaporation in a Thin Liquid Layer at Reduced Pressure*, Journal of Engineering Thermophysics, 2013, 22(4): pp. 257-287.
[10] **KONTUR I., KORIS K., WINTER J.**: *Hidrológiai számítások (Hydrological calculations)*, Linográf Kiadó, Budapest, Hungary, 2003.
[11] **CARRIER W. H.:** *The temperature of evaporation*, ASHVE Transaction, 1918, 24: pp. 25-50.
[12] **TANG R., ETZION Y.:** *Comparative studies on the water evaporation rate from wetted surface and that from a free water surface*, Building and Environment, 2004, 39(1): pp. 77-86.
[13] **HIMUS G. W., HINCHLY J. W.**: *The effect of a current of air on the rate of evaporation of water below the boiling point*, Journal of the Society Chemistry and Industry, 1924, 43(34): pp. 840–845.
[14] **ROHWER C.**: *Evaporation from free water surface*, US Department of Agriculture Technical Bulletin, *1931, p.* 271.
[15] **LURIE M., MICHAILOFF N.:** *Evaporation from free water surface*, Industrial and Engineering Chemistry,1936, 28(3): pp. 345–350.
[16] **MEYER A. F.:** *Evaporation from lakes and reservoirs*, Minnesota Resources Commission, USA, 1942.
[17] **SMITH C. C., JONES R. W., LOF G. O. G.:** *Energy requirements and potential savings for heated indoor swimming pools*, ASHRAE Transactions, 1993, 99(2): pp. 864–874.
[18] **MCMILLAN W.**: *Heat dispersal–Lake Trawsfynydd cooling studies*, Symp. on Freshwater Biology and Electrical Power Generation Part 1: pp. 41–80., 1971
[19] **GANGOPADHYAYA M., HARBECK G. E., NORDENSON T. J., OMAR M. H., URYVAEV V. A.**: *Measurement and estimation of evaporation and evapotranspiration*, World Meteorological Organization In. Techn.: 83(92)., 1966
[20] **CAVELIUS R., ISAKSSON C., PEREDNIS E., READ G. E. F.**: *Passive Cooling Technologies*, Austrian Energy Agency, 2013, Wien, Austria.
[21] **SARTORI E.**: *A critical review on equations employed for the calculation of the evaporation rate from free water surfaces*, Solar Energy, 2000, 68(1): pp. 77-89.
[22] **WATMUFF J. H., CHARTERS W. W. S., PROCTOR D.:** *Solar wind induced external coefficients for solar collectors*, COMPLES, 2: 56., 1977.
[23] **BOWER S. M., SAYLOR J. R.**: *A study of the Sherwood-Rayleigh relation for water undergoing natural convection-driven evaporation*, *Interna*tional Journal of Heat and Mass Transfer, 2009, 52: pp. 3055-3063.
[24] *Evaporating from water surfaces*, 24.09.2014: http://www.engineeringtoolbox.com/evaporation-water-surface-d_690.html
[25] **SHAH M. M.**: *Improved method for calculating evaporation from indoor water pools*, Energy and Buildings, 2012, 49: pp. 306-309.
[26] **GARBAI L., SÁNTA R.**: *Flow pattern map for in tube evaporation and condensation*, 4th International Symposium on Exploitation of Renewable Energy Sources, ISBN: 978-86-85409-70-7: 125-130, Subotica, Serbia, 2012.
[27] **SANTA R.**: *The Analysis of Two-phase Condensation Heat Transfer Models Based on the Comparison of Boundary Condition*, Acta Polytechnika Hungarica, 2012, 9(6): pp. 167-180.

DETERMINATION OF SOLAR RADIATION VALUES FOR SODA CAN HEATERS

[1]POÓS Tibor, Dr., [2] FEHÉR BOTH Kinga, Dr., [3]WEINHANDL Róbert

[1] Budapest University of Technology and Economics, Faculty of Mechanical Engineering
poos@vegyelgep.bme.hu

[2] Budapest University of Technology and Economics, Faculty of Mechanical Engineering
feher@vegyelgep.bme.hu

[3] Budapest University of Technology and Economics, Faculty of Mechanical Engineering
weinhandl.robert1991@gmail.com

Abstract
The use of soda can heaters, due to their low cost and simplicity, is widespread. These devices, however, have not yet been linked to extensive scientific research. The presented mathematical model calculates the solar radiation values for soda can heaters, using the isotropic sky model. The model makes it possible to define the optimal position of the device under given meteorological circumstances, while also making it possible to predict the cost-effectiveness of varying designs. If the appropriate meteorological data are provided, the model is capable of making the calculations for any location.

Keywords: *Solar radiation, Renewable energy, Soda can heater.*

1. INTRODUCTION

The soda can heater is used for directly heating the interior of buildings. The air from inside the building gets transferred into the soda can heater by a fan, where it is exposed to solar radiation. Firstly, the air is transported to a distributor-box, from where it travels through pipes made from soda cans, which are exposed to the aforementioned solar radiation. From the pipes, the air gets into a uniting box. Lastly, the heated air is transported back to the interior of the room. The goal is to find the most economical design, while also taking the prices of natural gas and electricity into account. The simplest and most inexpensive optimization process is maximizing the absorbed solar radiation by the device. The introduced mathematical model makes it possible to calculate the optimal tilt angle of the soda can heater from the meteorological data of any given location. There are various models used for solar radiation calculations, namely the Klein-Theilacker method [1], [2], the Hay model [3], the Kucher model [4], the isotropic sky model [5], the Badescu model [6] and the Perez model [7]. During these calculations, the applied model was the isotropic sky model, taking into account the direct and diffuse components of radiation and the reflectance of the ground and of the cover of the device [8]. The effect of the atmosphere was calculated based on Armstrong et al [9]. The radiation components were determined by Angstrom constants [10]. The model was based on conventional Earth-Sun geometry [11].

2. METHODS

In practice, the surface exposed to solar radiation is the cover of the device. As the absorptivity of the cover itself is negligible, the radiation transmitted through the cover can be calculated by the incident radiation and the reflected radiation component. In the present frequency range, this amount equates to the radiation absorbed by the device. To calculate the incident radiation, the mathematical model has to include the position of the Sun on the sky, the sky clearness and the orientation and inclination of the cover. The reflectance of the cover also depends on the angle of incidence of the radiation. This makes it necessary to use the formulas of Earth-Sun geometry.

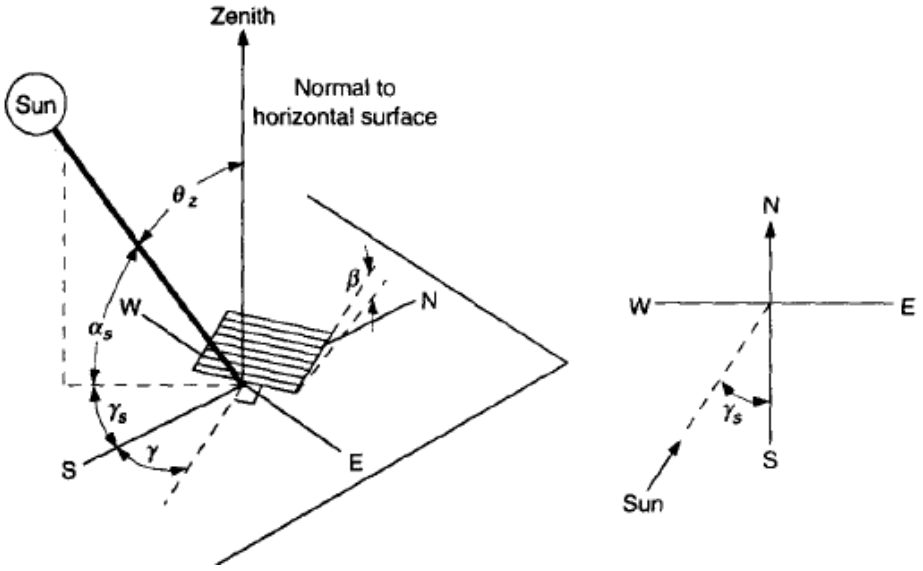

Figure 1. Earth-Sun geometry [8]

For the determination of the radiation values, the model has to calculate the incident radiation for a horizontal surface without the effect of the atmosphere. The Solar constant is the energy from the Sun, per unit time, received on a unit area of surface perpendicular to the direction of propagation of the radiation, at mean Earth-Sun distance, outside of the atmosphere, G_{sc}=1367 W/m^2 [8]. The incident radiation for a horizontal surface can be determined using the Solar constant and the zenith angle:

$$G_0 = G_{sc}\left[1 + 0{,}33\cos\left(\frac{360n}{365}\right)\right] cos\theta_z \tag{1}$$

Here n refers to the day of the year and θ_z is the zenith angle (see Figure 1). This value has to be adjusted for the effect of the atmosphere. For this correction, the Angstrom constants (a, b) [10] can be used. In the calculations, the provided Angstrom constants for Budapest [12] were used. For calculations regarding different areas, the actual Angstrom constants need to be provided.

The incident radiation for a horizontal surface, adjusted for the effect of the atmosphere, can be stated:

$$G = G_0\left(a + b\frac{\sigma}{N}\right) \tag{2}$$

where N is the length of the day in hours and σ is the sunshine duration in hours. The variables N and σ can be found in the database of the local meteorological service [13].

According to the isotropic sky model, the radiation consists of three components: beam, diffuse and reflected radiation. For horizontal surfaces, ratio of diffuse radiation to global radiation can be determined using the clearness index k_T. There are numerous formulas used to calculate the ratio of diffuse and global radiation (Orgill et al [14], Erbs [15]). The actual formula used for the model (S. Armstrong et al [9]):

$$\frac{I_d}{I} = \begin{cases} 1{,}02 - 0{,}254k_T - 0{,}0123\sin(90° - \theta_z) & ,if\ k_T \le 0{,}3 \\ 1{,}4 - 1{,}749k_T - 0{,}0177\sin(90° - \theta_z) & ,if\ 0{,}22 < k_T \le 0{,}78 \\ 0{,}486k_T - 0{,}182\sin(90° - \theta_z) & ,if\ k_T > 0{,}78 \end{cases} \tag{3}$$

where I_d is the diffuse radiation component, I is the global radiation and θ_z is the zenith angle. The (3) equation determines the diffuse radiation, and the reflected radiation equates to the product of the global radiation and the reflectance of the ground. On grass, the reflectance is ρ_g=0,3 [8]. To calculate the values for a tilted surface, each component has to be modified by tilted surface factors. For a surface oriented south, the total radiation can be stated by the following formula:

$$I_T = I_b R_b + I_d\frac{1+cos\beta}{2} + I\rho_g\frac{1-cos\beta}{2} \tag{4}$$

where β is the tilt angle (see Figure 1) and I_b is the beam radiation. The R_b beam radiation modification factor can be calculated using Earth-Sun geometry. In the northern hemisphere, on a surface oriented south, R_b can be calculated:

$$R_b = \frac{\cos(\emptyset-\beta)cos\delta cos\omega+\sin(\emptyset-\beta)sin\delta}{\cos(\emptyset)cos\delta cos\omega+\sin(\emptyset)sin\delta} \tag{5}$$

where ω is the hour angle, $\emptyset$ is the latitude angle, β is the tilt angle and δ is the declination. The declination can be stated:

$$\delta = 23{,}45\sin\left(360\frac{284+n}{365}\right) \tag{6}$$

To calculate the amount of radiation reflected by the cover, the reflectance of the cover also has to be calculated. To determine the reflectance, the angle of incidence θ_1 has to be known, along with the refractive index of the cover n_r and the refraction angle. The angle of incidence can be stated:

$$\theta_1 = \arccos(\cos(\emptyset - \beta)\, cos\delta cos\omega + \sin(\emptyset - \beta)\, sin\delta) \tag{7}$$

As one medium is air (refractive index of nearly unity), the refraction angle can be stated:

$$\theta_2 = arcsin\left(\frac{sin\theta_1}{n_r}\right) \tag{8}$$

With the knowledge of the two angles, the parallel and perpendicular reflectance of a non-polarized radiation can be calculated:

$$r_\perp = \frac{sin^2(\theta_2-\theta_1)}{sin^2(\theta_2+\theta_1)} \tag{9a}$$

$$r_\parallel = \frac{tan^2(\theta_2-\theta_1)}{tan^2(\theta_2+\theta_1)} \tag{9b}$$

Using the parallel and perpendicular reflectance, the *r* reflectance of the cover can be calculated:

$$r = \frac{I_r}{I_i} = \frac{1}{2}(r_\perp + r_\parallel) \tag{10}$$

The *r* reflectance can only be applied to the beam radiation component. For diffuse and reflected components, a different algorithm has to be used. Using the isotropic sky model [5], an incident angle of 60° can be used for calculating the r_{dif} and r_{refl} reflectances. The total absorbed radiation on a unit area of surface can be determined by the following formula:

$$I_{abs} = (I_b R_b)(1-r_b) + (I_d \frac{1+cos\beta}{2})(1 - r_{dif} + (I\rho_g \frac{1-cos\beta}{2})(1-r_{refl}) \tag{11}$$

$$\dot{q}_{Sun} = I_{abs} \tag{12}$$

3. RESULTS

Table 1 Calculated tilt angles

Day	Calculated tilt angle [°]	Absorbed radiation [kWh/m^2/day]
15. October	51	2,613
15. November	59	1,505
15. December	62	1,212
15. January	61	1,371
15. February	53	2,074
15. March	43	3,167
15. April	28	4,474

Using the presented mathematical model, the expected daily absorbed heat on any given day on a south oriented surface can be calculated. The calculations can be made with any inclination of the soda can heater, on any given location. Figure 2 shows the expected total

heat absorption per day on a unit area of surface on the 15th of every month during the heating season, depending on the inclination angle of the device. The meteorological properties of Budapest have been used.

As the adjusting of the position of a soda can heater is impractical, the reasonably expected procedure of a user is a monthly adjustment. Therefore, Table 1 shows the inclination angle with the most absorbed heat per day unit area of surface on the 15th of every month.

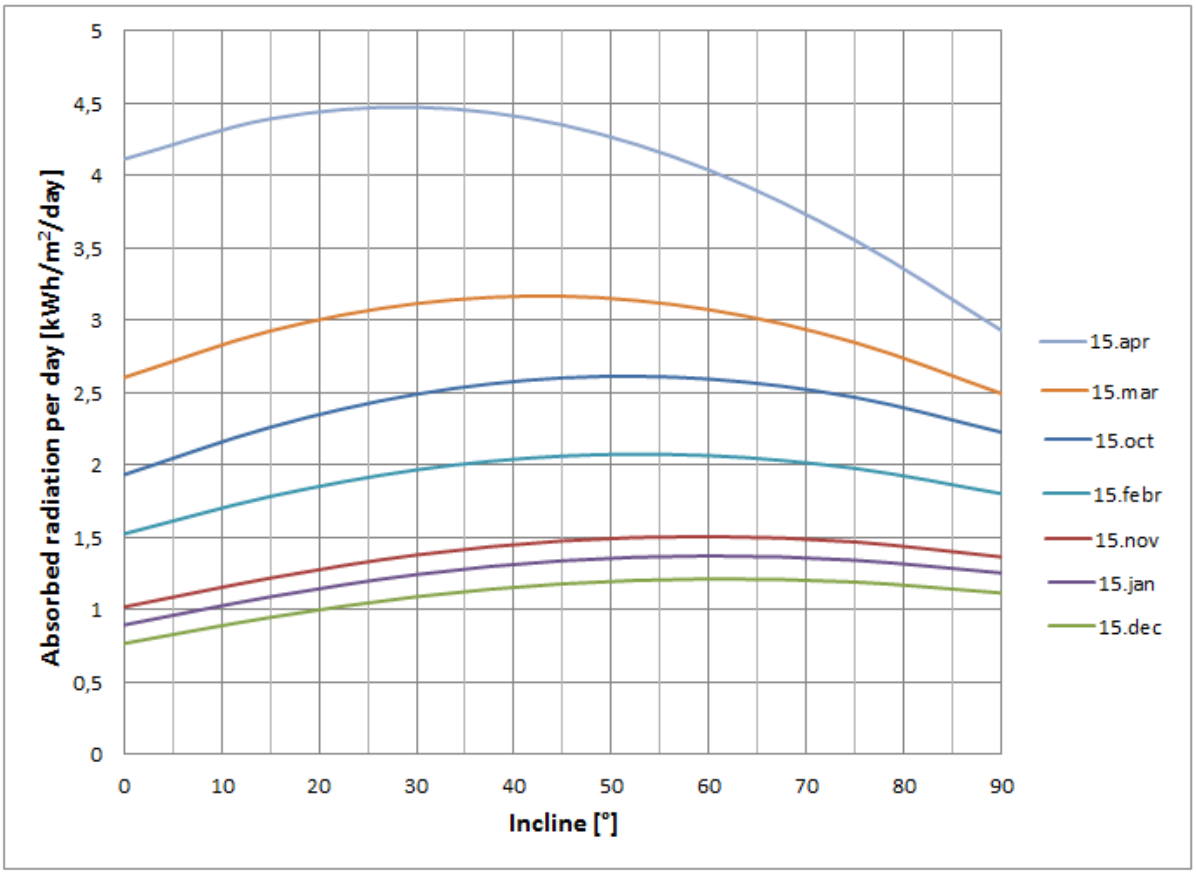

Figure 2. Absorbed radiation

4. CONCLUSION

The presented mathematical model is capable of determining an optimal inclination angle for the installation of soda can heaters. As seen in Table 1, this angle varies greatly (28°-62° in Budapest) over the course of a heating season. A monthly adjustment therefore is justified, as it can significantly increase the absorbed heat of the device, as seen in Figure 2. The presented results have been calculated using the meteorological properties of Budapest, however, after providing the Angstrom constants and the expected sunshine hours of any given location, the model is capable of determining the optimal inclination angles.

5. REFERENCES

[1] **KLEIN, S. A., BECKMAN, W. A.:** *Review of Solar Radiation Utilizability*, Journal of Solar Energy Engineering, 1984, 106: pp. 393-397.

[2] **NG, K. M., ADAM, A. M., INAYATULLAH, O., KADIR, M. Z. A. A.:** *Assessment of solar radiation on diversely oriented surfaces and optimum tilts for solar absorbers in Malaysian tropical latitude*, International Journal of Energy and Environmental Engineering, 2014, 5: pp. 1-13.
[3] **HAY, J. E.:** *Calculating solar radiation for inclident surfaces: practical approaches*. Renewable Energy, 1993, 3(4/5): pp. 373-380.
[4] **KLUCHER, T. M.:** *Evaluation of models to predict insolation on tilted surfaces*. Solar Energy, 1979, 23(2): pp. 111–114.
[5] **HOTTEL, H.C., WOERTZ, B.B.:** *Evaluation of flat-plate solar heat collector*. Trans. ASME, 1994, 64: 91.
[6] **BADESCU, V.:** *3D isotropic approximation for solar diffuse irradiance on tilted surfaces*. Renewable Energy, 2002, 26: pp. 221–233.
[7] **PEREZ, R., SEALS, R., INEICHEN, P., STEWART, P., MENICUCCI, D.:** *A new simplified version of the Perez diffuse irradiance model for tilted surfaces*. Solar Energy, 1987, 39: pp. 221–231.
[8] **JOHN, A., D., WILLIAM, A. B.:** *Solar engineering of thermal processes*, Second edition, A Wiley Interscience Publication, 1980.
[9] **ARMSTRONG, S., HURLEY, W. G.:** *A new methodology to optimise solar energy extraction under cloudy conditions*. Renewable Energy, 2010, 35(4): pp. 780-787.
[10] **SALIMA, G., CHAVULA, G.M. S.:** *Determining Angstrom Constants for Estimating Solar Radiation in Malawi*, International Journal of Geosciences, 2012, 3(2): pp. 391-397.
[11] **BARÓTFI, I.:** *Környezettechnika*, Mezőgazda Kiadó, Budapest, Hungary.
[12] **M. HORVÁTH:** *Analysis of buildings solar heat gain*, IEEEXplore, 4th International Youth Conference, 2013, 1-5.
[13] OMSZ database:
URL:http://owww.met.hu/eghajlat/eghajlati_adatsorok/bp/Navig/201.htm
[14] **ORGILL, J. F., HOLLANDS K. G. T.:** *Correlation equation for hourly diffuse radiation on a horizontal surface*. Solar Energy, 1977, 19(4): pp. 357–359.
[15] **ERBS, D. G., KLEIN, S. A., DUFFIE, J.A.:** *Estimation of the diffuse radiation fraction for hourly, daily and monthly-average global radiation*. Solar Energy, 1982, 28(4): pp. 293–302.

INTERNATIONAL SCIENTIFIC CONFERENCE ON
ADVANCES IN MECHANICAL ENGINEERING
PROCEEDINGS

CONTROLLING OF A 4 DOF MODEL ROBOT

[1]RÓNAI László, [2]SZABÓ Tamás, Dr.

[1]*Robert Bosch Department of Mechatronics, University of Miskolc*
ronai-laci@hotmail.com

[2] *Robert Bosch Department of Mechatronics, University of Miskolc*
szabo.tamas@uni-miskolc.hu

Abstract
Kinematical investigation of a 4 DOF model robot is discussed in this paper. Denavit Hartenberg parameters are used to describe the motion of the robot. The analytical solution of the inverse kinematical problem is based on the transformation matrix. The DC motors of the robot are of sequentially controlled by AVR microcontroller. A motor shield is used to control the motors of the joints, furthermore four encoders also are implemented to measure the rotations. A simple schematic has been applied to control the end effector mechanism.

Keywords: *robot, kinematics, Denaivt Hartenberg, Arduino.*

1. INTRODUCTION

The robot is a mechatronical system, which can be taught for different tasks. It is widely used for automation of technological processes, like welding, painting, assemble, etc. in industry. Instead of human workforce it is advantageous to apply for monotonous work. In this paper a 4 DOF model robot is developed for educational and research purposes. The original model robot is produced by Velleman® [4] and its DC motors are controlled manually.

In order to have a good automatic control system for the robot, first of all one is need to prescribe forward and inverse kinematics of the mechanism [1]. A commonly used convention for selecting frames of reference in robotic applications is the Denavit Hartenberg, or DH convention [2]. The control system of the model robot is implemented on AVR type microcontroller, which is based on an Arduino developer board [3]. A motor shield is attached to the controller to measure the rotation of the joints and also to regulate the DC motors. The control program is written in C programming language.

The purpose of the development is to program the robot for intelligent packing of small objects. The geometric and physical parameters of the robot as well as its kinematics are given in Section 2. The control system and the source code written in C are discussed in Section 3. A simple packaging problem is solved in Section 4 and finally some concluding remarks are given in the Summary.

2. THE KINEMATICS OF THE MODEL ROBOT

The model robot is delivered in disassembled package by Velleman®. Assemble and wiring of the plastic elements and the DC motors are tasks of the user, which gives the possibility its further development. The maximum projection distance is 380 mm and the payload is 100 g. The commercial robot can be controlled manually to run the 5 DC motors.

Its extension for automatic control also available, but its possibilities are a bit restricted and expensive. The extension cannot provide the rotation angles of the joints, i.e., there is no feedback. Therefore intelligent process neither with manual control nor with its extension can be performed repeatedly. The purposed extension of the system is given in Section 3.
The forward kinematical analysis of the model robot with the DH parameters requires appropriate set up of the coordinate systems [1] at the joints, which are given in Figure 1. In addition to the coordinate systems DH parameters are shown in Figure 2. We noticed that the position of the end effector are determined by the first three joints and its angle is given by the angle of the fourth joint. The coordinate system $X_0,\ Y_0,\ Z_0$ is attached to the base.

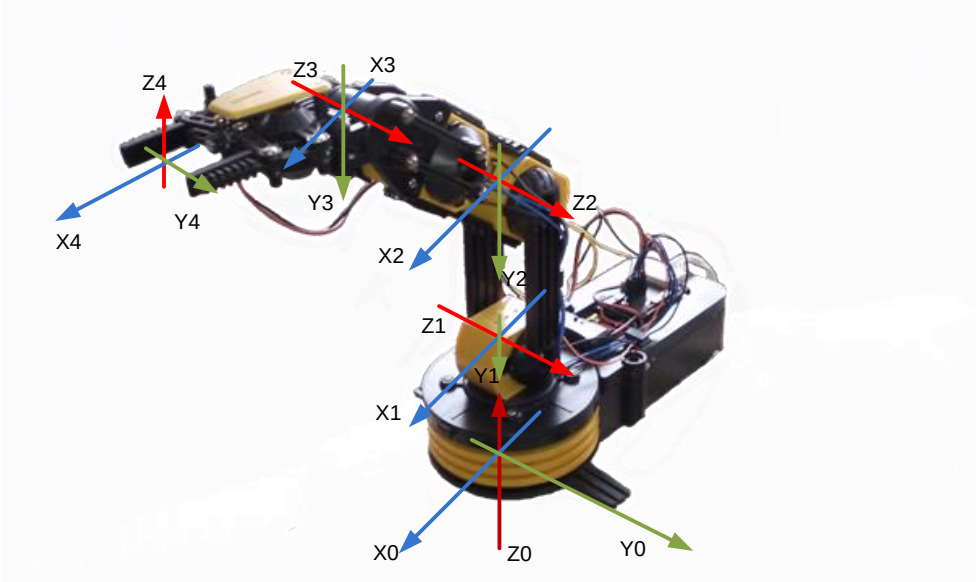

Figure 1. The model robot and its coordinate systems

The definitions of the DH parameters are given as follows [1], [2]:

- a_i is the link length, i.e., the distance of axes Z_{i-1} and Z_i (normal transverse, which shouldn't be negative),
- b_i is the link offset, i.e., the coordinate Z_{i-1} of the section point of axes X_i and Z_{i-1},
- α_i is the angle of the joint, i.e., the rotation angle around axis Z_{i-1} , which rotates axis X_{i-1} into axis Z_i,
- β_i is the link twist, i.e., the rotation angle around axis X_i , which rotates axis Z_{i-1} into axis Z_i.

The specific DH parameters are given in Table 1.

Table 1. DH parameters of the robot [5]

Link number:	$\boldsymbol{a_i}$	$\boldsymbol{b_i}$	$\boldsymbol{\beta_i}$	$\boldsymbol{\alpha_i}$
1.	0	$b_1 = 65\ mm$	-90°	$\alpha_1 = J1$
2.	$a_2 = 90\ mm$	0	0	$\alpha_2 = J2$
3.	$a_3 = 60\ mm$	0	0	$\alpha_3 = J3$
4.	$a_4 = 100\ mm$	0	90°	$\alpha_4 = J4$

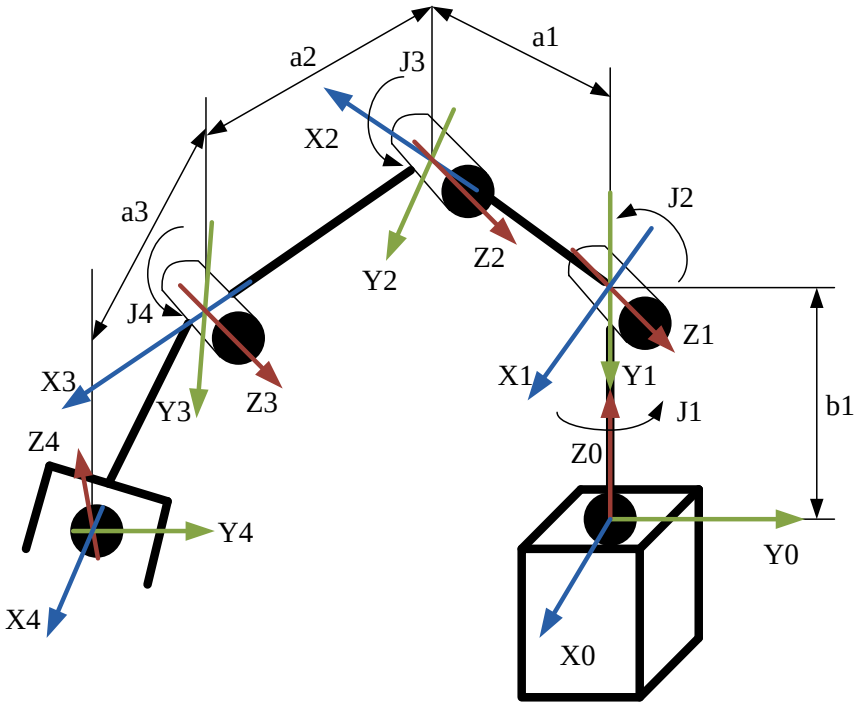

Figure 2. Coordinate systems and DH parameters

The homogenous transformation $\mathbf{D_{i-1,i}}$ between coordinate systems $i-1$ and i is a product of basic transformations (translation, rotation, translation and rotation) [2]:

$$\mathbf{D_{i-1,i}} = \mathbf{Trans_Z} * \mathbf{Rot_Z} * \mathbf{Trans_X} * \mathbf{Rot_X}, \tag{1}$$

where $\mathbf{D_{i-1,i}}$ in matrix form

$$\mathbf{D_{i-1,i}} = \begin{bmatrix} \cos(\alpha_i) & -\sin(\alpha_i)\cos(\beta_i) & \sin(\alpha_i)\sin(\beta_i) & a_i\cos(\alpha_i) \\ \sin(\alpha_i) & \cos(\alpha_i)\cos(\beta_i) & -\cos(\alpha_i)\sin(\beta_i) & a_i\sin(\alpha_i) \\ 0 & \sin(\beta_i) & \cos(\beta_i) & b_i \\ 0 & 0 & 0 & 1 \end{bmatrix} \tag{2}$$

and $Trans_X$, $Trans_Z$ are translation matrices along axes X, Z and Rot_X, Rot_Z are rotational matrices around axes X, Z respectively.
The investigated robot consists of four links, thus the homogenous transformation between the base and the end effector given as:

$$\mathbf{DH_{0,4}} = \prod_{i=1}^{4} \boldsymbol{D_{i-1,i}}\,. \tag{3}$$

The mathematical problem of the inverse kinematics can be composed in the following simple equation [1]:

$$q = f^{-1}(s), \tag{4}$$

where q denotes the angles of the joints and s denotes the X_0, Y_0, Z_0 coordinates of the end effector.

Problem (4) can be solved algebraic, geometric and numerical methods. In this paper the algebraic method is given in the sequel.

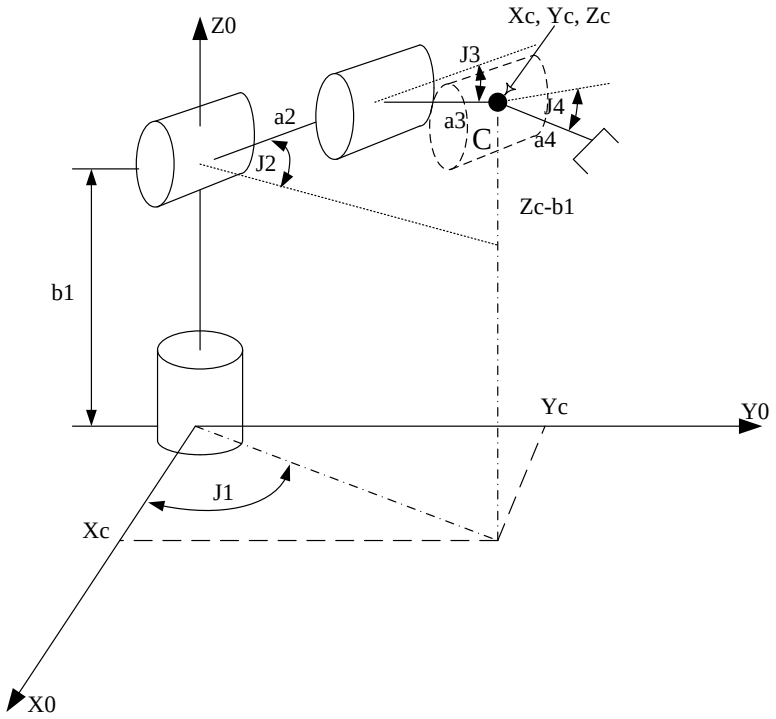

Figure 3. Definition of the joint angles

The position of the end effector depends on the homogenous transformation $\mathbf{D_{0,3}}$ between the base and the link 3:

$$\mathbf{D_{0,3}} = \begin{bmatrix} c(J1)c(J2+J3) & -c(J1)s(J2+J3) & -s(\mathrm{J1}) \\ s(J1)c(J2+J3) & -s(J1)s(J2+J3) & c(J1) \\ -s(J2+J3) & -c(J2+J3) & 0 \\ 0 & 0 & 0 \end{bmatrix}, \quad \begin{bmatrix} a_3c(J1)c(J2+J3)+a_2c(\mathrm{J2})c(J1) \\ a_3s(J1)c(J2+J3)+a_2c(\mathrm{J2})s(J1) \\ -a_3s(J2+J3)-a_2s(\mathrm{J2})+b_1 \\ 1 \end{bmatrix}. \tag{5}$$

The coordinates of joint C (shown in Figure 3) are equal to the entries of the 4th column of homogeneous transformation matrix:

$$\begin{aligned} X_C &= cosJ1(a_2\cos J2 + a_3\cos(J2+J3)), \\ Y_C &= sinJ1(a_2\cos J2 + a_3\cos(J2+J3)), \\ Z_C - b_1 &= -a_2 sinJ2 - a_3\sin(J2+J3). \end{aligned} \tag{6}$$

One can determine the rotation angle J_3 first taking the sum of squared coordinates X_C, Y_C, Z_C and expressing $cosJ3$ and $sinJ3$

$$cosJ3 = \frac{{X_C}^2 + {Y_C}^2 + (Z_C - b_1)^2 - a_2^2 - a_3^2}{2a_2a_3}, \qquad sinJ3 = \pm\sqrt{1 - cos^2 J3}, \tag{7}$$

then using function atan2(), which can provide angles between +180° and -180°, i.e.,

$$\mathrm{J}_3 = \mathrm{atan2}(\sin(\mathrm{J3}), \cos(\mathrm{J3})). \tag{8}$$

The angle of joint 1 is obtained as follows:

$$\mathrm{J}_1 = \mathrm{atan2}(Y_C, X_C). \tag{9}$$

The angle of joint 2 can be determined after a straight forward manipulation of (6):

$$cosJ2 = \frac{\frac{X_C}{cosJ1}(-a_2 - a_3 cosJ3) + (Z_C - b_1)a_3 \sin J3}{(-a_2^2 - a_3^2 - 2a_2a_3\cos(J3))}, \qquad sinJ2 = \pm\sqrt{1 - cos^2 J2}, \tag{10}$$

which results in

$$\mathrm{J}_2 = \mathrm{atan2}(\sin(\mathrm{J2}), \cos(\mathrm{J2})). \tag{11}$$

The angle of joint 4 depends on the specific user defined task, e.g., horizontal orientation of the end effector:

$$\mathrm{J}_4 = -(\mathrm{J}_3 + \mathrm{J}_2). \tag{12}$$

3. CONTROLLING OF THE ROBOT

The controlling of the robot is based on an Arduino UNO platform, which uses an AVR ATmega328 microcontroller. The chip is an 8 bit architecture, which contains a low power consumption option. The UNO module has some digital I/O and also analogue inputs. The regulation of the motors is performed by a motor shield, which has two Half H Bridges (L293D), by these Integrated Circuits the rotational direction of the motors can be changed. This shield can be mounted on the upper face of the controller. The shield can control only four motors, therefore a schematic has been developed, to control the grip mechanism of the end effector. A 250 line long C code has been written to control the model robot in a packaging problem.

4. PACKAGING PROBLEM

An intelligent packaging task has been programmed and performed by the model robot (see Figure 4). The task is to fill the storage with pieces of rubber on the left hand side of the robot from the Rubik's cube until the weight reach a given limit. Above this limit, a micro switch below the storage sends a signal to the controller to continue the packaging to the storage on the right hand side of the robot. Feeding the system with rubber pieces provided by

external human force.

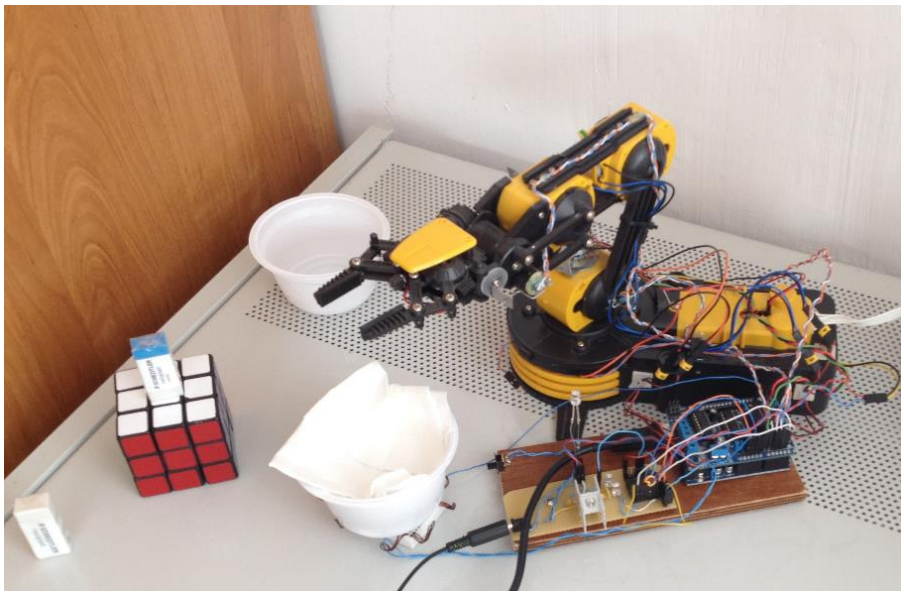

Figure 4. The robot performs a packaging task

5. RESULTS AND CONCLUSIONS

Forward and inverse kinematics have been derived for a model robot. The Arduino platform is well applicable for the control of 4 DOF model robot. At present the DC motors are controlled sequentially. The parallel working of the four DC motors require strong enough power supply, otherwise the encoder may provide noisy signal.

6. ACKNOWLEDGEMENT

This research was carried out in the framework of that Center of Excellence of Mechatronics and Logistics at the University of Miskolc.

7. REFERENCES

[1] **KIRÁLY B.:** *Ipari robotok kinematikai és dinamikai elemzése*, oktatási segédlet, Miskolc, 1995.
[2] **SPONG, W. M., HUTCHINSON, S., VIDYASAGAR, M.:** *Robot Modelling and Control*, Wiley, 2006
[3] *Arduino platforms*: http://arduino.cc/
[4] Velleman® KSR10 Robotic Arm – *User Manual*
[5] **RÓNAI L, SZABÓ T.:** *Egy 4 szabadságfokú modell-robot inverz kinematikai feladata*, OGÉT konferencia, Nagyszeben, 2014

SIMULATION OF THE CRACK PROPAGATION THROUGH A PLANAR PLATE WITH THE MIDDLE POSITIONED CYLINDRICAL HOLE

[1]STANKOVIĆ Miloš, [2]GRBOVIĆ Aleksandar, [3]MARINKOVIĆ Aleksandar, [4]MILOVIĆ Ljubica, [5]LAZOVIĆ Tatjana

[1]Research Associate
[1]Inovation Center, University of Belgrade, Faculty of Mechanical Engineering,
mstankovic@mas.bg.ac.rs

[2, 3, 5]Associate Professor
[2, 3, 5]University of Belgrade, Faculty of Mechanical Engineering
agrbovic@mas.bg.ac.rs

[4]Associate Professor
[4]University of Belgrade, Faculty of Technology and Metallurgy
acibulj@tmf.bg.ac.rs

Abstract
A prediction of crack propagation is subject of research of many scientists. Understanding crack occurrence and propagation could save lives (i.e. in airplane industry), or at least reduce the costs occurred by unexpected failures and stoppages. In this paper it is provided a brief theoretical background of the crack propagation regarding to stress intensity factor, and simulation of crack propagation through a planar plate made of steel with the middle positioned cylindrical hole, by means of Abaqus software. In addition, it is performed calculation of stress intensity factors with MORFEO, software that could be implemented onto Abaqus.

Keywords: *Crack Propagation, Abaqus, Morfeo, Stress Intensity Factor*

1. INTRODUCTION

If taken on macro-level polycrystalline materials could be assumed as homogenous. But if it is observed in micro-level, they are certainly not. Due to this inhomogeneity, and under applied load, there occur micro cracks between the grains of crystals. They are usually initiated on the surface of the specimen, and represent the stress concentration factors, which locally increase the stress value. When this value achieves the critical value, the crack begins to propagate. Usually, only one of the micro cracks continues to propagate, until the final fracture of the specimen occurs.

Prediction of the crack propagation is very important in sense of economical and safety reasons as well. By predicting the crack propagation, it is possible to evaluate the remaining time before the final fracture occurs, and plan the replacement of the part.

Stress intensity factor analysis of interface cracks using X-FEM was presented by Nagashima et al [1]. It was 2D bi-material interface crack problem. Shi et al. [2] developed a 3D finite element method for the analysis of fatigue crack growth based on the extended finite element method (X-FEM). The crack morphology was described by level set methods, which

is convenient modelling of growing cracks without remeshing. Numerical modelling crack propagation under Mode II fracture in plain concretes containing siliceous fly-ash additive was presented by Golewski et al [3]. Xue et al. [4] did numerical modelling crack propagation of sheet metal forming based on stress state parameters using XFEM method, applying ABAQUS program and its user subroutine UVARM. It is found that the stress state parameters can well reflect the micro-crack propagation, which is useful for the prediction of service life and it plays an important role in the damage tolerance design field. Zhuang and Cheng [5] performed Development of X-FEM methodology and study on mixed-mode crack propagation. The computational results show that the fracture mode and the crack growth path can be strongly affected by the interface of bi-materials and the loading asymmetry.

2. THEORETICAL BACKGROUND

Alan Arnold Griffith was the first to explain the phenomena of local stress increase due to crack occurrence. He made assumption that crack could be considered as elliptic hole (

Figure 1).

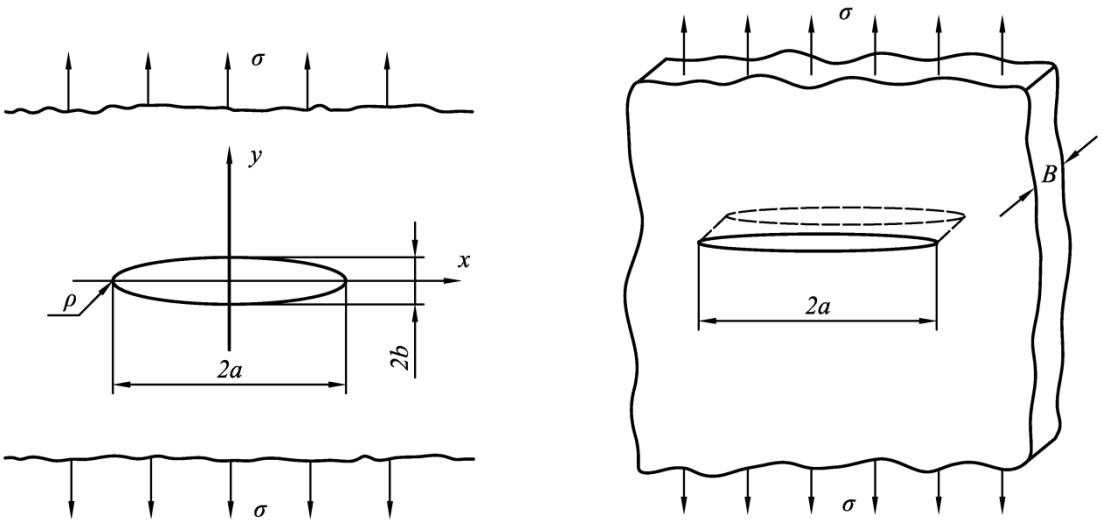

Figure 1. Griffith criterion: a) elliptical hole, b) crack

For the above case, highest value of the stress is given by the following formula:

$$\sigma_{\max} = \sigma\left(1+\frac{2a}{b}\right) = \sigma\left[1+2\left(\frac{a}{\rho}\right)^{1/2}\right] \quad (1)$$

There are three load modes, which cause three different movement of one crack surface relative to the other (Figure 2):

1. Mode I – opening, symmetrical opening of crack surfaces. Load type – tension stress σ
2. Mode II – sliding of the crack surfaces at the same plane. Load type – shear stress τ
3. Mode III – tearing of the crack surfaces at the different planes. Load type – shear stress τ

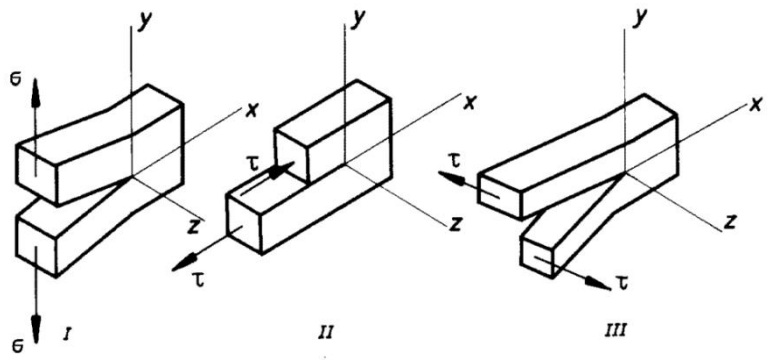

Figure 2. Modes of crack propagation regarding to load direction and relative movement of crack surfaces

2.1. Stress intensity factor

Stress intensity factors are proportional to stresses around the tip of the crack. They define amplitude of the stress singularity. In other words, with the stress intensity factor it is taken into account an influence of stresses, deformations and displacements around the tip of the crack. A unite for the stress intensity factor is MPa $\sqrt{\text{m}}$. The formula for the stress in dependence of the stress intensity factor for the element very close to the tip of the crack is:

$$\lim_{r\to o}\sigma_{ij}^{(I)}=\frac{K_I}{\sqrt{2\pi r}}f_{ij}^{(I)}(\theta),\ \lim_{r\to o}\sigma_{ij}^{(II)}=\frac{K_{II}}{\sqrt{2\pi r}}f_{ij}^{(II)}(\theta),\ \lim_{r\to o}\sigma_{ij}^{(III)}=\frac{K_{III}}{\sqrt{2\pi r}}f_{ij}^{(III)}(\theta) \qquad (2)$$

In the case of the plate of infinite length and width with middle positioned hole stress intensity factor is given by the following formula:

$$K_I=\sigma\sqrt{\pi a} \qquad (3)$$

In case if finite dimensions of the plate, there is coefficient *Y* added to the formula. This coefficient depends on type and position of the crack, as well as of dimensions of the plate.

$$K_I=Y\sigma\sqrt{\pi a} \qquad (4)$$

2.2. XFEM Method

XFEM Method is developed to improve solutions for problems with local discontinuities (cracks, surface contacts…), which cannot be improved by further mesh refinement. First to introduce this method was Ted Belytschko, back at 1999. It is well known concept of FEM, in which there are standard polynomial functions to describe displacements of the nods. At the XFEM method in addition to polynomial function, there are functions of discontinuity applied to nods which are close to given discontinuity (crack or contact). By means of these functions, it is possible to avoid remeshing in every step of calculation. In other words, only one mesh generation is needed to perform entire simulation of crack propagation

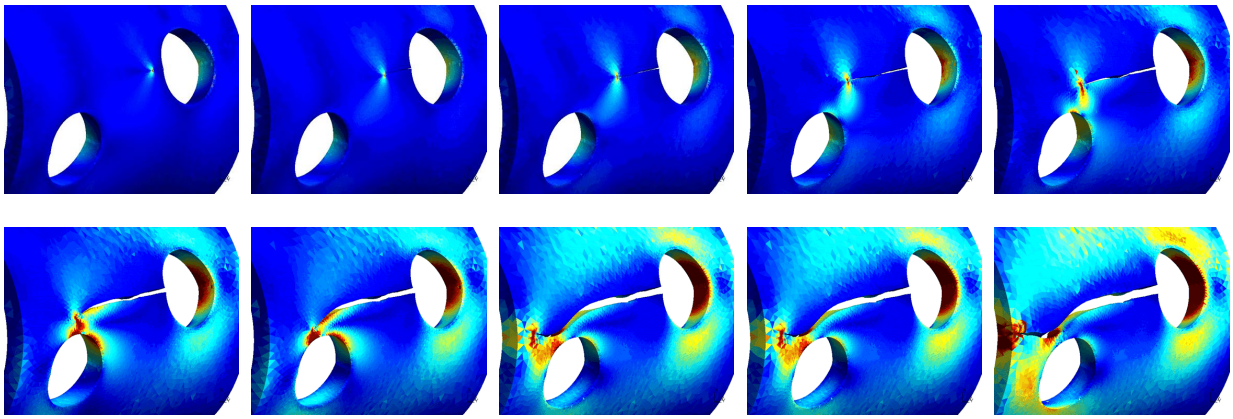

Figure 3 Simulation of the crack propagation by means of XFEM Method [6]

3. CRACK PROPAGATION ANALYSIS BY MEANS OF ABAQUS + MORFEO SOFTWARE

Subject of the simulation was a plate, with dimensions 300x300x20 and middle positioned hole Ø30 (Figure 4a). One end of the plate is cantilevered, while the opposite is subjected to axial load of 10 MPa. At the area of central hole, it is initiated a crack, in direction normal to the direction of load. The length of crack initiation is 10 mm left and right to the hole. The material of the plate is construction steel, which properties are given at the Table 1. It is performed meshing with hexahedral elements. Mesh was much denser in the region of expected crack propagation (Figure 4b) in order to obtain better accuracy. Total number of elements was 11208.

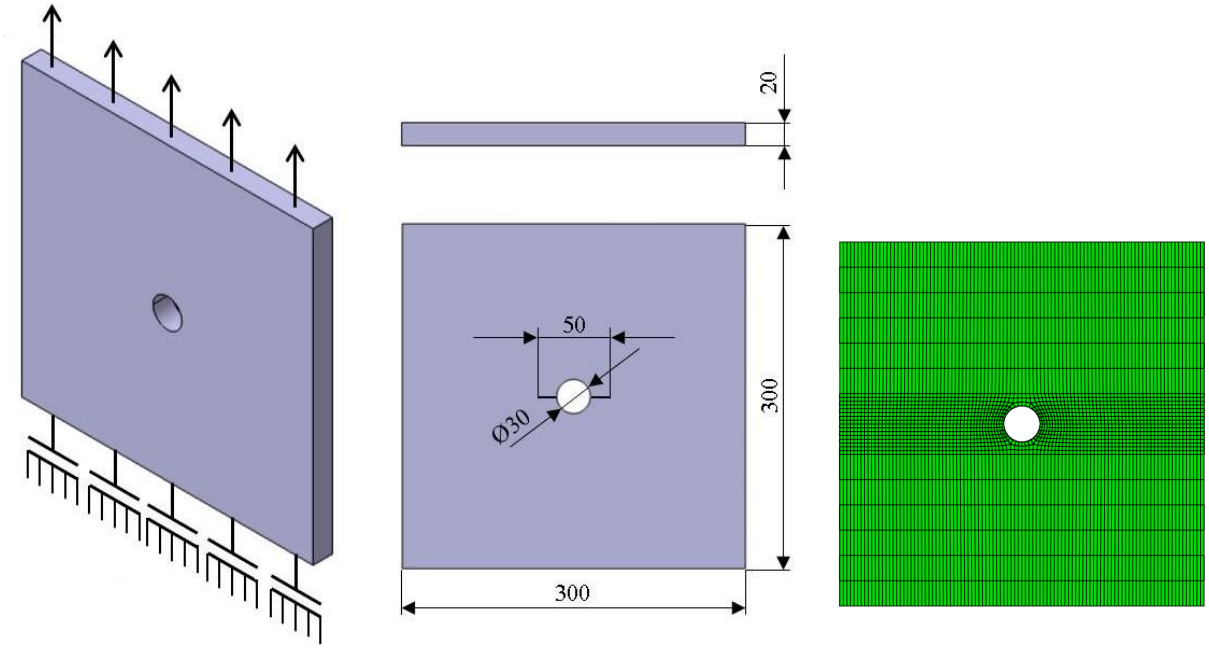

a) b)

Figure 4 a) Boundary conditions, loads and dimensions, b) Mesh of FE

Table 1. Material properties

Material:	Construction steel
Modulus of elasticity	200 [GPa]
Poisson's ratio	0,33
Maximal principal stress	150 [MPa]

MORFEO is special software developed by GEONX Company, which integrates with ABAQUS as an additional module, and it is able to extract stress concentration factors. To do that, it is necessary to perform "opening" of the crack in ABAQUS, and afterwards to continue with the crack propagation in MORFEO. Input data that should be inserted into MORFEO are number of steps of crack propagation (in this case it was 10 steps) and magnitude of every step (0.5 mm). An output file of MORFEO is consisted of coordinates of each node *x*, *y* and *z*, and values of K_I, K_{II}, K_{III} and K_{ekv} in every single node which belongs to crack front. Since the output file is quiet big to be presented in this paper, there follows a table with average values of K_I, K_{II}, K_{III} and K_{ekv} for every step of crack propagation.

Table 2. Average values of stress intensity factors for every step of crack propagation

Step	K_{ekv} **[MPa√m]**	K_I **[MPa√m]**	K_{II} **[MPa√m]**	K_{III} **[MPa√m]**
1	105,2461071	105,279679	1,28901464	-0,00223466
2	108,6275	108,574214	-0,71594982	0,002269525
3	107,5497857	107,502214	-0,07436818	-0,00236342
4	108,3113214	108,292607	-0,13395814	-0,007464
5	108,9173571	108,991857	0,48802629	0,003186372
6	108,8736429	108,905286	-0,23319675	0,013746009
7	109,4125357	109,352857	0,40155	-0,02416928
8	110,6215333	110,631267	-0,4388207	-0,0003283
9	111,7147333	111,776033	0,25279895	0,007164186
10	112,4803214	112,365286	0,01584482	0,003702531

It was expected for K_I factor to be much higher than other two coefficients K_{II} and K_{III} because of nature of load, which tends to open the crack (Mode I). If we compare the results from

Table *2*, it is obvious that assumption is fulfilled. K_I is for two orders of magnitude higher than K_{II} and K_{III}. Also K_{II} and K_{III} are very close to 0, which makes us conclude that their

value is just the numerical error. That is also in accordance with Mode I theory.

On the other hand, stress intensity factor should increase for every next step of crack propagation. There follows a diagram which confirms this assumption, too.

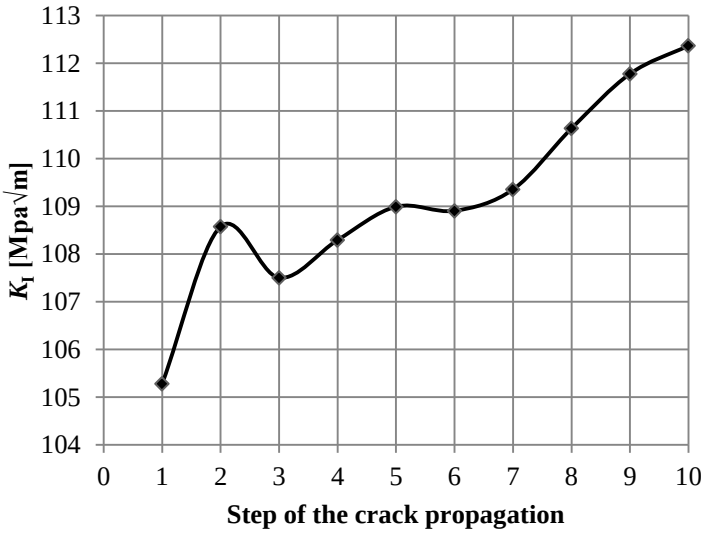

Figure 5. Trend of K_I factor for 10 steps of crack propagation

4. CONCLUSIONS

In this paper it was given a short theoretical background for the crack propagation theory, with special accent on explanation of term of stress intensity factor. Afterwards it was performed modelling of a plate with cylindrical hole in the middle with crack initiations positioned normal to the load direction. By means of ABAQUS software, it was performed complete opening of the crack. Then, it was performed partial opening of the crack by means of MORFEO, and it was obtained values of all stress concentration factors K_I, K_{II} and K_{III}.

In accordance with the theory, regarding to the nature of load, it was obtained the highest values for K_I factor. The other two factors are close to the numerical error.

It is observed the increase of the K_I in every next step of crack propagation. Since the remaining surface of the plate which carries the load is decreasing as the crack propagates, it is also expected behaviour.

5. ACKNOWLEDGEMENT

This work has been performed within the projects TR 35011, and TR 35021. These projects are supported by the Republic of Serbia, Ministry of Education, Science and Technological Development, whose financial help is gratefully acknowledged.

6. REFERENCES

[1] **NAGASHIMA, T., OMOTO, Y., TANI, S.**: *Stress intensity factor analysis of interface cracks using X-FEM,* International Journal for Numerical Methods in Engineering, 2003, 56: pp. 1151–1173.

[2] **SHI, J., CHOPP, D., LUA, J., SUKUMAR, N., BELYTSCHKO, T.**: Abaqus implementation of extended finite element method using a level set representation for three-dimensional fatigue crack growth and life predictions, Engineering Fracture

Mechanics, 2010, 77: pp. 2840–2863
[3] **GOLEWSKI, G.L. , GOLEWSKI, P., SADOWSKI, T.:** Numerical modelling crack propagation under Mode II fracture in plain concretes containing siliceous fly-ash additive using XFEM method, Computational Materials Science, 2012, 62: pp. 75–78
[4] **Xue, F., Li, F., Li, J., He, M., Yuan, Z., Wanga, R**.: *Numerical modeling crack propagation of sheet metal forming based on stress state parameters using XFEM method,* Computational Materials Science, 2013, 69: pp. 311–326
[5] **ZHUANG, Z., CHENG, B. B.:** *Development of X-FEM methodology and study on mixed-mode crack propagation,* Acta Mech. Sin. 2013 27(3): pp. 406–415
[6] http://www.xfem2011.com/index.html
[7] **JELASKA, D.:** *Osnovi mehanike loma, II. dio: Rast pukotine*, Ukorak s vremenom 27, 2013, pp. 25-30
[8] **SEDMAK, A.**: *Primena mehanike loma na integritet konstrukcija* : 1. Edition, Faculty of Mechanical Engineering, University of Belgrade, 2013
[9] **ROYLANCE, D.:** *Introduction to Fracture Mechanics*, Massachusetts Institute of Technology, 2001

INTERNATIONAL SCIENTIFIC CONFERENCE ON
ADVANCES IN MECHANICAL ENGINEERING
PROCEEDINGS

INVESTIGATION OF PHASE TRANSFORMATION INDUCED ACOUSTIC EMISSON IN SHAPE MEMORY ALLOYS

[1]SZABÓ Sándor, Dr., [2]TÓTH Z. László, M.Sc.,
[3]DARÓCZI Lajos, Dr., [4]BEKE L. Dezső, Dr.

[1]Department of Physics and Production Engineering, College of Nyíregyháza, Hungary
H-4400 Nyíregyháza, Sóstói street 31/b
sg_szabo@nyf.hu

[1,2,3,4]Department of Solid State Physics, University of Debrecen, Hungary
H-4010, Debrecen, P.O.Box 2.

Abstract
In order to get useful information about industrial materials and equipment, detection and evaluation of acoustic emission can be useful. This non-destructive method is important for development of engineering materials, especially for investigation of shape memory alloys (SMA). In this work Ni_2MnGa has been investigated during martensite – austenite transformation. Acoustic emissions (AE) were detected during heat treatment with 0.1 K/min heating rate. Mathematical analysis of the acoustic signals provided power law behaviour. Acoustic activity and critical exponents were evaluated. We got asymmetric activity and a slight difference in exponents while heating and cooling process were compared. Value of the exponents and characterization of thermal properties are detailed in [1]. Results are in agreement with literature [2], [3] and they also complete the measurements performed, till today.

Keywords: *shape memory alloy, acoustic signal, asymmetry*

1. INTRODUCTION

Martensitic transformation of a shape memory alloy is discontinuous process. This leads to a series of acoustic emission signals. During the jerky propagation of interfaces between austenite and martensite phase, individual acoustic signals are created and they can be separated. We prepared statistical analysis of the separated signals. It shown that the acoustic energy, amplitude or duration time distribution follows a power law [2]

$$\rho(X) = CX^{-\alpha}\, exp(\frac{-X}{Xo}) \qquad (1)$$

In (1), ρ(X) is the probability density, α is the critical exponent and Xo is the cut off value. The equation is connected with self-organized criticality. The sensitivity of acoustic activity and critical exponents to up or down direction of heat treatment is not known in details. However the symmetric or asymmetric behaviour and reasons of these properties can be important for understanding the austenite - martensite transformation as a part of self-organised criticalities. With this object we concentrated to the detection of the acoustic signals and to the symmetric or asymmetric character of them.

2. METHODS

We published experimental details in [1] and [4]. Single crystalline Ni_2MnGa billets, from AdaptaMat Co. (Finnlad) were investigated by Perkin Elmer DSC7 equipment. Commonly used high frequency (up to 1MHZ filtering and up to 16MHZ sampling rate) acoustic emission equipment was used. The applied Sensophone AED – 404 Acoustic Emission Diagnostic equipment can be seen in figure (1).

Figure 1. Sensophone AED – 404, acoustic emission diagnostic equipment. Details of AED-40 family can be found in [5].

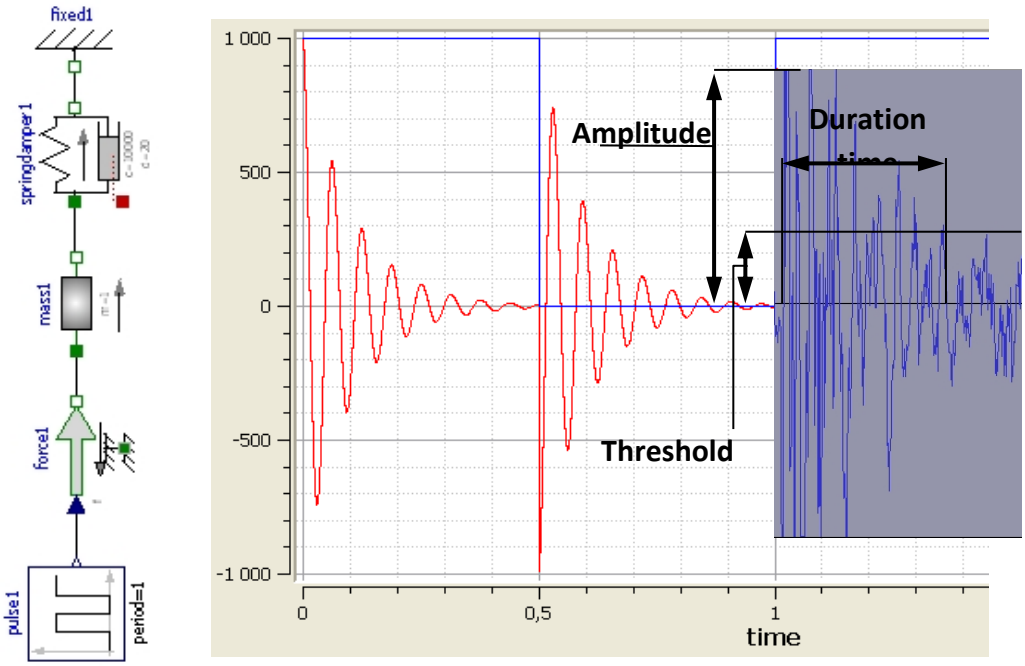

Figure 2. Modelled and real acoustic signals, with evaluated parameters.

In [4] we have shown that a special damped spring model can explain the shape of acoustic signal. Figure (2) shows the model with the signals and also we marked the parameters used for mathematical evaluation of power behaviour and symmetry - asymmetry properties.

3. RESULTS

During heating up and cooling down, i.e. during the phase transformation, well separated individual acoustic and thermal signals were detected. Figure 1 shows acoustic and thermal activity versus time [1]. Thermal and acoustic peaks were correlated in the most cases. However there were some seconds where acoustic or the thermal peaks were absent. This calls for the investigation of the similarity and difference between acoustical and thermal effects during austenite – martensite transformation, and also investigation of the reasons and statistics of the thermal and acoustic signals. Since mush more acoustic peaks can be detected, the acoustic information probably can characterize the samples in a lower structural scale. Steps of structural changes of during austenite – martensite transformation can be followed by acoustic emission in a finer time scale, as well. Therefore in this work we focused on acoustical signals, chiefly symmetrical or asymmetrical behaviour of the acoustical activity and of the exponents of characteristic power functions.

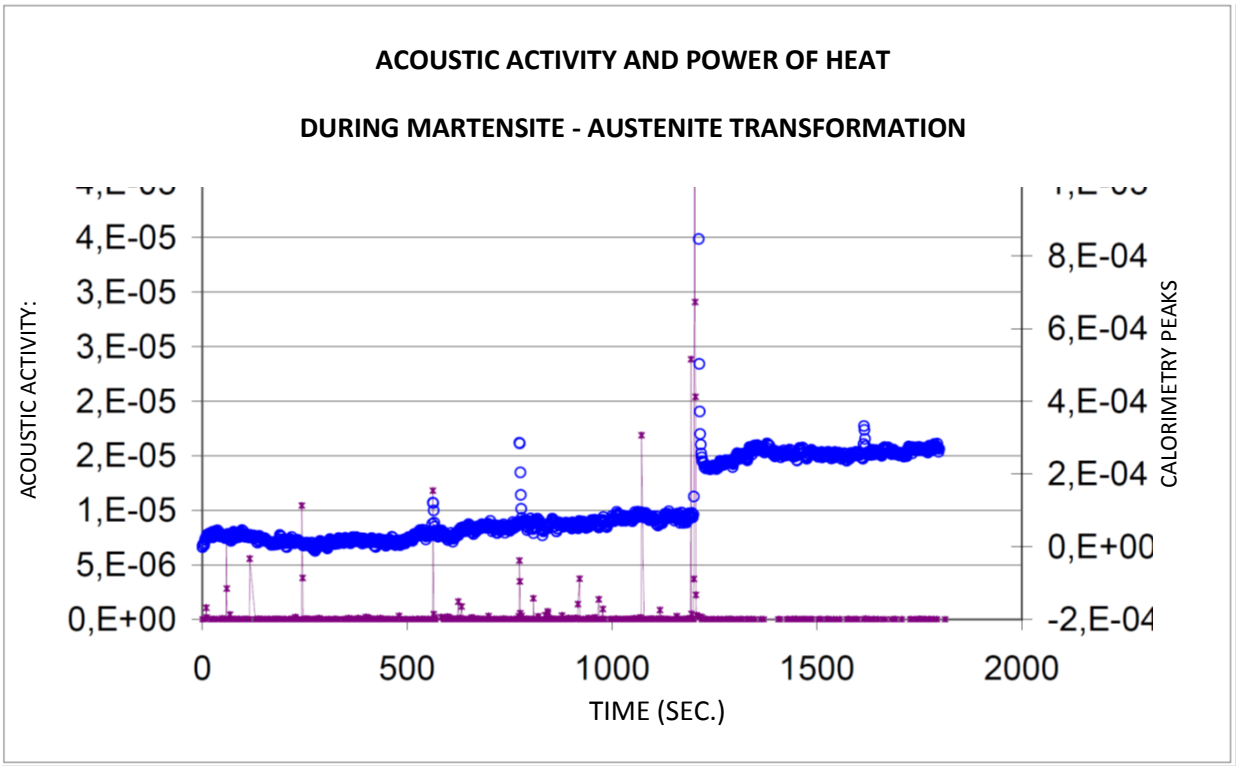

Figure 3. Thermal peaks and acoustic activity versus time.

We detected clear asymmetric behaviour of acoustic activity. Number of acoustic hits is considerably larger for cooling than for heating. Acoustic activity during austenite to martensite transformation is much higher than activity during the opposite, martensite to austenite transformation. Fig 4 shows [1] the amplitudes and the sum of amplitudes during the above two types of transformations. Thermal peaks, the appearance of “latent-heat” -

characteristic to firs order transformations – can be detected at the time periods where sum of acoustic amplitudes jumps.

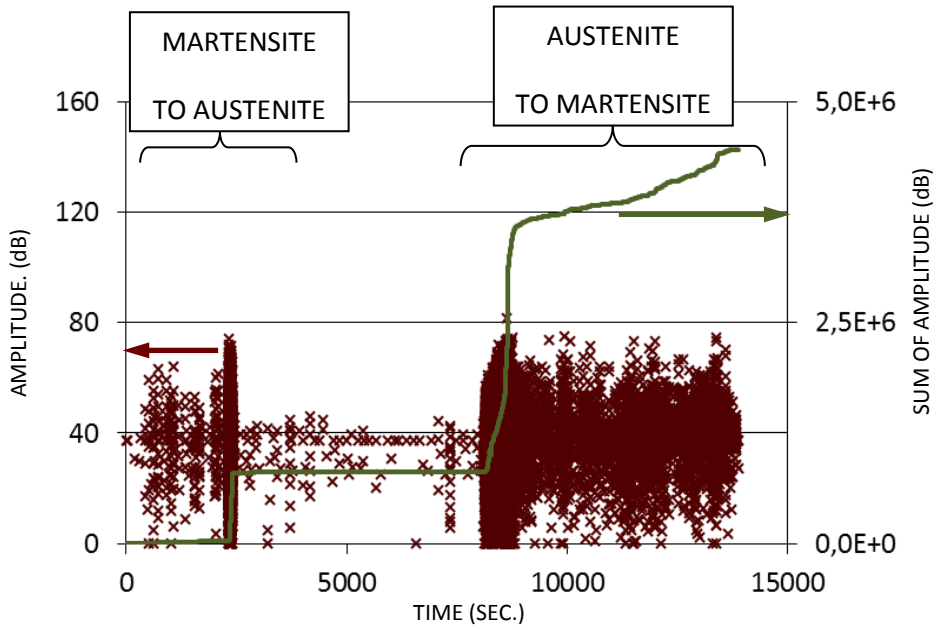

Figure 4. Asymmetry of acoustic activity during heating and cooling.

We prepared statistical analysis of acoustic signals. Figure 5 illustrates that energy distribution satisfy power-law behaviour, with exponential cut off. Exponents were slightly sensitive to direction of heat treatment. Absolute value of energy exponents decreased with 12% on the average while heat treatment changed to cooling down from heating up. This means that near asymmetric behaviour of acoustic activity there is a slight asymmetry of exponents as well. Asymmetry behaviour can be attributed to the relaxation of the martensite structure (change of the distribution of martensite variants) and also can be related to nucleation problems: generally the nucleation of the low symmetry phase is more difficult than nucleation of the high symmetry phase.

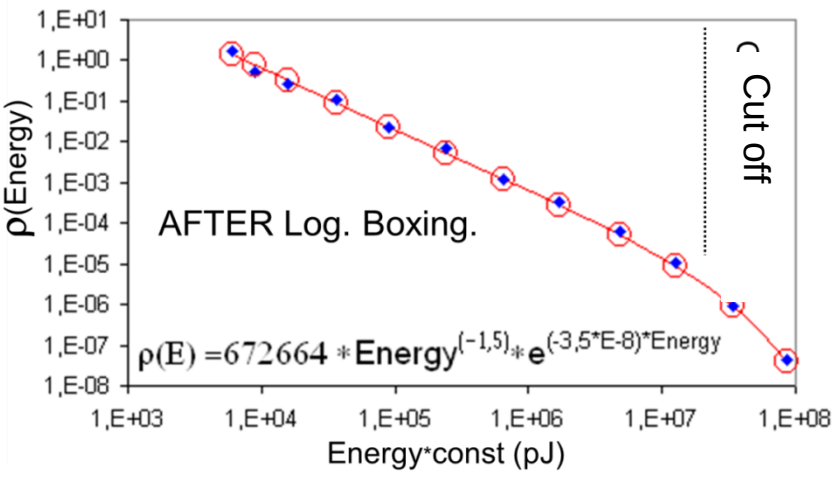

Figure 5. Evidence of the power behaviour, energy distribution of a heated sample [1].

4. CONCLUSIONS

The probability density of acoustic signals satisfies power function with exponential cut off (see equ. (1)). Comparison of the signals from the austenite to martensite and the martensite to austenite transformations shows a slight difference in the exponents. In addition clear asymmetrical behaviour of acoustic activity was detected. Reason of asymmetry, as discussed in [1] in details, can be attributed to relaxation of the martensite structure, and also difference between nucleation kinetics of low and high symmetry phase can be important.

5. ACKNOWLEDGMENTS

This work is supported by TÁMOP-4.2.2.A-11/1/KONV-2012-0036 and TÁMOP-4.2.2/B-10/1-2010-0024 projects which are implemented through the New Hungary Development Plan, co-financed by the European Social Fund, and the European Regional Development Fund. Work was also supported by OTKA Board of Hungary (K84065).

6. REFERENCES

[1] **TÓTH L. Z., SZABÓ, S., DARÓCZI, L., BEKE, D. L.:** *Calorimetric and acoustic emission study of martensitic transformation in single crystalline Ni2MnGa alloys*, Submitted to Phys. Rev. B, September, 2014.

[2] **LUDWIG, B. ET AL.:** *"An acoustic emission study of the effect of a magnetic field on the martensitic transition in Ni2MnGa"* Appl. Phys. Lett. 94, 121901, 2009.

[3] **GALLARDO, M.C., MANCHADO, J., ROMERO, F.J., DEL CERRO, J., SALJE, E.K.H, PLANES, A., VIVES E.:** *"Avalanche criticality in the martensitic transition of CuZnAl shape memory alloys: A calorimetric and acoustic emission study"* Phys. Rev. B 81, 174102, 2010

[4] **SZABÓ, S., DARÓCZI, L., BEKE, D.:** *Investigation of acoustic emission of shape memory alloys*, Proceedings of the international scientific conference on advances in mechanical engineering, ISBN 978-963-473-623-3, pp. 169 – 175, 2013

[5] *Gereb and Co, Technical Development LTD,* www.sensophone.hu

SUSTAINABILITY STUDY FOR WHEAT STRAW TORREFACTION TECHNOLOGY

[1]SZAMOSI Zoltán, M.Sc., [2]ROSAS-CASALS Martí, Dr.

[1]University of Miskolc, Institute of Energy Engineering and Chemical Machinery, Department of Chemical Machinery,
szamosi@uni-miskolc.hu

[2]Universidad Politécnica de Catalunya, Sustainability Measurement and Modeling Lab
rosas@mmt.upc.edu

Absract
The aim of this article is to examine the torrefaction production technology placed in two power plant environment (Rankine-Clausius, and Organic Rankine-Clausius circular procedures). The torrefaction is a heat treatment process at 280 – 300 °C obturated from oxygen, this heat treatment effectively changing the structure of the material, and the feedstock's heating value improves. Our study is restricted is wheat pallet because we conducted the laboratory experiments with material. In Hungary the agricultural industry produces raw materials in big amounts (mainly combustibles that is energetically renewables) which are at the moment, mixed with nitrogen-based fertilizers and biodegradable anaerobe bacteria ploughed back into the tillage as a form of nutrient supply. It takes 9 months to become nutriment from this inorganic material.
The object of our study is the key equipment of a production technology which continuously works, double-jacketed, and can be subjected to vacuuming. This equipment is a cylindrical furnace in which the torrefaction is realized.

Keywords: *biomass, heat treatment, power plant, torrefaction wheat straw*

1. ABOUT THE TORREFACTION PROCESS

The torrefaction is a three-stepped heat treatment technology: a heating, a torrefaction and a cooling section included. Inside of the reactor the moisture content evaporates in the first place, when the biomass reaches the 200 °C the physically bounded water is released. When the temperature reaches the 280°C the de-polymerization of the hemi-cellulose occurs. The torrefaction frees the water, the volatile organic compounds, and the hemicellulose from the cellulose and lignin.

With all of the polymers involved the dehydration process takes place, it destroys the "OH" groups that are responsible for H_2 that binds the water. This reaction limits the ability to absorb water into the torrefied material [1]. This is a significant feature of the torrefied material because of its undemanding storing needs. It is possible to store the produced materials under the sky without an expensive storage building.

2. ANALYSIS OF THE THEORETICAL REACHABLE HEAT RADIATION POWER

We want to create clear radiation inside of a furnace, which is not possible because of the surface contact of the cylindrical shell of the bale with the surface of the furnace. During our

investigation we do not take into account the heat transfer and heat conduction, as a result we are investigating a process which is that good from the thermodynamic perspective. The heat source is only the cylindrical shell of the furnace. The heat transfer with heat-radiation we can analyze with the following formula:

$$Q = A \cdot \varepsilon \cdot \sigma \cdot F_{1-2}(T_2{}^4 - T_1{}^4) \quad (1)[2]$$

where,
A: absorbing area [m^2],
ε: emissivity coefficient, wheat straw 0,91[2],
σ: Stefan-Boltzmann constant, [$W/(m^2 \cdot K^4)$].
F_{1-2}: view-factor,
T_2: temperature of the heat source, here 300°C,
T_1: temperature of the absorber, here 20°C.
The view-factor can be determined with the following formula:

$$F_{1-2} = \frac{1}{\pi R_2}\left[\begin{array}{l} \frac{1}{2}\left(R_2^2 - R_1^2 - 1\right)\cos^{-1}\frac{R_1}{R_2} + \pi R_1 - \frac{\pi}{2}AB \\ -2R_1\tan^{-1}\left(R_2^2 - R_1^2\right)^{1/2} + \left\{\left(1+A^2\right)\left(1+B^2\right)\right\}^{1/2}\tan^{-1}\left\{\frac{\left(1+A^2\right)B}{\left(1+B^2\right)A}\right\}^{1/2} \end{array}\right] \quad (2)[3]$$

Within this formula we can find the following variables: ratio of the radiuses and the height, and the two cyclinder's radiuses can be analyzed from the following draft's marking:

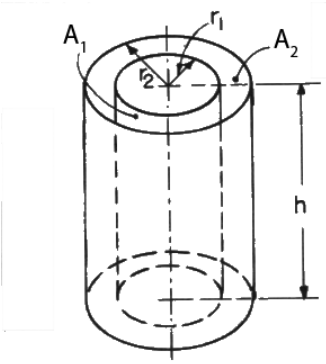

Figure 6. The marking belonging to the furnace and the bale

$$R_1 = \frac{r_1}{h} \quad (3)[3]$$

$$R_2 = \frac{r_2}{h} \quad (4)[3]$$

$$A = R_2 + R_1 \quad (5)[3]$$

$$B = R_2 - R_1 \quad (6)[3]$$

Its value is 0.9844. To define it, the diagram in literature [2] can be helpful.

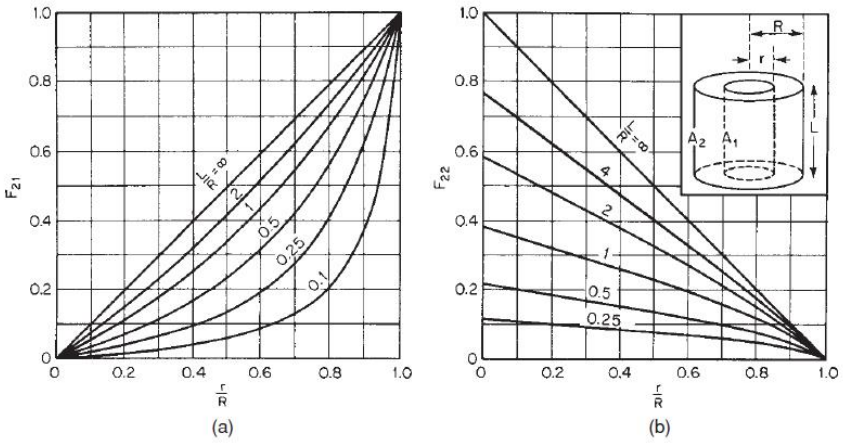

Figure 7. Choosing the view factor on the basis of the diagram [2]

With the application of the above mentioned guidelines we defined heat relations in the different h/d relational, but in volume equal furnaces. Our aim was to examine in every single h/d relationally different furnaces the same weight. 1 m^3 volume furnace can handle 90 kg wheat, while 10 m^3 furnace can handle 900 kg wheat.

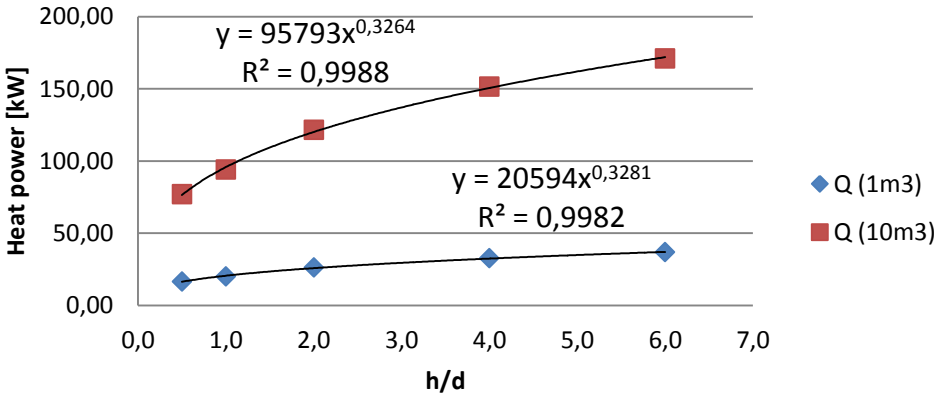

Figure 8. The theoretical reachable heat radiation flow in the 1, and 10 m3 furnace

On the Figure 3. what we can get out from the system with such temperature and material characteristics.

3. DETERMINATION OF THE ENERGY DEMAND OF THE TORREFACTION

To heat up the given amount of the straw we need to input the following energy:

$$Q = \dot{m} \cdot c \cdot (T_2 - T_1) = 90 \frac{kg}{h} \cdot 1{,}7 \frac{kJ}{kgK} \cdot (300 - 20°C) = 11{,}9kW \quad (7)[4]$$

It seems like we miss the energy demand of the reaction, because this is an endotherm reaction, but we lose mass during the process so we assume the energy demand according to the [1] literature.

$$Q = \dot{m} \cdot c \cdot (T_2 - T_1) = 900 \frac{\text{kg}}{\text{h}} \cdot 1{,}7 \frac{kJ}{kgK} \cdot (300 - 20°C) = 119\ kW \quad (8)[4]$$

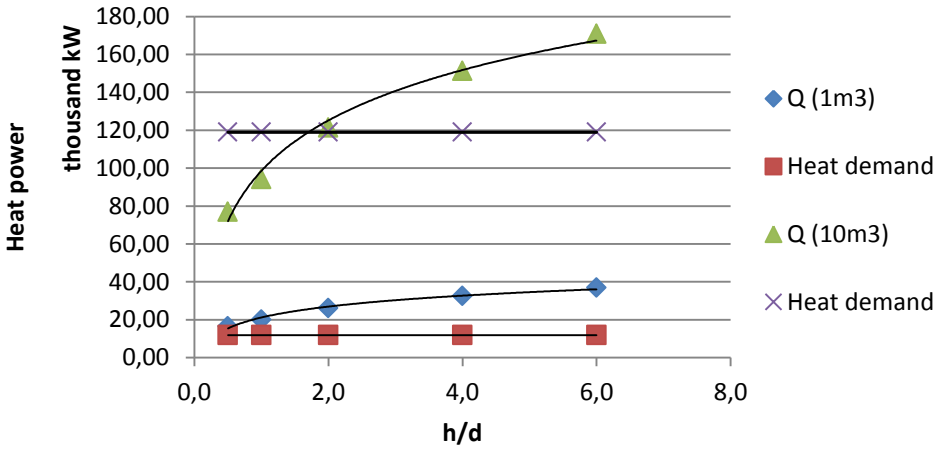

Figure 9. The heat power demand of the wheat straw for torrefaction fitted into the Figure 3.

4. CONCLUSIONS

According to our analysis of the scale-up of the torrefaction furnace has some difficulties occurred by the heat power demand. If we want to treat for example 900 kg of basic material, the shape and the h/d ratio of the furnace are very important. If we choose h/d ratio below 2 we will have heat transfer problems. In the future we should examine the heat transfer relations, we should determine the heat transfer coefficients, and choose the proper heat transfer fluid.

5. ACKNOWLEDGEMENT

This research was supported by the **European Union** and the **State of Hungary, co-financed by the European Social Fund** in the framework of TÁMOP-4.2.4.A/ 2-11/1-2012-0001 'National Excellence Program'.

6. REFERENCES

[1] **BASU, P.:** *Biomass Gasification, Pyrolysis and Torrefaction*, Elsevier, 2013. http://www.sciencedirect.com/science/article/pii/B9780123964885000083.

[2] **DON, R.H.P., GREEN, W.:** *Heat and Mass Transfer*, in: Perry's Chem. Eng. Handb., McGraw-Hill, 2008: pp. 1–87. doi:10.1036/0071511288.

[3] **SIEGEL, R., HOWELL, J. R.:** *Thermal radiation heat transfer*, Taylor & Francis, 1992. http://adsabs.harvard.edu/abs/1992STIA...9317522S?

[4] **AHN, H. K., SAUER, T. J., RICHARD, T. L., GLANVILLE, T. D.:** *Determination of thermal properties of composting bulking materials.*, Bioresour. Technol. 100 (2009) 3974–81. doi:10.1016/j.biortech.2008.11.056.

COMPUTER PROGRAM FOR THE CALCULATION OF THE PERFORMANCE PARAMETERS OF PNEUMOBILES

[1]SZÍKI Gusztáv Áron, Dr., [2]JUHÁSZ György, Dr., [3] KONDOR Nagyné, Rita, Dr., [4] JUHÁSZ Botond

[1]*Faculty of Engineering, University of Debrecen*
szikig@eng.unideb.hu

[2]*Faculty of Engineering, University of Debrecen*
juhasz@eng.unideb.hu

[3]*Faculty of Engineering, University of Debrecen*
rita@eng.unideb.hu

[4]*Faculty of Engineering, University of Debrecen*
botondjuhsz@yahoo.com

Abstract
The presented computer program is capable of calculating the performance parameters of pneumobiles from the technical parameters of their machine parts. The technical parameters of the pneumatic engine were measured by our own system built up of National Instruments devices. Reached speed and covered distance within a given period of time and also the top speed of the vehicles can be calculated by the program. Moreover, the optimal values of the technical parameters (such as the optimal gear ratio in the chain drive and in the internal gear hub) can be determined indirectly. Thus the program is a useful help for designers of pneumobiles and also a useful tool to predict the performance of a given model in the competition.

Keywords: *pneumobiles, calculation of performance parameters, optimization of technical parameters*

1. INTRODUCTION

The pneumobil competition was first organised in 2008 by the Bosch Rexroth Company for the students of institutions of higher education of Hungary. The aim of the competition is to build a vehicle that uses commercially available pneumatic devices of the company as the components of the engine. The competition – which is held every year in May, in Eger – soon gained great popularity amongst colleges and universities and in the third year it became an international competition. The competition has the following categories:

- Long-distance category
- Slalom track category
- Acceleration category

For every category each team get a 10l tank, which contains $2m^3$ of compressed air on 200bars. The team of the University of Debrecen Faculty of Engineering has been taking part in the competition since the beginning and based on the result it is the most successful team on the field.

Figure 1. Racing Pneumobile

2. TECHNICAL DESCRIPTION OF THE PNEUMOBILE AND MEASURING SYSTEM

The pneumobil is a four-wheeled vehicle on two-tracks. The vehicle is equipped with a rollbar and seatbelt. The vehicle's drive consists of two pneumatic cylinders. The torque is transferred to the wheels with the help of two freewheels and a variable-ratio transmission.
The pneumobil is designed in a way so that it is capable of completing every categories, it is suitable for both acceleration race and the long-distance category. We suit the requirements arising from the different categories by changing the control of the vehicle. Figure 2 shows the parts and the function of the engine.

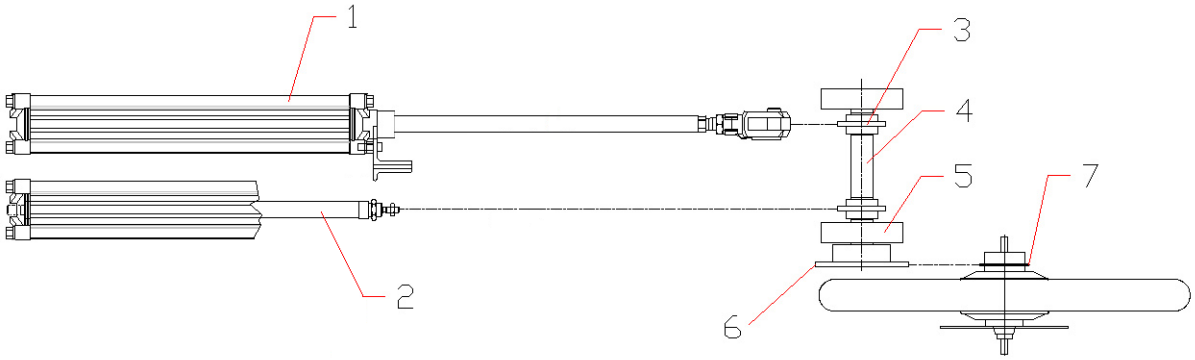

Figure 2. Parts of the engine of the pneumobil

The two ∅80 cylinders (1) are arranged parallel next to each other. The cylinders work independently only in pulling mode. These are connected to two ∅25 cylinders (2) with a chain, they are responsible for pulling back the bigger cylinders. The force of the cylinders drive the crankshaft (4) through two sprockets (3) integrated on two freewheels. The crankshaft is attached to the frame of the vehicle with two Y-bearings (5). The drive sprocket (6) is fixed at the end of the crankshaft, which transfers the torque to the wheel through the driven sprocket (7). We use an internal gear hub which makes us possible to change gears while driving.

In 2013 a new category enriched the competition. We created a measuring system for the first announced telemetry category. We could observe the parameters of the pneumatic engine with this system. This measuring system consisted of Bosch Rexroth devices, where we used the PLC as a data acquisition device. We wanted to upgrade this system so that we could get

more data of our vehicle and its engine, in this way we could develop and optimize more accurately.

When we tried to expand the system we soon realized that the PLC was not going to be able to full fill its role as a data acquisition device. That is why we decided to build up our system from National Instruments devices. The measured quantities with the system:

- The air pressure inside the cylinders
- The air pressure flowing out of the tank
- The position of the piston
- The quantity of the air used by the system
- The velocity of the pneumobil

Derived, to be displayed parameters:

- Time-path diagram of the piston
- Velocity-path diagram of the piston
- Acceleration-path diagram of the piston
- Force-displacement diagram
- The actual speed of the vehicle
- The performance curve of the vehicle
- Graphical display of the correlations between the piston speed, vehicle speed and air consumption

Devices:

Table 1. Devices

Name	Type	Manufacturer	Feature
Distance measuring sensor	SM6	Bosch Rexroth	Range:0-503 mm
Pressure sensor	PE5	Bosch Rexroth	0-10 bar; AO: 0-10V/4-20 mA; PNP
Flow rate sensor	AF1	Bosch Rexroth	250-5000 l/h; AO: 4-20 mA
NI CompactRIO 9024	9024	National Instruments	800 MHz, 512 DDR2 RAM
Module	NI 9201 module	National Instruments	8-channel analog input
Wi-Fi router	Cisco E2500	Cisco	300 MBs

3. MEASUREMENT RESULTS

Figure 3/a shows the air pressure inside the ∅80- cylinders and the air pressure flowing out of the tank (main pressure) against the running time of the pneumobile.
Figure 3/b shows the absolute value of the velocity of the piston.

The red line shows the air pressure inside the 1st cylinder, the green line shows the air pressure inside 2nd cylinder, and the blue one shows the main pressure. We can see that pressures inside1st and the 2nd cylinder complement each other creating a continuous line. The difference between the air pressure inside the cylinders and the main pressure is resulted from the pneumatic loss of the connections and the valves. Figure 3/b shows the velocity magnitude of the piston against the running time of the pneumobile. In Figure 4 – utilizing the

data presented in Figure 3a and b – the air pressure inside the cylinder is plotted against the velocity magnitude of the piston.

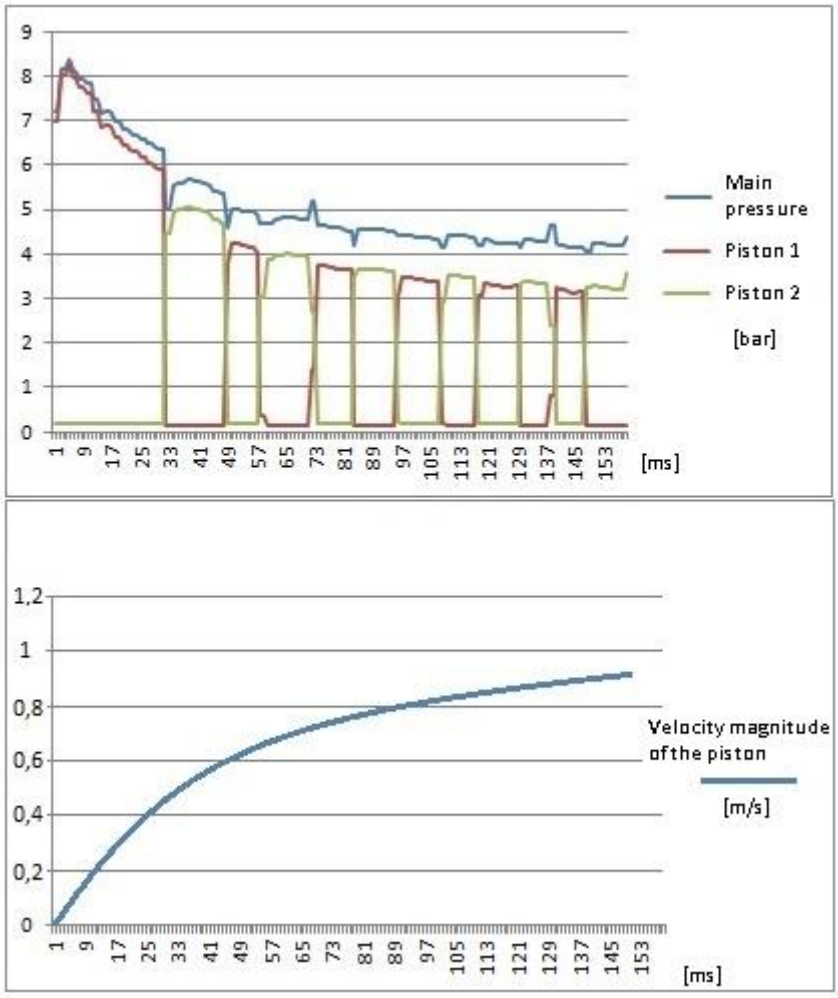

Figure 3. Air pressure inside the cylinder and flowing out of the tank (a) velocity magnitude of the piston (b) as the function of the running time of the pneumobil

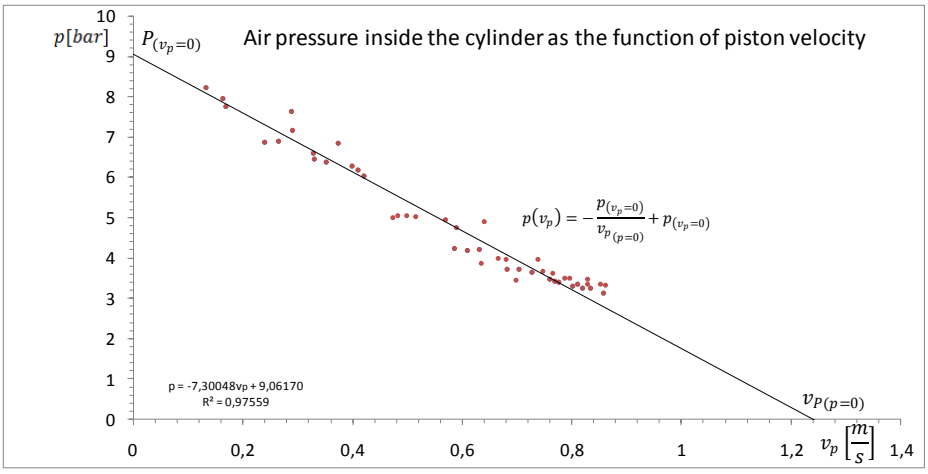

Figure 4. Air pressure inside the cylinder as the function of piston velocity magnitude

The figure represents that the relation between air pressure and piston velocity magnitude can be considered as linear. The intersections of the fitted line with the p and v_p axes serve as input parameters of the computer program.

4. DESCRIPTION OF THE COMPUTER PROGRAM

The first part of the Excel [1] program (see columns *A-I*, *Figure 5*) is for the input of technical parameters.

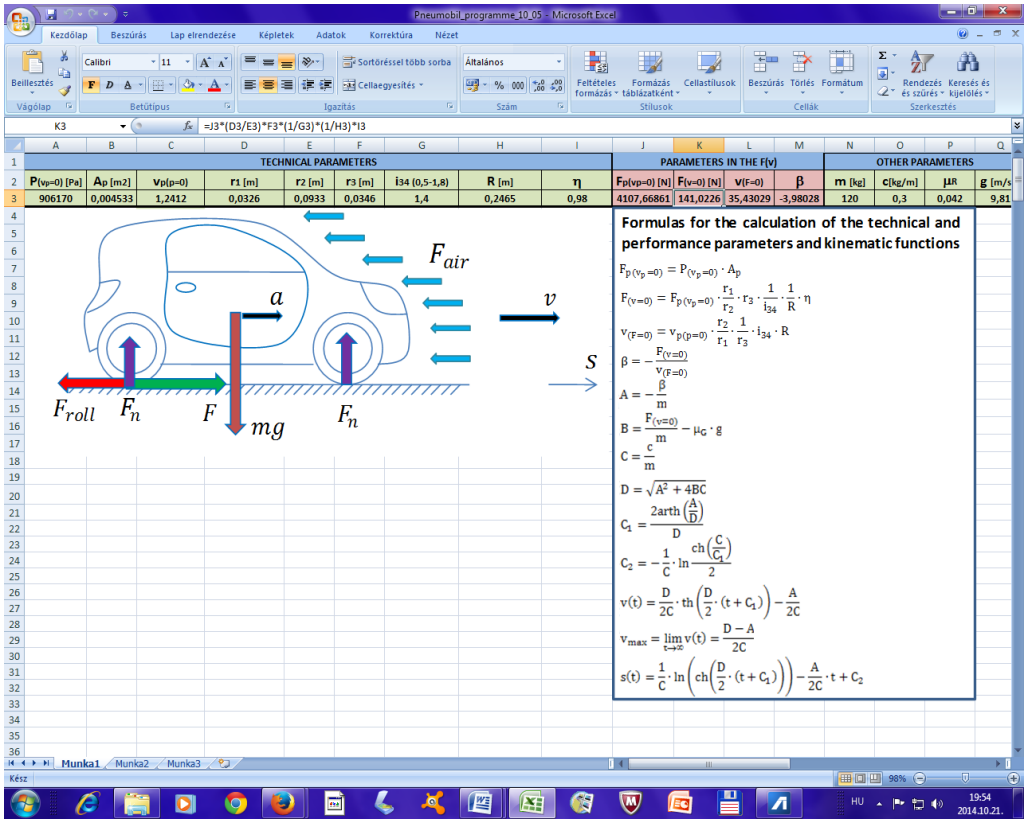

Figure 5. The Excel program (columns A- M)

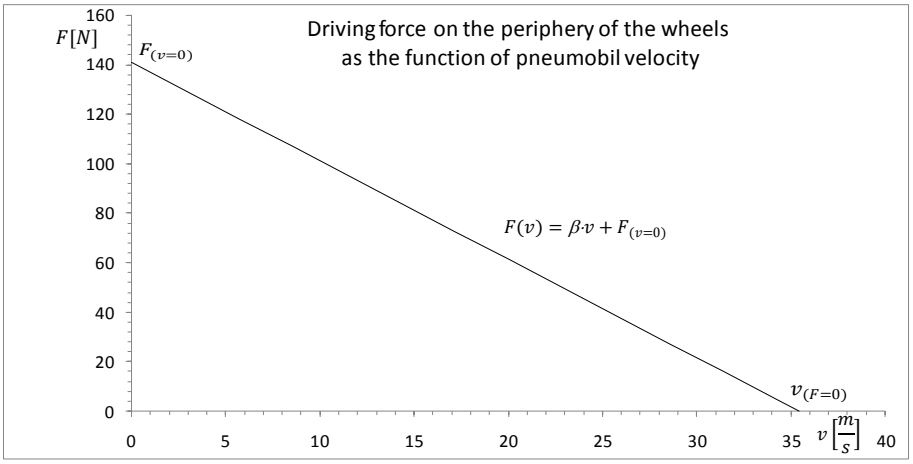

Figure 6. Driving force on the periphery of wheels as the function of pneumobil velocity

These parameters are the intersection of the $p(v_p)$ function with the p and v_p axes (see Figure 4), effective piston area (A_p), radius of sprocket 3, 6 and 7 (r_1, r_2, r_3, Figure 2), gear ratio in the internal gear hub (i_{34}), radius of driven wheels (R), efficiency of driving (η).

The second part of the program (see columns *J-M*, *Figure 5*) calculates the force on the zero velocity piston ($F_{p(v_p=0)}$) which is exerted by the compressed air in the cylinder, the intersection of the $F(v)$ function with the F and v axes (Figure 6) and the slope of the $F(v)$ function (β).

The third part of the program (see columns *N-Q*, *Figure 7*) is for the input of other necessary constants and parameters.

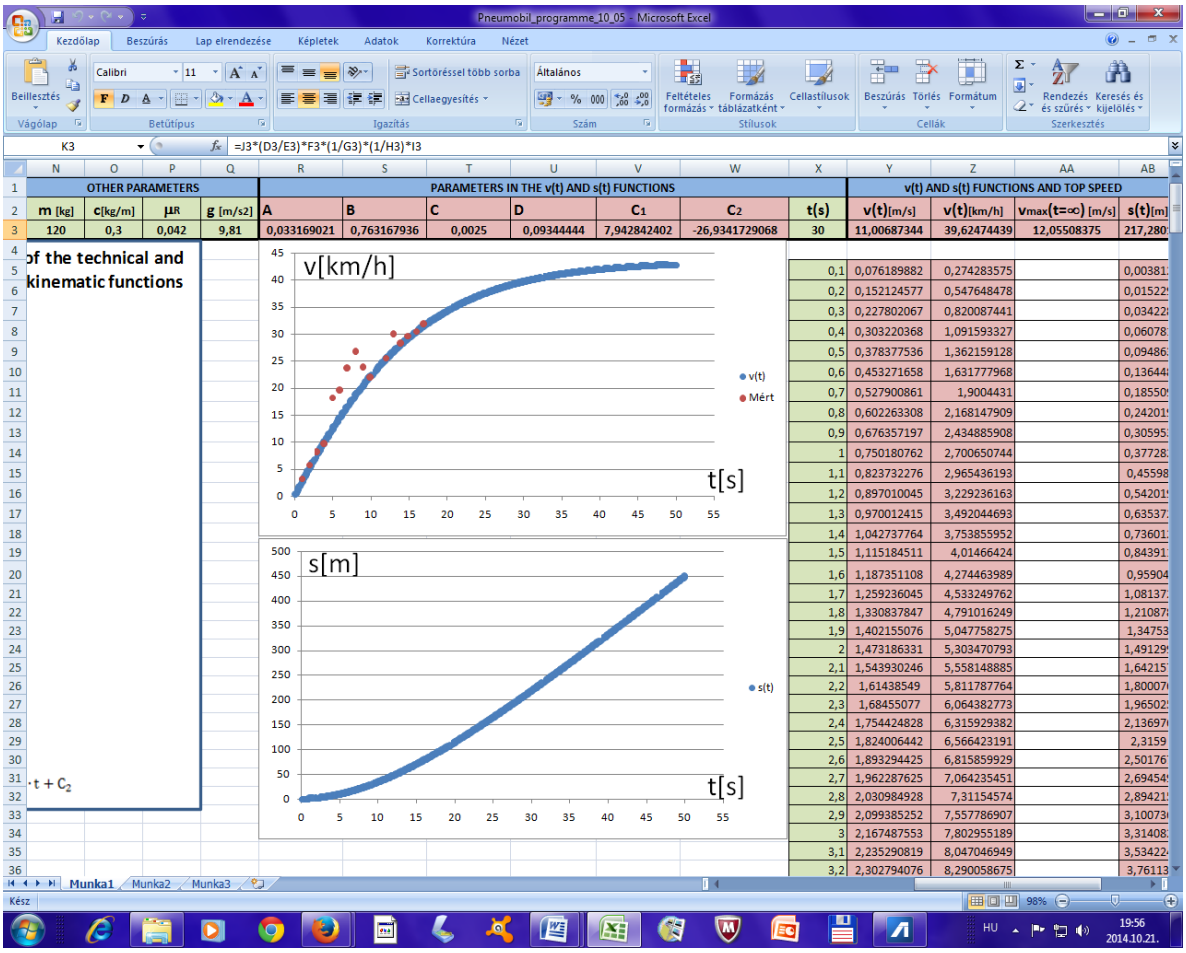

Figure 7. The Excel program (columns N-AB)

These constants and parameters are: total mass of the pneumobile (m), coefficient of air and rolling resistance (c, μ_R), magnitude of gravitational acceleration (g).

The fourth part of the program (see columns *R-AB*, *Figure 7*) calculates the values of the A, B, C, D, C_1 and C_2 constants in the velocity-time $v(t)$ and covered distance-time $s(t)$ functions (providing that the vehicle starts from rest) and also the reached speed and covered distance within running time t, finally the top speed of the vehicle (v_{max}). For the determination of the $v(t)$ and $s(t)$ functions we solved the differential equation of the motion of the pneumobile. Before solving the equation we had examined whether the tyres will slip

on the surface of the road when the vehicle starts from rest. The tyres will roll without slipping if the inequality bellow is true:

$$F_{(v=0)} \leq \mu_0 \cdot m \cdot g \tag{1}$$

In the above equation μ_0 is the coefficient of static friction. Provided that the road has a dry asphalt surface ($0.5 \leq \mu_0 \leq 0.8$) we got that the tyres won't slip.

Figure 5 shows the forces which act on the vehicle. The formulas of driving force, air and rolling resistance are the following [2]:

$$F = F_{(v=0)} + \beta \cdot v, \quad F_{air} = c \cdot v^2 = c \cdot \dot{s}^2, \quad F_{roll} = \mu_R \cdot F_n = \mu_R \cdot m \cdot g \tag{2}$$

Newton's second law of motion for the pneumobile is as follows:

$$F - F_{air} - F_{roll} = m \cdot a = m \cdot \dot{v} \tag{3}$$

Thus the differential equation of the motion is the following:

$$F_{(v=0)} + \beta \cdot v - c \cdot v^2 - \mu_R \cdot m \cdot g = m \cdot \dot{v} \tag{4}$$

$$-\frac{c}{m} \cdot v^2 + \frac{\beta}{m} \cdot v + \frac{F_{(v=0)}}{m} - \mu_R \cdot g = \dot{v} \tag{5}$$

Introducing the following constants:

$$A = -\frac{\beta}{m}, \quad B = \frac{F_{(v=0)}}{m} - \mu_R \cdot g, \quad C = \frac{c}{m}, \quad D = \sqrt{A^2 + 4BC} \tag{6}$$

$$-\frac{c}{m} \cdot v^2 + \frac{\beta}{m} \cdot v + \frac{F_{(v=0)}}{m} - \mu_R \cdot g = \dot{v} \tag{7}$$

$$-C \cdot v^2 - A \cdot v + B = \dot{v} \tag{8}$$

The differential equation is separable:

$$dt = \frac{1}{-C \cdot v^2 - A \cdot v + B} dv \tag{9}$$

Solving the differential equation we get the $v(t)$ function of the pneumobile:

$$\mathrm{v(t)} = \frac{\mathrm{D}}{2\mathrm{C}} \cdot \mathrm{th}\left(\frac{\mathrm{D}}{2} \cdot (\mathrm{t} + \mathrm{C_1})\right) - \frac{\mathrm{A}}{2\mathrm{C}} \tag{10}$$

The s(t) function comes from the v(t) function by integration:

$$\mathrm{s(t)} = \frac{1}{\mathrm{C}} \cdot \ln\left(\mathrm{ch}\left(\frac{\mathrm{D}}{2} \cdot (\mathrm{t} + \mathrm{C_1})\right)\right) - \frac{\mathrm{A}}{2\mathrm{C}} \cdot \mathrm{t} + \mathrm{C_2} \tag{11}$$

The C_1 and C_2 constants are determined using the $s(0) = 0$ and $v(0) = 0$ initial values. In this case the formulas for the constants are the following:

$$C_1 = \frac{2\text{arth}\left(\frac{A}{D}\right)}{D}, \quad C_2 = -\frac{1}{C} \cdot \ln \frac{\text{ch}\left(\frac{C}{C_1}\right)}{2} \tag{12}$$

The top speed is calculated with the following formula:

$$v_{max} = \lim_{t \to \infty} v(t) = \frac{D-A}{2C} \tag{13}$$

5. CONCLUSIONS

The presented computer program is capable of the calculation of the performance parameters of pneumobiles from their other technical parameters. Reached speed and covered distance within a given period of time and also the top speed of the vehicles can be calculated. Moreover, the optimal values of the technical parameters (such as the optimal gear ratio in the chain drive and in the internal gear hub) can be determined indirectly. The minimum length of time in which the vehicle can cover a given distance can also be calculated providing that the vehicle starts from rest. Thus the program is a useful help for designers of pneumobiles, and a useful tool to predict the performance of a given model on the competition.

6. REFERENCES

[1] **WALKENBACH J.:** *Excel 2003 Bible,* Wiley Publishing Inc., Indianapolis, Indiana, 2003, ISBN 0764539671.
[2] **BUDÓ Á.:** *Mechanika,* Nemzeti Tankönyvkiadó, Budapest, 1994, ISBN 9631859703.

INTERNATIONAL SCIENTIFIC CONFERENCE ON
ADVANCES IN MECHANICAL ENGINEERING
PROCEEDINGS

DESIGN OF THE STATOR FRAME AND AIR COMPRESSOR DRIVE FOR REPLACING THE INTERNAL COMBUSTION ENGINE OF THE IVECO 150E EUROCARGO HARD-PRESS GARBAGE TRUCK

[1]TIBA Zsolt, Dr., [2]KERTÉSZ József, B.Sc.

[1,2]University of Debrecen, Faculty of Engineering,
4028 Debrecen, Ótemető Street 2-4
[1] tiba@eng.unideb.hu, [2] kertesz_jozsef@eng.unideb.hu

Abstract: *A garbage truck is powered by diesel engine. The diesel engine may be replaced by an electric motor. In this paper we show the stator frame construction and the implementation of the air compressor drive. The rebuilding is supported by the GOP-1.1.1-11-2012-0617 Economy Developing Operative Programme implemented at the Electrical Engineering and Mechatronics Department, Faculty of Engineering, University of Debrecen.*

Keywords: *stator frame, bracket support, electric drive*

1. INTRODUCTION

In the urban area when collecting garbage, the average speed of the vehicle is approximately 3-4 km/h, due to the non-stationary operation. If the solid waste treatment facility situates close to the urban area, inside the operating range of an electrical vehicle, it is expedient to replace the internal combustion engine of the truck by electric motor and Lithium-chloride battery.

The main features of the truck powered by 6 cylinders 5.88 litres capacity diesel engine (see Fig. 1) are the following [1]:

- Engine: Iveco Tector
  - P 217/160 [PS/kW]
  - n 2700 [min^{-1}]
  - M 680 [Nm] (1200 min^{-1} – 2100 min^{-1})
- Gearbox: ZF 6S700 Manual
- Gear ratios:
  - / 1^{st} = 6.02 / 2^{nd} = 3.32 / 3^{rd} = 2.07 / 4^{th} = 1.40 / 5^{th} = 1.00 / 6^{th} = 0.79 /
- Geared speed: 122 km/h
- Differential: Meritor MS 10-164 Hypoid, ratio: 4.56
- Maximum bodyload: 150 kN
- Gradeability: 25%
- Tyres: 285/70R19.5
- Rolling diameter: 895 mm
- Deflection angle of the U joints in stationary state: 4^{o}

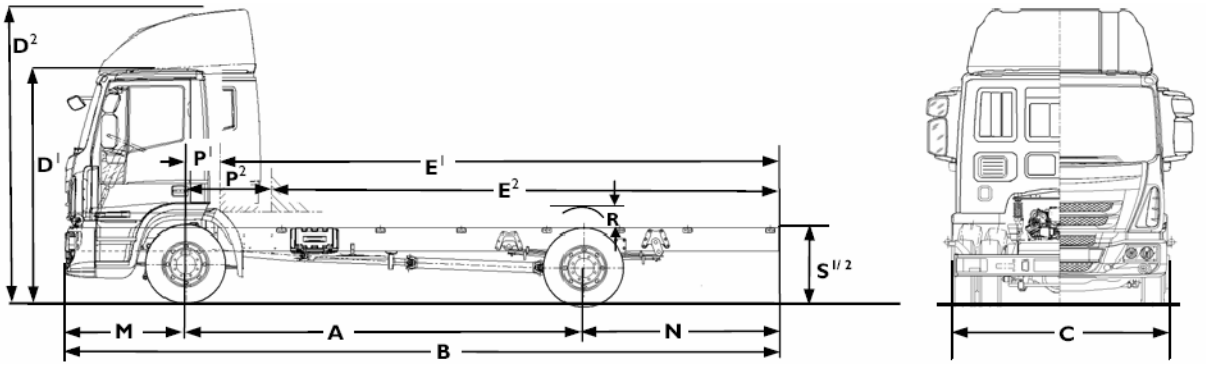

Figure 1. IVECO 150E Eurocargo

2. DYNAMICS OF LINEAR MOTION

The tractive force of the vehicle has to overcome the total running resistance at a given vehicle speed. The rest of it may be utilized for speed-up (acceleration).
The equation of equilibrium of tractive force is as follows:

$$F_{tr} = F_w + F_{acc} \tag{1}$$

where:

$$F_w = F_R + F_D + F_G \tag{2}$$

- F_w total rolling resistance
- F_R rolling resistance, F_D aerodynamic drag, F_G gradient resistance

2.1.Required torque of the universal joint shaft

The maximum required torque of the universal joint shaft is arising when ascend gradient. With the maximum bodyload the vehicle according to its specification has to overcome at least a gradient of 14^o (it corresponds to 25% gradeability).
The gradient resistance is calculated as:

$$F_G = G\sin\alpha \approx 36kN \tag{3}$$

The required torque of the driven wheel:

$$M_{wheel} = F_G R_{wheel} \approx 16kNm \tag{4}$$

The maximum required torque of the universal joint shaft:

$$M_{shaft\ req.} = \frac{M_{wheel}}{i_{diff}} \approx 3.5kNm \tag{5}$$

2.2. Determining the power requirement of the electric motor

The electric motor power requirement depends on whether a transmission is applied or not.

- If transmission is applied, the torque requirement on the shaft may be satisfied by appropriate choosing of the gear ratio. The motor power may affect the maximum speed of the vehicle.
- If there is no transmission applied, and the electric motor is connected directly to the universal joint shaft, the torque required has to be produced by the electric motor.

After considering the vehicle dynamic requirements of the truck, the necessary three-phase star connected electric motor parameters are the following:

$P = 110kW$, $U = 350V$, $n = 2880\,\mathrm{min}^{-1}$,
$M_{nom} = 320Nm$
$M_{\max} = 10M_{nom} = 3.2kNm$

(in the rpm range from 0 to 2880 min^{-1}, with frequency control, see Fig. 3)

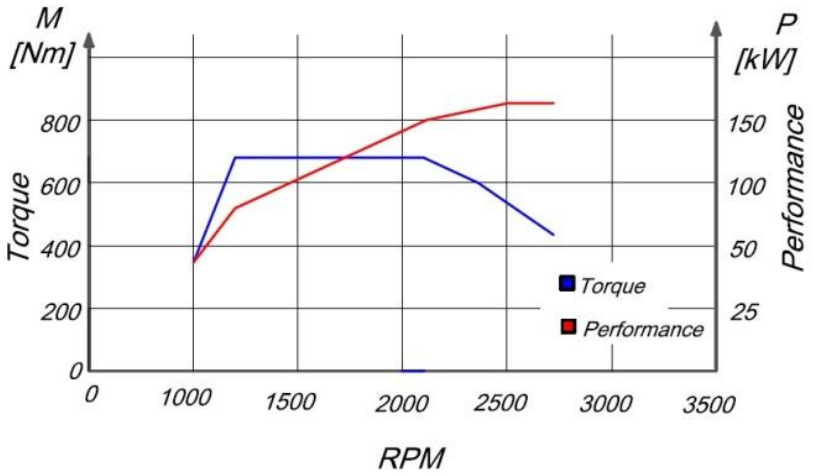

Figure 2. Engine characteristic

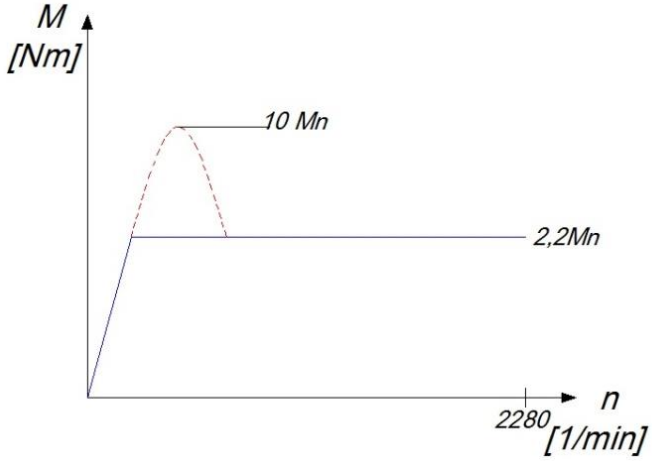

Figure 3. Electric motor characteristic

3. STATOR FRAME CONSTRUCTION

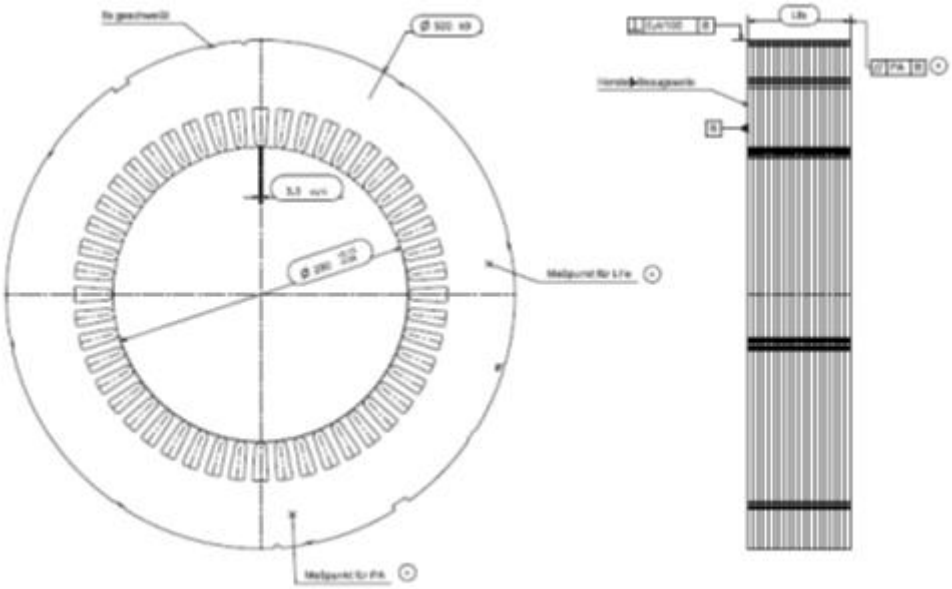

Figure 4. Stator packet

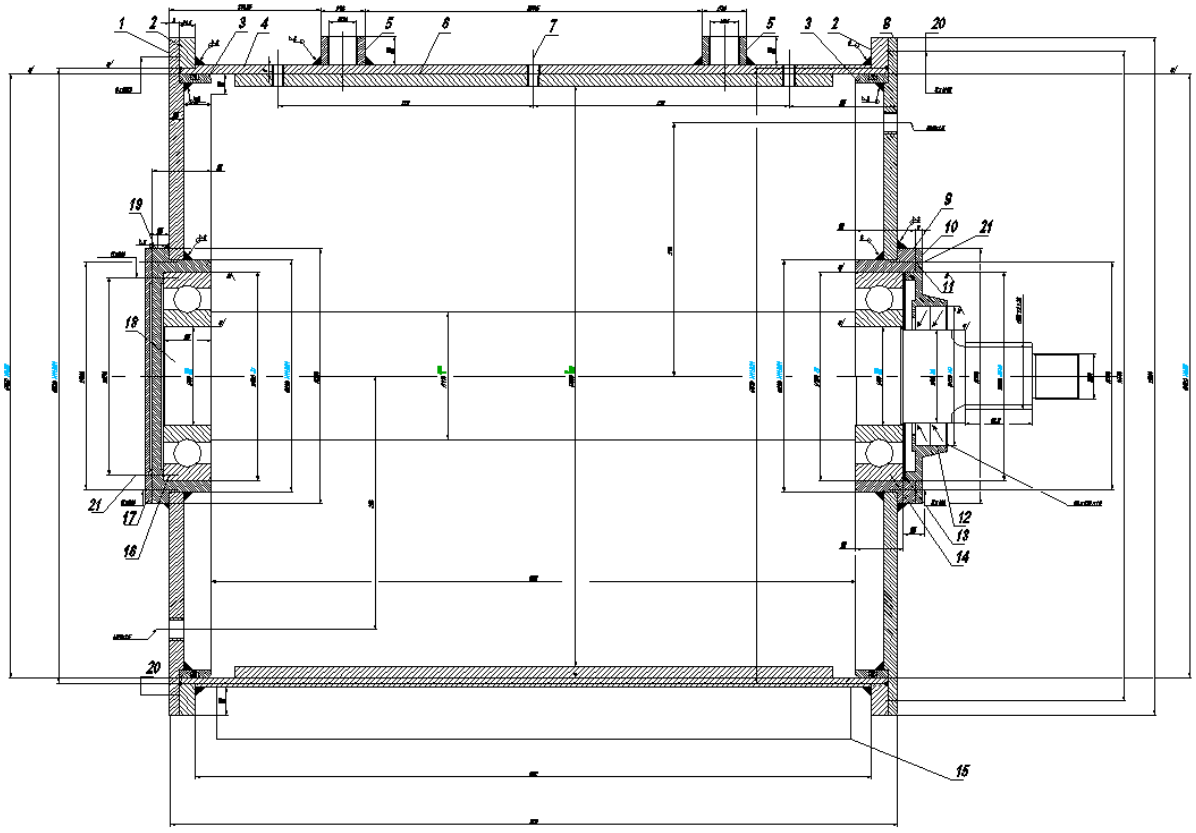

Figure 5. Stator frame construction

The stator packet (see Fig. 4) and the rotor are produced by the Kienle und Spiess GmbH. The shaft for the rotor with the bearing and sealing system and the stator frame made of 10 mm gauge number rolled steel were constructed at the department of mechanical engineering, see Fig. 5.

The electric motor is connected directly to the U joint shaft at the joint deflection angle of 4^{o}, see Fig. 6 [2].

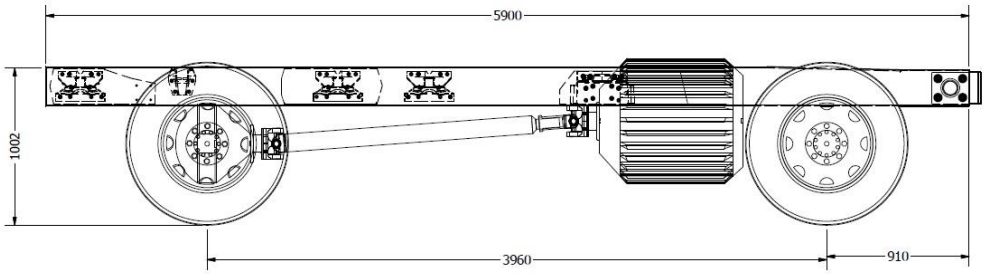

Figure 6. Electric motor installation

4. AIR COMPRESSOR DRIVE

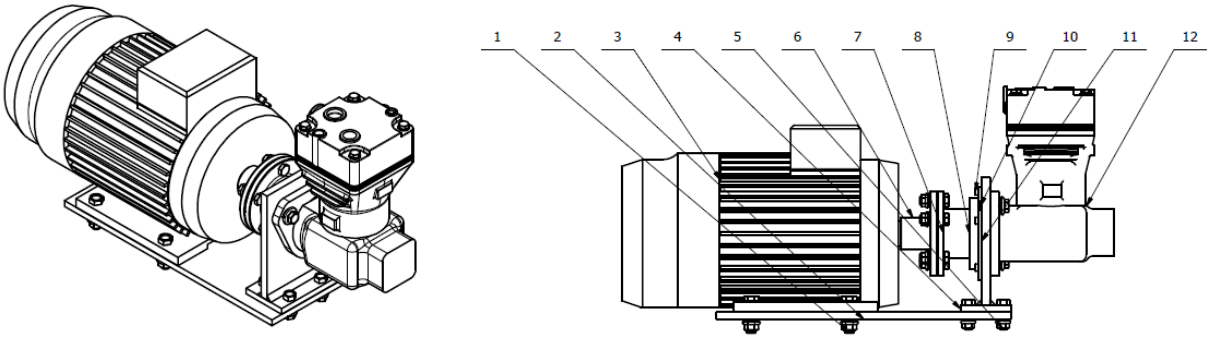

Figure 7. Pump drive

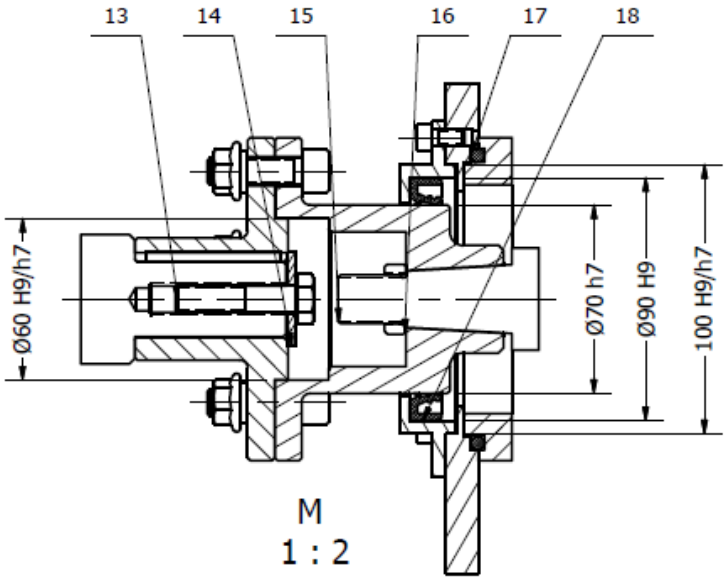

Figure 8. Disc coupling and the pump house sealing

The air compressor supplies high pressure air to the steering unit of the truck. It was attached to the ICE block and driven by gear drive. The lubrication of the piston pump was provided by the ICE lubrication system with circulating oil. After replacing the ICE by electric motor, we had to implement the driving and lubrication of the pump applying only electric motor. The pump is fixed to a bracket and sealed with it, see Fig. 7, Fig. 8, and driven by a 5kW electric motor through a disc coupling. The cooling of the pump is effected by a fan.

5. CONCLUSIONS

The rebuild of the IVECO 150E Eurocargo Hard-Press Garbage Truck supported by the GOP-1.1.1-11-2012-0617 Economy Developing Operative Programme covers the replacing the ICE by electric motor. For this special task the stator packet and the rotor may be ordered however the stator frame has to be designed. When replacing the ICE, all of the auxiliary drive of it must be implemented like air compressor and the air compressing pump. The air compression pump was driven by belt drive originally without common lubrication with the ICE hence its drive with electric motor by belt drive can be implemented without redesign.

6. REFERENCES

[1] *IVECO Ltd. catalogue:* PD/RB/150E22Truck/01/10
[2] *VOITH High-Performance Universal Joint Shafts Products Catalogue*

INTERNATIONAL SCIENTIFIC CONFERENCE ON
ADVANCES IN MECHANICAL ENGINEERING
PROCEEDINGS

ZIGBEE BASED WIRELESS SENSOR NETWORKS

VARGA Attila K.

Department of Automation and Infocommunication
Institute of Electrical Engineering
Faculty of Mechanical Engineering and Informatics
University of Miskolc
varga.attila@uni-miskolc.hu

Abstract
Today, several wireless communication standards are available in medium and high-speed data for voice, image, video, and PC networks. Wireless network standards have extended over the years. At the end of the 90s, it became necessary to create an organization that deals with the development of global, open, reliable, cost-effective, low-power wireless networking solutions in the field of automation. Similar standards were already in place, but these solutions focused only on high data speed and battery performance, which did not really satisfy the market needs.

Keywords: *wireless, sensor networks, ZigBee, mesh, routing.*

1. INTRODUCTION

A solution was needed that focused on the following aspects:

- Wide Area Networks (many devices, geographically large extent), which are capable of reliable and safe operation for many years without of human intervention,
- High-capacity batteries (to be operated for several years by using either a pair of AA batteries) with low infrastructure cost (low cost devices and installation) and small size,
- Relatively low data rates,
- Standardized protocol that allows products from different manufacturers to work together.

In order to harmonize these objectives was established in 2002, the ZigBee Alliance, to which joined more than 220 well-known companies. The organization's slogan: "It's wireless control", which is clear from the real needs of end users. The ZigBee Alliance created such a technology, which provides intelligent, wireless communication, can be easily adapted in the field of automation and monitoring through low-cost infrastructure. The ZigBee specification [1] is based on the IEEE 802.15.4 wireless standard, which describes WPAN networks. ZigBee uses the ISM radio band (2.4 GHz), and provides a self-organizing ad-hoc network with high throughput and low latency capacity for network devices operating in lower cycle (eg. Sensors).

2. ZIGBEE VS. TRADITIONAL WIRELESS STANDARDS

ZigBee application profiles can be manufacturer specific and public as well. The manufacturer-specific profiles operate as a closed network, so they are tested for such

purposes. The public application profiles tested in cooperation with other ZigBee products. In this case the cooperation (interoperability) is tested. The two profiles are shown in Figure 1. The traditional technologies focus on the transfer of large amounts of data streams over the Internet. ZigBee perform simple tasks such as lighting control or sending temperature readings.

ZigBee is designed for many years of operation. We meet several forms of wireless communication [2] in our everyday life. ZigBee networking standard eliminates the problems of other wireless solutions. While such standards provide higher data rates, the ZigBee targeted low data rate. The goal was to create radios operating in low data rate and short-range, low-power, low complexity network system. This concept enables the creation of wireless devices for that Bluetooth, Wi-Fi, Wi-Max, Wireless USB and other standards did not provide an adequate solution.

(cooperation) (interoperability)

Figure 1. Cooperation and interoperability in ZigBee wireless networks

The IEEE 802.11 standard is practically a family. The IEEE working in 802.11.ba 2.4GHz band (as well as Bluetooth and ZigBee), provides high data rate (11 Mbps) through a wireless Internet access, and is typically used within 30 to 100 meters range. Bluetooth provides a medium data rate (less than 3 Mbps) and suitable for communication within 2-10 meters. ZigBee provides the lowest data rate, but long battery life.

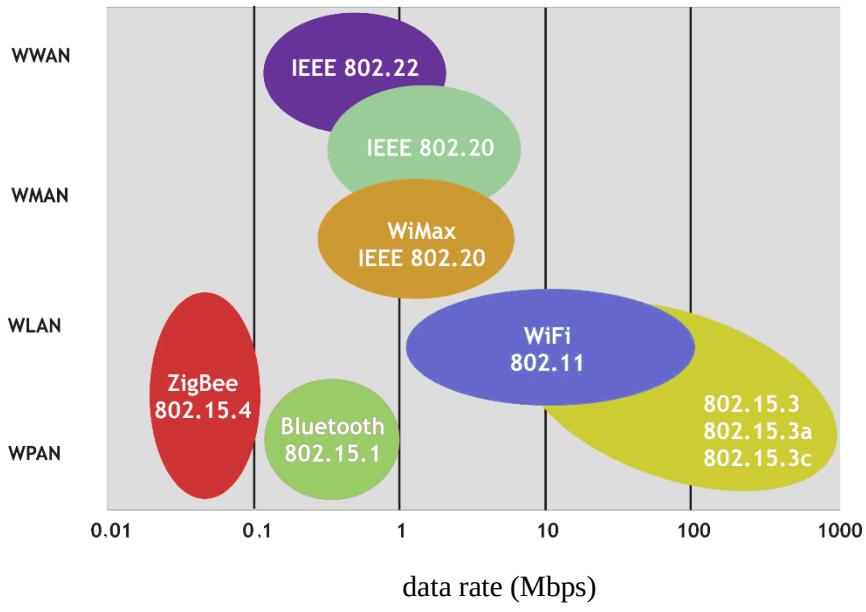

Figure 2. Wireless communication standards

ZigBee has low speed for wireless personal area networks (LR-WPAN) where text-based transmission is relevant (machine to machine communication). Bluetooth has been regarded as a mature standard, a lot of hardware and software support. ZigBee is a reasonable choice for low power consumption and complex ad-hoc network structures. Bluetooth provides communication between laptops, PDAs, phones and focuses on replacement of wiring. ZigBee is a low power consumption and small package solutions for dealing with the data, while Bluetooth has a higher transmitting power consumption and is suitable for larger packages. ZigBee devices are connected to rapidly exchange information and disconnected from the network back to a deep sleep state, reaching a very long battery life. A Bluetooth device requires about 100 times more energy for the same operation than a ZigBee based device. Compared to Bluetooth, in ZigBee network a larger number of participants can be served at a greater distance from each other.

Table 1. Comparison of ZigBee, WiFi and Bluetooth

Aspects	ZigBee	WiFi	Bluetooth
standard	802.15.4	802.11a,b,g	802.15.1
application	automation, control	Web, e-mail, video	replacement of cableing
data rate	50 - 60 kbyte	> 1 Mbyte	> 250 kbyte
battery lifetime	> 1000	1 -5	1 -7
network size	65535	32	7
bandwith (kb/s)	20 - 250	11000	720
transmission distance	100+ m	100 m	10 m
advantage	reliability, performance, cost	data rate, flexibility	cost, comfortable

Development of a communication network provides the basic concept of the network layer structure. Each layer is responsible for a network function. Layers normally send only data and commands to the layer above or below it. The organization of the network into layer has a number of advantages. For example, if the protocol changes over time, it is much easier to remove or modify the layer, which is affected by the change, as if removing the entire protocol. In addition, in case of application development the lower layers of the protocol are independent of the application, so that applications can be obtained from various companies, and changes can be made when the application is inserted into the network.

3. ROLES AND TYPES OF ZIGBEE DEVICES

ZigBee wireless network devices can be classified into two categories: full-function devices (Full-Function Device - FDD) and limited-function devices (Reduced-Function Device - RFD). An FDD can serve all tasks and can play any role in an IEEE 802.15.4 network [3], while an RFD device has limited capabilities. For example, an FDD able to communicate with any other device, but a device RFD can only communicate with FFD devices. RFD devices perform simple tasks, such as turn on or off a light. For this reason, an

RFD device energy consumption and memory size is less than an FFD device. Different device classes enable applications with optimal tool selection and reduction of cost. FFD is a network device that can play three different roles: coordinator, PAN coordinator, router, or a device. The coordinator is an FFD device to transfer messages. If the coordinator controls over a personal area network (PAN) too, then it is a PAN coordinator. Simply talking device if there is no role of coordinator in the network. The coordinator initiates and controls the network devices. The Coordinator stores all information about the network. The router expands the coverage area of the network, and is dynamically searching for routes avoiding network barriers. Routers can connect to the coordinator or other routers.

4. ZIGBEE'S SELF-ORGANIZING SELF-REPAIRING PROPERTIES

A ZigBee network can be established when devices are active. For example, in a mesh network when an FFD device wants to communicate with ZigBee coordinator becomes the first, after which other devices can connect to the network by sending a connection request. As additional monitoring is not required to create a network, ZigBee networks can operate as a self-organizing network. If you create a mesh network, sending a message can be solved in several ways. Of course, the selection of the most optimal way to deliver the message is the main goal. In this case, if a router is not working properly, for example because of the weak elements, or something is blocking the path of the message, the network selects an alternative route. This is called the ZigBee mesh network self-healing ability. ZigBee routing algorithm is based on "distance vector" [4]. To do this, all suitable route search device has a routing table. This includes both the logical distance to the destination, and the path to the destination address of the next router. The device (A) initiates a process of discovery of a route seeker broadcast command before the target device (B) sends back a route reply. Devices provide multiple paths algorithm. You may find that a device cannot establish a route, the route will take over search for the ZigBee coordinator, which has a more hierarchical path. In some cases, all the devices on the network can send data to the so-called aggregator. This occurs when multiple devices are looking for a device. Large systems, it is possible that the generator does not include the path to all the participants..

5. CONCLUSIONS

Traditional technologies transfer of large amounts of data streams over the Internet. Wireless standards used in our everyday life, are only able to operate on battery power for some hours, while ZigBee is designed for many years of operation. Due to the low data rate property of ZigBee, it should not be used in such applications where the expected rate is 1 Mbps, . Therefore, for example, a wireless Internet connection or CD-quality wireless headset communication it is not suitable. As wireless communication designed to transmit or receive simple commands and gather information from sensors (eg. temperature, humidity), ZigBee is the most efficient and most cost-effective solution compared to Bluetooth and IEEE 802.11.b standards.

6. ACKNOWLEDGEMENTS

The research was carried out within the project TÁMOP 4.2.4 / 2-11-1-2012-0001 National Excellence Program, supported by the European Union and co-financied by the European Social Fund.

7. REFERENCES

[1] **ZIGBEE ALLIANCE:** *ZigBee Specification*, Version 1.0, ZigBee Document 053474r06, December 14th, 2004.

[2] **WILLIAM STALLING:** *Wireless Communication and Networks*, Fourth Edition, Pearson Publication Limited, 2004, pp. 39-118.

[3] **KOHVAKKA, M., KUORILEHTO, M., HÄNNIKÄINEN, M., & HÄNNIKÄINEN, T. D.:** *Performance analysis of IEEE 802.15.4 and ZigBee for large-scale wireless sensor network applications*. Proceedings of the 3rd ACM International Workshop on Performance Evaluation of Wireless Ad Hoc, Sensor and Ubiquitous Networks, Terromolinos, Spain, 2006, pp. 48-57.

[4] **RAN, P., SUN, M., ZOU, Y.**: *ZigBee routing selection strategy based on data services and energy-balanced ZigBee routing*. APSCC '06, December 2006, pp. 400-404.

STRUCTURAL ANALYSIS AND STATISTICAL EVALUATION OF A CLOSED-CELL METAL FOAM

[1]VARGA Tamás Antal, [2]MANKOVITS Tamás, Dr., [3]BUDAI István, Dr., [4]BALOGH Gábor, [5]GÁBORA András, [6]KOZMA István, [7]MANÓ Sándor, [8]KOCSIS Imre, Dr.

[1,2,4,5]Department of Mechanical Engineering, University of Debrecen, Debrecen, Hungary
[1]tomivarga27@gmail.com
[2]tamas.mankovits@eng.unideb.hu
[4]balogh.gabor@eng.unideb.hu
[5]andrasgabora@eng.unideb.hu

[3]Department of Engineering Management and Enterprise, University of Debrecen, Debrecen, Hungary
budai.istván@eng.unideb.hu

[6]Department of Material Sciences and Technology, Széchenyi István University, Győr, Hungary
kozma@sze.hu

[7]Orthopedic Clinic, University of Debrecen, Debrecen, Hungary
manos@med.unideb.hu

[8]Department of Basic Technical Studies, University of Debrecen, Debrecen, Hungary
kocsisi@eng.unideb.hu

Abstract
The development of an efficient procedure for 3D modeling and finite element simulation of metal foams is one of the greatest challenges to engineer researchers nowadays. Creating a 3D CAD model is alone a demanding engineering task due to its extremely complex geometry, and the proper finite element analysis process is still in the focus of research. The increasingly widespread application of the metal foams, e.g. in vehicle and medical industry, requires this knowledge in the design phase. A closed-cell metal foam is studied using different analyzing methods where the aim is to collect information about the composition and geometry (structure) that is satisfactory for later research. Using statistical methods, microscopic, X-ray and surface analyzing studies on the specimens produced according to the concerning standard are evaluated. The main goal of this part of the project is to obtain structural information and to determine the homogeneity or the in-homogeneity property of the metal foam specimens taken from different locations.

Keywords: *metal foam, composition analysis, quantitative image analysis, statistical evaluation*

1. INTRODUCTION

Metal foams are relatively new and advanced materials with high stiffness to weight ratio, good thermal conductivity, good acoustic insulation and excellent energy absorption

capability which make them ideal materials for a variety of applications [1-3]. Therefore, they have increasingly been employed for a wide range of applications, such as structural elements, automotive parts, sound and vibration absorbers or even biomedical implants [4-9]. Basically, the mechanical properties of metal foams are influenced by three dominating factors, namely the property of the solid phase, the relative density of the solid phase and the spatial arrangement, that is, the structure of the metal foam (cell distribution, cell shape). Knowledge of the structure property correlations in metal foams is required for optimizing its mechanical performance for a given application [10].

Although metal foams are popular, they are still not sufficiently characterized due to their extremely complex structure which is highly stochastic in nature. In the past few years, several researchers focused on the finite element modeling of metal foams with more or less success, but it is still one of the greatest challenges. Instead of modeling the complex internal structure directly, idealized structural approaches (unit cell, statistical models, etc.) are often used where the cells are represented by miscellaneous two- or three dimensional models according to the structure behavior [11-15]. A 3D model created with the help of X-ray tomography (beam model, voxel and tetrahedral element methods) [16,17] is another possibility. In detail, different numerical approaches for the simulation of metal foams were proposed [11-17].

To be able to prepare for the numerical simulation, extensive information is needed from the applied solid phase (density, Young's modulus) and from the metal foam structure (relative density, cell distribution, cell shape).

In this paper, a closed-cell aluminum foam is investigated. The aim of this research is the preparation for the finite element simulation of the metal foam under compression using a 3D CAD model. In order to reach this target, firstly, the applied solid aluminum was studied and the density and the Young's modulus were determined. Then a microscopic analysis of the metal foam was performed to determine the average cell size for obtaining the required size of the specimens according to the ISO 13314 [18]. Statistical analyses are done to select from the specimens with the same material properties for the further investigation. To provide information on the cell distribution, manual and digital quantitative image analyses were performed using macroscopic records from the specimen's surfaces. The results of the two image analyses were evaluated and compared.

2. METHODS

2.1. Investigation of the solid phase

The first step of the study was to compare the qualities of the used material with the data provided by the manufacturer. It is essential to do that since even small deviations can have a great influence on the subsequent finite element analysis. First, an X-ray analysis was carried out with a Hitachi Tabletop 3030 SEM microscope to which an EDX X-ray instrument was attached. The image made by this device is presented in *Figure 1*.

The density of the tested material was calculated and a compression test was performed to determine the modulus of elasticity. The compression test was carried out using an INSTRON 8874 instrument. The commercial data [19] and the measured data of the investigated material (Durcalan F3S.20S Metal Matrix Composite) are included in *Table 1*.
Then, the SiC median particle size was determined at a magnification of x500 (*Figure 2*).

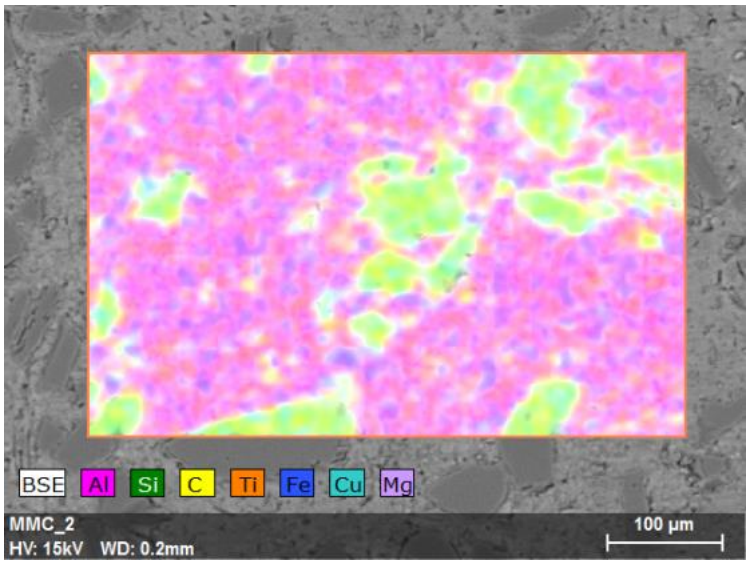

Figure 1. Composition analysis of the Duralcan F3S.20S MMC

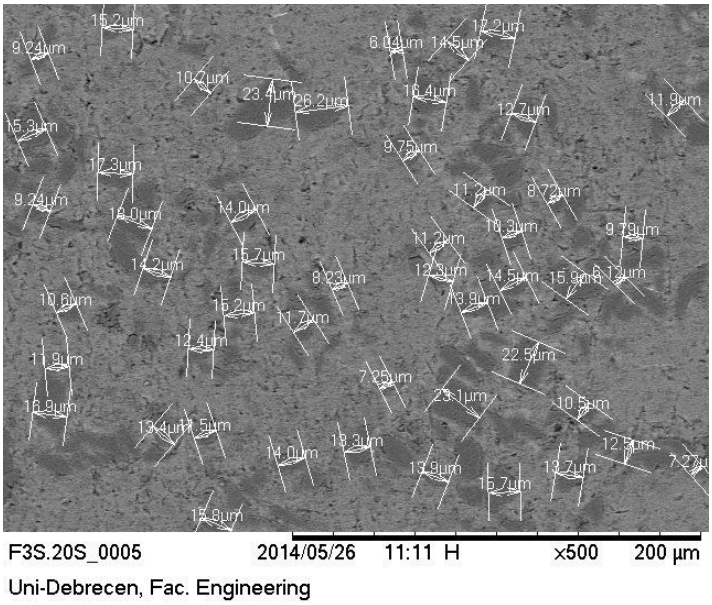

Figure 2. SiC median particle size determination

Table 1 Properties of the F3S.20S Metal Matrix Composite Duralcan

Properties	Commercial data [19]	Measurement
Density (kg/m^3)	2850.00	2875.12
Modulus of elasticity (*GPa*)	98.60	97.20
Si content (%)	9.30	9.21
Mg content (%)	0.55	0.53
Fe content (%)	0.11	0.11
Ti content (%)	0.10	0.98
Cu content (%)	0.01	0.01
SiC median particle size (*mm*)	12.80	13.24

2.2. Metal foam specimens

The specimens were created according to the ISO13314 [18] standard according to which the width of the lateral edge should be such that ten cells could be placed next to each other. Therefore, the median particle size had to be determined first. For the determination of the average cell size, a Hitachi Tabletop SEM microscope was used. An image of x30 enlargement was made in which the diameters of the cells are indicated (*Figure 3*).

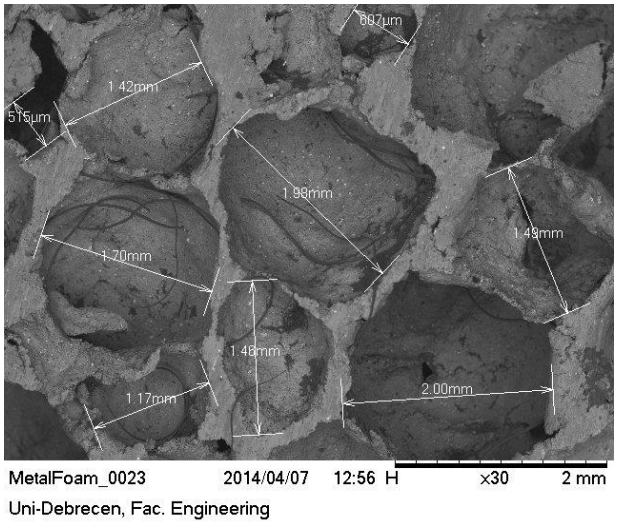

Figure 3. Measurement of the average cell size

In the study, three specimens were measured at three locations and the obtained average cell size was 1.33 mm. Then, the size of the specimens to be manufactured was determined according to the ISO standard as 14.5x14.5x14.5 mm. The specimen cut was carried out by a STRUERS Labotom-15, 16 pieces of test specimen were manufactured. Since the edge length of the specimens is not uniform, an range limit of 14.5 *mm*±1 *mm*=[13.5 *mm*, 15.5 *mm*] was made. The edge lengths of the specimens are presented in *Figure 4*, it can be seen that four specimens were out of the range, therefore, these were excluded from the further measurements.

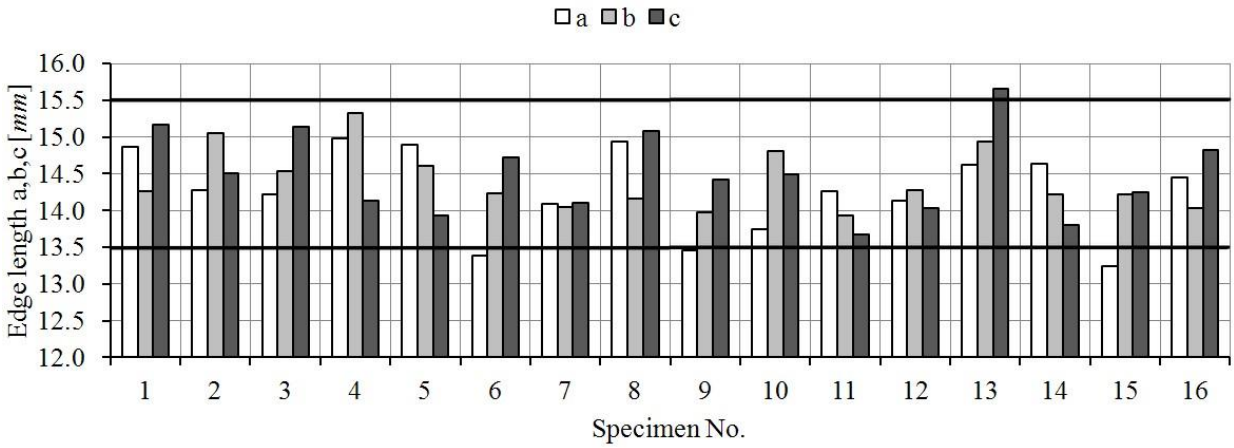

Figure 4. Edge lengths (a,b,c) of the specimens

2.3. Quantitative image analysis of the specimens

The next phase was the determination of the metal foam structure. The two methods used were area fraction analysis and line analysis. The area fraction analysis can be performed using a software, while line analysis can be done manually.
For the measurements, macro images had to be made about the edges of the metal foams as presented in *Figure 5*.

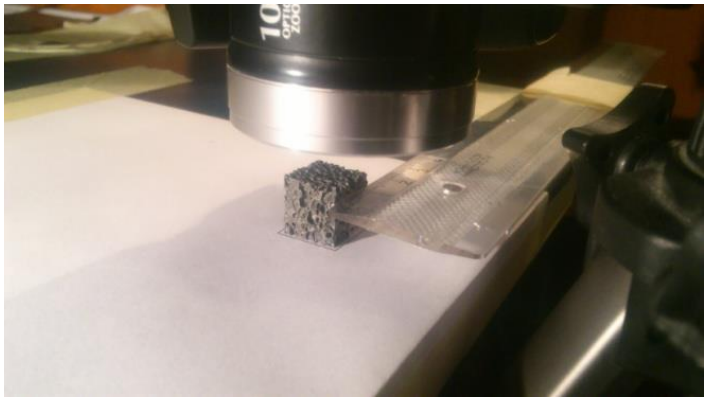

Figure 5. Preparing macroscopic picture for the area fraction and line analysis

2.3.1. Area fraction analysis

The macro images had to be modified so that the analysing software could process them, the steps of this are shown in Figure 6. After the modification of the pictures, the binaries were loaded into an image-analysing software, using which the edge density was determined.

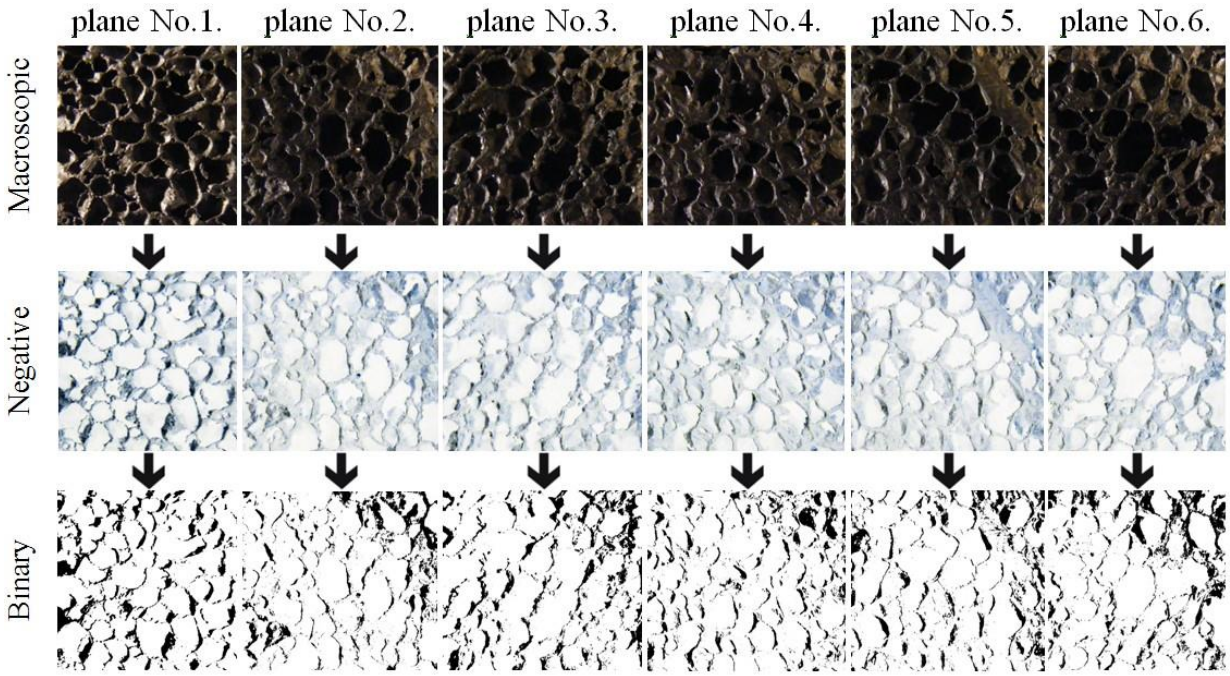

Figure 6. Process of the surface analysis

2.3.2. Line analysis

The line analysis was finished manually. The macroscopic pictures about the edges of the specimens were examined along 10 lines horizontally and vertically. A line analysis was determined so that the sum of the cells' sizes was divided by the edge lengths. This is a very precise though time-consuming method.

2.3.3. Comparison of the methods

In the case of metal foams, the second phase is air, so the volume ratio can be directly determined by weight measurement. This fact gives the opportunity to control the applied methods. The results of the weight measurement, the area fraction analysis and the line analysis can be seen in (*Figure 7*)

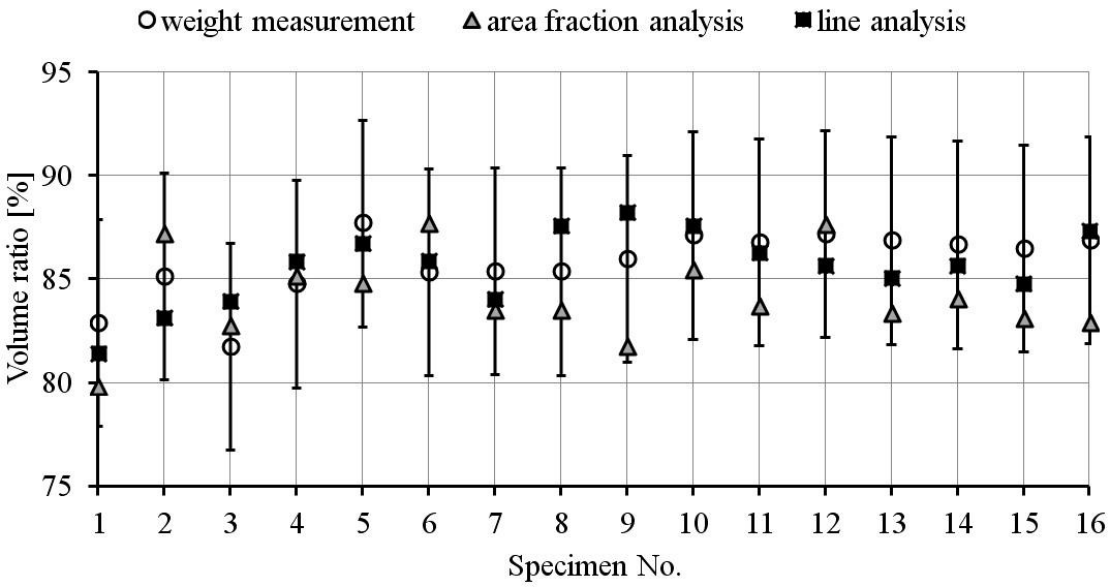

Figure 7. Volume ratio determined by the three methods

3. RESULTS AND CONCLUSION

In this paper a closed-cell aluminum foam was investigated. Considering the later finite element simulations, the relevant physical and mechanical properties of the solid phase were measured and the composition was also studied which was compared with the available commercial and literature data. The specimens cut from the metal foam were classified on the basis of the geometrical parameters.

Quantitative image analysis has also been done, which gives detailed information about the structure of the metal foam. The image analysis is also a useful tool for the determination of the volume ratio. The volume ratio, the specific quantity of foam materials, was derived by area fraction and line analysis as well. The two applied methods were compared. Although the line analysis is more accurate, it is much more time-consuming than the area fraction analysis. The results showed that the easily and rapidly performable area fraction analysis is sufficiently precise.

4. REFERENCES

[1] **ASHBY, M.F., EVAN, A.G., FLECK, N.A., GIBSON, L.J., HUTCHINSON, J.W., WADLEY, H.N.G.:** *Metal Foams: A Design Guide*. Butterworth-Heinemann, 2000.

[2] **CZEKANSKI, A., ATTIA, M.S., MEGUID, S.A., ELBESTAWI, M.A.:** *On the Use of a New Cell to Model Geometric Asymmetry of Metallic Foams.* Finite Elements in Analysis and Design, 41(13), 2005, pp. 1327-1340.

[3] **BANHART, J.:** , *Manufacture, Characterization and Application of Cellular Metals and Metal Foams.* Progress In Materials Science, 46(6), 2001, pp 559-632.

[4] **VENDRA, L.J., RABIEI, A.**: *Evaluation of Modulus of Elasticity of Composite Metal Foams by Experimental and Numerical Techniques*. Materials Science and Engineering: A, 527(7-8), 2007, pp. 1784-1790.

[5] **TUNCER, N., ARSLAN, G.**: *Designing Compressive Properties of Titanium Foams.* Journal of Materials Science, 44(6), 2009, pp. 1477-1484.

[6] **KÁDÁR, CS., CHMELÍK, F., RAJKOVITS, ZS., LENDVAI, J.**: *Acoustic Emission Measurements on Metal Foams.* Journal of Alloys and Compounds, 378(1-2), 2004, pp. 145-150.

[7] **DJEBBAR, N., SERIER, B., BOUIADJRA, B.B., BENBAREK, S., DRAI, A.:** *Analysis of the Effect of Load Direction on the Stress Distribution in Dental Implant*, Materials&Design, 31(4), 2010, pp. 2097-2101.

[8] **KASHEF, S., ASGARI, A., HILDITCH, T.B., YAN, W., GOEL, V.K., HODGSON, P.D.**: *Fracture Toughness of Titanium Foams for Medical Applications.* Materials Science and Engineering: A, 527(29-30), 2010, pp. 7689-7693.

[9] **MANKOVITS, T., TÓTH, L., MANÓ, S., CSERNÁTONY, Z.**: *Mechanical Properties of Titanium Foams*, a Review. Proceedings of the 1st International Scientific Conference on Advances in Mechanical Engineering, 10-11 October, 2013, Debrecen, Hungary.

[10] **SAADATFAR, M., MUKHERJEE, M., MADADI, M., SCHRÖDER-TURK, G.E., GARCIA-MORENO, F., SCHALLER, F.M., HUTZLER, S., SHEPPARD, A.P., BANHART, J., RAMAMURTY, U.**: *Structure and Deformation Correlation of Closed-cell Aluminium Foam Subject to Uniaxial Compresion.* Acta Materiala, 60(8), 2012, pp. 3604-3615.

[11] **HODGE, A.M., DUNAND, D.C.**: *Measurement and Modeling of Creep on Open-cell NiAl Foams.* Metallurgical and Materials Transactions A, 34(10), 2003, pp. 2353-2363.

[12] **HASAN, A.:** *An Improved Model for FE Modeling and Simulation of Closed Cell Al-Alloy Foams.* Advances in Materials Science and Engineering, Article ID 567390, 2010, 12 pages, doi:10.1155/2010/567390

[13] **KOU, D.P., LI, J.R., YU, J.L., CHENG, H.F.**: *Mechanical Behavior of Open-cell Metallic Foams with Dual-size Cellular Structure.* Scripta Materialia, 59(5), 2008, pp. 483-486.

[14] **FILICE, L., GAGLIARDI, F., UMBRELLO, D.:** *Simulation of Aluminium Foam Behavior in Compression Tests.* The Arabian Journal for Science and Engineering, 34(1), 2009, pp. 129-137.

[15] **MIEDZINSKA, D., NIEZGODA, T.:** *Initial Results of the Finite Element Analyses of the Closed Cell Aluminium Foam Microstructure under the Blast Load.* CMM-2011 Computer Methods in Mechanics, 9-12 May, 2011, Warsaw, Poland.

[16] **ADZIMAN, M.F., DESPHANDE, S., OMIYA, M., INOUE, H., KISHIMOTO, K.**: Compressive Deformation in Aluminium Foam Investigated Using a 2D Object

Oriented Finite Element Modeling Approach. Key Engineering Materials, 2007, pp. 353-358, 651-654.

[17] **JIROUSEK, O., DOKTOR, T., KYTYR, D., ZLÁMAI, P., FÍLA, T., KOUDELKA, P., JANDEJSEK, I., VAVRIK, D.**: *X-ray and Finite Element Analysis of Deformation Response of Closed-cell Metal Foam Subjected to Compressive Loading.* Journal of Instrumentation, 8 C02012, 2013, doi:10.1088/1748-0221/8/02/C02012

[18] *ISO 13314:2011* Mechanical Testing of Metals – Ductility Testing – Compression test for Porous and Cellular Metals.

[19] **CURLE, U.A., IVANCHEV, L.:** *Wear of Semi-solid Rheocast SiCp/Al Metal Matrix Composites.* Transactions of Nonferrous Metals Society of Chine, 20, 2010, pp. 852-856.

INTERNATIONAL SCIENTIFIC CONFERENCE ON
ADVANCES IN MECHANICAL ENGINEERING
PROCEEDINGS

SCALE-UP OF A JACKETED STIRRED TANK RECTOR

VENCZEL Gábor, M.Sc.

University of Miskolc, Department of Chemical Machinery
venczel@uni-miskolc.hu

Abstract
The small scale model experiments should be used for example in the initial phase of design of the stirred reactor. This article shows how to scale-up the experiment results, when must be taken of reactor heat transfer. The small scale equipment geometric similar to the large scale, but the determination of the process conditions are complicated.

Keywords: *scale-up, hear transfer, reactor, stirring, jacket*

1. INTRODUCTION

Scale-up problems for jacketed stirred reactor design are not always obvious. Problems involving chemical reactions, where kinetics and mixing interact, are often difficult to scale-up accurately. In a batch technology with an exothermic reaction, a cooling jacket around the outside of the reactor transfers heat away from the reactor. As the size of the reactor increases, the generated heat and the removable heat ratio is not equal. That is, as the diameter and height of the reactor increases, the surface area for heat transfer divided by the reactor volume decreases, and thus the reactor temperature increases.

2. METHODS

In the exothermic reaction, the component A is not involved in the reaction, it is only transfer medium. Component B is transformed to component C during the reaction. Energy balance of this process:

$$\frac{d(N_A \cdot H_A)}{d\tau} + \frac{d(N_B \cdot H_B)}{d\tau} + \frac{d(N_C \cdot H_C)}{d\tau} = \Delta H \cdot r_B \cdot V - Q \qquad (1)$$

where

- N_A moles of component A
- N_A, N_B moles of reactant B and C
- H_A, H_B, H_C enthalpy of A, B and C
- τ time
- ΔH heat of reaction
- r_B rate of reaction
- V volume of reactor
- Q transferred heat

The mass balances:

$$\frac{dN_A}{d\tau} = 0 \tag{2}$$

$$\frac{dN_B}{d\tau} = r_B \cdot V \tag{3}$$

$$\frac{dN_C}{d\tau} = -r_B \cdot V \tag{4}$$

Rate of reaction:

$$r_B = -k_o \cdot e^{\frac{-E}{RT}} \cdot C_B \tag{5}$$

where

- k_o pre-exponential factor
- E activation energy
- R ideal gas constant
- T temperature of reaction
- C_B concentration of reactant B, $C_B = N_C / V$

Conducting the operation of differentiation and substitution of the left side of equation (1):

$$\left\{N_A \cdot \frac{dH_A}{d\tau}\right\} + \left\{H_B \cdot r_B \cdot V + N_B \cdot \frac{dH_B}{d\tau}\right\} + \left\{H_C \cdot (-r_B) \cdot V + N_C \cdot \frac{dH_C}{d\tau}\right\} = \Delta H \cdot r_B \cdot V - Q \tag{6}$$

The transferred heat of the jacket:

$$Q = U \cdot A \cdot LMTD \tag{7}$$

The heat transfer coefficient:

$$U = \frac{1}{\frac{1}{h_R} + \frac{s}{\lambda} + \frac{1}{h_J}} \tag{8}$$

and Log Mean Temperature Difference:

$$LMTD = \frac{(T - T_{In}) - (T - T_{Out})}{\ln \frac{T - T_{In}}{T - T_{Out}}} \tag{9}$$

where

- A surface area for heat transfer
- h_R surface heat transfer coefficient inside the reactor (stirred side)
- h_J surface heat transfer coefficient outside the reactor (jacketed side)
- T_{in} inlet temperature of cooling liquid
- T_{Out} outlet temperature of cooling liquid

In case of stirred reactor with the heat transfer, the stirred side surface heat transfer coefficient - without phase change - calculated with the following equation:

$$Nu = C\,\mathrm{Re}^m\,\mathrm{Pr}^o\left(\frac{\eta}{\eta_w}\right)^p = \frac{h_R D}{\lambda} \tag{10}$$

where

- C,m,o,p constants
- Re Reynolds number, $\mathrm{Re} = \frac{nd^2\rho}{\eta}$
- Pr Prandtl number, $\mathrm{Pr} = \frac{\eta c_p}{\lambda}$
- d and D impeller and reactor diameter
- n a gitator speed
- η_w average dynamic viscosity of the stirred fluid
- η dynamic viscosity of the stirred fluid in the heat transfer surface
- λ heat conductivity of the stirred fluid
- c_p specific heat of the stirred fluid

The constants depend on the design of the impeller type, geometrical dimensions, etc. According to the literature [2] the exponents are the following in the case of jacketed vessels:

$$m = 2/3 \;\; o = 1/3 \;\; p = 0{,}14$$

The C constant in Eq. (10) takes into account all the geometrical effects. In case of jacketed vessels with turbine impeller and baffles $C = 0{,}73 - 0{,}16$ *(Re > 400)*, in propeller impeller without baffles C = 0,54 (Re > 10.000), in paddle impeller C = 0,36 – 0,50 (Re > 100.000).

Because of the goal of the scale-up, the ratio of the Nusselt numbers expressed. Assuming the similarity of the material properties in the small and large scale equipment:

$$\frac{Nu_L}{Nu_S} = \frac{h_L D_L}{h_S D_S} = \frac{(n_L d_L^{\,2})^{2/3}}{(n_S d_S^2)^{2/3}} \tag{11}$$

where *L* subscript represent the large scale equipment and *S* subscript represent small equipment.

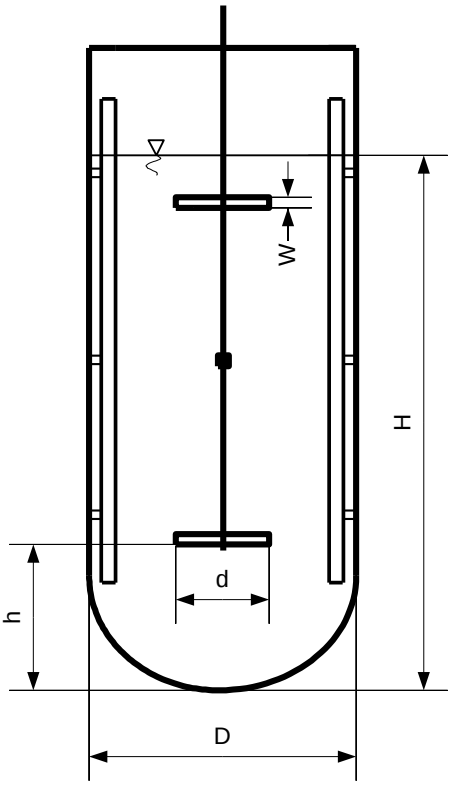

Figure 1. A stirred vessel dimensions

Take into account that small and the large scale are equivalent in geometric ratio (*d*~*D*):

$$\frac{h_L}{h_S} = \left(\frac{n_L}{n_S}\right)^{2/3} \left(\frac{d_L}{d_S}\right)^{1/3} \tag{12}$$

The effects of scale-up should be examined according to numerous criteria.

- equivalent of the power demand per unit volume:

$$\frac{N_L}{V_L} = \frac{N_S}{V_S} \tag{13}$$

The foundation of that is recognition about stirring efficiency and the stirring time proportion the power demand per unit volume. In stirring reactors usually turbulent flow occurred (where the impeller specific resistant is constant):

$$\frac{N}{V} \sim \frac{n^3 d^5 \rho}{d^3} = n^3 d^2 \rho \tag{14}$$

For a better overview of the scale-up ratio is: $k = d_L / d_S$

- Impeller speed: $n_L = k^{-2/3} n_S$
- Circumferential speed: $w_L = k^{-1/3} w_S$
- Reynolds number: $\mathrm{Re}_L = k^{4/3}\,\mathrm{Re}_S$
- Surface heat transfer coefficient: $h_L = k^{-1/9} h_S$
- Heat transfer per unit volume: $\frac{Q_L}{V_L} = k^{-10/9}\frac{Q_S}{V_S}$

- equivalent of the power demand per unit volume:

$$w_L = w_S \tag{15}$$

Obviously this criterion can be applied if the efficiency of the stirring is proportion with the circumferential speed in this case these examined parameters are:

- Impeller speed: $n_L = k^{-1} n_S$
- Reynolds number: $\mathrm{Re}_L = k\,\mathrm{Re}_S$
- Surface heat transfer coefficient: $h_L = k^{-1/3} h_S$
- Heat transfer per unit volume: $\frac{Q_L}{V_L} = k^{-4/3}\frac{Q_S}{V_S}$
- Power deamand per unit volume: $\frac{N_L}{V_L} = k^{-1}\frac{N_S}{V_S}$

- equivalent of the surface heat transfer coefficiants:

$$h_L = h_S \tag{16}$$

The left side of deducted basic equation (12) to surface heat transfer coefficient is 1 and the impeller speed can be determined, furthermore the equations can be calculated:

- Impeller speed: $n_L = k^{-1/2} n_S$
- Circumferential speed: $w_L = k^{1/2} w_S$
- Reynolds number: $\mathrm{Re}_L = k^{3/2}\,\mathrm{Re}_S$
- Heat transfer per unit volume: $\frac{Q_L}{V_L} = k^{-1}\frac{Q_S}{V_S}$
- Power demand per unit volume: $\frac{N_L}{V_L} = k^{1/2}\frac{N_S}{V_S}$

- equivalent of the heat transfer per unit volume:

$$\frac{Q_L}{V_L} = \frac{Q_S}{V_S} \tag{17}$$

- Impeller speed: $n_L = k n_S$

- Circumferential speed: $w_L = k^2 w_S$
- Reynolds number: $\mathrm{Re}_L = k^3 \mathrm{Re}_S$
- Surface heat transfer coefficient: $h_L = k h_S$
- Heat transfer per unit volume: $\frac{Q_L}{V_L} = k^{-1} \frac{Q_S}{V_S}$
- Power demand per unit volume: $\frac{N_L}{V_L} = k^5 \frac{N_S}{V_S}$

3. RESULTS

The used expressions above in general are the exponential function of the scale-up ratio. So in the next table the exponents collected for the better overview.

Table 1 Results of the exponents of the criteria

	N/V=áll.	w=áll.	h=áll.	Q/V=áll.
n	-2/3	-1	-1/2	1
w	-1/3	0	1/2	2
Re	4/3	1	3/2	3
h	-1/9	-1/3	0	1
Q/V	-10/9	-4/3	-1	0
N/V	0	-1	1/2	5

4. CONCLUSIONS

In the case of the first and second criteria (N/V and w equivalent) which are the most common in stirred vessels, the transferred heat through the jacket considerably decreased. If the heat transfer per unit volume would be constant, the power demand would be significantly increased. Because of that in the case of jacketed equipment (with heat transfer) the usage of the first and second criteria are not recommended.

5. ACKNOWLEDGEMENT

This research was carried out as part of the TAMOP-4.2.1.B-10/2/KONV-2010-0001 project with support by the European Union, co-financed by the European Social Fund.

6. REFERENCES

[1] **NICOLAS P. CHOPHEY, DAVID S. DICKEY:** *Handbook of Chemical Engineering Calculations*, McGraw-Hill, USA, 2004, 438-467 p.
[2] *VDI Heat Atlas*, N3 chapter, Springer-Verlag Berlin Heidelberg 2010, DOI 10.1007/978-3-540-77877-6_63
[3] **BAEHR, H. D.:** *Verfahrenstechnische Berechnungsmethoden*, Teil 1: Wärmeübertrager. Springer-Verlag, 1988
[4] **NUSSELT W.:** *Die Oberflä chenkondesation des Wasserdampfes*, Z. Ver. Dt. Ing. 60, 1916, pp. 541–546.
[5] **VENCZEL G.:** *Hőelvonás polimerizációs reaktorból,* Miskolci Egyetem

Doktoranduszok Fóruma, Miskolc, 2003.

[6] **DONALD Q. KERN:** *Process Heat Transfer*, New York, McGraw-Hill Book Company, Inc., 1950.